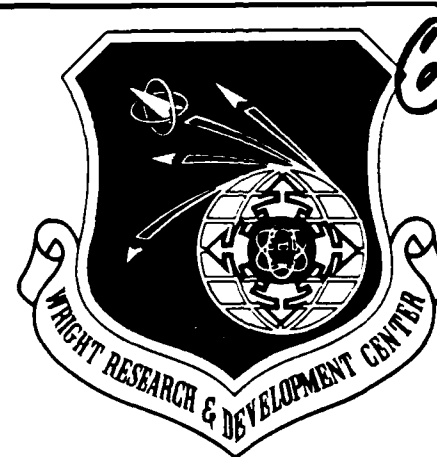


WRDC-TR-89-4094



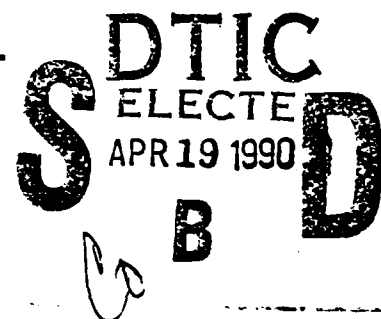
**THE EFFECTS OF SLIP CHARACTER  
AND CRACK CLOSURE  
ON THE GROWTH OF SMALL FATIGUE CRACKS  
IN TITANIUM-ALUMINIUM ALLOYS**

**James M. Larsen  
Materials Behavior Branch  
Metals and Ceramics Division**

**February 1990**

**Final Report for Period September 1982 – December 1987**

**Approved for public release; distribution unlimited.**



**MATERIALS LABORATORY  
WRIGHT RESEARCH AND DEVELOPMENT CENTER  
AIR FORCE SYSTEMS COMMAND  
WRIGHT-PATTERSON AIR FORCE BASE, OHIO 45433-6533**


90 04 16 016

AD-A220 714

## NOTICE

WHEN GOVERNMENT DRAWINGS, SPECIFICATIONS, OR OTHER DATA ARE USED FOR ANY PURPOSE OTHER THAN IN CONNECTION WITH A DEFINITELY GOVERNMENT-RELATED PROCUREMENT, THE UNITED STATES GOVERNMENT INCURS NO RESPONSIBILITY OR ANY OBLIGATION WHATSOEVER. THE FACT THAT THE GOVERNMENT MAY HAVE FORMULATED OR IN ANY WAY SUPPLIED THE SAID DRAWINGS, SPECIFICATIONS, OR OTHER DATA, IS NOT TO BE REGARDED BY IMPLICATION, OR OTHERWISE IN ANY MANNER CONSTRUED, AS LICENSING THE HOLDER, OR ANY OTHER PERSON OR CORPORATION; OR AS CONVEYING ANY RIGHTS OR PERMISSION TO MANUFACTURE, USE, OR SELL ANY PATENTED INVENTION THAT MAY IN ANY WAY BE RELATED THERETO.

THIS TECHNICAL REPORT HAS BEEN REVIEWED AND IS APPROVED FOR PUBLICATION.

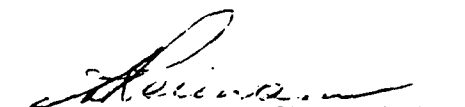


JAMES M. LARSEN



ALLAN W. GUNDERSON  
Technical Area Manager  
Metals and Ceramics Division

FOR THE COMMANDER



WALTER H. REIMANN  
Chief, Materials Behavior Branch  
Metals and Ceramics Division

IF YOUR ADDRESS HAS CHANGED, IF YOU WISH TO BE REMOVED FROM OUR MAILING LIST, OR IF THE ADDRESSEE IS NO LONGER EMPLOYED BY YOUR ORGANIZATION PLEASE NOTIFY WRDC/MLLN, WRIGHT-PATTERSON AFB, OH 45433-6533 TO HELP MAINTAIN A CURRENT MAILING LIST.

COPIES OF THIS REPORT SHOULD NOT BE RETURNED UNLESS RETURN IS REQUIRED BY SECURITY CONSIDERATIONS, CONTRACTUAL OBLIGATIONS, OR NOTICE ON A SPECIFIC DOCUMENT.

REPORT DOCUMENTATION PAGE				Form Approved OMB No. 0704-0188	
1a. REPORT SECURITY CLASSIFICATION UNCLASSIFIED			1b. RESTRICTIVE MARKINGS		
2a. SECURITY CLASSIFICATION AUTHORITY			3. DISTRIBUTION/AVAILABILITY OF REPORT Approved for public release; distribution is unlimited.		
2b. DECLASSIFICATION/DOWNGRADING SCHEDULE					
4. PERFORMING ORGANIZATION REPORT NUMBER(S)  WRDC-TR-89-4094			5. MONITORING ORGANIZATION REPORT NUMBER(S)		
6a. NAME OF PERFORMING ORGANIZATION Wright Research & Development Center, Materials Laboratory		6b. OFFICE SYMBOL (If applicable) WRDC/MLLN	7a. NAME OF MONITORING ORGANIZATION		
6c. ADDRESS (City, State, and ZIP Code) WRDC/MLLN Wright-Patterson AFB OH 45433-6533			7b. ADDRESS (City, State, and ZIP Code)		
8a. NAME OF FUNDING/SPONSORING ORGANIZATION		8b. OFFICE SYMBOL (If applicable)	9. PROCUREMENT INSTRUMENT IDENTIFICATION NUMBER		
8c. ADDRESS (City, State, and ZIP Code)			10. SOURCE OF FUNDING NUMBERS		
			PROGRAM ELEMENT NO. 61102F	PROJECT NO. 2302	TASK NO. P1
11. TITLE (Include Security Classification) The Effects of Slip Character and Crack Closure on the Growth of Small Fatigue Cracks in Titanium-Aluminum Alloys					
12. PERSONAL AUTHOR(S) JAMES M. LARSEN					
13a. TYPE OF REPORT Final		13b. TIME COVERED FROM Sep 82 TO Dec 87		14. DATE OF REPORT (Year, Month, Day) December 1987	
15. PAGE COUNT 261					
16. SUPPLEMENTARY NOTATION					
17. COSATI CODES			18. SUBJECT TERMS (Continue on reverse if necessary and identify by block number)		
FIELD	GROUP	SUB-GROUP			
11	06				
19. ABSTRACT (Continue on reverse if necessary and identify by block number)					
<p>An investigation was performed to study the effects of slip character and crack closure on the propagation of small fatigue cracks in titanium-aluminum alloys. The materials examined were solution-treated Ti-4Al and Ti-8Al, as well as aged Ti-8Al. The propagation of naturally initiated surface cracks of depths as small as 25 <math>\mu</math>m was compared with the behavior of large through-thickness cracks. An extensometer was used to monitor crack closure throughout the large-crack tests, and the closure behavior of the small cracks was measured using a computerized laser interferometric displacement gage having a displacement resolution of 0.01 <math>\mu</math>m. The measurements of</p>					
20. DISTRIBUTION/AVAILABILITY OF ABSTRACT <input checked="" type="checkbox"/> UNCLASSIFIED/UNLIMITED <input type="checkbox"/> SAME AS RPT. <input type="checkbox"/> DTIC USERS			21. ABSTRACT SECURITY CLASSIFICATION		
22a. NAME OF RESPONSIBLE INDIVIDUAL JAMES M. LARSEN			22b. TELEPHONE (Include Area Code) (513) 255-1357		22c. OFFICE SYMBOL WRDC/MLLN

(BLOCK 19)

crack closure were used to compute an effective stress intensity factor range.

$$\Delta K_{\text{eff}} = K_{\text{max}} \cdot K_{\text{cl.}}$$

In all three alloys and for all test conditions, which included a range of stress levels and stress ratios, small cracks propagated faster than large cracks subjected to an equivalent  $\Delta K$ , and the small cracks propagated under conditions that were significantly below the large-crack threshold,  $\Delta K_{\text{th}}$ . Although the character and distribution of slip in Ti-Al alloys may have a dramatic influence on fatigue crack initiation and on the propagation of large cracks, this effect was minimal for small cracks. When plotted against  $\Delta K_{\text{eff}}$ , the small-crack growth rate data from the three materials were collapsed into a single band and were in reasonable agreement with similar large-crack results. The observed disparity between large-and small-crack behavior was due largely to differences in microstructurally-controlled fatigue crack closure of large versus small cracks. Whereas large cracks exhibited fully developed crack closure, the small cracks experienced a transient period during which closure achieved the long-crack value. For the available data, the crack depth required for closure to develop ranged from 5 to 18 times the material's grain size. Crack closure arguments were only partially able to explain the behavior of small fatigue cracks. For surface cracks of depth less than approximately 1.5 times the material's grain size, the data of large and small cracks were not consolidated by  $\Delta K_{\text{eff}}$  in some instances. An extensive fractographic investigation revealed little evidence of differences in crack growth mechanism between the large and small cracks, and fracture-surface roughness was independent of crack length.

Accession For	
NTIS GRA&I	<input checked="checked" type="checkbox"/>
DTIC TAB	<input type="checkbox"/>
Unannounced	<input type="checkbox"/>
Justification	
By	
Distribution/	
Availability Codes	
Dist	Avail and/or Special
A-1	



CARNEGIE MELLON UNIVERSITY

THE EFFECTS OF SLIP CHARACTER AND CRACK CLOSURE  
ON THE GROWTH OF SMALL FATIGUE CRACKS  
IN TITANIUM-ALUMINUM ALLOYS

A DISSERTATION  
SUBMITTED TO THE GRADUATE SCHOOL  
IN PARTIAL FULFILLMENT OF THE REQUIREMENTS  
for the degree  
DOCTOR OF PHILOSOPHY  
in  
METALLURGICAL ENGINEERING AND MATERIALS SCIENCE

by

JAMES MILLIGAN LARSEN

Pittsburgh, Pennsylvania

December, 1987

## TABLE OF CONTENTS

<b>1. INTRODUCTION</b>	<b>1</b>
<b>2. BACKGROUND</b>	<b>5</b>
2.1 Small-Crack Phenomena	5
2.2 Definitions of a Small Crack	11
2.3 Inaccurate Characterization of Crack Driving Force	13
2.4 Small Cracks at Notches	16
2.5 Local Microstructural Effects	19
2.5.1 Effects of Grain Boundaries	21
2.5.2 Effects of Grain Size	25
2.5.3 Effects of Multiphase Microstructures	28
2.5.4 Effect of Alloy Slip Character	30
2.5.5 Effects of Crystallographic Texture	31
2.5.6 Differences in Crack Growth Mechanism	32
2.6 Crack-Shape Effects	33
2.7 Multiple-Crack Interactions	35
2.8 Effects of Crack Closure	37
2.9 Differences in Local Crack-Tip Environment	50
2.10 An Assessment of the Literature on the Growth of Small Cracks	50
2.10.1 Rationale for the Present Investigation	50
2.10.2 Selection of an Alloy System	53
2.11 Titanium-Aluminum Alloys	54
2.11.1 Physical Properties of Ti-Al Alloys	54
2.11.2 Mechanical Behavior of Ti-Al Alloys	57

2.12 Objective of the Research	64
<b>3. EXPERIMENTAL PROCEDURE</b>	<b>65</b>
3.1 Materials: Processing and Heat Treatment	65
3.2 Microstructural Characterization	68
3.2.1 Light Metallography	68
3.2.3 Crystallographic Pole-Figure Analysis	69
3.2.4 Transmission Electron Microscopy	69
3.3 Mechanical Property Characterization	69
3.3.1 Tensile Testing	70
3.3.2 High-Cycle-Fatigue Testing	71
3.3.3 Large-Crack Fatigue Testing	72
3.3.4 Small-Crack Fatigue Testing	76
3.3.5 Determination of Crack Closure	89
3.4 Fractography	92
3.4.1 Scanning Electron Microscopy	92
3.4.2 Quantitative Fractography	92
<b>4. RESULTS</b>	<b>94</b>
4.1 Microstructural Characterization	97
4.1.1 Light Metallography	94
4.1.2 Transmission Electron Microscopy	97
4.1.3 Characterization of Rolling Texture	97
4.2 Characterization of Mechanical Properties	102
4.2.1 Tensile Testing	102
4.2.2 High-Cycle-Fatigue Testing	104
4.2.3 Large-Crack Fatigue Testing	106

4.2.4	Anticipated Small-Crack Behavior	125
4.2.5	Small-Crack Fatigue Testing	127
4.2.5.1	Initiation of Small Cracks	127
4.2.5.2	Characterization of Crack Shape	128
4.2.5.3	Measurement of Small Cracks	128
4.2.5.4	Propagation of Small Cracks	134
4.2.5.4.1	Effect of Stress Level	135
4.2.5.4.2	Effect of Stress Ratio	139
4.2.5.4.3	Effect of Alloy Condition (Slip Character)	144
4.2.5.5	Measurement of Closure of Small Cracks	147
4.2.5.6	The Utility of $\Delta K_{eff}$	157
4.2.5.6.1	Effect of Stress Level	157
4.2.5.6.2	Effect of Stress Ratio	167
4.2.5.6.3	Effect of Alloy Condition (Slip Character)	168
4.3	Fractography	168
4.3.1	Scanning Electron Microscopy	169
4.3.1.1	Large-Crack Specimens	169
4.3.1.2	Small-Crack Specimens	178
4.3.2	Quantitative Fractography	187
4.3.2.1	Large-Crack Specimens	187
4.3.2.2	Small-Crack Specimens	191
5.	DISCUSSION	195
5.1	Secondary Experimental Variables	195
5.1.1	Multiple-Crack Effects	195
5.1.2	Differences in Local Crack-Tip Environment	196
5.1.3	Crack-shape Effects	196

5.1.3.1	Initiation from Inherent Material Defects	196
5.1.3.2	Initiation from Persistent Slip Bands	197
5.1.3.3	Crack-Shape Effects on the Stress Intensity Factor	198
5.2	Primary Experimental Variables	201
5.2.1	Effects of Crack-Tip Plasticity	201
5.2.2	Local Microstructural Effects	205
5.2.2.1	Effects of Grain Boundaries	205
5.2.2.2	Effects of Grain Size	208
5.2.2.3	Effects of Crystallographic Texture	211
5.2.2.4	Differences in Crack Growth Mechanism	212
5.2.2.5	Effects of Alloy Slip Character	213
5.2.2.5.1	Effects of Alloy Slip Character on Fatigue Crack Propagation	215
5.2.2.6	Effects of Crack Closure	218
5.2.2.6.1	Closure of Small Cracks	223
5.3	Implications for Design of Damage Tolerant Alloys	227
6.	SUMMARY AND CONCLUSIONS	228
7.	RECOMMENDATIONS FOR FUTURE RESEARCH	233
8.	APPENDIX 1 - MODIFIED INCREMENTAL POLYNOMIAL METHOD	235
9.	APPENDIX 2 - SUMMARY OF CRACK GROWTH TESTS	239
10.	REFERENCES	240

## List of Figures

Fig. 2.1	Crack growth rate data demonstrating the "anomalous" behavior of small fatigue cracks [20,21].	6
Fig. 2.2	Fatigue-limit stress predicted by combining crack initiation and crack growth concepts.	8
Fig. 2.3	Threshold stress intensity factor range predicted by combining crack initiation and crack growth concepts.	8
Fig. 2.4	Small crack data illustrating the utility of the normalizing parameter $a_0$ [26].	10
Fig. 2.5	Growth rate data for small fatigue cracks emanating from notches [58].	17
Fig. 2.6	Limiting stress intensity factor solutions for a crack emanating from a hole [60]. A numerical solution is also presented [65].	18
Fig. 2.7	Schematic illustration of a small crack propagating within a notch field [66].	20
Fig. 2.8	Schematic illustration of the growth behavior of a small crack emanating from a notch [66].	20
Fig. 2.9	Schematic illustration of the crack sizes that are argued to be limits for the valid application of crack initiation ( $a_1$ ) and $\Delta K_{Ih}$ ( $a_2$ ) concepts [86].	22
Fig. 2.10	The effect of grain size on vacuum fatigue crack propagation data of large through-cracks and small surface cracks in aged Ti-8.6Al [112].	27
Fig. 2.11	A comparison fatigue crack growth rates of short and long cracks in fine-grain (FG) and coarse-grain (CG) Astroloy [114].	29
Fig. 2.12	Surface-crack shape changes that produce artificially rapid growth rates based on observations of the specimen surface [after 131,132]. The observed $dc/dN$ strongly resembles the behavior of a small crack approaching a microstructural barrier.	34
Fig. 2.13	Ti-8.6Al small-crack shapes determined by serial polishing [113]. Small, shallow cracks were found to develop from slip bands that were pinned at grain boundaries. Repetition of this process eventually produced a crack of approximately semicircular shape.	36
Fig. 2.14	Schematic illustration of the various mechanisms of fatigue crack closure [after 137].	38

Fig. 2.15	Normalized crack-opening stresses as function of stress ratio (R) under constant-amplitude fatigue [156]. The effect of plastic constraint is shown, including a calculation for Irwin's plane-strain condition which simulates three-dimensional constraint.	40
Fig. 2.16	Three-dimensional surface-crack opening behavior often observed as the mode I load is increased from zero [after 190].	45
Fig. 2.17	SEM measurements of residual crack-tip-opening displacement of surface cracks in Ti-6Al-2Sn-4Zr-6Mo showing the apparent dependence of crack closure on crack length [198-200].	48
Fig. 2.18	Crack growth rate data from notched specimens demonstrating the ability of $\Delta K_{eff}$ to consolidate growth rates from long and short cracks [201].	49
Fig. 2.19	Titanium-aluminum phase diagram of Blackburn [212] showing a modification by Nambodhiri et al [229] for alloys of low oxygen concentration.	56
Fig. 2.20	TEM micrographs showing the influence of aluminum content and aging on the dislocation structures produced by cyclic loading ( $\Delta\epsilon/2 = 1\%$ ). (a) Ti-4Al; (b) Ti-8Al; (c) aged Ti-8Al.	62
Fig. 3.1	The specimen used for monotonic tensile testing.	70
Fig. 3.2	The hourglass specimen used to determine fatigue strength.	71
Fig. 3.3	The large-crack, compact-type, C(T), specimen.	73
Fig. 3.4	The small-crack fatigue specimen.	78
Fig. 3.5	The surface-crack geometry illustrating various dimensions and parameters.	82
Fig. 3.6	Schematic illustrating the principle of operation of the interferometric displacement gage (IDG).	85
Fig. 3.7	Schematic illustration of the computerized interferometric system.	85
Fig. 3.8	Photograph of the small-crack test apparatus showing both the laser interferometric displacement system and the microscope used by the photographic system.	87
Fig. 3.9	Typical load versus crack-mouth-opening displacement data for a small surface crack. Differential load-displacement data are also shown.	90
Fig. 4.1	Equiaxed, recrystallized microstructure of Ti-4Al.	95

Fig. 4.2	Example of isolated unrecrystallized grains occasionally observed near the midthickness of the rolled Ti-4Al plate. The unrecrystallized grains are elongated along the rolling direction.	95
Fig. 4.3	Equiaxed, recrystallized microstructure of Ti-8Al.	96
Fig. 4.4	Bright- and dark-field TEM micrographs of precipitate structure in the aged Ti-8Al alloy.	98
Fig. 4.5	Ti-4Al basal (0002) pole figure.	99
Fig. 4.6	Ti-4Al prism ( $10\bar{1}0$ ) pole figure.	99
Fig. 4.7	Ti-4Al pyramidal ( $10\bar{1}1$ ) pole figure.	100
Fig. 4.8	Ti-8Al basal (0002) pole figure.	100
Fig. 4.9	Ti-8Al prism ( $10\bar{1}0$ ) pole figure.	101
Fig. 4.10	Ti-8Al pyramidal ( $10\bar{1}1$ ) pole figure.	101
Fig. 4.11	Stress versus life (S-N) data for Ti-4Al tested under $R = -1.0$ fatigue.	105
Fig. 4.12	Stress versus life (S-N) data for Ti-8Al(s) tested under $R = -1.0$ fatigue.	105
Fig. 4.13	Stress versus life (S-N) data for Ti-8Al(a) tested under $R = -1.0$ fatigue.	106
Fig. 4.14	Crack propagation data for large cracks in C(T) specimens tested under $R = 0.1$ , constant load-amplitude fatigue.	108
Fig. 4.15	Crack propagation data for large cracks in C(T) specimens tested under $R = 0.5$ , constant load-amplitude fatigue.	109
Fig. 4.16	Effect of stress ratio on the propagation of large cracks in Ti-4Al.	110
Fig. 4.17	Effect of stress ratio on the propagation of large cracks in Ti-8Al(s).	111
Fig. 4.18	Effect of stress ratio on the propagation of large cracks in Ti-8Al(a).	112
Fig. 4.19	Normalized crack-closure levels for Ti-Al alloys tested under $R=0.1$ fatigue.	113
Fig. 4.20	Normalized crack-closure levels for Ti-Al alloys tested under $R=0.5$ fatigue.	115
Fig. 4.21	Absolute crack-closure levels for Ti-Al alloys tested under $R=0.1$ fatigue.	116



Fig. 4.22	Absolute crack-closure levels for Ti-Al alloys tested under $R=0.5$ fatigue.	117
Fig. 4.23	Crack propagation data for large cracks in C(T) specimens tested under $R = 0.1$ fatigue. Data plotted as $da/dN$ versus $\Delta K_{eff}$ .	119
Fig. 4.24	Crack propagation data for large cracks in C(T) specimens tested under $R = 0.5$ fatigue. Data plotted as $da/dN$ versus $\Delta K_{eff}$ .	120
Fig. 4.25	Effect of stress ratio on the propagation of large cracks in Ti-4Al. Data plotted as $da/dN$ versus $\Delta K_{eff}$ .	121
Fig. 4.26	Effect of stress ratio on the propagation of large cracks in Ti-8Al(s). Data plotted as $da/dN$ versus $\Delta K_{eff}$ .	122
Fig. 4.27	Effect of stress ratio on the propagation of large cracks in Ti-8Al(a). Data plotted as $da/dN$ versus $\Delta K_{eff}$ .	123
Fig. 4.28	"Kitagawa" diagram constructed for the three Ti-Al alloy using both $\Delta K_{th}$ and $\Delta K_{eff(th)}$ .	125
Fig. 4.29	Crack-shape data obtained from measurements of heat-tinted fracture surfaces.	129
Fig. 4.30	Typical data showing the correspondence between crack length measurements obtained photographically and from compliance (Ti-8Al(s), $R = 0.1$ , $\sigma_{max}/\sigma_y = 0.6$ ).	131
Fig. 4.31	Crack growth rate data reduced from <u>photographic</u> measurements of the length of a small fatigue crack in the alloy Ti-8Al(s); $R = 0.1$ , $\sigma_{max}/\sigma_y = 0.6$ .	132
Fig. 4.32	Crack growth rate data reduced from <u>compliance</u> measurements of the length of a small fatigue crack in the alloy Ti-8Al(s); $R = 0.1$ , $\sigma_{max}/\sigma_y = 0.6$ . The superimposed solid line represents the corresponding data from photographic measurements shown in Fig. 4.31.	133
Fig. 4.33	Plot of $da/dN$ - $\Delta K$ illustrating the effect of stress level on the growth of small cracks in Ti-4Al fatigued at $R = 0.1$ .	136
Fig. 4.34	Plot of $da/dN$ - $\Delta K$ illustrating the effect of stress level on the growth of small cracks in Ti-8Al(a) fatigued at $R = 0.1$ .	137
Fig. 4.35	Plot of $da/dN$ - $\Delta K$ illustrating the effect of stress level on the growth of small cracks in Ti-8Al(s) fatigued at $R = 0.1$ .	138
Fig. 4.36	Plot of $da/dN$ - $\Delta K$ illustrating the effect of stress level on the growth of small cracks in Ti-8Al(s) fatigued at $R = -1.0$ .	140
Fig. 4.37	Plot of $da/dN$ - $\Delta K$ illustrating the effect of stress level on the growth of small cracks in Ti-8Al(s) fatigued at $R = 0.5$ .	141

Fig. 4.38	Plot of $da/dN-\Delta K$ illustrating the effect of stress ratio ( $R$ ) on the growth of small cracks in Ti-8Al(s) tested with $\sigma_{\max}/\sigma_y = 0.6$ .	142
Fig. 4.39	Plot of $da/dN-\Delta K$ illustrating the effect of stress ratio ( $R$ ) on the growth of small cracks in Ti-8Al(s) tested with $\sigma_{\max}/\sigma_y = 0.9$ .	143
Fig. 4.40	Plot of $da/dN-\Delta K$ illustrating the effect of alloy condition on the growth of small cracks propagated under $R = 0.1$ fatigue with $\sigma_{\max}/\sigma_y = 0.6$ .	145
Fig. 4.41	Plot of $da/dN-\Delta K$ illustrating the effect of alloy condition on the growth of small cracks propagated under $R = 0.1$ fatigue with $\sigma_{\max}/\sigma_y = 0.9$ .	146
Fig. 4.42	Normalized small-crack closure behavior observed in each of the three alloy conditions tested under $R = 0.1$ fatigue ( $\sigma_{\max}/\sigma_y = 0.6$ ).	148
Fig. 4.43	Normalized small-crack closure behavior observed in each of the three alloy conditions tested under $R = 0.1$ fatigue ( $\sigma_{\max}/\sigma_y = 0.9$ ).	149
Fig. 4.44	The effect of stress ratio on normalized small-crack closure behavior in Ti-8Al(s) ( $\sigma_{\max}/\sigma_y = 0.6$ ).	150
Fig. 4.45	The effect of stress ratio on normalized small-crack closure behavior in Ti-8Al(s) ( $\sigma_{\max}/\sigma_y = 0.9$ ).	151
Fig. 4.46	Absolute small-crack closure behavior observed in each of the three alloy conditions tested under $R = 0.1$ fatigue ( $\sigma_{\max}/\sigma_y = 0.6$ ).	152
Fig. 4.47	Absolute small-crack closure behavior observed in each of the three alloy conditions tested under $R = 0.1$ fatigue ( $\sigma_{\max}/\sigma_y = 0.9$ ).	153
Fig. 4.48	The effect of stress ratio on absolute small-crack closure behavior in Ti-8Al(s) ( $\sigma_{\max}/\sigma_y = 0.6$ ).	154
Fig. 4.49	The effect of stress ratio on absolute small-crack closure behavior in Ti-8Al(s) ( $\sigma_{\max}/\sigma_y = 0.9$ ).	155
Fig. 4.50	Plot of $da/dN-\Delta K_{\text{eff}}$ illustrating the effect of stress level on the growth of small cracks in Ti-4Al fatigued at $R = 0.1$ .	158
Fig. 4.51	Plot of $da/dN-\Delta K_{\text{eff}}$ illustrating the effect of stress level on the growth of small cracks in Ti-8Al(a) fatigued at $R = 0.1$ .	159
Fig. 4.52	Plot of $da/dN-\Delta K_{\text{eff}}$ illustrating the effect of stress level on the growth of small cracks in Ti-8Al(s) fatigued at $R = 0.1$ .	160
Fig. 4.53	Plot of $da/dN-\Delta K_{\text{eff}}$ illustrating the effect of stress level on the growth of small cracks in Ti-8Al(s) fatigued at $R = -1.0$ .	161

Fig. 4.54	Plot of $da/dN-\Delta K_{eff}$ illustrating the effect of stress level on the growth of small cracks in Ti-8Al(s) fatigued at $R = 0.5$ .	162
Fig. 4.55	Plot of $da/dN-\Delta K_{eff}$ illustrating the effect of stress ratio ( $R$ ) on the growth of small cracks in Ti-8Al(s) tested with $\sigma_{max}/\sigma_y = 0.6$ .	163
Fig. 4.56	Plot of $da/dN-\Delta K_{eff}$ illustrating the effect of stress ratio ( $R$ ) on the growth of small cracks in Ti-8Al(s) tested with $\sigma_{max}/\sigma_y = 0.9$ .	164
Fig. 4.57	Plot of $da/dN-\Delta K_{eff}$ illustrating the effect of alloy condition on the growth of small cracks propagated under $R = 0.1$ fatigue with $\sigma_{max}/\sigma_y = 0.6$ .	165
Fig. 4.58	Plot of $da/dN-\Delta K_{eff}$ illustrating the effect of alloy condition on the growth of small cracks propagated under $R = 0.1$ fatigue with $\sigma_{max}/\sigma_y = 0.9$ .	166
Fig. 4.59	Fracture surface of a Ti-4Al C(T) specimen fatigued at $R = 0.1$ ; $\Delta K = 5.1 \text{ MPa}\sqrt{\text{m}}$ and $da/dN = 10^{-10} \text{ m/cycle}$ .	171
Fig. 4.60	Fracture surface of a Ti-4Al C(T) specimen fatigued at $R = 0.1$ ; $\Delta K = 9.7 \text{ MPa}\sqrt{\text{m}}$ and $da/dN = 10^{-8} \text{ m/cycle}$ .	172
Fig. 4.61	Fracture surface of a Ti-8Al(s) C(T) specimen fatigued at $R = 0.1$ ; $\Delta K = 12.4 \text{ MPa}\sqrt{\text{m}}$ and $da/dN = 10^{-10} \text{ m/cycle}$ .	173
Fig. 4.62	Fracture surface of a Ti-8Al(s) C(T) specimen fatigued at $R = 0.1$ ; $\Delta K = 20.4 \text{ MPa}\sqrt{\text{m}}$ and $da/dN = 10^{-8} \text{ m/cycle}$ .	174
Fig. 4.63	Fracture surface of a Ti-8Al(a) C(T) specimen fatigued at $R = 0.1$ ; $\Delta K = 7.2 \text{ MPa}\sqrt{\text{m}}$ and $da/dN = 10^{-10} \text{ m/cycle}$ .	176
Fig. 4.64	Fracture surface of a Ti-8Al(a) C(T) specimen fatigued at $R = 0.1$ ; $\Delta K = 13.0 \text{ MPa}\sqrt{\text{m}}$ and $da/dN = 10^{-8} \text{ m/cycle}$ .	177
Fig. 4.65	Fracture surface of a Ti-4Al small-crack specimen fatigued at $R = 0.1$ and having $\sigma_{max}/\sigma_y = 0.6$ .	179
Fig. 4.66	Fracture surface of a Ti-8Al(s) small-crack specimen fatigued at $R = 0.1$ and having $\sigma_{max}/\sigma_y = 0.9$ .	181
Fig. 4.67	Fracture surface of a Ti-8Al(a) small-crack specimen fatigued at $R = 0.1$ and having $\sigma_{max}/\sigma_y = 0.6$ .	182
Fig. 4.68	Fracture surface of a Ti-4Al small-crack specimen fatigued at $R = 0.1$ and having $\sigma_{max}/\sigma_y = 0.9$ . A large unrecrystallized grain is shown near the site of crack initiation, which is located above the Vickers indentation.	184

Fig. 4.69	Fracture surface of a Ti-8Al(a) small-crack specimen fatigued at $R = 0.5$ and having $\sigma_{\max}/\sigma_y = 0.6$ . The crack initiation site is located above the Vickers indentation, which is visible on the surface of the specimen.	186
Fig. 4.70	C(T) specimen fracture surface profiles obtained from regions of two different growth rates in the each of the three Ti-Al alloy conditions.	189
Fig. 4.71	Measured lineal roughness of the fracture surface profiles illustrated in Fig. 4.63.	190
Fig. 4.72	Measured lineal roughness of the fracture surface profiles illustrated in Fig. 4.63 plotted against the corresponding measurement of $K_{cl}$ .	190
Fig. 4.73	Fracture surface profiles obtained from each of the small-crack specimens.	192
Fig. 5.1	Dimensionless stress intensity factor as a function of the parametric angle $\phi$ (see Fig. 3.5) for a range in aspect ratios ( $a/c$ ), assuming that $a$ and $c \ll$ specimen dimensions. The figure shows that the surface-crack stress intensity factor solution is only mildly sensitive to variations in $a/c$ .	199
Fig. 5.2	Schematic illustration of the form of the development of small-crack closure in in the three Ti-Al alloys.	225
Fig. 8.1	Schematic illustrating the principles of the modified incremental method for reduction of crack growth data.	237

## List of Tables

Table 2.1: Classes of Small Fatigue Cracks [44,45].	11
Table 2.2: Slip and Twinning Modes in $\alpha$ -Phase Titanium [232].	58
Table 3.1: Chemical Composition of Ti-Al Alloys (Weight %).	66
Table 3.2: Heat Treatment of Ti-Al Alloys.	68
Table 4.1: Ti-Al Alloy Grain-Size Measurements.	97
Table 4.2: Tensile Properties of Ti-Al Alloys.	103
Table 4.3: Fatigue Strength of Ti-Al Alloys.	106
Table 4.4: Threshold Stress Intensity Factor Ranges.	124
Table 4.5: Experimental Data and Calculated Parameters Used in Constructing Fig. 4.28.	126
Table 4.6: Small-Crack Test Conditions.	134
Table 4.7: C(T) Specimen Fracture Surface Roughness Measurements.	188
Table 4.8: Small-Crack Fracture Surface Roughness Measurements.	193
Table 5.1: Normalized Plastic Zone Size Calculations.	204
Table 5.2: Effect of Grain Size on Threshold Stress Intensity Factor Range and Crack Closure Stress Intensity Factor for Tests Conducted at $R = 0.1$ .	209
Table 5.3: Crack Size at Which Small and Large-Crack Data Converge When Plotted Versus Nominally Applied $\Delta K$ .	211

## ACKNOWLEDGMENT

This research was performed in the Materials Behavior Branch, Materials Laboratory, Wright Research and Development Center, Wright-Patterson Air Force Base, Ohio and was funded by the Air Force Office of Scientific Research under project 2302P101. I would like to acknowledge the continued encouragement and advice of Dr. T. Nicholas, the in-house research group leader, who also provided the long-term support necessary to implement the automated interferometric displacement gage used in the research. Dr. Nicholas has been responsible for establishing and maintaining a first-rate laboratory, while also providing a healthy, professional research environment. Beyond this direct technical support within the Materials Laboratory, I wish to thank Dr. J. P. Henderson, Chief of the Metal Behavior Branch, who continually supported my efforts both technically and managerially throughout the research project.

I would further like to acknowledge and thank my primary thesis advisor, Dean J. C. Williams who initially encouraged me to attend Carnegie Mellon University and has since been an ever present source of technical advice and stimulation. I am also indebted to Professor A. W. Thompson who served as a co-advisor throughout the research and provided invaluable guidance. Thanks also go to the other members of my thesis committee: Professors W. M. Garrison and J. H. Griffin of Carnegie Mellon University and Professor S. D. Antolovich of Georgia Institute of Technology. They each made valuable comments regarding the research, and their time and effort are greatly appreciated. I would also like to thank Dr. J. E. Allison of Ford Research Laboratory for providing the Ti-4Al, as well as for his enlightening discussion regarding mechanical behavior of the Ti-Al alloys.

Many of my colleagues and friends at the Materials Laboratory at Wright-Patterson were of invaluable assistance. Notably, J. R. Jira and Dr. T. Weerasooriya should be credited with automating the interferometric displacement gage, making possible some critical elements of the experimental program. In the early portion of the fatigue testing, S. Ramsey provided experimental assistance, and during the final months, R. Goodman was a valued participant. I also wish to thank R. K. Lewis, E. C. Harper, R. D. Brodecki, R. E. Omlor, and Dr. A. G. Jackson for their help with various aspects of specimen preparation and microscopy. During the final preparation of the manuscript, D. Coker was extremely helpful with data reduction and in preparing the final document.

I would like to thank my parents who were of unending support over the years, although at times I'm sure they were "puzzled" by my approach. Finally, I would like to thank, gratefully, my wife Elizabeth, who never wavered in her patience and understanding over the years. This dissertation contains much of both of us.

## CHAPTER 1

### INTRODUCTION

The ability to predict accurately the life of structural components that experience cyclic loading is essential to the reliability and cost effectiveness of many modern structures, vehicles, and propulsion systems. A primary example of a system that requires such a life prediction capability is the high-performance gas turbine engine. The useful life of major rotating components in these engines traditionally has been determined through the use of crack initiation concepts [1,2]; however, more recently, an approach based on crack growth and fracture mechanics concepts has been used. Under a program known as Retirement-for-Cause of Turbine Engine Components [3- 6], the United States Air Force is implementing a crack growth methodology for life management of selected components in the F100 engine, which propels the F-15 and F-16 aircraft. In addition, under a separate effort known as the Engine Structural Integrity Program (ENSIP) [7-10] the Air Force has established a damage tolerant design specification for fracture-critical components in future engines. According to this requirement, flaws or defects must be assumed to exist in the components at the time of production, and design calculations and component testing must demonstrate that such defects will not grow to a critical size for catastrophic failure within the lifetime of the engine.

In support of the damage tolerant approach, extensive research has been conducted to develop analytical models of crack growth, which are used to predict the life of engine components under anticipated operating conditions [11-14]. In general, the required experimental data have been produced by testing specimens containing relatively large



cracks and using fracture mechanics methods to predict the behavior of smaller, naturally occurring cracks in actual components.

Implicit in the damage tolerant approach is the assumption of similitude between the behavior of the large cracks grown in laboratory specimens and the small cracks that occur in actual service. Recently, however, a number of investigators have observed that very small fatigue cracks may grow anomalously fast when compared to large cracks in conventional specimens subjected to a nominally equivalent crack driving force. Furthermore, small cracks have been observed to propagate under conditions that are well below the threshold stress intensity factor range,  $\Delta K_{th}$ , which is known to limit the propagation of long cracks. These deficiencies of currently available fracture mechanics methods to predict the behavior of very small cracks have serious implications with regard to damage tolerance, because such errors could lead to a significant overestimate of the actual component life [15-18].

To date, errors in the predictions of the growth of small fatigue cracks in turbine components have apparently not caused serious problems. The reason for this good fortune appears to be connected jointly with the characteristics of the specific materials involved and the capability of existing nondestructive inspection methods for monitoring the growth of cracks. For most materials used in high-performance turbine engines, the size of a reliably detectable crack has generally been greater than the crack size for which there are appreciable errors in predictions of the growth of small cracks. However, improvements in nondestructive inspection methods are forthcoming [19], and the crack size that can be reliably detected will be reduced significantly. As the inspectable crack size decreases, the accuracy of predictions of crack propagation will become increasingly in question due to the potentially rapid growth of small cracks. In fact, recent data on the nickel-base superalloy Astroloy [15] indicate that a factor-of-two reduction in the

inspectable crack size will result in an order-of-magnitude error in the prediction of crack growth in turbine disks. Thus, it appears that the absence of a significant "small-crack problem" in advanced turbine engines has been fortuitous and that the behavior of small fatigue cracks will become much more significant as the technology of nondestructive inspection improves.

In addition to concerns pertaining to life prediction of actual engine hardware, the behavior of small fatigue cracks has important implications with regard to the selection of new materials for the next-generation engines. Microstructural modifications that improve crack initiation properties often do so at the expense of crack propagation resistance, and the reverse is also true. Optimization of alloy microstructures to produce durable, defect-tolerant materials requires a fundamental understanding of the relative roles of crack initiation and crack propagation in governing the total fatigue life of a structural component. Although, historically, fatigue research has often focused separately on crack initiation or on crack propagation, the study of small fatigue cracks serves to link the two phenomena and should provide insight into micromechanisms that control overall fatigue performance.

Study of the mechanics and physics of the propagation of small fatigue cracks is, therefore, fundamental to both life management of actual structural components and to the design of improved materials. Although numerous experimental and analytical investigations of the behavior of small fatigue cracks have been conducted to date, many questions remain unanswered. While there exists a large body of literature dealing with effects of microstructural variables on both crack initiation and crack propagation, relatively little research has been performed specifically to study metallurgical aspects of the growth of small cracks while maintaining a fracture mechanics framework. Such research is necessary to support a damage-tolerant life-management philosophy and is

essential to developing an understanding of the structure/property relationships that control an alloy's fatigue performance.

It is the goal of the present research project to investigate the influence of microstructural variables on the growth of small cracks, to isolate specific mechanisms that may lead to fundamentally different behavior of large and small cracks, and to determine the useful limits of linear elastic fracture mechanics as applied to small cracks. The complete background and rationale for the research will be developed in the following section.

## CHAPTER 2

### BACKGROUND

#### 2.1 Small-Crack Phenomena

The central concern pertaining to small fatigue cracks regards their "anomalous" growth behavior when compared with large cracks grown in conventional specimens. Within the framework of linear elastic fracture mechanics (LEFM), Pearson [20] first demonstrated the disparity between large- and small-crack propagation behavior in fatigue tests of two commercial aluminum alloys. Figure 2.1 presents some of these data for the British alloy DTD 5050 along with more recent results of Lankford [21] on the similar aluminum alloy 7075-T6. The small-crack data are from naturally initiated surface flaws, while the corresponding large-crack data were generated using conventional single-edge-notch (SEN) specimens. As shown in the figure, when crack growth rate is plotted versus the nominal applied stress intensity factor range ( $\Delta K$ ), the small cracks propagate significantly faster than equivalent large cracks. Furthermore, the small cracks often grow under loading conditions that are well below the threshold stress intensity factor range ( $\Delta K_{th}$ ) required for the propagation of large cracks. The smallest cracks may initially decelerate as crack length increases and may arrest under some conditions. Otherwise, after achieving a minimum growth rate, the small cracks accelerate and eventually join the data for large cracks.

Kitagawa and Takahashi [22] presented an alternative view of the "small-crack problem" by showing that threshold crack growth rate data display a dependence on crack

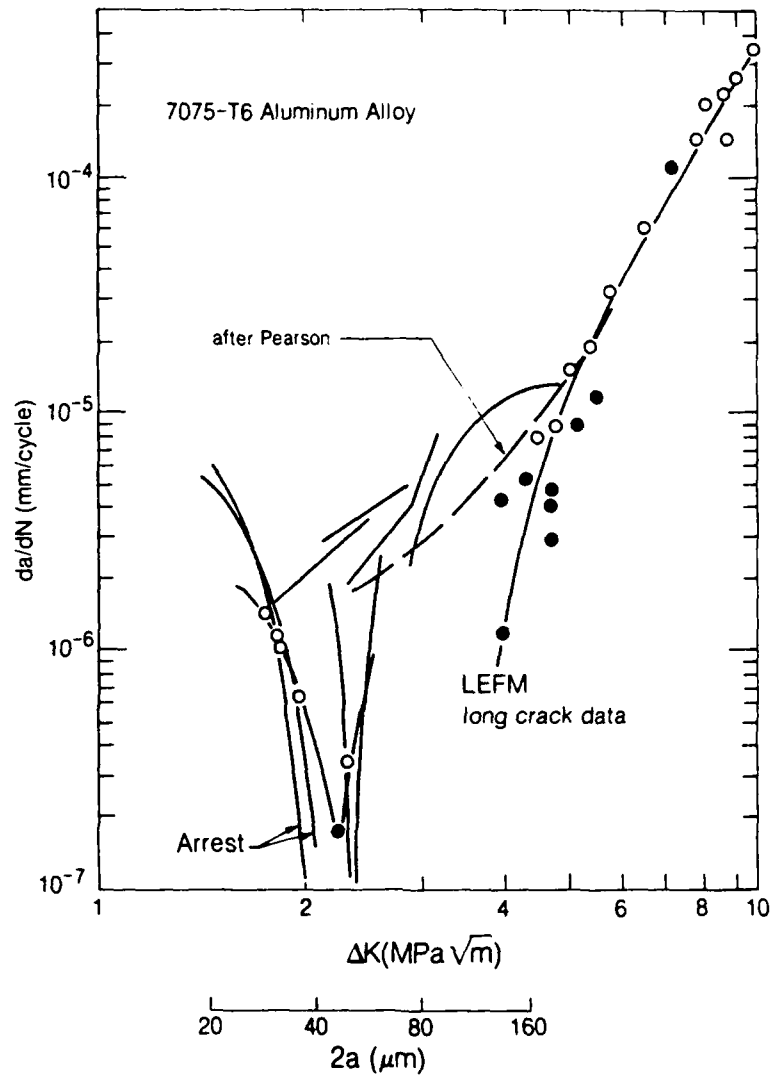


Fig. 2.1 Crack growth rate data demonstrating the "anomalous" behavior of small fatigue cracks [20,21].

size that is related to the material's fatigue strength ( $\Delta\sigma_e$ ) and  $\Delta K_{th}$ . This idea, which combines fatigue crack initiation and propagation concepts, is illustrated schematically in Figure 2.2. Considering crack initiation, and disregarding the possibility of a preexisting crack, specimen failure should occur only if  $\Delta\sigma_{applied} > \Delta\sigma_e$ . Alternatively, considering a fracture mechanics approach, crack growth should occur only if

$$\Delta K_{applied} > \Delta K_{th} = f\Delta\sigma(\pi a)^{0.5}, \quad (2.1)$$

where  $f$  is a function of crack and specimen geometry and  $a$  is the crack length. Solving this equation for  $\Delta\sigma$  gives

$$\Delta\sigma = \Delta K_{th}/(f(\pi a)^{0.5}), \quad (2.2)$$

indicating that crack propagation should only occur in the region above the line of slope equal to  $-1/2$ . Thus, the utility of  $\Delta K_{th}$  as a "material property" is limited to cracks of length greater than that given by the intersection of the two lines ( $a_0$ ). The crack-size dependence of  $\Delta K_{th}$  may be illustrated in the alternative form shown in Fig. 2.3, which plots  $\Delta K_{th}$  as a function of crack length. Here again, a constant value of  $\Delta K_{th}$  is maintained for large cracks, while small cracks exhibit a  $\Delta K_{th}$  that is dependent on crack length.

In an effort to maintain the utility of the available large-crack data base that has been generated using  $\Delta K$  as a correlative parameter, El Haddad et al [23-25] proposed the modified equation

$$\Delta K = f\Delta\sigma(\pi(a + a_0))^{0.5} \quad (2.3)$$

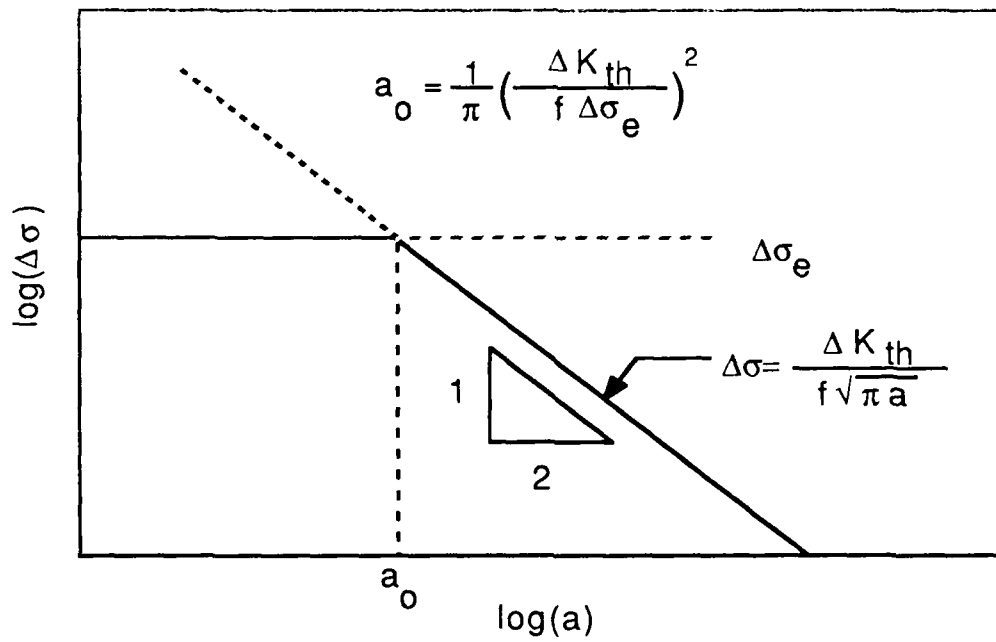


Fig. 2.2 Fatigue-limit stress predicted by combining crack initiation and crack growth concepts.

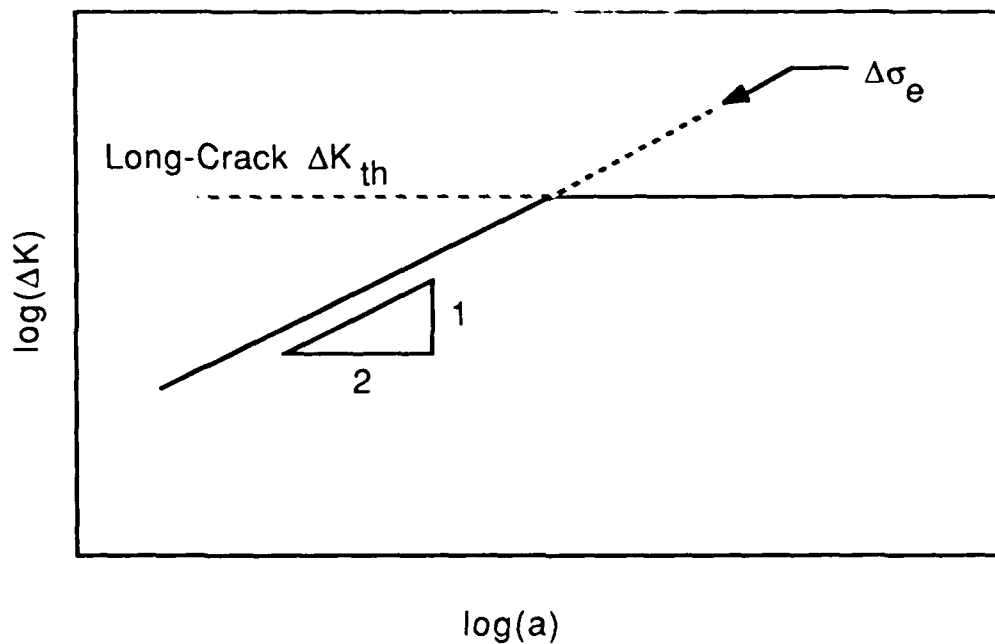


Fig. 2.3 Threshold stress intensity factor range predicted by combining crack initiation and crack growth concepts.

where

$$a_0 = (\Delta K_{th} / (f \Delta \sigma_e))^2 / \pi. \quad (2.4)$$

Purely from an empirical point of view, Eq. 2.3 suitably represents the experimentally observed behavior of small cracks at near-threshold growth rates, and the calculation of  $a_0$  provides a simple approximation of the crack length necessary for validity of  $\Delta K_{th}$ . The generality of the parameter  $a_0$  is illustrated in Fig. 2.4 [26], which shows data from a number of materials fatigued under various loading conditions. On the normalized axes shown, the collection of data generally follows the predicted trends. In spite of its apparent utility, however, the parameter  $a_0$  has not been shown to have any fundamental physical basis and provides no insight into the underlying reasons for the rapid growth of small cracks.

Since the small-crack problem was first identified, substantial effort has been devoted to the experimental and analytical characterization of small cracks. The study of small cracks has been the focus of a number of symposia [27-30], and the rapidly expanding literature on small cracks has been the subject of numerous review articles [31-43]. The objective of the present discussion of the literature, therefore, is not an exhaustive survey, but rather an attempt to summarize the current understanding of the small-crack problem, identify unresolved questions, and establish a framework for discussing the experimental results to be presented later. In addition to considering the mechanics and physics of the small-crack problem, a discussion of the physical and mechanical metallurgy of Ti-Al alloys, which are the focus of the present investigation, will also be presented.



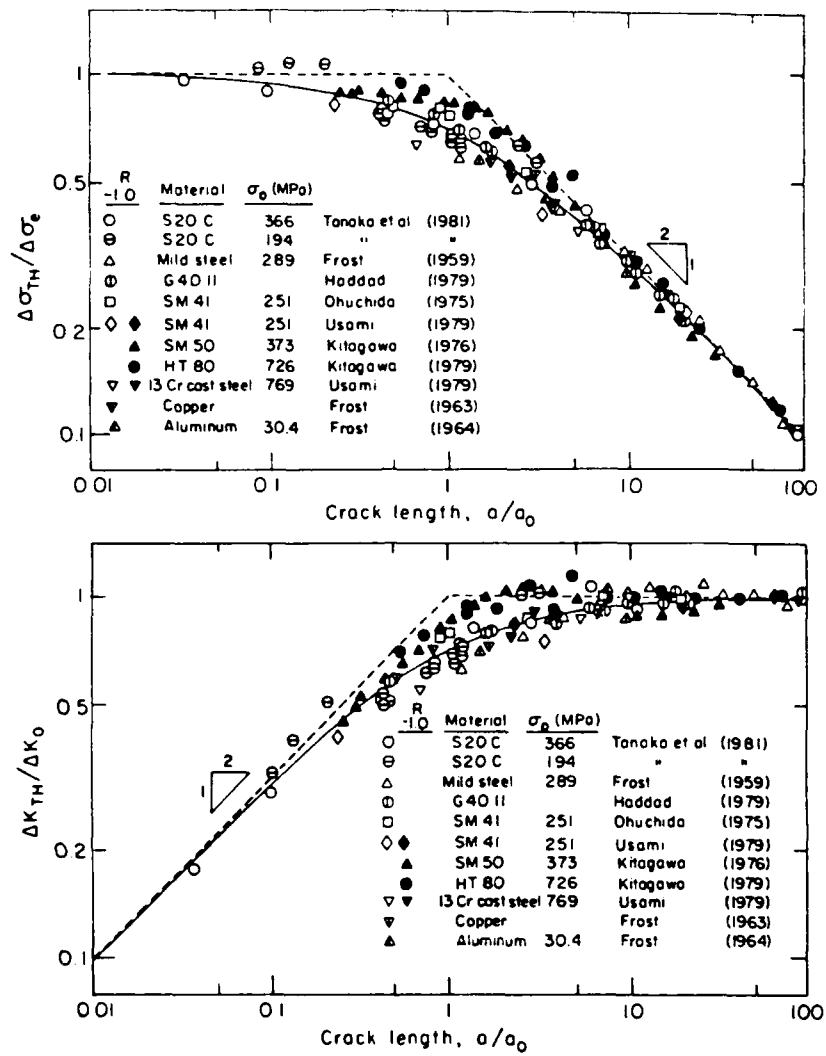


Fig. 2.4 Small crack data illustrating the utility of the normalizing parameter  $a_0$  [26].

## 2.2 Definitions of a Small Crack

For more than a decade the definition of a small (or short) crack has been argued extensively. Within the current context, a small crack will be defined as any crack that, due to its small size, grows at a rate different than a large crack (of the order of 25 mm in length) subjected to a nominally equivalent crack driving force. Beyond this general definition, small cracks are often categorized by one or more descriptive terms which further classify the small cracks as being: mechanically-, microstructurally-, physically-, or chemically-small. The bases for this nomenclature, which is gaining general acceptance [30,44,45], are outlined in Table 2.1 [44,45]. The table also lists mechanisms that are thought to be primarily responsible for the given small-crack behavior. As indicated, mechanically-small cracks have a length of the order of the crack-tip plastic zone size, while microstructurally-small cracks have a length of the order of the dominant microstructural dimension. Furthermore, although a crack may be both mechanically- and microstructurally-large, its physically-small size may dictate its propagation behavior due to the influence of crack shielding mechanisms – primarily crack closure. Finally, due to its size, a small crack may respond differently to a

Table 2.1: Classes of Small Fatigue Cracks [44,45]

<u>Type of Small Crack</u>	<u>Approximate Dimension</u>	<u>Responsible Mechanism</u>
Mechanically-small	$a \leq r_y^a$	excessive (active) plasticity
Microstructurally-small	$a \leq d_g^b$ ; $2c \leq 5-10 d_g$	crack-tip shielding, enhanced $\Delta\epsilon_p$ , crack shape
Physically-small	$a \leq 1 \text{ mm}$	crack-tip shielding (crack closure)
Chemically-small	up to $10 \text{ mm}^c$	local crack-tip environment

(a)  $r_y$  is the plastic zone size or plastic field of a notch.

(b)  $d_g$  is the critical microstructural dimension, e.g., grain size,  $a$  is the crack depth, and  $2c$  is the surface length.

(c) critical size is a function of frequency and reaction kinetics.

chemically aggressive environment than a corresponding large crack.

Current terminology also distinguishes between small and short cracks. The term "small crack" has come to designate a crack that is small in three dimensions, while a "short crack" is small in only two dimensions. Short cracks are often formed by *machining away all but the tip of a long, through-thickness crack*. Thus, a small crack normally interacts with relatively few microstructural features, while the front of a short crack may be of substantial length and thus controlled by average, rather than local, features of the microstructure. Moreover, a transient period associated with the transition from crack initiation to early crack propagation may be eliminated when a short crack is produced from a previously longer crack. Thus, as defined here, short and small cracks may behave differently.

The underlying reasons for the failure of linear elastic fracture mechanics to consolidate the data of large and small cracks are potentially many and varied. Ultimately, however, all of these reasons can be traced to a breakdown of the very general assumption that a unique similarity exists between the process zones that control the growth of large and small cracks. The breakdown in similitude appears to be traceable to one or more of the following factors:

- (1) Inaccurate characterization of the crack driving force due to excessive crack-tip or notch plasticity.
- (2) Local microstructural effects that influence large and small cracks differently, possibly resulting in different mechanisms of crack propagation.
- (3) Crack-shape effects.
- (4) Multiple-crack interactions.
- (5) Differences in crack closure behavior.
- (6) Environmental effects.

Each of these factors will be discussed individually in the following pages.

### 2.3 Inaccurate Characterization of Crack Driving Force

According to linear elastic fracture mechanics, the driving force for crack propagation may be characterized by the stress intensity factor range ( $\Delta K$ ) so long as three primary requirements are satisfied: (i) the material must behave as a continuum, (ii) a dominant crack-tip stress singularity must exist, and (iii) crack-tip plasticity must be sufficiently contained by surrounding elastic material so as not to significantly alter the form of the elastically calculated crack-tip stress field. The first of the criteria concerns microstructurally-small cracks, and will be discussed in detail later. Assuming that continuum behavior exists, it has been shown independently [46,47] that, for very small cracks, free surface effects may lead to a violation of the second assumption. Thus, as crack length decreases, the crack-tip stress field is no longer sufficiently dominated by the stress intensity factor,  $K$ , and higher order terms of the stress field solution should be included.

The assumption of contained crack-tip plasticity (small-scale yielding) is violated when the size of the crack-tip plastic zone is of the order of the crack length [48] – a “mechanically-small” crack. Useful estimates of the size of the monotonic plastic zone [49],  $r_p$ , and the cyclic plastic zone [50],  $\Delta r_p$ , are

$$r_p = \alpha(K/\sigma_y)^2 \quad (2.5)$$

$$\Delta r_p = \alpha(K/(2\sigma_y))^2 \quad (2.6)$$

where  $\sigma_y$  is the material's yield strength and  $\alpha = 1/\pi$  for plane stress and  $1/3\pi$  for plane strain. These simple estimates, however, do not indicate the shape of the plastic zone nor do they reflect any dependence of crack-tip deformation on specific material slip characteristics, which have been shown to be important [51].

Theoretically, the contained plasticity requirement can be relaxed if the crack-tip driving force is characterized by Rice's J-integral [52] instead of K. Calculations of the J-integral using the finite element method have shown that the error in K for a small crack becomes significant as the remotely applied net-section stress approaches the material's yield strength [53,54]. Trantina and deLorenzi [53] suggested that deviations from LEFM behavior occurred approximately for  $\sigma_{\max}/\sigma_y \geq 0.7$ . Dowling [55] conducted strain-controlled fatigue experiments in the plastic regime and employed a J-integral approach to correlate the growth of small surface cracks in A533B steel. Although  $\Delta J$  effectively correlated the data over a large range in crack size, growth rates for cracks smaller than approximately ten times the average grain size were consistently faster than the large-crack trend. These data were subsequently reconciled using the empirical approach of El Haddad et al [56], but as stated earlier, the physical basis of this success is unknown. Other attempts [57] in using the J-integral have also been ineffective in consolidating data of large and the very smallest cracks. Noting that, for elastic loading,  $\Delta J = (\Delta K)^2/E$  (i.e.,  $\Delta J$  and  $\Delta K$  approaches are equivalent), Chan [58] argued that it was necessary to use a near-tip estimate of  $\Delta J$  to characterize small cracks in specimens subjected to nominally elastic loading. Employing a Barenblatt-Dugdale crack model, he suggested that  $\Delta J = \Delta\sigma(\delta_t)$ , where  $\delta_t$  is the cyclic crack-tip opening displacement. Using displacement measurements made at the tip of a small crack in overaged 7075 aluminum alloy, he found calculated values of local  $\Delta J$  and  $\Delta K$  to be substantially greater than the remotely calculated values. The difference between the local and remote values was argued to be due to a high stress level and microstructural (noncontinuum) effects.

Attempts to use alternative elastic-plastic crack driving force parameters such as crack-tip-opening displacement (CTOD) [36] and the crack-tip plastic strain range [59] also have not been fully successful in rationalizing the differences in growth rates between large and small cracks. In an investigation of power metallurgy (PM) Astroloy, Vecchio and Hertzberg [60] were able to use a strain energy density ( $\Delta S$ ) criterion to consolidate the data of long, through-thickness cracks with data from short, edge cracks. All of their short cracks, however, were at least ten times the material's grain size, indicating that the cracks were microstructurally-large. The utility of  $\Delta S$  has not been determined for cracks of microstructural dimensions.

The inability to find a parameter capable of uniquely correlating the growth of fatigue cracks, regardless of size, has been emphasized by experimental measurements of the near-tip deformation fields of both large and small cracks. Using SEM stereoimaging and electron channeling methods [61,62], Lankford, Davidson, and Chan [63] and Lankford and Davidson [64] have characterized the local crack-tip field of large and small cracks in 7075 aluminum alloy. Although electron channeling measurements indicated that large and small cracks subjected to the same nominal  $\Delta K$  have essentially equivalent plastic zone sizes, the potentially more accurate stereoimaging measurements indicated that the small-crack plastic zone was significantly larger than the corresponding large-crack plastic zone. Furthermore, the stereoimaging measurements indicated that the crack-tip strain and the crack-tip opening displacement of the small cracks were greater than corresponding large cracks and that the distribution of crack-tip strain was also dependent on crack size. Overall, the characterization of local deformation underscored the loss of crack-tip similitude between small and large cracks in the aluminum alloy examined and highlighted the inadequacy of both  $K$  and CTOD for small cracks.

## 2.4 Small Cracks at Notches

In addition to crack-tip plasticity effects, there are also difficulties in applying fracture mechanics methods to the specific problem of cracks emanating from mechanical notches. Experimental data from Leis and Forte [65] illustrating this problem for notches of various geometries are presented in Fig. 2.5. The authors demonstrated that, for a number of materials and stress concentration factors, the accelerated growth of small cracks persisted until the crack tip reached the boundary of the plastic field of the notch [66]. Dowling [67] showed that small cracks emanating from notches have two limiting stress intensity factor solutions, as shown in Fig. 2.6. For small cracks of length  $l$  growing from a notch of depth  $c$ ,

$$K_{\text{short}} = 1.12 k_t \sigma (\pi l)^{0.5} \quad (2.7)$$

where  $k_t$  = stress concentration factor for the notch. When the crack length is much greater than the notch depth,

$$K_{\text{long}} = f \sigma (\pi a)^{0.5} \quad (2.8)$$

where  $a = c + l$  and  $f$  = function of geometry. As shown in the figure, these limiting solutions compare favorably with a numerical solution for this crack geometry [68]. The extent of the notch stress field ( $l'$ ) is given approximately by the equation

$$l' = c / ((1.12 k_t / f)^2 - 1), \quad (2.9)$$

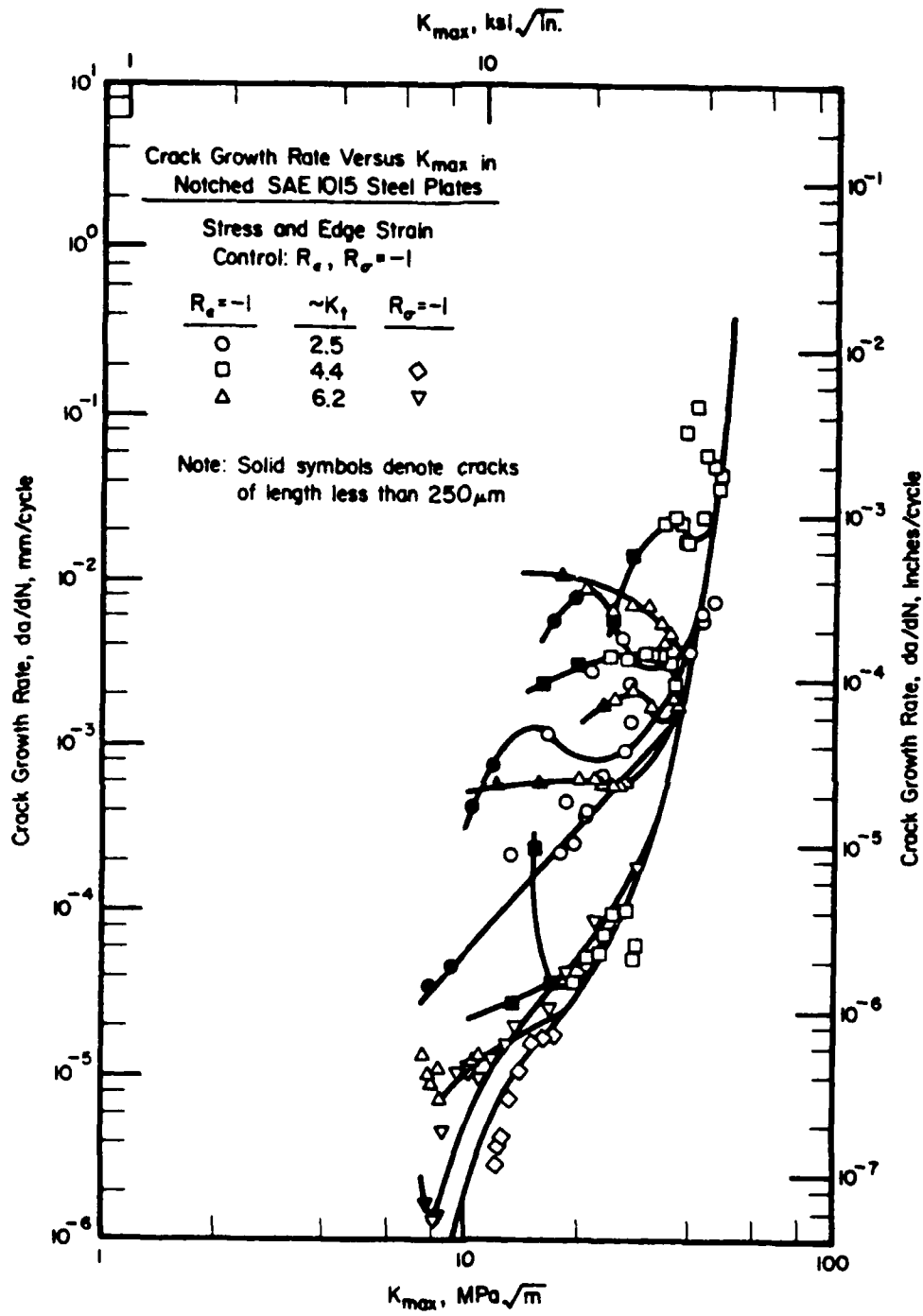


Fig. 2.5 Growth rate data for small fatigue cracks emanating from notches [58].



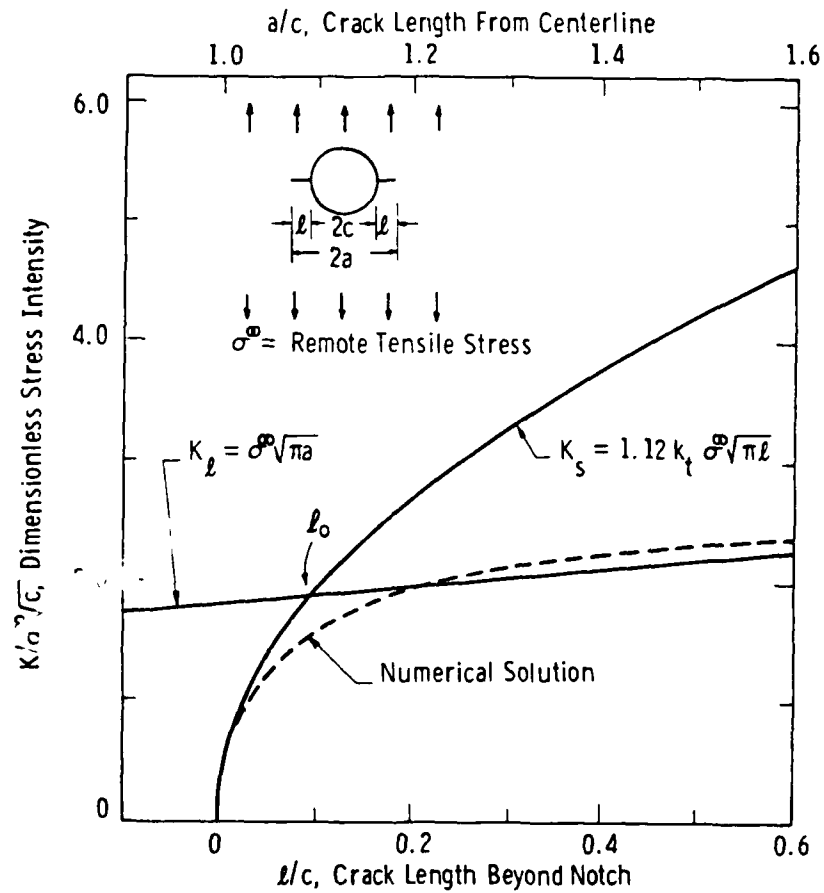


Fig. 2.6 Limiting stress intensity factor solutions for a crack emanating from a hole [60]. A numerical solution is also presented [65].

and values of  $l'$  for moderately sharp notches often fall in the range  $r/20 \leq l' \leq r/4$ , where  $r$  is the notch radius. Crack growth behavior in the field of a notch was also investigated by Hammouda and Miller using the finite element method [69]. Their calculations indicated that a small crack was initially influenced by the notch plastic field and later by the elastic stress field of the notch as shown in Fig. 2.7. This resulted in the variation in crack growth rate with  $\Delta K$  that is illustrated in Fig. 2.8.

Considering effects of both crack-tip and notch plasticity on the growth of small fatigue cracks, it is clear that some of the "anomalous" small-crack data reported in the literature can be at least partially explained by the inappropriate use of the linear elastic parameter  $\Delta K$ . The LEFM assumption of small-scale yielding is obviously invalid for a small crack propagating in the plastic field of a notch, and  $\Delta K$  should not be used. The small scale yielding assumption is also violated for small fatigue cracks having a ratio of plastic zone size to crack length,  $r_p/a$ , approaching 1. Although the use of an appropriate elastic-plastic fracture mechanics parameter such as  $\Delta J$  or  $\Delta S$  appears to overcome the plasticity limitations of  $\Delta K$ , these approaches have not been shown to be effective when cracks are of a length of the order of microstructural dimensions.

## 2.5 Local Microstructural Effects

The conventional parameters of both linear-elastic and elastic-plastic fracture mechanics were developed assuming that material properties are homogeneous, isotropic, and continuous. While these assumptions are never strictly satisfied by real materials, the scale of microstructural anisotropy is often much smaller than any dimension of large cracks in conventional specimens. Although a large crack propagating at a near-threshold growth rate may possess a plastic zone of a size comparable with the size of the material's critical microstructural unit (e.g., grain size, Widmanstätten colony size), the crack

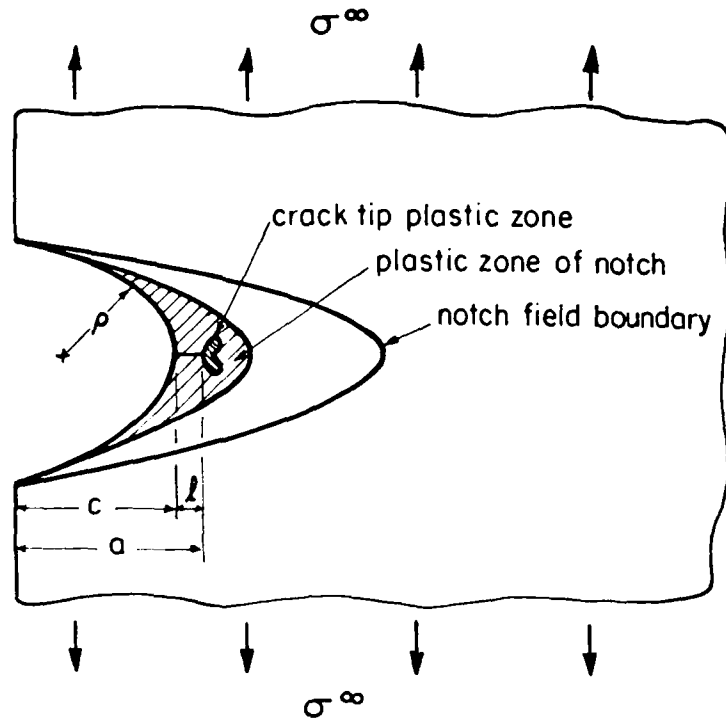


Fig. 2.7 Schematic illustration of a small crack propagating within a notch field [66].

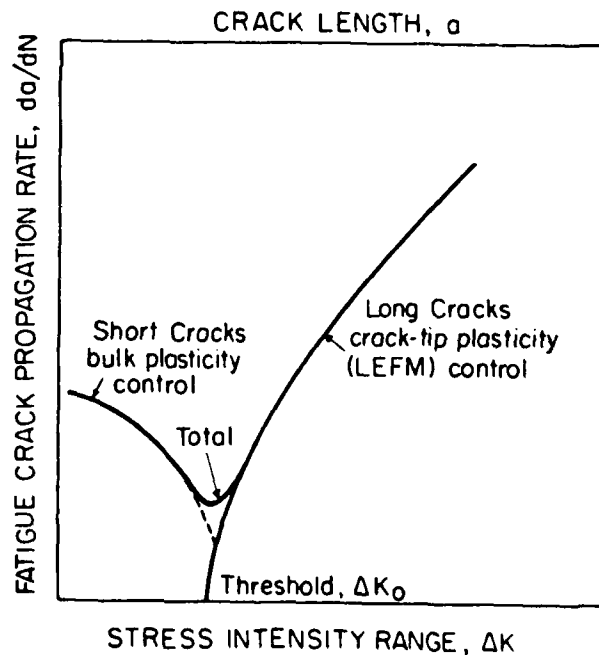


Fig. 2.8 Schematic illustration of the growth behavior of a small crack emanating from a notch [66].

front normally interacts simultaneously with many of these microstructural features, and the resulting macroscopic crack growth rate reflects the collective behavior of microstructural interactions all along the crack front. On a macroscale, therefore, the fracture mechanics description of the crack-tip stress and strain fields of a large crack are reasonably approximated by the isotropic continuum assumption. On the other hand, a "microstructurally-small" crack, being of a size of the order of the microstructural unit, may be significantly affected by local elastic and plastic anisotropy, as well as discrete microstructural barriers, and the small crack's propagation behavior may not coincide with that of a large crack subjected to a nominally equivalent crack driving force.

Although effects of microstructure on the growth of large cracks are relatively well known [e.g., 70-83], most of the small-crack research that has been reported to date has not focused specifically on the effects of microstructure. Moreover, effects of microstructure on crack propagation are often manifested indirectly, for example, by influencing crack shape and crack closure. Therefore, the discussion within the ensuing subsections will address only the more direct microstructural effects, while the more subtle, indirect effects of microstructure will be considered in the other subsections.

### **2.5.1 Effects of Grain Boundaries**

From a continuum mechanics point of view, it has been suggested [84,85] that the limit of applicability of conventional linear elastic fracture mechanics should be based on the size of a material's smallest structural feature. Defining this feature as a subgrain slip band ( $\sim 0.5 \mu\text{m}$ ) results in an estimate of the fundamental limit of LEFM to be  $\sim 25 \mu\text{m}$  (50 times the feature size). Although very small microstructural features may produce noncontinuum deformation, the influence of microstructure on small cracks often occurs on a scale much larger than a slip band. The majority of the reported effects of

microstructure have dealt with unusual interactions of small cracks with grain boundaries and second phases in a small number of alloy systems including primarily steels, aluminum alloys, titanium alloys, and a few nickel-base superalloys.

An early assessment of the effect of microstructural anisotropy and inhomogeneity on the propagation of small fatigue cracks was presented by Taylor and Knott [86-88], who suggested that the rapid growth of small cracks occurred because these cracks were able to "exploit weak microstructural features." In addition to the characteristic crack size  $a_0$  discussed earlier, they defined the two related crack lengths illustrated in Fig. 2.9. In this figure,  $a_1$  is the maximum crack size for which the material's fatigue limit fully applies, and  $a_2$  is the minimum crack size for which linear elastic fracture mechanics is completely adequate. These researchers have suggested that, in a number of alloys,  $a_2$  is approximately ten times the average dimension of the primary microstructural feature and that  $a_2 \approx 4a_0$ .

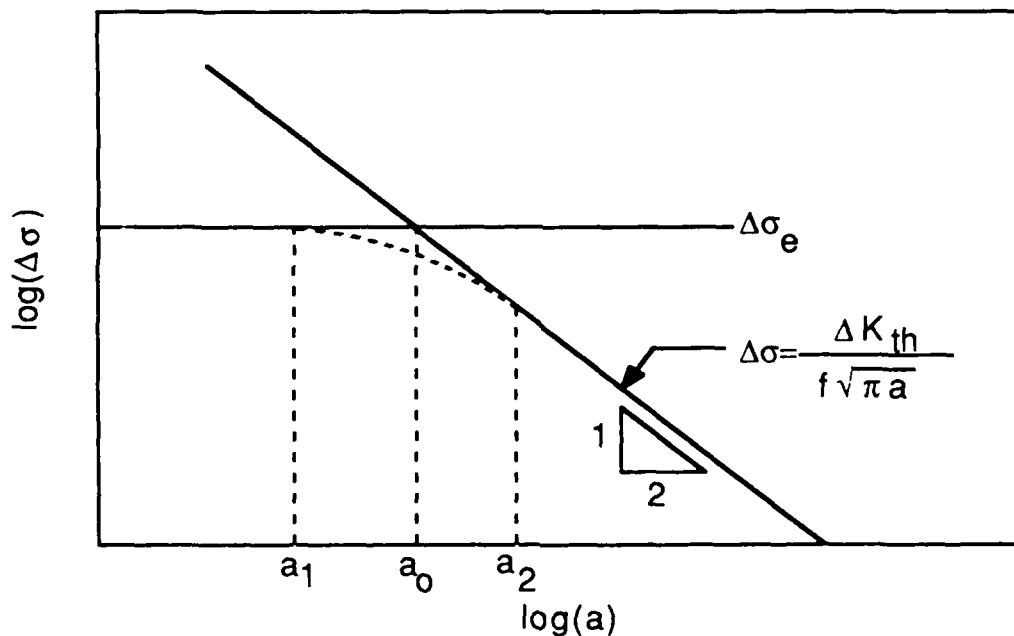


Fig. 2.9 Schematic illustration of the crack sizes that are argued to be limits for the valid application of crack initiation ( $a_1$ ) and  $\Delta K_{th}$  ( $a_2$ ) concepts [86].

Much of the literature dealing with grain boundary effects has highlighted the role of grain boundaries as barriers to small-crack growth [e.g., 21,89-104], and it appears that the growth-rate minimum (or minima) often observed for small cracks is associated with the crossing of grain boundaries. In the extreme case, the crack arrests at the grain boundary. It has been suggested that the initiation of a small crack within a single grain results from the accumulation of local microplasticity and that the propagation of a small crack across a grain boundary requires that the adjacent grain also have undergone microplastic deformation [105,106]. In some instances, a transition from Forsyth's [107] Stage I (crystallographic; crack inclined to the axis of loading) to Stage II (multiple slip systems; cracking perpendicular to axis of loading) crack growth appears to occur as the crack crosses the first grain boundary, although Stage I propagation has been shown to continue into adjacent grains in some cases [89-91].

The most sophisticated model of grain boundary effects is probably that of Tanaka et al [103-104]. Essentially, this model considers the blockage of a crack-tip slip band by a grain boundary, and crack growth occurs only if a microscopic stress intensity factor (MSIF) ahead of a blocked crack-tip slip band is sufficient to initiate a crack in the adjacent grain. As a special case, the model reduces to the form proposed by El Haddad et al [23-25]. Both of these models, however, rely on empirically determined parameters.

The growth of a small crack within a single grain has been said to follow the form

$$da/dN = C(d-a)^{1-\alpha} (a)^\alpha \quad (2.10)$$

where  $d$  is the grain size,  $a$  is the crack length, and  $\alpha$  is an empirical constant [99]. Thus,

$da/dN$  is predicted to approach zero as the crack length approaches the grain size. This form is a reasonable representation of the experimentally observed early deceleration of small cracks. A model for crack growth along a slip band has been proposed by De Los Rios et al [100] who predicted that

$$da/dN = f \tau (L-a)/\mu \quad (2.11)$$

where  $f$  is the fraction of dislocations on the slip band that take part in the crack initiation process,  $\tau$  is the shear stress acting on the slip band,  $L$  is the slip band length,  $a$  is the crack length, and  $\mu$  is the shear modulus of the material. Both of these models describe the deceleration of a small crack but do not predict the subsequent growth of the crack into an adjacent grain.

Although enhanced blockage of small cracks by grain boundaries has been observed in a number of materials, the effectiveness of a grain boundary as a barrier to the growth of small cracks varies significantly, depending on the relative orientation of adjacent grains. In the absence of crystallographic texture, wherein neighboring grains are aligned preferentially, the relative orientation of adjacent grains should be random, and the tendency of cracks to propagate across a given grain boundary should be a random variable. For example, in research on the nickel-base superalloys Astroloy and Waspaloy [108-110], in situ SEM measurements have shown that approximately 30% of the grain boundaries crossed by small cracks acted as barriers to growth [110]. In the remainder of the cases, the small cracks propagated easily across grain boundaries. As compared to large-crack data, the increased variability in  $da/dN$  for small cracks appears to be associated with the enhanced influence of grain boundaries. The effectiveness of a grain boundary in resisting the propagation of a small crack, however, correlates inversely with the crack's growth rate. The fastest growing, or worst-case, small crack is the one

that propagates freely across the grain boundaries due to favorable crystallographic orientation. These cracks pose the most serious concern to fatigue life, making the slower, grain-boundary-affected small cracks of secondary importance.

### 2.5.2 Effects of Grain Size

Relatively little research has been performed to establish the effect of grain size on the growth of small fatigue cracks. Thompson and Backofen [89,90] performed an investigation of the effect of grain size on long-life fatigue of alpha brass, copper, and aluminum and found a strong grain-size dependence in brass, while the long-life fatigue performance of the other two materials was independent of grain size. From crack length measurements on metallographic sections, they concluded that the grain-size effect resulted almost solely from Stage I cracking, which was enhanced in alpha brass, a planar-slip material. Materials such as copper and aluminum, which exhibit easy cross slip, develop dislocation cell structures which mask the influence of grain boundaries and allow an early transition to Stage II crack growth. Since the fatigue life of copper and aluminum did not exhibit a grain-size dependence, the small-crack  $da/dN$  in these materials should be approximately independent of grain size. Moreover, recognizing that the grain-size effect in brass was closely correlated with the average Stage I crack length,  $\bar{p}$ , estimates of  $da/dN$  ( $\approx \bar{p}/N$ ) suggest that small-crack growth rates in this material were also approximately independent of grain size. Thus, although the data from these fatigue experiments were not analyzed in terms of fracture mechanics, the results from the three different materials suggest the absence of an appreciable grain-size effect on the growth of small cracks. These results are particularly significant because grain sizes were varied by an order of magnitude, which is a maximum practical range for most materials. In addition, the findings demonstrate the importance of slip character in determining fatigue performance.



Zurek et al [111] performed small-crack fatigue experiments on 7075-T6 aluminum alloy specimens having 12 and 130  $\mu\text{m}$  average grain sizes and found a slightly faster growth rate in the smaller grain-size material. However, X-ray measurements made on the samples indicated that compressive surface residual stresses had developed during the  $R = 0$  fatigue testing. The compressive residual stresses were significantly greater in the large grain material, accounting for the grain-size dependence of  $da/dN$ . Consistent with earlier reports, they noted that a large fraction of the cracks observed were pinned at the first or second grain boundary; grain boundaries had less influence on cracks larger than twice the grain size. The resistance to crack growth offered by the grain boundaries was apparently less significant than the effect of the fatigue-induced residual stresses.

Gerdes et al [112] and Wagner et al [113] investigated small fatigue cracks in an aged Ti-8.6Al alloy in two grain-size conditions (20  $\mu\text{m}$  and 100  $\mu\text{m}$ ). As shown in Fig. 2.10, the larger grain size condition of this very planar-slip material was significantly more resistant to the propagation of large cracks, but the smaller grain-size material was found to be slightly more resistant to the propagation of small fatigue cracks, apparently due to interaction with the higher density of grain boundaries. An unusual finding of this research, however, was that the crack-growth-rate minimum in materials of both grain sizes corresponded to a surface crack length of approximately 50  $\mu\text{m}$ . Moreover, this crack size was slightly larger in the alloy having the smaller grain size. The minimum crack propagation rates were reported to be associated with a change in the direction of crack growth, irrespective of the presence of a grain boundary.

Effects of 12 and 50  $\mu\text{m}$  grain size on the propagation of small cracks in the powder-metallurgy, nickel-base superalloy Astroloy were studied by Brown et al [114].

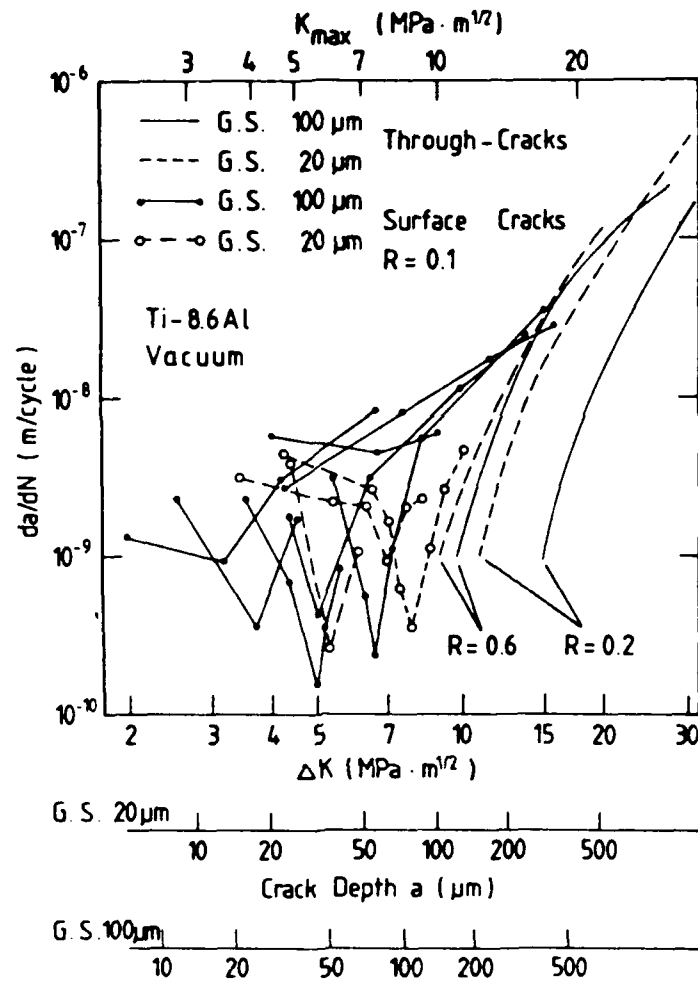


Fig. 2.10 The effect of grain size on vacuum fatigue crack propagation data of large through-cracks and small surface cracks in aged Ti-8.6Al [112].

The grain size effects observed in this alloy were consistent with the Ti-8.6Al results. As shown in Fig. 2.11, the coarse-grain condition was much more resistant to the propagation of large cracks, while the trend was slightly reversed for small cracks. A third microstructural condition possessing a partially recrystallized, necklace grain structure having a bimodal grain size of 5 and 40  $\mu\text{m}$  exhibited the best overall resistance to the growth of small and large cracks. The researchers concluded that the inverse grain-size effect on small-crack growth rates resulted collectively from crack arrest and crack deflection at grain boundaries.

### 2.5.3 Effects of Multiphase Microstructures

In addition to variations in grain size of the Astroloy, Brown et al [114] varied the size, morphology, and volume fraction of strengthening  $\gamma'$  precipitates, while holding the coarse grain size constant. None of these small-scale microstructural variations, however, affected the behavior of small cracks in the alloy. Furthermore, the same researchers reported that the coarse-grain PM Astroloy small-crack growth data were essentially equivalent to small-crack data in conventionally forged Waspaloy of the same grain size.

Hicks and Brown [115,116] tested an IMI 685 titanium alloy that was solution treated and  $\beta$ -processed to achieve a microstructure composed of 5 mm diameter prior- $\beta$  grains containing Widmanstätten colonies approximately 1 mm diameter. They found that the growth rates of small corner cracks of depths as great as 3.5 mm were much faster than those of nominally equivalent large cracks. The growth rates of the small cracks were also dependent on the local mechanism of crack growth. Small-crack propagation rates were successively faster for each of the following mechanisms: non-crystallographic, colony boundary separation, and crystallographic cracking.

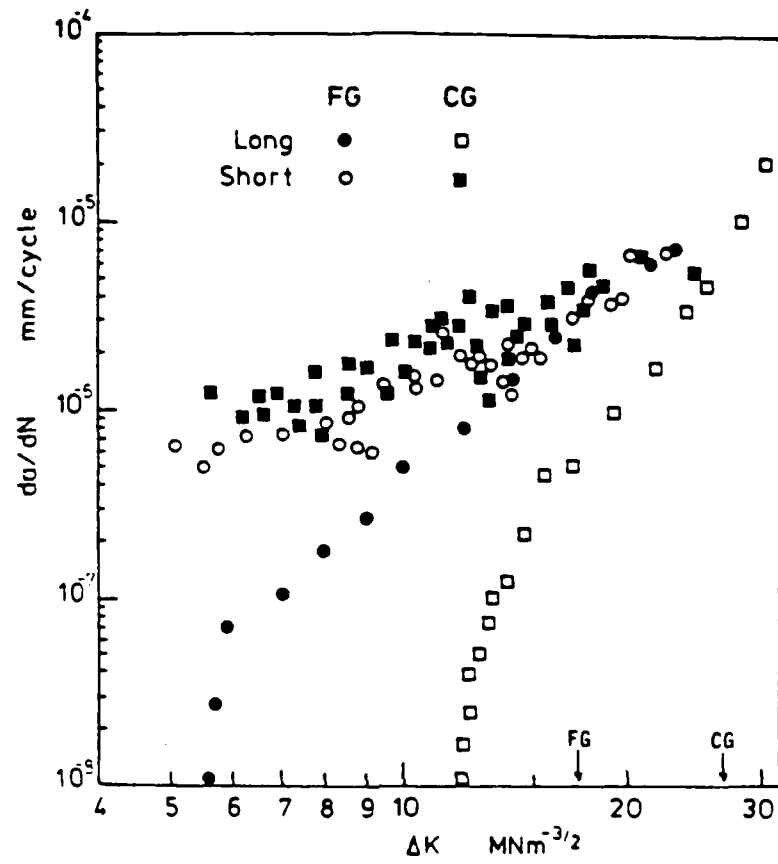


Fig. 2.11 A comparison fatigue crack growth rates of short and long cracks in fine-grain (FG) and coarse-grain (CG) Astroloy [114].

Research on the  $\alpha+\beta$  titanium alloys IMI 550 and IMI 318 [117] indicated that  $\alpha/\beta$ -processed microstructures had superior resistance to the growth of small cracks as compared to  $\beta$ -processed materials. This was generally the reverse of the trend for large cracks. It was further reported that of the  $\alpha/\beta$ -processed alloys, microstructural conditions that permitted small cracks to propagate primarily in the  $\alpha$  phase had inferior small-crack growth resistance compared to alloys where cracking was regularly forced to cross transformed  $\beta$  regions.

In a study of small cracks in eutectoid steels, Daeubler and Thompson [118] produced four microstructural variants: coarse and fine prior austenite grain sizes, each with coarse and fine cementite lamellar spacings. The experimental results indicated that the growth rate of small cracks was faster for microstructures having a coarse lamellar spacing than for microstructures with a fine lamellar spacing. There was no appreciable influence of changing prior austenite grain size. A minimum in small-crack growth rate was observed to correspond to the transition from Stage I to Stage II crack propagation.

#### 2.5.4 Effect of Alloy Slip Character

Other than the work by Thompson and Backofen [89,90] discussed earlier, there have apparently been no controlled studies of the effect of slip character on the growth of small cracks. Moreover, because those experiments were not analyzed in terms of fracture mechanics, it is unclear how variations in slip character might affect the growth rates of small cracks when correlated with  $\Delta K$ . It is well known that changing from wavy to planar slip generally promotes crack initiation while improving crack growth resistance. It is shown that increased slip planarity concentrates fatigue damage, leading to early crack formation [119,120]. Alternatively, increased slip planarity is believed to lead to reduced crack growth rates as a result of improved slip reversibility [121] and crack

closure at low stress ratios [122-124]. As will be discussed later, closure is probably the more important mechanism influencing crack growth. In light of the opposing effects of slip planarity on crack initiation and crack propagation, it is unclear how variations in slip character might affect the propagation of small fatigue cracks. This is an important issue, since total fatigue life is governed by the combination of crack initiation and crack growth, and in many instances a significant fraction of the fatigue life is consumed by the propagation of small cracks.

### 2.5.5 Effects of Crystallographic Texture

The effect of texture on the propagation of small fatigue cracks has received little attention in the literature. Gregory et al [125] investigated microcrack propagation in an extruded 7475 aluminum alloy plate having a well defined texture with a major texture component oriented such that  $\{011\}$  was parallel to the extrusion plane and  $\langle 211 \rangle$  was parallel to the extrusion direction. Hourglass fatigue specimens were oriented parallel ( $0^\circ$ ) and  $45^\circ$  to the extrusion direction within the extrusion plane, and it was found that small fatigue cracks in both orientations propagated well below the large-crack  $\Delta K_{th}$ . However, small cracks of length as great as  $100 \mu\text{m}$  in the  $45^\circ$  specimens were temporarily arrested at grain boundaries, while grain boundaries were not significant barriers to cracks of length greater than  $30 \mu\text{m}$  in the  $0^\circ$  specimens. It was concluded that this difference was due to more severely deflected crystallographic cracking in the  $45^\circ$  specimen. Aside from the grain boundary effects, however, no significant influence of texture on small cracks was reported.

The effect of texture on the growth of small cracks in basal-textured Ti-6Al-4V was investigated by Brown and Taylor [126]. The test material, which was acquired in the form of a 100 mm square billet, was investigated in a mill-annealed microstructure

and a similar grain-coarsened microstructure (4.7 and 11.7  $\mu\text{m}$  grain sizes, respectively). It was found that cracks oriented parallel to the dominant basal plane exhibited a slightly higher long-crack  $\Delta K_{\text{th}}$ , while the small-crack growth rates in this specimen orientation were somewhat faster than when cracking was perpendicular to the dominant basal plane. These differences were attributed to elastic modulus, environmental, and crack closure effects, with the latter probably being most important. The texture in the alloy was apparently weakly developed, however, making definitive evaluation of texture effects difficult.

### 2.5.6 Differences in Crack Growth Mechanism

Crack initiation often occurs crystallographically as the result of a maximum shear stress, and the crack plane tends to assume an orientation  $45^\circ$  from the axis of loading (Stage I crack growth [107]). Under these circumstances, initial crack propagation occurs under a combination of Mode I (opening) and Mode II (in-plane sliding) loading, and propagation continues in Stage I until multiple slip systems can operate, allowing deformation to become more homogeneous. At this point, the crack assumes an orientation that is perpendicular to the axis of loading (Stage II crack growth [107]). Most data from tests of large-crack specimens are developed under Stage II conditions, while naturally initiated small cracks may initially propagate under Stage I. Variations in the mode of crack initiation and constraint due to free-surface effects may be expected to produce differences in crack extension mechanism for small and large cracks.

A detailed review of the available literature on the propagation of small fatigue cracks, however, reveals little evidence of a crack-size dependence of crack growth mechanism. Although there are occasional reports of variations in small-crack  $da/dN$  associated with local microstructural variations [e.g., 115,116], these influences appear

to be consistent with the behavior of large cracks. When the plastic zone size of both large and small cracks is of the order of the grain size, Stage I propagation is often observed. This might be expected to lead to different behavior of large and small fatigue cracks due to the difference in the number of grains affected, and the local mixed mode I and mode II crack opening displacement might be expected to influence large- and small-crack growth differently. However, the mechanism of crack growth does not appear to be fundamentally different for small and large cracks.

## 2.6 Crack-Shape Effects

Natural fatigue cracks in components and structures most often form as surface or corner cracks, and it is important that the mathematical description of the crack and its stress field accurately reflect the actual shape of the crack. Experimentally, propagating surface cracks often maintain a nearly semicircular shape, however, a number of factors may modify this shape for very small, naturally occurring cracks. The formation of a small crack may result from the linkup of several surface microcracks, producing a long, shallow surface crack. Alternatively, surface compressive residual stresses produced by machining, shot peening, ion implantation, or some other surface treatment may alter the stress intensity factor locally, and small surface cracks that form may be much deeper than expected. In addition to the influence of residual stresses, free surface effects may influence the shape of small cracks. Trantina and deLorenzi [53] employed three-dimensional finite element calculations to show that the high stresses that are generally required to initiate small cracks may exaggerate the effect of the plane stress state at the free surface, leading to significant changes in crack shape and the associated stress intensity factor. Although the effect on stress intensity factor calibrations of variations in crack shape [127,128] and residual stresses [129,130] have been effectively modeled, these effects must be recognized and included in predictions of the



growth of small cracks if component life calculations are to be accurate.

Changes in the shape of a small propagating crack may lead to "anomalously" rapid growth of small cracks based on surface crack length measurements. Clement et al [131] and Pineau [132] have shown that a crack that initiates from a surface inclusion may appear to propagate rapidly initially, followed by a period of decelerating crack growth, simulating the behavior of a small crack approaching a grain boundary. As shown in Fig. 2.12, a crack that initiates from an embedded spherical inclusion intersecting the specimen surface may form as a deep crack ( $a/c > 1$ ). Subsequently, such cracks often tend to propagate rapidly along the specimen surface in order to achieve a more stable, approximately semicircular, shape ( $a/c \approx 1$ ). Surface measurements of crack length thereby show an artificial pattern of initially rapid growth followed by deceleration.

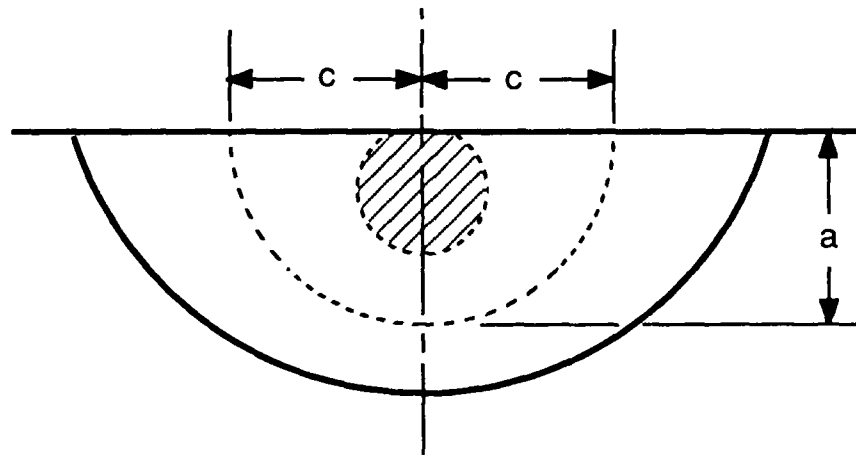


Fig. 2.12 Surface-crack shape changes that produce artificially rapid growth rates based on observations of the specimen surface [after 131,132]. The observed  $dc/dN$  strongly resembles the behavior of a small crack approaching a microstructural barrier.

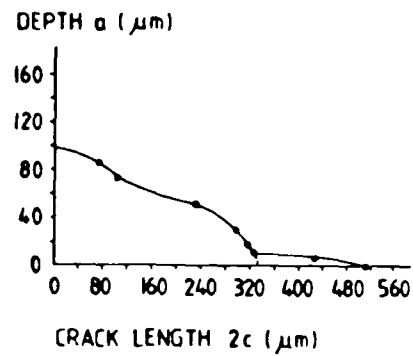
Irregular changes in the shape of small fatigue cracks have also been reported by Wagner et al [113] in aged Ti-8.6Al, which exhibits extremely planar slip. The process

is illustrated in Fig. 2.13. Crack initiation in this material normally occurs at a persistent slip band within a single grain. By serial removal of layers of the specimen surface, it was found that a long, shallow crack normally forms within a slip band and is temporarily pinned by grain boundaries at the tips. Although further crack growth is temporarily blocked at the specimen surface, the depth of the small crack increases, and the crack shape becomes approximately semicircular. Subsequently, a surface slip band forms at the crack tip in the adjacent grain and eventually becomes a shallow crack pinned by the next grain boundary. Small cracks were found to continue this trend until achieving a surface crack length of approximately five grain diameters, after which the general crack shape remained approximately semicircular. Although this behavior is probably limited primarily to planar-slip materials, such irregular development of crack shape may produce large variations in crack growth rate (measured at the surface) which may lead to "anomalous" growth of small cracks.

## 2.7 Multiple-Crack Interactions

Depending on material and stress level, cyclic loading may result in the formation of a single crack or an array of small cracks. When several cracks are present, their stress fields may interact, and the result may be to increase or decrease the individual stress intensity factors of the cracks. Some orientations give rise to reductions in  $K$ , while the stress intensity factors for two approaching crack tips tend to be magnified. It has recently been shown, however, that for two crack tips approaching each other along the same plane and separated by one quarter of their length, the magnification in  $K$  is less than approximately ten percent [133]. Alternatively, a single small crack may bifurcate, and the resulting pair of crack tips generally shield each other, effectively reducing the net crack driving force [134].

## Measured Crack Shape



## Development of a Semicircular Crack

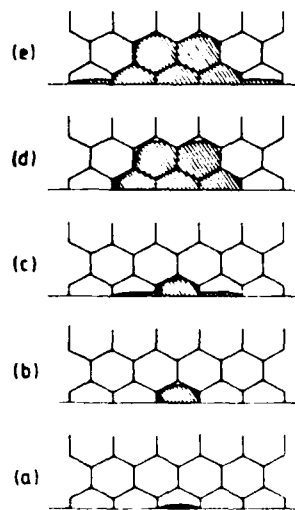


Fig. 2.13 Ti-8.6Al small-crack shapes determined by serial polishing [113]. Small, shallow cracks were found to develop from slip bands that were pinned at grain boundaries. Repetition of this process eventually produced a crack of approximately semicircular shape.

## 2.8 Effects of Crack Closure

It has often been suggested that the anomalous behavior of small fatigue cracks may be at least partially due to differences in the crack closure characteristics of large and "physically-small" cracks. The concept of fatigue crack closure, originally introduced in 1970 by Elber [135,136], has been the focus of extensive research on large cracks and has recently been the subject of a number of review articles [137-139] and a symposium [140]. Essentially, crack closure may be described as the premature contact of a crack's fracture surfaces during cyclic unloading in fatigue, effectively terminating further crack-tip deformation until the crack reopens at some point later in the tensile portion of the fatigue cycle. In the absence of significant hysteresis, the experimental evidence indicates that the stress intensity factor at crack closing ( $K_{cl}$ ) and crack opening ( $K_{op}$ ) are often nearly equal. In the present discussion crack closing and crack opening loads will be assumed to be equal unless specifically stated otherwise, and the terms will therefore be used interchangeably. As a result of crack closure, the tip of a crack that is subjected to a nominal applied stress intensity factor range,  $\Delta K = K_{max} - K_{min}$ , may actually experience a lesser effective stress intensity factor range,  $\Delta K_{eff} = K_{max} - K_{cl}$ . Thus, variations in closure level may alter the effective driving force for fatigue crack propagation. Crack closure has been shown to arise from a number of sources associated with the fracture surface plasticity [135,136], oxides [141-143], roughness (asperities) [144-146], viscous fluids [147,148], and stress-induced phase transformations [149,150]. Although a number of these mechanisms may operate simultaneously, the first three are thought to be of primary importance in most metals.

Each of the five mechanisms of closure, illustrated schematically in Fig. 2.14 and discussed separately below, is considered to be a form of extrinsic material toughness which shields the crack tip from a portion of the nominally applied crack driving force

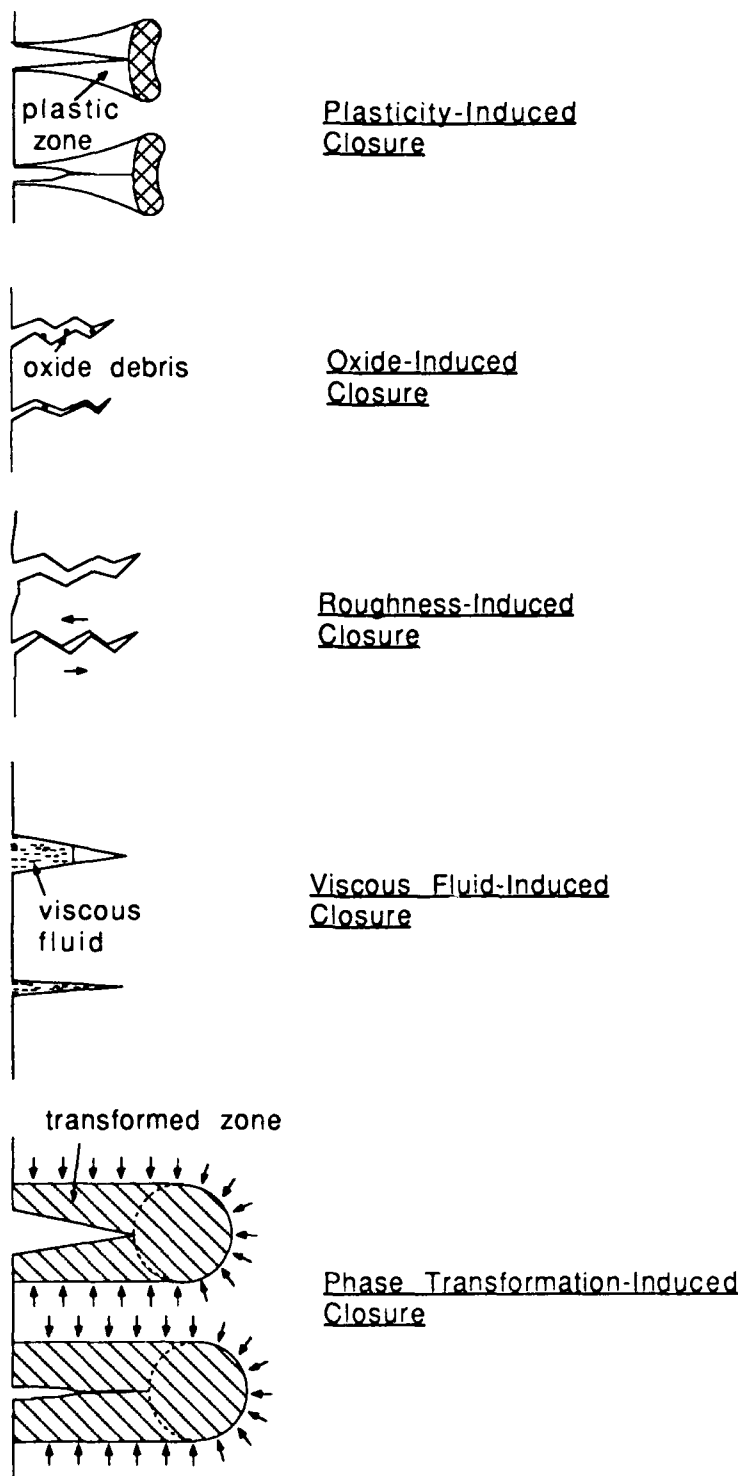


Fig. 2.14 Schematic illustration of the various mechanisms of fatigue crack closure [after 137].

[151]. Extrinsic toughness is additive to a material's intrinsic toughness (innate resistance to crack propagation) and may significantly increase a material's total resistance to crack growth. Although intrinsic toughness is thought to be independent of crack geometry, the contribution of an extrinsic toughening mechanism such as crack closure may be a function of crack length, as first suggested by Broek [152]. Since closure operates behind the crack tip, a crack of zero length cannot experience closure, and the full development of closure is argued to require some finite crack extension. Thus, during the period of initial crack extension and associated development of crack closure, there is a lack of similitude between the closure levels of small and large cracks, producing different effective crack driving forces for the two nominally equivalent cracks.

According to Elber's original mechanism [135,136], termed plasticity-induced closure, the crack-tip plastic zone forms a wake of residual tensile deformation behind the crack tip as the crack propagates. The material in the plastic wake has incurred residual tensile plastic deformation perpendicular to the crack face, and upon unloading, the faces of the crack contact prematurely. Plasticity-induced closure operates primarily in the plane-stress, near-surface region of a crack, although a small plane-strain contribution has also been demonstrated experimentally [153] and numerically [154]. It has been shown analytically [155] and numerically [156] that  $K_{Op} > K_{Cl}$  under plasticity-induced closure and that the level of plasticity-induced closure is accentuated by cyclic hardening [155] and high stress ratios [155-157]. The calculated dependence of plasticity-induced crack closure on stress state, stress level, and stress ratio is illustrated in Fig. 2.15 [156]. Finite element method calculations by Newman [156] have indicated that the development of plasticity-induced closure can account for the rapid growth of small cracks. These predictions of small-crack growth rate have been shown to be in good agreement with experimental data from materials for which plasticity-induced closure was dominant [156,158-162].

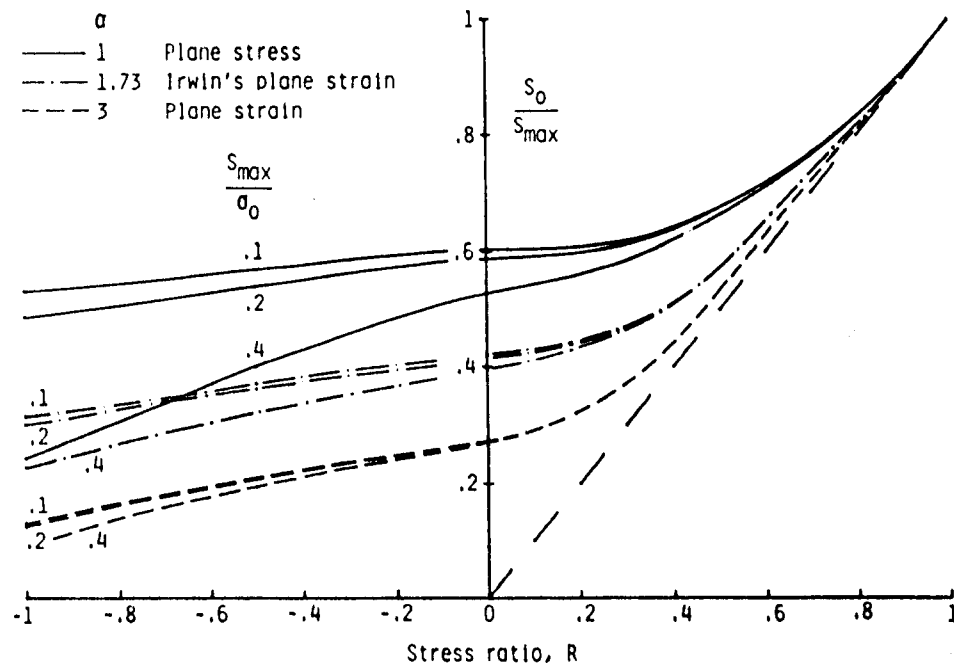


Fig. 2.15 Normalized crack-opening stresses as function of stress ratio ( $R$ ) under constant-amplitude fatigue [156]. The effect of plastic constraint is shown, including a calculation for Irwin's plane-strain condition which simulates three-dimensional constraint.

A second mechanism, termed oxide-induced closure, results from the build up of oxide or corrosion debris on the fracture surfaces, wedging the crack open. This mechanism was first suggested by Paris et al [141] and later refined by Stewart [142] and Ritchie et al [143]. Generally, oxide-induced closure only becomes significant when the total wedging thickness due to accumulation of an oxidation or corrosion product at the crack tip approaches the crack-tip opening displacement. This mechanism is significantly enhanced by fretting [163,164], which can only occur if another form of contact closure is present or if compressive loading occurs. Since oxide-induced closure is enhanced by fretting, this mechanism operates primarily in a region immediately behind the crack tip at near-threshold stress intensity levels [163].

The concept of roughness-induced crack closure was initially suggested by Cooke and Beevers [144] in 1974 and more formally introduced later by Walker and Beevers [145] in 1979. According to this mechanism, which is also known as asperity-induced crack closure, residual shear displacements and asperities on the fracture surface produce imperfectly mating fracture surfaces that contact and transfer load prior to complete remote unloading. Whereas the first two closure mechanisms are primarily the result of mechanical and environmental effects, respectively, roughness-induced closure is largely a manifestation of the material's microstructure [e.g., 78,79,81,122-124,165]. The shear offsets produced on the fracture surface are the result of crystallographic slip, and the scale of the surface roughness has been observed to correlate reasonably with the scale of the continuous slip length of the microstructure [122]. Although roughness-induced closure is considered to be more important in the  $\Delta K$  regime corresponding to near threshold crack growth rates, it has been observed to be a dominant closure mechanism well into the mid- to upper- $\Delta K$  range for some materials [122-124,166-169]. Roughness-induced crack closure has been represented by a number of simple models [146,170-172] that incorporate parameters that attempt to quantify the character and



magnitude of fracture surface roughness.

The mechanism of viscous fluid-induced crack closure [147,148] operates when a crack is submerged in a liquid environment, producing hydrodynamic wedging due to the viscous medium inside the crack. This mechanism is enhanced by low stress ratios but is often accompanied by competing mechanisms which include minimization of oxide-induced closure and suppression of a moisture-related corrosion fatigue process that might occur in humid air. Viscous fluid-induced crack closure is generally of secondary importance, partially because of offsetting effects of viscosity. Increased viscosity leads to greater internal fluid pressure within the crack, but this is opposed by a decrease in penetration of the fluid into the crack as viscosity increases.

Phase transformation-induced crack closure [149,150] occurs when material in the process zone ahead of a propagating crack undergoes a stress-induced phase transformation that results in a dilation of the transformed material. As the crack propagates, the wake of transformed material produces a wedging action behind the crack tip. This mechanism appears to operate in a very limited number of materials, primarily Transformation Induced Plasticity (TRIP) steels and transformation-toughened ceramics.

In many instances the primary contribution of crack closure occurs in the near-threshold crack growth region, and there is significant evidence that  $\Delta K_{th}$  is influenced appreciably by crack closure. In a number of materials  $K_{op}/K_{max}$  has been found to approach 1 as  $\Delta K$  approaches  $\Delta K_{th}$  [e.g., 173-175], indicating that crack closure is largely responsible for crack arrest at  $\Delta K_{th}$ . Moreover, measured levels of crack closure were found to be abruptly reduced by careful removal of the wake of the crack, and during subsequent crack propagation the closure level increased smoothly with increasing

crack length, while the accompanying fatigue crack growth rate was commensurate with the instantaneous level of  $\Delta K_{\text{eff}}$ . It has been shown numerically [156] and experimentally [176,177], however, that the high values of closure measured at near-threshold growth rates may be an artifact of the decreasing-load history normally used in  $\Delta K_{\text{th}}$  experiments. This possibility remains a point of discussion and concern.

Although closure measurements on large cracks may be obtained routinely with the aid of a microcomputer, a number of complexities and uncertainties remain regarding both the acquisition and analysis of the experimental data [139,178,179]. A number of investigators [180-186] have reported that the level of crack closure obtained from crack-opening-displacement measurements is dependent on the location of the measurement. Holding all other variables fixed,  $K_{\text{op}}/K_{\text{max}}$  has been found to increase as the measurement location approaches the crack tip. It has been suggested that this behavior may be a near-surface effect (at least for plasticity-induced closure) and that a remote measurement, which reflects the bulk response of the specimen, is more appropriate. From a practical point of view, calculations of  $\Delta K_{\text{eff}}$  based on remote closure measurements often provide a means of consolidating crack growth rate data from different materials under various loading conditions. Fundamentally, however, the significance of near-tip crack closure behavior remains an important question.

The measurement and interpretation of crack closure is also complicated by three-dimensional effects, which may be important for through cracks in thick plates [187] and surface cracks [188-190]. Experimental characterization of three-dimensional crack-opening behavior is extremely difficult in metals but has been thoroughly investigated in transparent materials using Newton interferometry [187,190]. In both through-crack and surface-flaw geometries in these materials, crack closure has been shown to be dominated by near-surface plasticity. For

polymethylmethacrylate specimens containing surface flaws loaded in bending, crack-opening behavior has been found to be very complex, and although not a unique trend, a number of cracks have been found to open as illustrated schematically in Fig. 2.16 [190]. This figure shows that the interior of the crack is open at zero load, and as the load is increased the crack opens progressively: first at the depth, then at the crack mouth, and finally at the surface crack tip. It appears that each of these three conditions of crack opening can be detected independently by careful remote measurements of crack opening displacement. Considering the three-dimensional quality of crack opening behavior, it is difficult to quantify surface-flaw crack closure with a single parameter, and it is unclear which aspect (or combination of aspects) of three-dimensional crack closure controls crack growth rate.

Examinations of the closure behavior of surface cracks in bending in low-strength steels [188,189] also suggest that crack closure load is a maximum at the specimen surface. James and Smith [188] infiltrated small cracks with epoxy resin under load and performed careful sectioning experiments to determine crack opening behavior at the depth of the crack. They concluded that  $K_{op}$  determined from remote load-displacement measurements was primarily associated with crack opening at the crack depth. Although these findings on metals are consistent with the observations reported for transparent materials, all of the available results appear to be from materials that are dominated by plasticity-induced closure. The three-dimensional aspects of crack closure may be of much less significance for materials and test conditions where oxide- or roughness-induced crack closure are appreciable, since these mechanisms are believed to operate extensively in the plane-strain region of the crack.

The dependence of crack closure on crack length has been examined experimentally in a number of investigations. Several researchers measured crack closure and crack

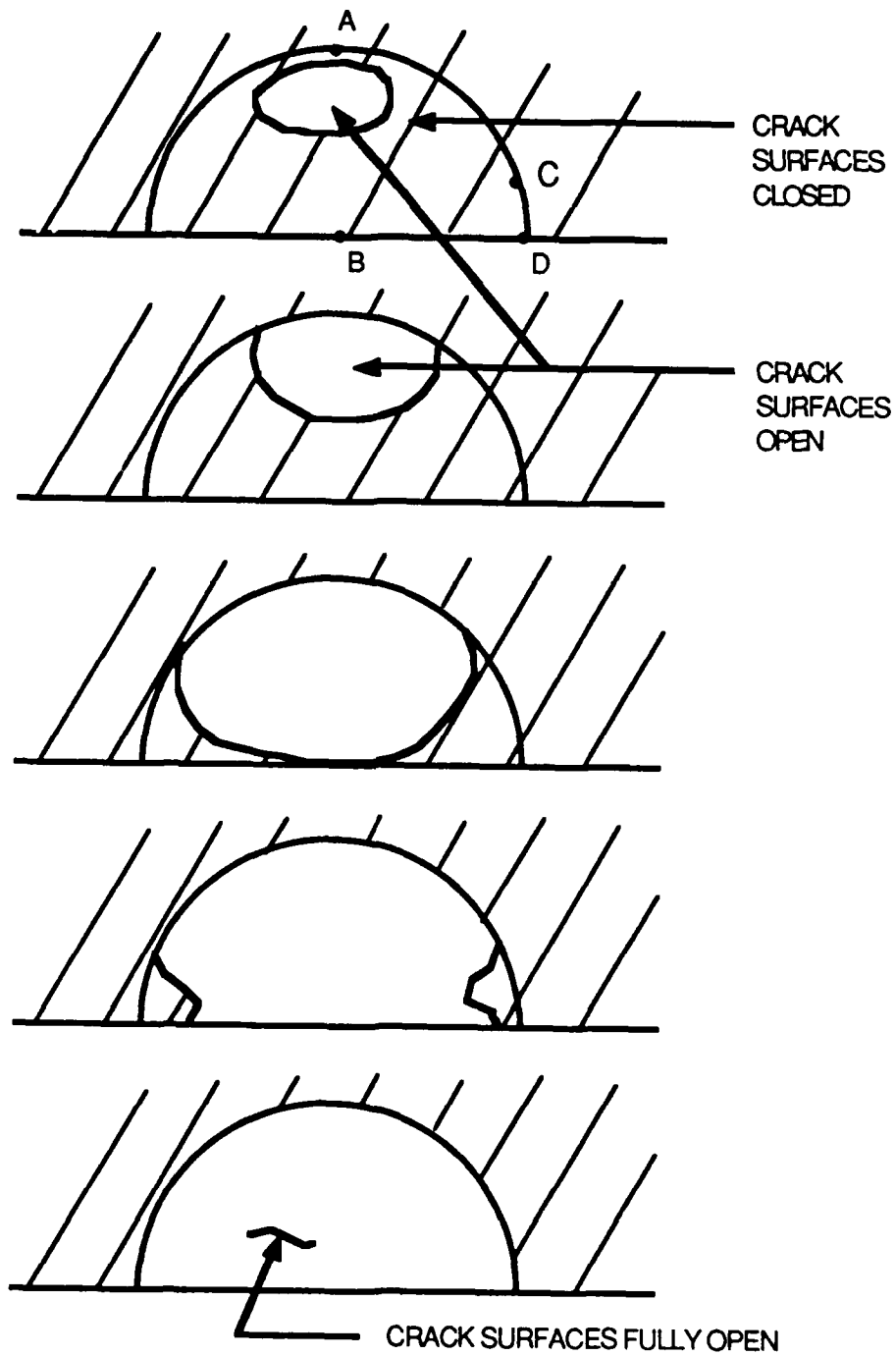


Fig. 2.16 Three-dimensional surface-crack opening behavior often observed as the mode I load is increased from zero [after 190].

growth rate after removal of the wake of long, through-thickness cracks in aluminum alloys [173-175,191,192], steel [193], and Inconel 718 [194]. After wake removal, long cracks that had been arrested at  $\Delta K_{th}$  exhibited significantly lower closure loads (higher  $\Delta K_{eff}$ ) and propagated rapidly without increasing the applied load range [173-175,191]. Although much of the crack wake was found to contribute to closure, a region within approximately 500  $\mu m$  of the crack tip was of primary importance. For long cracks that had been propagated only at stress intensity factor ranges well above  $\Delta K_{th}$ , however, there was little or no change in closure following removal of the crack wake [192,194]. Collectively, the crack wake studies underline the important role of closure in determining  $\Delta K_{th}$ , although as discussed earlier, the high closure levels observed at near-threshold growth rates may be at least partially the result of the decreasing load history used to attain low growth rates.

Due to the great experimental difficulty involved, a very limited number of experiments have been performed to measure closure of small cracks. Morris and coworkers used scanning electron microscopy to obtain small-crack closure measurements on a series on aluminum alloys [92-94,195-197] and Ti-6Al-2Sn-4Zr-6Mo [198-200]. In the aluminum alloys they observed that closure of small surface cracks approximately followed the simple relationship

$$P_{cl}/P_{max} = C \delta(0)/L \quad (2.13)$$

where  $C$  is an arbitrary constant,  $\delta(0)$  is the residual crack-mouth opening at zero load, and  $L$  is the tip-to-tip crack length. After empirical determination of  $C$  from a limited number of load-displacement measurements in the SEM, it was possible to obtain an estimate of the level of closure for numerous small cracks simply by measuring  $\delta(0)$ .

In Ti-6Al-2Sn-4Zr-6Mo [198-200], SEM measurements of CTOD at zero load revealed the dependence of closure on crack length. As shown in Fig. 2.17, residual CTOD increased with increasing crack length until achieving a stabilized value for  $2c > 150 \mu\text{m}$ . It was concluded that the data represented the development of roughness-induced crack closure, and a model was constructed that predicted a decrease in  $\Delta K_{Ih}$  based on measurements.

Tanaka et al [201,202] mounted strain gages across sharp notches in a low-strength steel to monitor closure of short, through-thickness cracks propagating in the notch field. Although such strain-gage methods normally have inadequate resolution for determination of small-crack closure, the reported measurements were facilitated by the presence of the notch, which sufficiently amplified the crack opening displacement. The closure measurements were used to calculate  $\Delta K_{eff}$ , which as shown in Fig. 2.18, was effective in consolidating the data of large and small cracks.

Clement et al [131] used a clip-gage extensometer to monitor the development of closure of short, through-thickness cracks in nodular cast iron. They reported closure measurements on cracks as short as approximately 0.4 mm and showed that a crack length of approximately 1.5 mm was required before closure was fully developed in this material. The authors suggested that the transient development of crack closure was primarily responsible for the rapid growth of small cracks in the nodular cast iron.

Iyyer and Dowling [203] used acetate replicas to monitor small-crack closure in 4340 steel specimens tested in strain-controlled fatigue at high strain amplitudes. The high-strain experiments generally produced bulk plasticity and cyclic ratcheting of the specimens, which gave rise to a significant residual crack opening at zero load. As a result of the significant hysteresis in the load-displacement measurements, crack closure did not

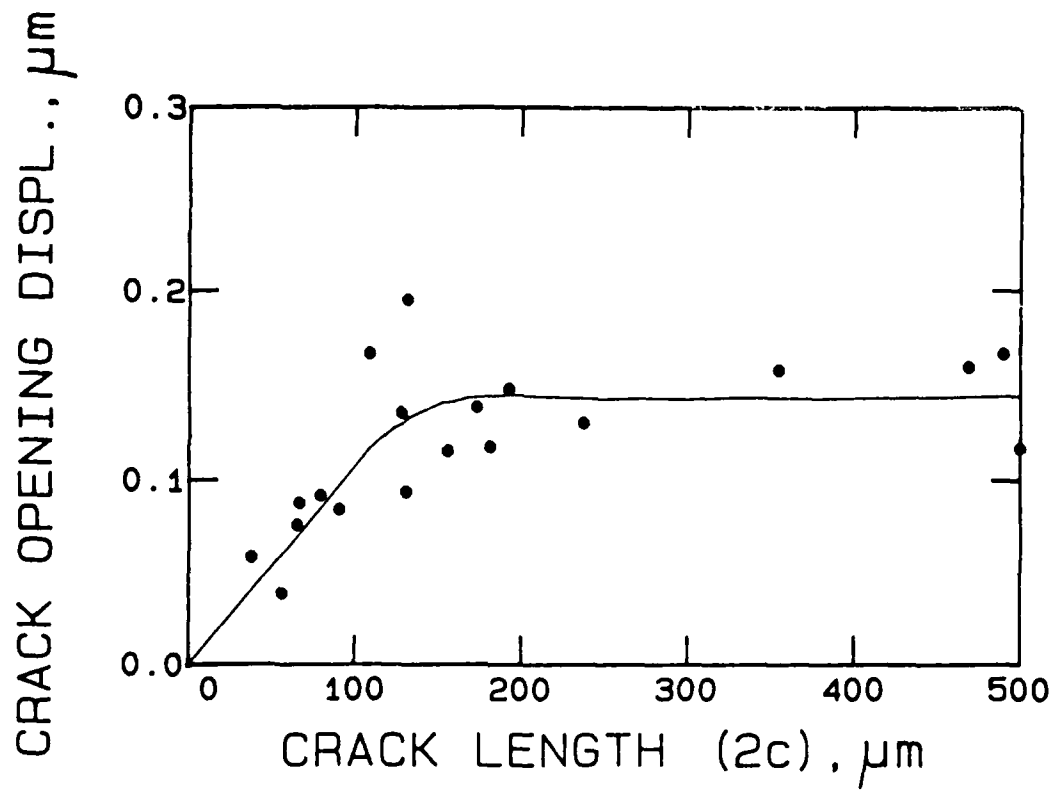


Fig. 2.17 SEM measurements of residual crack-tip-opening displacement of surface cracks in Ti-6Al-2Sn-4Zr-6Mo showing the apparent dependence of crack closure on crack length [198-200].

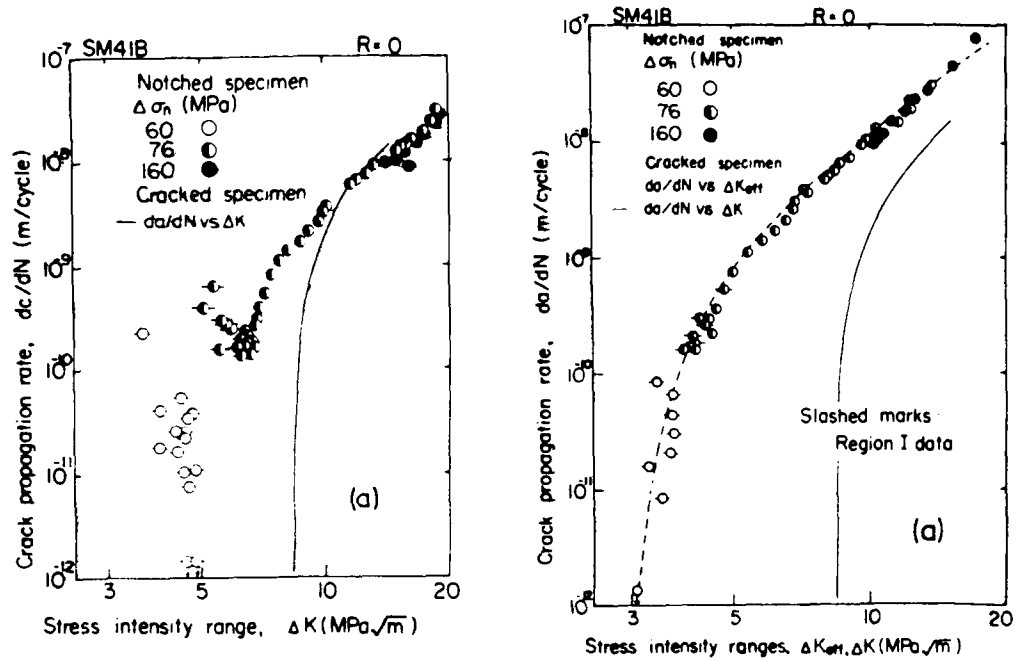


Fig. 2.18 Crack growth rate data from notched specimens demonstrating the ability of  $\Delta K_{eff}$  to consolidate growth rates from long and short cracks [201].



occur until the lowest stress level in the fatigue cycle was approached, and crack opening occurred in the compressive portion of the cycle.

## **2.9 Differences in Local Crack-Tip Environment**

Gangloff [204] first demonstrated that an aggressive environment may affect small and large cracks differently, leading to a difference in growth rates under nominally equivalent test conditions. He investigated crack growth in ultrahigh strength 4130 steel, which did not show a crack-size effect when tested in air. Using an electrical potential method [205-207] to monitor the growth of small cracks in a 3% NaCl aqueous solution, growth rates of small cracks were found to be two orders of magnitude faster than for equivalent large cracks. This effect was attributed to differences in the hydrogen ion concentration in the region of the crack tip due to differences in the fluid pumping efficiency for small and large cracks. Similar small-crack behavior has been reported by Saxena et al [208] for an austenitic steel in an environment of 95% H<sub>2</sub> and 5% moist air. In testing of the aluminum alloy 7075-T6, Lankford [209] found an unexpected change in the mechanism of growth for small cracks in an environment of moist air. In this instance, the change in crack growth mechanism was offset by the normally aggressive influence of the environment. In general, cracks that are characterized as "chemically-small" may not satisfy the definition of a small crack based on mechanics or microstructural considerations.

## **2.10 An Assessment of the Literature on the Growth of Small Cracks**

### **2.10.1 Rationale for the Present Investigation**

The available literature on small fatigue cracks may be organized conceptually

according to the present terminology of the field which distinguishes cracks as mechanically-, microstructurally-, physically-, or chemically-small. These classifications reveal the breadth of the small-crack problem and highlight the variety of scientific disciplines that are relevant to research in this area. Due to the multifaceted nature of the problem, it is desirable to conduct a number of focused investigations which selectively emphasize mechanical, microstructural, physical, and electrochemical aspects of the problem. By isolated study of these various features, it should be possible to evolve a fundamental understanding of the overall small-crack problem.

Although considerable effort has been devoted to understanding mechanically-small cracks, the search for a general parameter capable of describing crack driving force independent of crack size has proved elusive. A number of modifications to existing parameters have been proposed, but none of these has been adequately supported fundamentally, and many are entirely empirical. Beyond the success of the various nonlinear parameters in dealing with elastic-plastic effects, a general analytical solution to the small-crack problem is lacking.

Much of the available literature has dealt with cracks that were microstructurally small, but many of these investigations did not actively address effects of microstructure. While a number of researchers have reported phenomenological aspects of small-crack behavior that included the influence of microstructure, there have been relatively few controlled investigations to examine microstructural effects on small cracks. Such research, however, should provide valuable insight into the effects of small-crack propagation on fatigue life, since as stated earlier, variations in microstructure often have opposing effects on crack initiation and crack propagation.

Although crack closure effects have often been cited as a possible explanation for small-crack effects, the difficulty of conducting critical experiments on these physically-small cracks has severely hampered research. The few reported measurements of small-crack closure have generally been performed under very restrictive conditions designed to enhance displacement-measurement resolution. This has been necessary because, with the exception of very time consuming SEM methods, the existing experimental techniques have generally been inadequate to measure closure of very small, naturally occurring cracks. Questions regarding the phenomenon of closure, specifically as induced by fracture surface roughness, remain largely unanswered. Moreover, the interrelationship between microstructural variables and crack closure has received only limited study in large-crack specimens and is virtually unexamined from the perspective of small cracks. Such research has a large potential payoff in the area of alloy design as well as in component life prediction.

Unusual effects of environment on the growth of chemically-small fatigue cracks represent an important, but unique, aspect of the small-crack problem and pertain to a relatively limited range of service applications. While this is an important area of study in many respects, it is largely separate from the more general crack-size effects that are widely observed in nonaggressive environments.

Although the review of the literature reveals a number of strong candidates for additional research, an investigation of the effects of microstructural variables and crack closure on small cracks appears to be extremely pertinent to both material design and application. The combined study of the two small-crack issues is both appealing and necessary. It appears that microstructural effects on crack growth are often manifested through an influence on crack closure, and from a reverse point of view, microstructural variations provide a method to manipulate crack closure characteristics for controlled

study. Moreover, with the selection of an appropriate alloy system, it should be possible to isolate microstructural and crack closure effects sufficiently to facilitate a systematic and fundamental investigation. Since variations in stress level in the nominally elastic range may influence the level of plasticity-induced crack closure as well as the extent of crack-tip plasticity, stress level should be included as an experimental variable to help isolate its effect.

### **2.10.2 Selection of an Alloy System**

To date, most of the research concerning the growth of small cracks has been performed on materials having cubic crystal structures, e.g., steels and alloys of aluminum and nickel. Only a limited amount of research has addressed materials with the more restricted deformation behavior exhibited by hexagonal-close-packed (HCP) crystal structures, such as titanium alloys. From a practical point of view, investigations of materials possessing the HCP structure would be of significant value, since such materials have a number of technically important applications. Moreover, intermetallics based on titanium appear to offer improved high-temperature capability if effective life-management methods can be developed and demonstrated. In addition to the practical value, variations in the microstructure of titanium alloys can have a marked effect on the materials' mechanical properties, including crack initiation, crack propagation, and crack closure characteristics. Based on these considerations, along with the existence of well-documented relationships between microstructure and the corresponding physical and mechanical properties [74,79,82,113,114,119,120,122-124,165,210-240], the  $\alpha$ -phase titanium-aluminum alloy system was chosen for investigation. The following discussion is intended to summarize the existing understanding of the physical and mechanical metallurgy of these alloys.

## 2.11 Titanium-Aluminum Alloys

### 2.11.1 Physical Properties of Ti-Al Alloys

As an element, titanium is a low-density metal that exhibits an allotropic transformation at 882.5°C [210]. Below this temperature, the hexagonal-close-packed (HCP)  $\alpha$  phase is stable, while the body-centered-cubic (BCC)  $\beta$  phase exists from 882.5°C to the melting point ( $\approx 1668^\circ\text{C}$ ). Although pure titanium is often used by the chemical and petroleum industries in aggressive environments at high temperature, in structural applications the metal is normally alloyed with other elements which tend to stabilize either the  $\alpha$  or  $\beta$  phase. The most important  $\alpha$ -phase stabilizers (and strengtheners) are Al and O, of which Al is the most important technically, while O is the most potent but quickly leads to embrittlement. Solute additions of Sn and Zr strengthen the  $\alpha$  phase but have an approximately neutral effect on the  $\alpha/\beta$  transformation temperature. The  $\beta$  phase can be stabilized by solute additions of refractory metals such as V, Mo, Nb, and Ta and transition metals such as Fe, Cr, Mn, and Ni.

Of the structural alloys, those having microstructures based on a combination of the  $\alpha$  and  $\beta$  phases are extremely important technically and have numerous applications in structural components requiring high strength, low density, and temperature capability up to approximately 550°C. Since many of the  $\alpha+\beta$  alloys consist primarily of the  $\alpha$  phase, the relationships between microstructure and mechanical properties of this phase are of fundamental interest. In  $\alpha+\beta$  alloys, aluminum partitions strongly to the  $\alpha$  phase, while the concentration of  $\beta$  stabilizers in the  $\alpha$  phase is low. Thus, the binary titanium-aluminum system (containing a very low concentration of oxygen) simulates the  $\alpha$  phase in the more important two-phase alloys. The physical and mechanical metallurgy of these alloys are well understood [74,79,82,113,114,119,120,122-124,165,

210-240], making the Ti-Al alloy system a very strong candidate for studying microstructurally related small-crack effects.

Figure 2.19 presents the accepted phase diagram of titanium-aluminum alloys containing up to approximately 15.8 weight % (25 atomic %) aluminum. This diagram was primarily the result of the work by Blackburn [212] and, later, by Nambodhri et al [229]. As shown, at low temperatures the  $\alpha$  phase exists at equilibrium in alloys having aluminum concentrations up to approximately 6% (all compositions will hereafter be given in percent by weight). The difference between the  $\alpha/\alpha+\alpha_2$  phase boundary found by the two investigations is due to differences in the concentration of oxygen, which stabilizes the  $\alpha$  phase. The  $\alpha$ -phase has a disordered HCP structure that is both elastically and plastically anisotropic. In pure titanium the anisotropy arises from the small  $c/a$  ratio of the crystal structure, which is 1.5873 [210] as compared to the 1.633 value calculated assuming a hard-sphere atomic model. Additions of aluminum tend to reduce both the  $a$  and  $c$  lattice vectors approximately uniformly [240].

At low temperatures, alloys having aluminum concentrations greater than approximately 12.5% Al consist entirely of the equilibrium  $\alpha_2$  phase which has an ordered hexagonal  $DO_{19}$  structure based on the stoichiometric composition  $Ti_3Al$ . This structure exhibits brittle behavior (cleavage fracture) in the bulk polycrystalline form due to the difficulty of activating the five independent slip systems necessary to accommodate an arbitrary, internal shape change (Von Mises criterion). This difficulty, coupled with the planar slip characteristic of superlattices, tends to favor the onset of fracture instead of flow. The limited number of slip systems is the result of differences in the critical resolved shear stress necessary to move superdislocations on the possible (non-equivalent) slip systems in the ordered structure [238]. Although  $a$  dislocations are easily generated,  $c+a$  dislocations are less commonly observed in  $Ti_3Al$  [238].

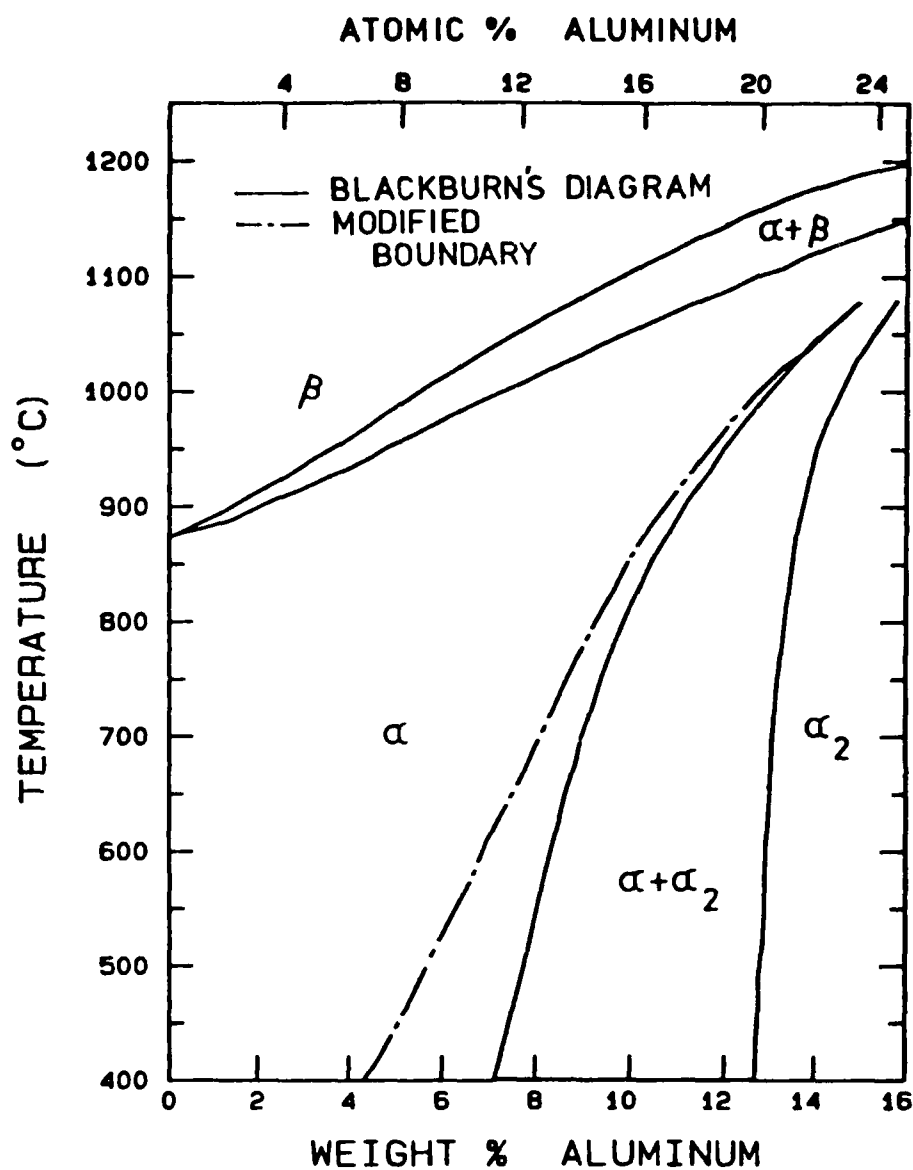


Fig. 2.19 Titanium-aluminum phase diagram of Blackburn [212] showing a modification by Namboodhiri et al [229] for alloys of low oxygen concentration.

Within the  $\alpha+\alpha_2$  phase field, near the  $\alpha/\alpha+\alpha_2$  phase boundary, solution-treated Ti-Al alloys may be aged to form a fine, uniform distribution of  $\alpha_2$  precipitates in an  $\alpha$ -phase matrix. Since the lattice misfit between the precipitates and the matrix is small ( $a$  misfit = 0.83%;  $c$  misfit = 0.35% [238]), the precipitates remain fully coherent with the matrix up to a size of approximately 120 nm [212]. The precipitates are spherical in shape until reaching a diameter of approximately 10 nm [227] to 50 nm [212], after which they become ellipsoidal, with the major axis of the ellipsoid aligned along [0001] in the matrix [212]. In the low-temperature  $\alpha$ -phase region near the  $\alpha/\alpha+\alpha_2$  boundary, electron diffraction results have indicated the presence of the ordered structure, although no precipitates could be detected at a resolution of 25Å [212]. This finding is believed to indicate the presence of short-range order in the  $\alpha$ -phase. The suggestion of short-range order is further supported by electric resistivity measurements, which suggest the presence of an ordered structure long before identifiable precipitates begin to form [229], and by the observations of a wavy to planar slip transition with increasing Al content [213].

### 2.11.2 Mechanical Behavior of Ti-Al Alloys

Although considerable research has been devoted to developing an understanding of  $Ti_3Al$ -type alloys, the present investigation will consider only solid-solution and precipitation-strengthened  $\alpha$ -phase alloys. Therefore, the following discussion of deformation and mechanical properties of Ti-Al alloys will not be extended to Al concentrations which correspond to alloys based on the  $Ti_3Al$  composition.

In addition to stabilizing the  $\alpha$  phase of titanium-aluminum alloys, aluminum (and oxygen) additions to titanium reduce density [213], increase Young's modulus [213], increase strength [210,213,221,230,232,236], reduce work hardening rate [31],



promote planar slip [213,230,232,236,238], and suppress twinning [213,230,232,238,239]. Plastic deformation of Ti-Al alloys is often very complex, occurring by a combination of slip and twinning on the possible systems identified in Table 2.2 [232]. Because of this, texture is an important variable in assessing the mechanical behavior of Ti-Al alloys. In tests of carefully prepared single crystals of Ti-Al alloys ranging in aluminum content from 0 to 6.6% Al, Paton, Baggerly, and Williams [230] determined the critical resolved shear stress (CRSS) required to promote a slip, on prism and basal planes, and  $c+a$  slip as a function of temperature. It was found that the CRSS for prism slip was lowest under all conditions, although both increasing aluminum content and increasing temperature tended to reduce the difference between CRSS for basal and prism slip. Slip with a  $c+a$  Burgers vector was always more difficult than a slip.

Table 2.2: Slip and Twinning Modes in  $\alpha$ -Phase Titanium [232]

<u>Slip Direction</u>	<u>Slip Planes</u>
$a$ Slip, $\langle 11\bar{2}0 \rangle$	$\{10\bar{1}0\}$ (0001) $\{10\bar{1}1\}$
$c+a$ Slip, $\langle 11\bar{2}3 \rangle$	$\{10\bar{1}0\}$ $\{10\bar{1}1\}$ $\{11\bar{2}1\}$ $\{11\bar{2}2\}$
<u>Twining Modes</u>	
$\{10\bar{1}2\}$ (Primarily operative [230,232])	
$\{11\bar{2}1\}$	
$\{11\bar{2}2\}$ (Observed in compression [231])	
$\{11\bar{2}3\}$	
$\{11\bar{2}4\}$	
$\{10\bar{1}1\}$	

Alloys having low aluminum contents deformed by a combination of slip and twinning, while increasing Al concentration suppressed the occurrence of twinning. The shear strain produced by twinning often requires accommodation by  $c+a$  dislocations in the matrix, and twinning may reorient the lattice to allow further a slip [232]. Although a combination of a slip and twinning can accommodate an arbitrary shape change, the suppression of twinning requires  $c+a$  slip to operate [230,232].

The character of deformation of  $\alpha$ -phase titanium-aluminum alloys depends on Al content and heat treatment [213,227,230,236,238], as well as on the concentration of oxygen [239]. In polycrystals, the observed deformation also depends on texture. Holding oxygen concentration constant, increases in aluminum content of Ti-Al alloys produces a change in slip character from fine (homogeneous) wavy slip in alloys with small amounts of aluminum ( $\leq$  approximately 4% Al) to coarse (heterogeneous) planar slip in alloys with higher aluminum content ( $\geq$  approximately 6% Al). For single-phase Ti-Al alloys within the compositional range of  $4\% \leq \text{Al} \leq 6\%$  there is a marked reduction in the incidence of cross slip, and slip planarity increases dramatically [213,230,232,236]. This behavior is believed to result from short-range order in the  $\alpha$  phase [213].

For alloys that have been aged in the  $\alpha+\alpha_2$  phase field, the presence of uniformly nucleated  $\alpha_2$  precipitates gives rise to a modest increase in strength, while severely reducing ductility [213,218,227,230,232,236,238]. The maximum increase in strength attainable during aging is associated with a precipitate diameter of approximately 10 nm [213,227]. Since the precipitates are coherent and have a small misfit strain, they are normally sheared by dislocations. Dislocation looping only occurs in extremely overaged material having very large precipitates separated by more than approximately 80 nm [227]. The presence of the ordered, coherent precipitates serves to enhance slip planarity and further concentrate (localize) slip into fewer widely-separated,

well-defined bands [119,120,213,227,230,232,236,238]. This strain localization results from strain softening within individual slip bands brought on by destruction of the ordered precipitates within the slip bands [119,214,221,224,230,232,236,238]. Since the brittle behavior of aged Ti-Al alloys generally results from cracking that initiates from dislocation pileups at grain boundaries [221,224,227,232], reducing the grain size improves ductility by reducing the average slip length and the corresponding number of dislocations within a pileup [221,234].

Due to plastic anisotropy of individual  $\alpha$ -phase grains in titanium-aluminum alloys, mechanical working of these materials in their polycrystalline form often produces crystallographic alignment, or texture, in the final product [79,112,232,235]. As a result, the finished product may exhibit bulk elastic and plastic anisotropy, which may strongly influence mechanical behavior. The most common crystallographic texture in rolled plate is associated with coordinated lattice rotations, wherein the average crystallographic orientation is no longer random but one having a majority of the crystals oriented such that their [0001] directions are aligned approximately normal to the plane of the rolled plate. This basal texture is often observed in Ti-Al alloys [122,228,232,235] and may produce approximately planar isotropy and relatively higher strength and modulus values in the short transverse (through-thickness) direction [232].

The mechanical performance of titanium-aluminum alloys under cyclic loading has been studied in terms of both crack initiation [119,120,220] and crack propagation [112,113,122-124,215-219,217-219]. In an extensive investigation of a series of Ti-Al alloys that was solution heat treated and quenched to prevent the formation of  $\alpha_2$  precipitates, Kim [119] and Kim et al [120] found a significant influence of slip character on the initiation of cracks that formed under strain-controlled low-cycle

fatigue (LCF). Although dislocation densities were higher under cyclic loading than under monotonic loading, the character of the dislocation arrays observed under monotonic and cyclic loading were qualitatively equivalent. The dominant deformation mode for both monotonic and cyclic deformation was confirmed to be a slip on prism planes. As shown in Fig. 2.20, a poorly developed cellular dislocation structure was produced by cyclic loading of Ti-4Al, while more closely spaced bands of dislocations were observed in solution treated and quenched Ti-8Al. The dislocation structure developed in aged Ti-8Al was localized in fewer, very intense, slip bands (Fig. 2.20c). Twinning was commonly observed in cyclically-loaded Ti-4Al and to some extent in Ti-8Al; twinning was not observed in Ti-8Al that was loaded monotonically. Increasing slip planarity was found to promote early crack initiation due to concentration of slip within a few slip bands. Thus, the single phase  $\alpha$  alloys that had low aluminum contents exhibited the best LCF performance, and alloys with higher concentrations of Al had inferior LCF capability, although they were of higher strength. The aged alloys, exhibiting strain localization, had the worst low cycle fatigue capability.

The correspondence between slip character and fatigue crack propagation showed a very different trend in research reported by Allison [122] and Allison and Williams [123,124,211]. Testing of large cracks performed to determine near-threshold crack growth behavior of a series of Ti-Al alloys indicated that solution-treated Ti-8Al had the highest threshold stress intensity factor range,  $\Delta K_{th}$ , while Ti-4Al exhibited the lowest  $\Delta K_{th}$ . The  $\Delta K_{th}$  for aged Ti-8Al was found to lie at an intermediate value. The differences in crack growth behavior among the three alloy conditions was found to be due to different levels of roughness-induced crack closure observed in the various materials. Measurements of crack closure were used to calculate values of  $\Delta K_{eff}$  for each of the three materials, and replotting the data against this parameter effectively collapsed the collection of data into a single band. It was concluded that differences in alloy slip

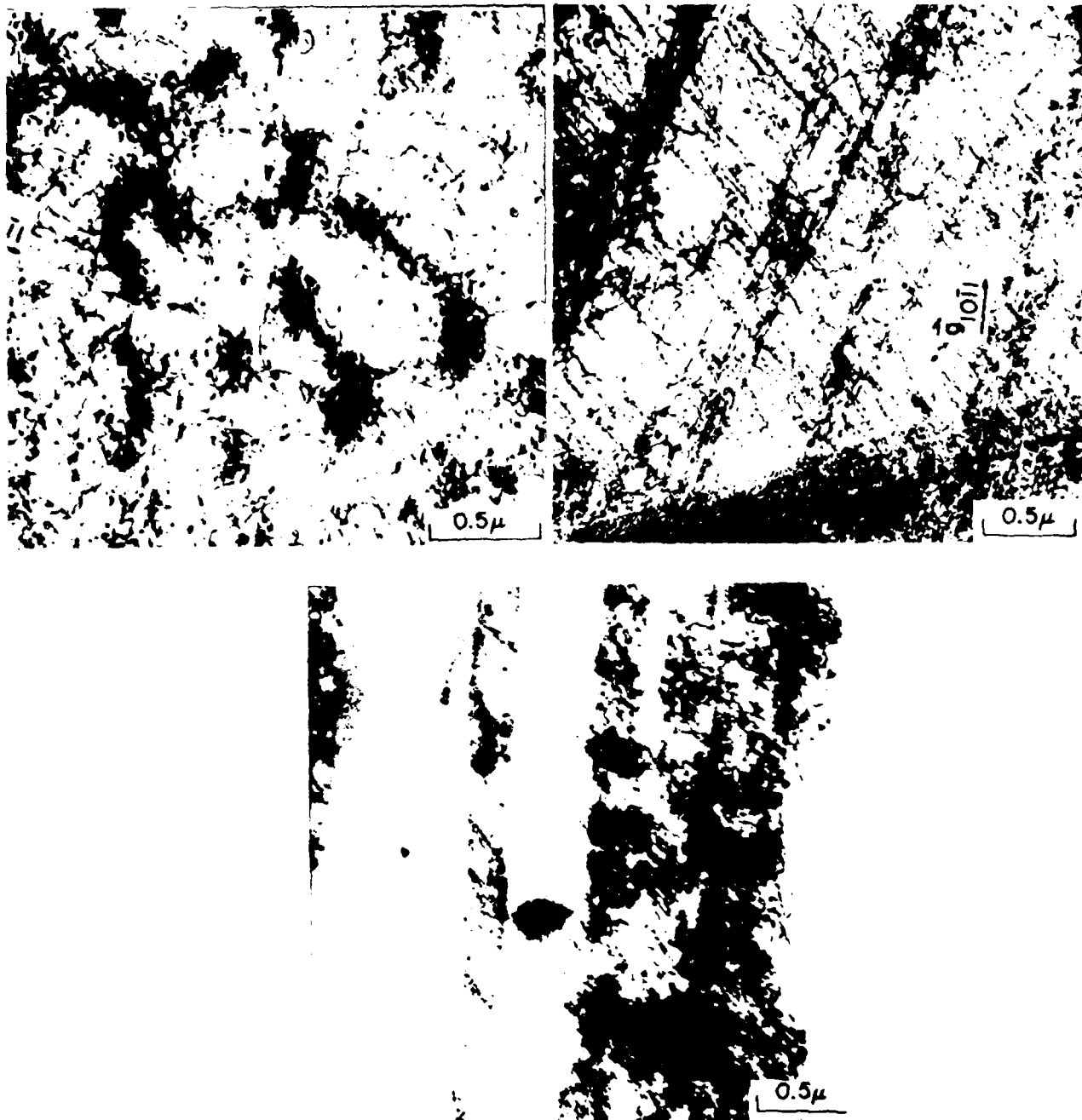


Fig. 2.20 TEM micrographs showing the influence of aluminum content and aging on the dislocation structures produced by cyclic loading ( $\Delta\epsilon/2 = 1\%$ ). (a) Ti-4Al; (b) Ti-8Al; (c) aged Ti-8Al.

character (controlled by microstructure and chemistry) were responsible for the differences in fracture roughness which, through crack closure, controlled crack propagation behavior of the alloy at low stress ratios. Previously, it had been believed [220,228] that microstructurally-produced differences in slip reversibility were primarily responsible for differences in fatigue crack propagation resistance of Ti-Al alloys. By the process of elimination, however, it now appears that slip reversibility does not exert a direct, major influence on fatigue crack propagation in titanium-aluminum alloys.

The effect of grain size on fatigue crack growth in aged Ti-8.6Al was examined by Lindigkeit et al [228]. These investigators conducted tests of large cracks in vacuum at  $R = 0.2$  and found that cracks in this material with a  $20\text{ }\mu\text{m}$  equiaxed grain size propagated at rates approximately an order of magnitude faster than similar cracks in  $100\text{ }\mu\text{m}$  grain size material. The alloy with the  $100\text{ }\mu\text{m}$  grain size exhibited a  $\Delta K_{th}$  of  $15\text{ MPa}\sqrt{\text{m}}$ , while  $\Delta K_{th}$  for the material with the small grain size was less than  $11\text{ MPa}\sqrt{\text{m}}$ . Although the difference between crack propagation in the two materials was initially attributed to slip reversibility characteristics, Gray and Luetjering [165] reexamined a similar Ti-8.6Al material and concluded that the grain-size effect on crack growth rate resulted primarily from roughness-induced crack closure. The authors suggested that a secondary factor that affected crack growth rates was a difference in the stress intensity factor produced by grain-size-dependent differences in crack-path deflection.

The behavior of small fatigue cracks in aged Ti-8.6Al was examined by Gerdes et al [112] and Wagner et al [113], and it was found that small semielliptical surface cracks grew faster than nominally equivalent large, through-thickness cracks, and that small-crack growth occurred below the large-crack  $\Delta K_{th}$  (see Fig. 2.10). Because the small-crack data obtained from tests of surface cracks at  $R = 0.1$  eventually converged

with large through-crack data at  $R = 0.6$ , it was concluded [112] that crack closure effects were minimal in surface cracks. Although the small cracks invariably grew faster than nominally equivalent large cracks, small cracks commonly exhibited a crack-growth-rate minimum, which was suggested to result from crack shape effects. Although small cracks maintained approximately semicircular shapes during the majority of their lives, initial crack shapes were found to be shallow, having values of  $a/c \ll 1$ . From this point, the small cracks propagated primarily into the depth of the specimen, and the crack length on the surface changed very little. Therefore, crack growth rates determined from length measurements made at the surface were artificially low. When the cracks assumed their equilibrium, semicircular shapes, crack growth on the specimen surface would again commence. Thus, the crack-growth-rate minimum was concluded to be an artifact of early irregularities in crack shape [113].

## 2.12 Objective of the Research

Based on consideration of the available literature, the assessment of the factors that are believed to contribute to the small-crack "problem," and the identification of a pertinent, otherwise well understood, alloy system, the following research objective has been established:

to investigate the interrelated effects of alloy slip character and crack closure on the propagation of naturally initiated small surface fatigue cracks in titanium-aluminum alloys containing 4 and 8% aluminum.

## CHAPTER 3

### EXPERIMENTAL PROCEDURE

#### 3.1 Materials: Processing and Heat Treatment

The titanium-aluminum alloys examined in this investigation were obtained from two sources. Approximately 7 kg of Ti-4Al alloy plate were obtained from a heat of material originally procured from Titanium Metals Corporation of America. This specific alloy plate was used in the research of J. E. Allison on the growth of large cracks reported in references [122-124,211]. The second material, approximately 20 kg of Ti-8Al plate, was purchased specifically for the present investigation from Reactive Metals Incorporated of Niles, Ohio. The chemical composition of both alloys is given in Table 3.1. Both alloys were hot rolled in the  $\alpha$ -phase field to limit grain growth and prepare the material for recrystallization. The Ti-4Al was cast and forged from 1150°C and repeatedly hot rolled from an initial temperature of 1010°C. The finished Ti-4Al plates were approximately 150 mm wide, 600 mm long, and 12.7 mm thick. The Ti-8Al was produced as a double-vacuum-melted ingot and repeatedly press forged from 1150°C until it had been reduced to approximately 50 mm in thickness; press forging was continued from 1010°C until the product thickness was 25 mm. This material was subsequently vacuum annealed for 48 hours at 780°C to remove internal hydrogen. The plate was cut into sections and repeatedly rolled from 1010°C to produce three plates of approximate dimensions: 140 mm wide, 500 mm long, and 15.2 mm thick.



Table 3.1: Chemical Composition of Ti-Al Alloys (Weight %)

<u>Alloy</u>	<u>Al</u>	<u>Fe</u>	<u>O</u>	<u>N</u>
Ti-4Al	4.18	0.042	0.076	0.004
Ti-8Al	7.7	0.03	0.065	0.008

Initial metallographic examination of the Ti-8Al plate indicated the presence of strain-induced, internal shear cracking. Similar cracking had been observed by Allison in Ti-8Al [241], and the problem has been observed in other titanium-aluminum alloys that were worked in the  $\alpha$ -phase field and had aluminum concentrations greater than approximately 6 weight percent [79]. The microcracking of the Ti-8Al alloy acquired for the present investigation probably resulted during rolling operations when the working temperature dropped substantially below the 1010°C starting condition.

To eliminate the microcracking observed in the Ti-8Al material, the plates were hot isostatically pressed (HIP) by Battelle Columbus Laboratories for 2 hours at a pressure of 207 MPa and a temperature of 927°C. Subsequent metallographic examination of the material both before and after final heat treatment indicated that the HIP cycle had effectively closed the microcracks by diffusion bonding. This successful result was expected, since similar HIP conditions are routinely used to eliminate porosity in titanium alloy castings.

The procedure used in heat treating and fabricating specimens from the Ti-Al alloys was dictated largely by the desire to minimize residual stresses that might adversely affect the fatigue experiments. It is well known that residual stresses induced by quenching can significantly influence crack growth behavior. Therefore, the as-received plate was cut into oversize specimen blanks, which were solution heat treated in air in the  $\alpha$ -phase field to fully recrystallize the material. The Ti-8Al blanks were quenched in

water to suppress the formation of  $\alpha_2$  precipitates. Since the Ti-4Al is entirely  $\alpha$  phase at equilibrium at room temperature, and is well removed from the  $\alpha/\alpha+\alpha_2$  phase boundary, quenching was unnecessary. Therefore, this material was air cooled from the solution-treatment temperature, thereby minimizing the development of residual stresses.

Following solution heat treatment of the oversize blanks, specimens were machined from the center of the blanks, which resulted in the removal of over 2.5 mm from each surface of the Ti-4Al blanks and almost 4 mm from each surface of the thicker Ti-8Al specimen blanks. Thus, the layer of material that contained the residual stress produced in quenching was eliminated. Furthermore, the surface removal eliminated the thin outer layer of material that was contaminated by oxygen during solution heat treatment. The depth of penetration of the oxygen during heat treatment was confirmed by both diffusion calculations and microhardness measurements to be less than 0.13 mm. Machining of most of specimens was performed by Metcut Research Associates Incorporated of Cincinnati, Ohio using a precision low-stress-grinding process that minimized the development of surface residual stresses commonly produced by conventional machining processes. A small number of additional small-crack specimens was fabricated using a wire electro-discharge-machining (EDM) process, which avoided the formation of mechanically-induced residual stresses.

Following machining, a number of the Ti-8Al specimens were aged in dynamic vacuum to produce a uniform distribution of fine  $\alpha_2$  precipitates. The specific heat-treatment sequence of all three material conditions is presented in Table 3.2. The solution-treated Ti-8Al is designated Ti-8Al(s), and Ti-8Al(a) refers to the aged condition of this material.

Table 3.2: Heat Treatment of Ti-Al Alloys

<u>Alloy</u>	<u>Heat Treatment</u>
Ti-4Al	900°C/2hr/air cool
Ti-8Al(s)	950°C/2hr/water quench
Ti-8Al(a)	950°C/2hr/water quench vacuum age: 550°C/48hr/furnace cool

### 3.2 Microstructural Characterization

#### 3.2.1 Light Metallography

The microstructures of the alloys were characterized by light metallography. Metallographic samples were prepared by routine manual grinding and polishing, followed by a final vibratory polishing operation using 0.05  $\mu\text{m}$  diameter alumina abrasive. Light micrographs of unetched samples were taken using polarized light to achieve image contrast. Average grain sizes (mean lineal intercept) were determined from the micrographs using the standard three-circle procedure [242]. The mean lineal intercept distance between grain boundaries obtained using the three-circle procedure may be converted to an average, 3-dimensional grain diameter by multiplying by a factor of 1.68 [243]. Although the average 3-dimensional grain diameter has advantages in certain applications, the mean lineal intercept distance is probably more useful when considering the interaction of a crack front with the crystallographic features of a polycrystalline material.

### 3.2.3 Crystallographic Pole-Figure Analysis

The character of the crystallographic texture produced during hot-rolling of the plates of Ti-Al alloys was quantified by the construction of X-ray diffraction pole figures taken in reflection. The pole-figure specimens were machined from the midthickness of the rolled plate and were oriented parallel to the rolling plane. The pole-figure construction was performed by Pratt and Whitney Aircraft of West Palm Beach, Florida using a Huber pole-figure goniometer operated by a Digital Equipment Corporation 11/34 computer that used control software originally developed at Oak Ridge National Laboratory, Oak Ridge, Tennessee. To interrogate a large number of grains, the pole-figure device employed a mechanical stage to oscillate the specimen such that the X-ray beam was swept over an area of approximate dimensions of 20 mm by 10 to 20 mm, depending on the incident angle of the X-ray beam. Pole figures were obtained using the basal (0002), prism ( $10\bar{1}0$ ), and pyramidal ( $10\bar{1}1$ ) reflections, and reflection intensities were calibrated relative to a texture-free sample of Ti-6Al-4V.

### 3.2.4 Transmission Electron Microscopy

A JEOL 2000 FX scanning-transmission electron microscope operating in transmission mode at a potential of 200 KV was used to characterize the precipitate size and distribution in the Ti-8Al. Conventional thin-foil samples were prepared by electropolishing.

## 3.3 Mechanical Property Characterization

To provide a foundation for developing a complete understanding of the physics and mechanics that govern the growth of small fatigue cracks in Ti-Al alloys, a full range of

tests was performed to characterize the mechanical properties of the alloys. These included both monotonic and cyclic tests as well as small- and large-crack growth rate tests. All mechanical testing was performed in laboratory air at room temperature (nominally 22°C), with the relative humidity ranging approximately from 40 to 60 percent.

### 3.3.1 Tensile Testing

Monotonic tensile testing was performed in accordance with ASTM specification E8 [245] using specimens of the geometry shown in Fig. 3.1. Specimens were machined such that their loading axes were oriented either longitudinally (L) or transversely (T) to the rolling direction of the plate. These tests provided measurements of tensile strength and ductility, while also furnishing an assessment of in-plane elastic and plastic anisotropy of the plate. All tests were performed on a screw-driven Instron tensile machine at a cross-head rate of 0.0021 mm/sec, which corresponded to an approximate strain rate of  $8 \times 10^{-5} \text{ sec}^{-1}$ .

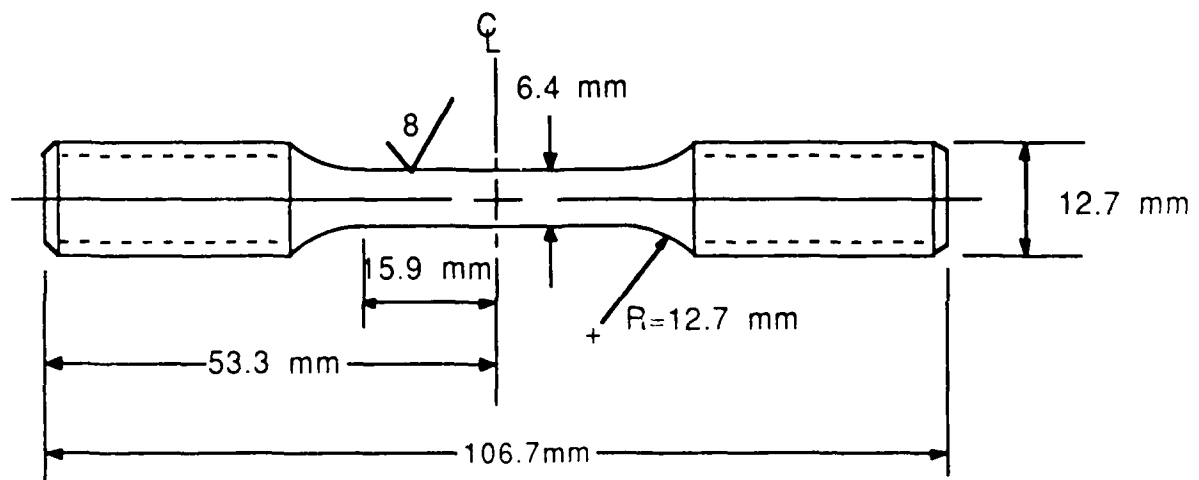


Fig. 3.1 The specimen used for monotonic tensile testing.

### 3.3.2 High-Cycle-Fatigue Testing

High-cycle-fatigue testing was performed in accordance with ASTM specification E466 [246] using specimens of the hourglass geometry pictured in Fig. 3.2. All specimens were fabricated with their loading axes aligned parallel to the transverse direction of the rolled plate. Although the greatest care was exercised to achieve a low-stress surface finish, X-ray residual stress analysis to characterize the specimen surface typically produced by the low-stress machining process suggested that a residual compressive stress existed in a surface layer of material up to 0.13 mm deep [247]. Therefore, to eliminate the possibly confounding effects of residual stresses, the gage section of each specimen was electropolished until a layer of material at least 0.19 mm deep was removed from each surface. The electropolishing was performed under a 20-volt potential at  $-40^{\circ}\text{C}$  in an agitated solution containing 600 ml perchloric acid ( $60\% \text{HClO}_4$ ), 590 ml methanol, and 350 ml butyl cellosolve.

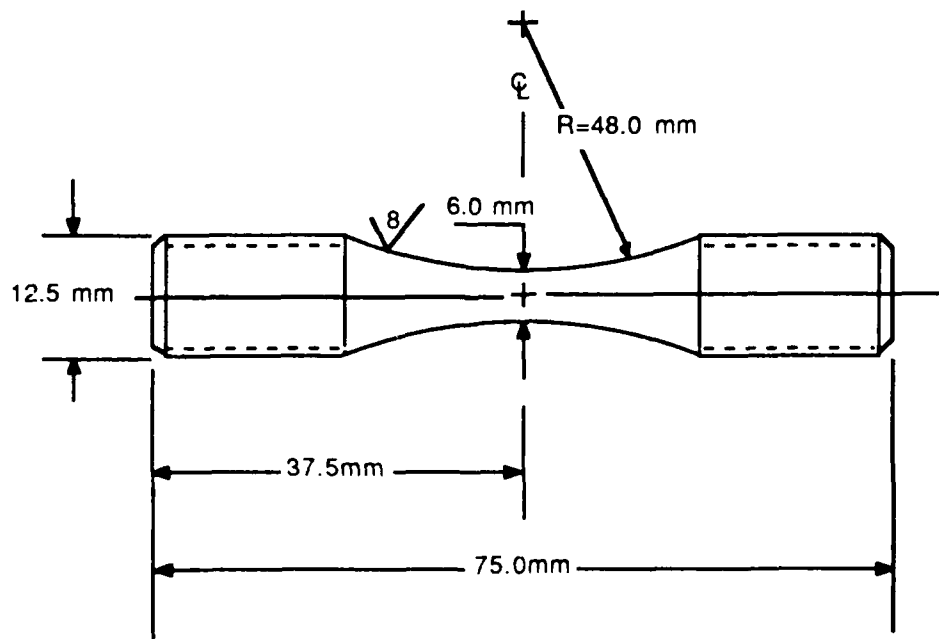


Fig. 3.2 The hourglass specimen used to determine fatigue strength.

The fatigue tests were performed on an MTS servo-hydraulic fatigue machine operating at 30 Hz with a load ratio of  $R = P_{\min}/P_{\max} = -1.0$ . Self-aligning hydraulic grips were used to prevent specimen bending under tension-compression loading. Since the results of the fatigue testing were to be used in the construction of "Kitagawa" diagrams (similar to that shown in Fig. 2.2) for each material, the primary objective of the fatigue tests was to quantify the alloy fatigue strength, which was defined as the stress required to produce specimen failure in  $10^7$  cycles.

### 3.3.3 Large-Crack Fatigue Testing

Testing was performed to determine the growth-rate behavior of large fatigue cracks using conventional compact-type, C(T), specimens illustrated in Fig. 3.3. In conformity with the primary orientation of the high-cycle-fatigue specimens (and the small-crack specimens to be discussed subsequently) the C(T) specimens were machined in the T-L orientation [248]. That is, the axis of specimen loading was perpendicular to the plate rolling direction, and the crack growth direction was parallel to the rolling direction. The crack-mouth notches shown in the figure were used to attach a clip-gage extensometer for use in determining crack-opening compliance.

All C(T) specimen fatigue crack propagation testing was conducted in accordance with ASTM specification E647-86a [249] on an MTS servo-hydraulic testing machine controlled by either an IBM PC or an IBM 9000 computer. The machine-control software was developed under U. S. Air Force Contract by the University of Dayton Research Institute, Dayton, Ohio and followed ASTM guidelines strictly. Crack length was determined from crack-mouth-opening compliance using the analytical expression developed for the C(T) specimen geometry [250]:

$$a/W = C_0 + C_1u + C_2u^2 + C_3u^3 + C_4u^4 + C_5u^5 \quad (3.1)$$

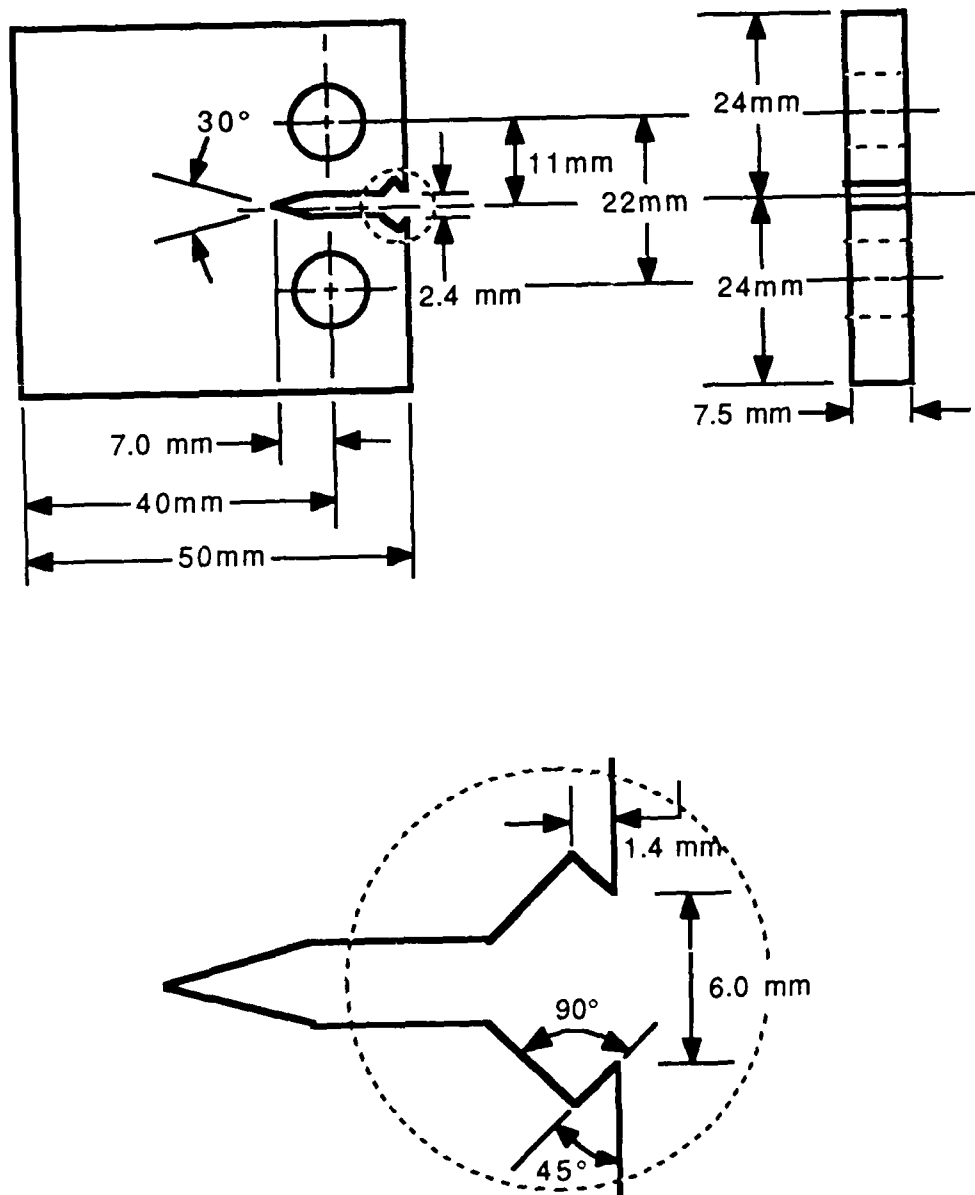


Fig. 3.3 The large-crack, compact-type, C(T), specimen.



where

$$u = 1/((BEV/P)^{0.5} + 1) \quad (3.2)$$

$a$  = crack length,

$W$  = specimen width,

$B$  = specimen thickness,

$E$  = Young's modulus,

$V$  = crack-opening displacement measured at the specimen edge, and

$P$  = applied load corresponding to the instantaneous displacement  $V$ .

The constants of the polynomial are:

$$C_0 = 1.0010$$

$$C_1 = -4.6695$$

$$C_2 = 18.460$$

$$C_3 = -236.82$$

$$C_4 = 1214.9$$

$$C_5 = -2143.6$$

Throughout the tests, the accuracy of the crack lengths determined from compliance were periodically confirmed by visual measurements made with a light microscope. The precision of the crack length measurements determined from compliance was better than 25  $\mu\text{m}$ , as estimated by the standard deviation of repeated measurements of the length of a non-growing crack.

The procedure used in conducting the C(T)-specimen tests is outlined as follows. In accordance with ASTM specification E647-86a [249], specimens were precracked at 30 Hz under  $R = 0.1$  cycling, and the load range was gradually reduced until a growth rate of approximately  $10^{-8}$  m/cycle was achieved. During load shedding, a minimum crack extension of 0.1 mm was required. A zone correction factor  $Y_p = 1/K(\sigma_p)^2$  was

was achieved during a ten percent reduction in load range. The total length of the precrack always exceeded 2.5 mm, as measured from the notch. After precracking, load control followed the ASTM-recommended expression

$$\Delta K = \Delta K_0 [\exp (C (a-a_0))] \quad (3.3)$$

where

$a_0$  = crack length after precracking,

$a$  = instantaneous crack length,

$\Delta K_0$  = stress intensity factor range corresponding to crack length  $a_0$ ,

$\Delta K$  = instantaneous stress intensity factor range, and

$C$  = load-shedding exponent =  $(dK/da)/K = -0.08 \text{ mm}^{-1}$ .

This load-shedding procedure has been demonstrated in round-robin testing to produce reliable crack growth rate data in the near-threshold regime [251]. Load shedding was continued until a growth rate of  $10^{-10} \text{ m/cycle}$  was achieved. Thereafter, load shedding was terminated, and the fatigue crack was propagated to failure under constant load amplitude.

Throughout a given test, the microcomputer sampled the crack length frequently, and as many as 500 crack length values were obtained. Although this number of data values may appear to be unnecessarily large, the frequent measurement of crack length facilitated the instantaneous control of test variables. Moreover, the large number of crack length measurements provided a body of data that was analyzed statistically to enhance interpretation. A modified incremental polynomial method was developed (Appendix 1) to reduce the crack length measurements to the form of  $da/dN$  versus  $\Delta K$ . Essentially, the method enforces the objectives of ASTM standard guidelines [249], while

utilizing all available crack length data to improve the statistical confidence in the crack growth rate calculations. The crack growth data were reduced using the standard expression to calculate  $\Delta K$  [249]:

$$\Delta K = (\Delta P / (B W^{0.5})) ((2 + \alpha) / (1 - \alpha))^{1.5} F \quad (3.4)$$

where

$$F = 0.886 + 4.64 \alpha - 13.32 \alpha^2 + 14.72 \alpha^3 - 5.6 \alpha^4 \quad (3.5)$$

$$\alpha = a/W$$

$a$  = instantaneous crack length,

$W$  = specimen width.

$\Delta P = P_{\max} - P_{\min}$  = load range, and

$B$  = specimen thickness.

This expression is valid for  $0.2 \leq a/W \leq 1.0$ .

### 3.3.4 Small-Crack Fatigue Testing

The procedure for small-crack testing was specifically developed to allow small cracks to initiate naturally. The use of an artificial crack starter was strictly avoided, because as discussed previously, artificially initiated cracks may not be equivalent to cracks that form naturally. For example, a small crack that is created by machining away much of the length of a longer crack may possess a crack wake that differs significantly from a naturally initiated crack of the same length. Furthermore, the machining may produce undesirable surface residual stress effects that may significantly affect early crack growth. Therefore, the small-crack test specimen is typically prepared by the

following paragraphs were carefully tailored to facilitate natural initiation of small cracks on a stress-free specimen surface.

Testing to investigate the growth of small fatigue cracks was performed using the specimen shown in Fig. 3.4. The specimens were machined such that the axis of loading was transverse to the plate rolling direction, and the notch faces were perpendicular to the rolling direction. This orientation was chosen because the plane of crack propagation is equivalent to that of the C(T) specimens (i.e. parallel to the rolling direction). The simple geometry, which was developed and demonstrated in a supporting investigation by Larsen [252], employed a mild notch to initiate surface cracks naturally in a localized field. The elastic stress concentration factor ( $K_t$ ) due to the notches was originally estimated using tabulations from a handbook [253], and a subsequent 2-dimensional elastic finite element stress analysis confirmed that  $K_t = 1.037$  [254]. Thus, the through-thickness stress was essentially uniform, while the reduced gage section effectively localized crack initiation within a small region that could be conveniently examined optically. In order to eliminate surface residual stresses and roughness produced during machining, the gage sections of all specimens were carefully electropolished to remove at least 0.19 mm from the surface. The electropolishing procedure was the same as that described earlier for preparing high-cycle-fatigue specimens. The electropolishing also produced a highly reflective surface that enhanced the detection and resolution of small surface cracks while highlighting the material's microstructure.

Testing was performed on an MTS servo-hydraulic fatigue machine using self-aligning hydraulic friction grips to insure axial loading. The specimens were cycled at a maximum stress level of  $\sigma_{\max} = 0.6 \sigma_y$  and a frequency of 20 Hz under fully reversed loading ( $R = -1.0$ ) until a semielliptical surface crack was initiated naturally in the

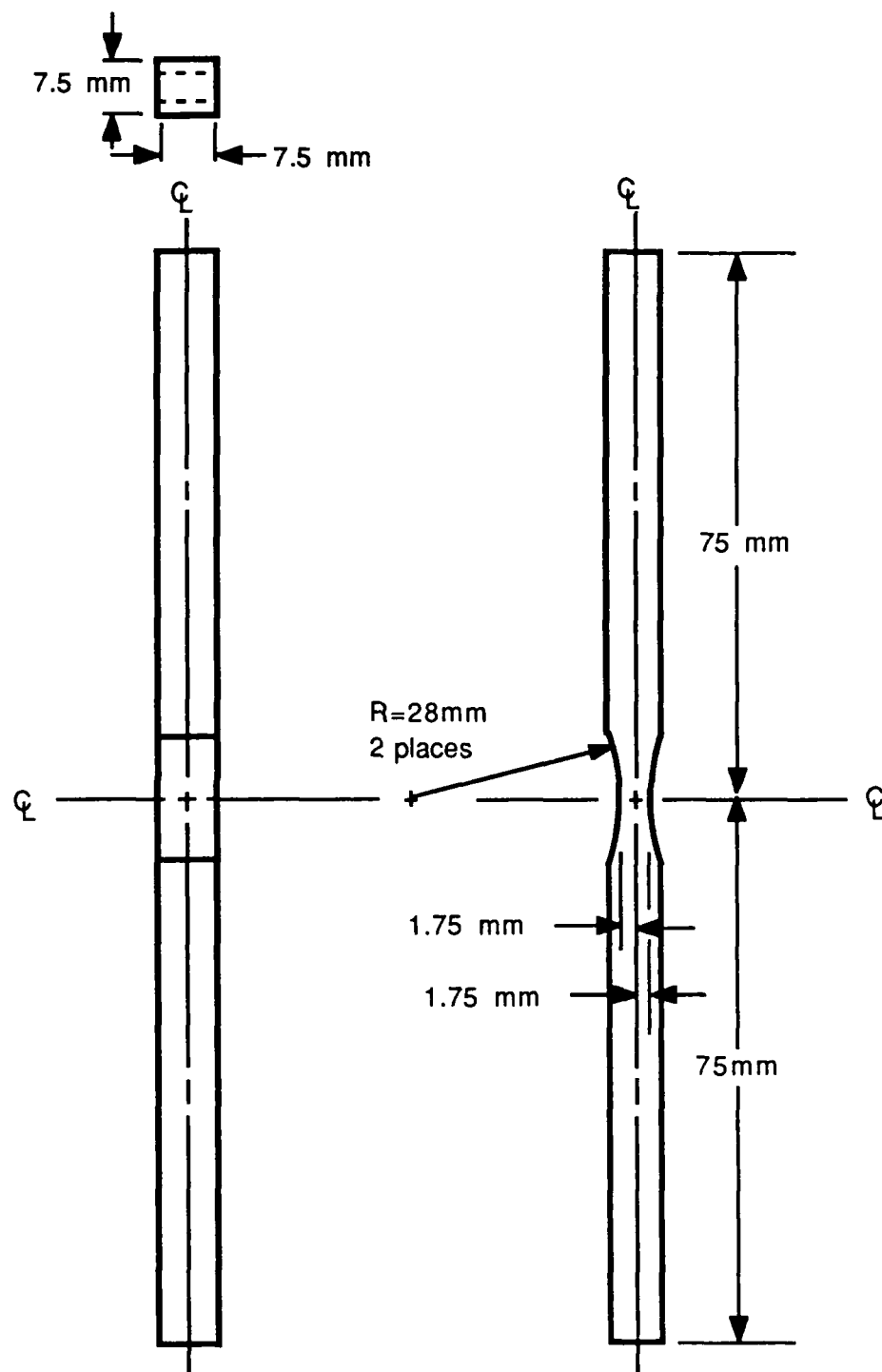


Fig. 3.4 The small-crack fatigue specimen.

reduced section of the specimen. Following visual detection of the precrack, the specimen was removed from the testing machine in order to place Vickers hardness indentations above and below the crack mouth for use in making crack-opening displacement measurements. Subsequently, the specimen was replaced in the testing machine, and crack length and crack closure measurements were obtained periodically as the crack was extended under constant load-amplitude fatigue at a selected stress level and stress ratio.

The propagation and closure behavior of the small cracks were monitored using two complementary techniques. Crack length data were acquired directly with a high-resolution computer-controlled photomicroscope [252], and a laser interferometric technique [255] was employed to determine crack length independently and to monitor the development of crack closure. Throughout a test, fatigue cycling was periodically interrupted briefly by the computer, and both techniques were used to acquire crack growth data. This procedure produced independent, and extremely comprehensive, records of crack growth behavior.

The photographic technique used a metallurgical microscope mounted with a motor-driven 35 mm camera having a 250-frame film magazine and powered by a standard motor drive. Using an electronic flash as the microscope's lighting source, high-resolution photographs were taken periodically while the crack was held briefly under a tensile load equal to 75% of the maximum fatigue load. To provide a view of the area immediately surrounding the crack, a low film-plane magnification of approximately 20X to 40X was used. The small-crack photographs were recorded on Kodak Panatomic-X film, with virtually no loss of resolution of the magnified image [256]. Since the resolution was more than adequate, this film was preferred over other less common technical films, because it did not require specialized batch processing and could be developed on commercial machinery. The camera and hydraulic fatigue testing machine

were controlled by a Digital Equipment Corporation 1124 minicomputer to automate testing and facilitate recording of various test parameters. Typically, 100 to 300 photographs were taken during a given test, allowing incremental crack advance to be monitored.

At the conclusion of a test, the film was developed, and a standard photographic enlarger was used to project the images of the small crack on a Tektronix 4956 digitizing tablet for convenient determination of crack tip positions. An enlarger magnification of approximately 15X was commonly used, which when combined with the original magnification, produced a projected image magnification in the approximate range of 300X to 600X. The exact image magnification was determined from a photograph of a precision micrometer slide, which was taken for each test. For the material and test conditions used, surface cracks of length ( $2c$ ) as small as  $40\text{ }\mu\text{m}$  were recorded, and the precision of the photographic crack length measurements was approximately  $1\text{ }\mu\text{m}$ , as estimated by the standard deviation of repeated measurements of the length of a non-propagating crack.

During each test the microcomputer recorded pertinent data including the photograph frame numbers and the corresponding values of fatigue cycle count. The cycle-count data were merged with the digitized crack lengths (calculated as the length projected onto a plane normal to the axis of loading) to produce a computer file of surface crack length ( $2c$ ) versus cycles ( $N$ ). The shapes of the surface cracks were determined by a heat tinting procedure wherein the test was temporarily interrupted, and the specimen was removed and heated for one hour in air at a temperature of approximately  $315^{\circ}\text{C}$ . This thermal exposure was sufficient to visibly oxidize the fracture surface of the existing fatigue crack and did not affect the microstructure of the Ti-4Al or the Ti-8Al(a). Specimens of these materials were returned to the machine for continued fatigue testing. Since the thermal cycle was expected to cause  $\alpha_2$  precipitation in the

Ti-8Al(s), specimens of this alloy condition were fractured under a single loading cycle following heat tinting. Subsequently, the heat-tinted crack shape (as projected onto a plane normal to the axis of loading) was measured with a light microscope. This procedure was repeated for a number of specimens to obtain an approximate relationship of crack shape as a function of crack size. This description of crack shape was used in combination with the measurements of crack length, and the crack growth data were reduced to the form of  $dc/dN$  versus  $\Delta K$  using the modified incremental polynomial method (Appendix 1) and the surface-crack stress intensity solution of Newman and Raju [127,128]. For completeness, this solution is presented in the following paragraph.

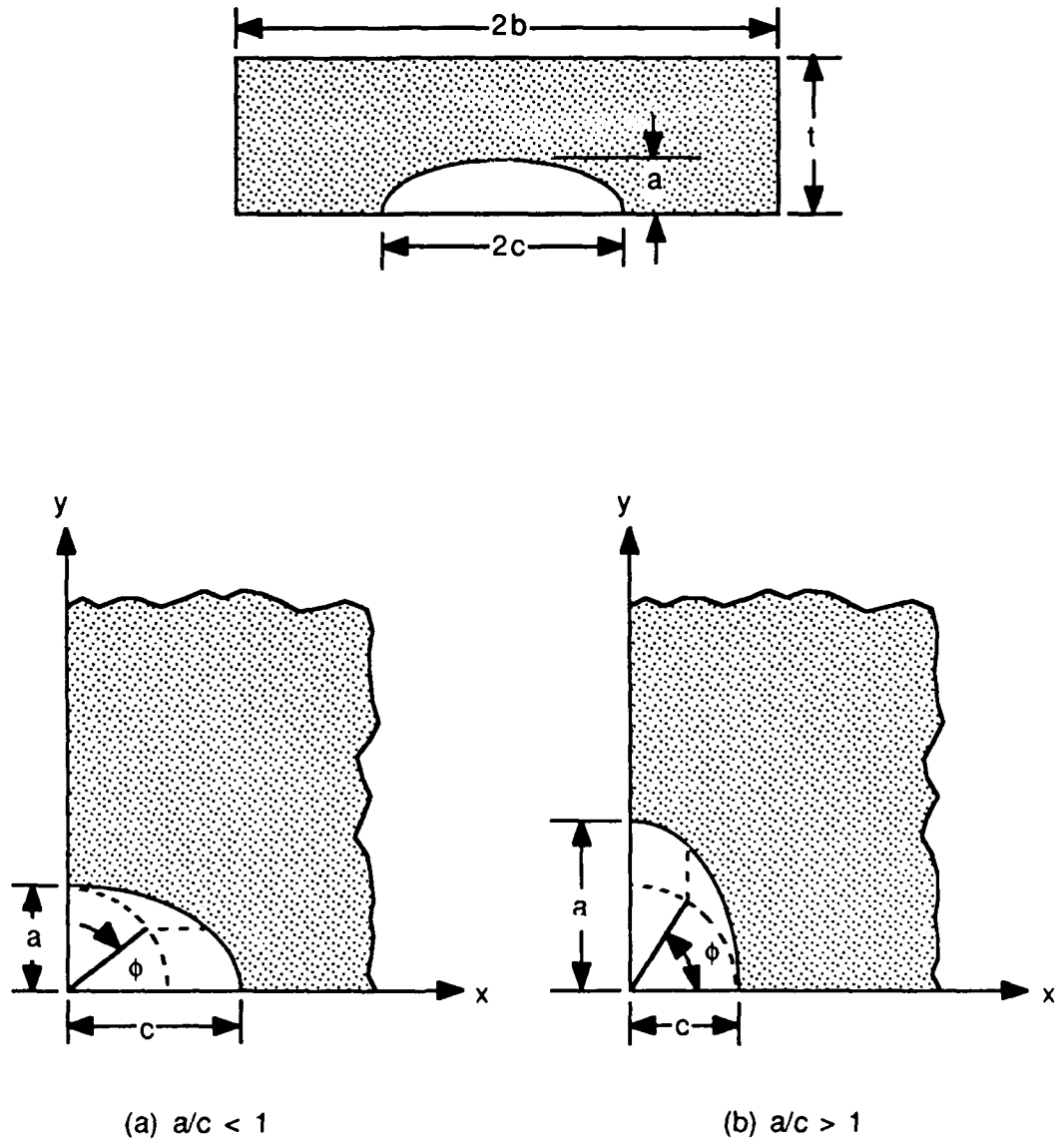
The surface-crack geometry is schematically represented in Fig. 3.5. The stress intensity factor solution was developed by Newman and Raju based on their three-dimensional finite element analysis of a finite body under elastic loading. The general expression for the Mode I stress intensity factor,  $K_I$ , for the semielliptical surface crack is of the form

$$K_I = \sigma(\pi a/Q)^{0.5} F_S(a/c, a/t, c/b, \phi) \quad (3.6)$$

for  $0 \leq a/c \leq 2$ ,  $c/b < 0.5$ ,  $0 \leq \phi \leq \pi$ , provided that  $a/t$  satisfies

$$a/t < 1.25(a/c + 0.6) \text{ for } 0 \leq a/c \leq 0.2, \text{ or } a/t \leq 1 \text{ for } 0.2 \leq a/c \leq \infty.$$





Coordinate system used to define parametric angle.

Fig. 3.5 The surface-crack geometry illustrating various dimensions and parameters.

The terms in Eq. 3.6 are defined as follows:

$\sigma$  = remotely applied stress,

$a$  = crack depth,

$c$  = half crack length,

$t$  = plate thickness,

$b$  = half plate width,

$\phi$  = parametric angle defined in Fig. 3.5,

$$Q = 1 + 1.464(a/c)^{1.65} \text{ for } a/c \leq 1, \quad (3.7)$$

$$Q = 1 + 1.464(c/a)^{1.65} \text{ for } a/c > 1, \text{ and} \quad (3.8)$$

$$F_S = [M_1 + M_2(a/t)^2 + M_3(a/t)^4] g f_\phi f_w. \quad (3.9)$$

For  $a/c \leq 1$

$$M_1 = 1.13 - 0.09(a/c), \quad (3.10)$$

$$M_2 = -0.54 + 0.89/(0.2 + (a/c)), \quad (3.11)$$

$$M_3 = 0.5 - 1/(0.65 + (a/c)) + 14(1 - (a/c))^{24}, \quad (3.12)$$

$$g = 1 + [0.1 + 0.35(a/t)^2] (1 - \sin(\phi))^2, \text{ and} \quad (3.13)$$

$$f_\phi = [(a/c)^2 \cos^2(\phi) + \sin^2(\phi)]^{0.25}. \quad (3.14)$$

For  $a/c > 1$

$$M_1 = (c/a)^{0.5} (1 + 0.04(c/a)), \quad (3.15)$$

$$M_2 = 0.2(c/a)^4, \quad (3.16)$$

$$M_3 = -0.11/(c/a)^4, \quad (3.17)$$

$$g = 1 + [0.1 + 0.35(c/a)(a/t)^2] (1 - \sin(\phi))^2, \text{ and} \quad (3.18)$$

$$f_\phi = [(c/a)^2 \sin^2(\phi) + \cos^2(\phi)]^{0.25}. \quad (3.19)$$

Finally, the finite-width correction factor,  $f_w$ , is given by:

$$f_w = [\sec((a/t)^{0.5} (\pi c)/(2b))]^{0.5}. \quad (3.20)$$

The determination of mouth-opening compliance and closure of small fatigue cracks was accomplished using a laser interferometric displacement gage (IDG) concept originally developed by Sharpe [e.g., 257-260] and implemented in the AFWAL Materials Laboratory primarily by J. R. Jira and T. Weerasooriya. In a supporting investigation, the method was applied and fully demonstrated by Larsen, Jira, and Weerasooriya [255] in a study of small fatigue cracks in the alloy Ti-6Al-2Sn-4Zr-6Mo. Additionally, application of the laser method in research under the present project has previously been reported by Larsen, et al [225,226,261].

In concept, the method utilizes the coherent light of a He-Ne laser to make very precise measurements of mouth-opening displacement across a small surface crack. Figure 3.6 illustrates the basic principle schematically. A beam of laser light illuminates a pair of Vickers hardness indentations placed approximately 80  $\mu\text{m}$  apart, spanning the crack mouth. Each indentation has the shape of a regular four-sided pyramid, and the four pairs of parallel faces of the indentations reflect the laser light to four positions in space. Of the four reflections, the two shown in the figure are used for crack-mouth-opening displacement measurement. Due to the coherent nature of the light, each pair of reflections interferes optically to produce observable fringe patterns as illustrated. The relationship between the fringe pattern and the gage length,  $d$ , separating the indentations is given by the equation

$$n\lambda = d \sin(\alpha_0) \quad (3.21)$$

where  $n$  is the order of the interference fringe,  $\lambda$  is the wavelength of the laser light

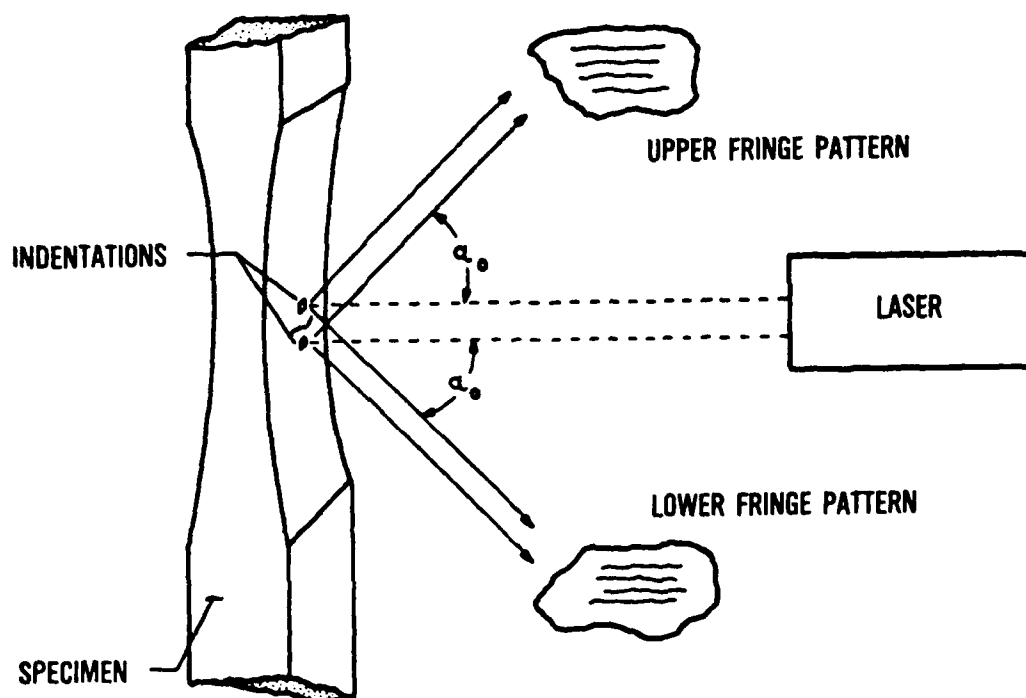


Fig. 3.6 Schematic illustrating the principle of operation of the interferometric displacement gage (IDG).

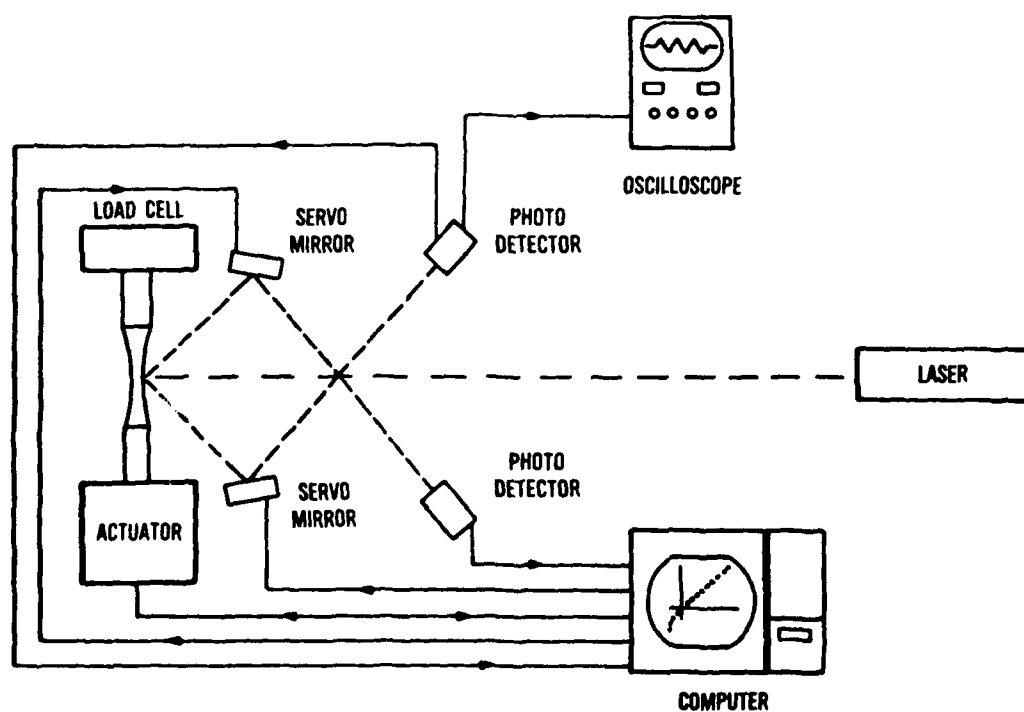


Fig. 3.7 Schematic illustration of the computerized interferometric system.

( $0.6328 \mu\text{m}$ ), and  $\alpha_0$  ( $\sim 44^\circ$ ) is the reflection angle shown in the figure. Solving for  $d$  and differentiating gives

$$\delta d = \delta n \lambda / \sin(\alpha_0) \approx 0.9 \mu\text{m} \quad (3.22)$$

for this geometry and  $\delta n = 1$ . Thus, movement of a single fringe past a fixed point in space corresponds to displacements between the indentations of approximately  $0.9 \mu\text{m}$ .

Greater displacement resolution was attained using the computer-controlled system shown schematically in Fig. 3.7 to monitor fractional fringe position. Basically, the system uses a pair of servo-controlled rotating mirrors to sweep the reflection of each fringe pattern across a photo detector covered by a narrow slit. Since the slit transmits a narrow band of light, the intensity level registered by the photo detector varies periodically as the alternating light and dark interference fringes are swept across the slit. By coordinating the intensity level with angular position of the rotating mirror, it is possible to determine the position of the fringe pattern at a given time and associated applied load. Using this approach, the laser interferometric system can locate the interference fringe position to within approximately 0.01 of the fringe wavelength, and this corresponds to a measurement precision for displacement between the indentations of  $\delta d \approx 0.009 \mu\text{m}$  ( $90 \text{ \AA}$ ). By repeating the described data acquisition procedure throughout a full cycle of loading, a high-precision record of crack-mouth-opening displacement versus applied load is produced.

A photograph of the laser system is presented in Fig. 3.8. The microscope used in the photomicroscopic system is also shown. As pictured, the physical position of the interferometric system required that the microscope be located to the side of the test setup, and a small mirror mounted on the objective lens was used to reflect the

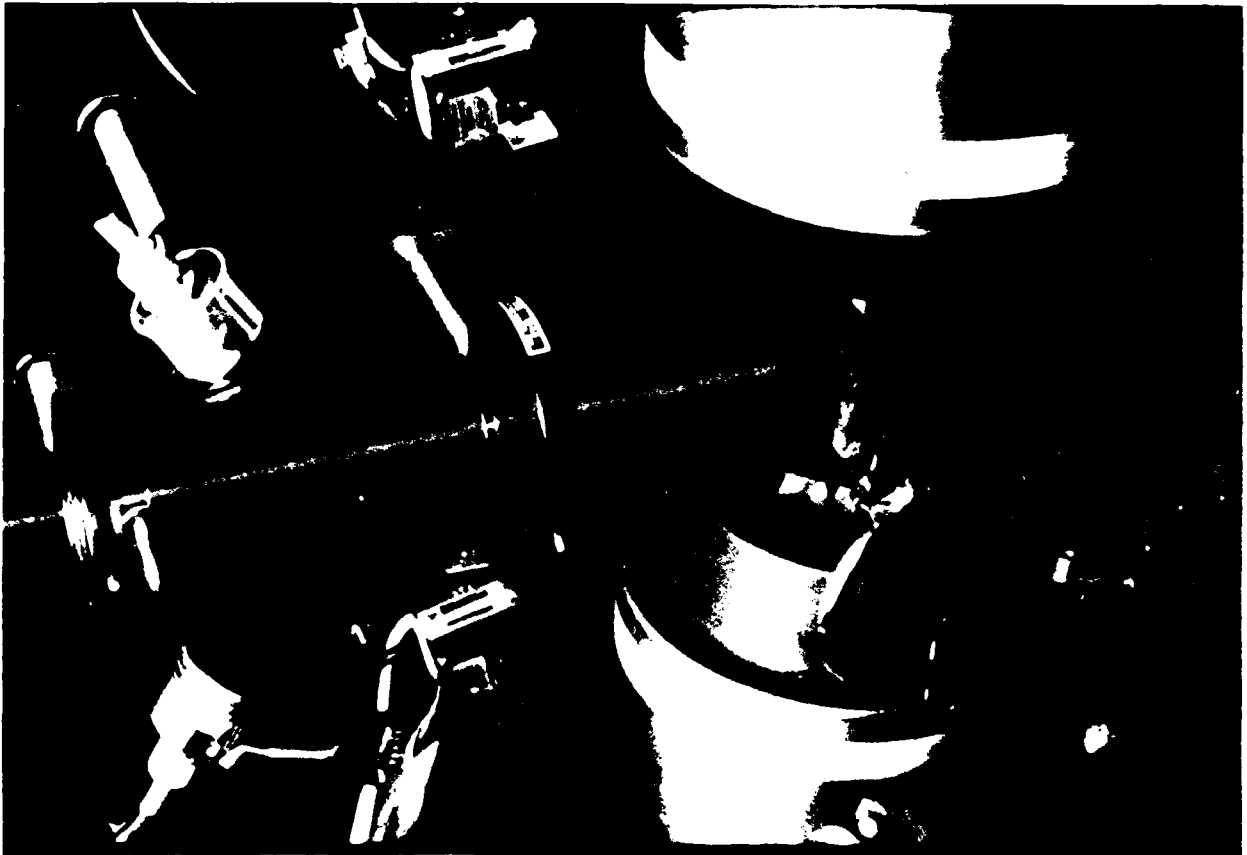


Fig. 3.8 Photograph of the small crack test apparatus showing both the laser interferometric displacement system and the microscope used by the photographic system.

small-crack image into the microscope.

A typical load-displacement trace obtained with the interferometric system is presented in Fig. 3.9 for a small crack in the Ti-8Al(s) alloy fatigued at a frequency of 20 Hz under  $R = -1.0$  loading with  $\sigma_{\max} = 0.6 \sigma_y$ . The approximately 300 data points shown were acquired during a 40-second fatigue cycle. For this case, the total crack-mouth-opening displacement measured at maximum load was approximately 3  $\mu\text{m}$ . The effective size of the small crack was calculated iteratively from the elastic compliance determined from the slope of the linear region of the unloading load-displacement data using the following analytical expression based on the work of Mattheck, et al [262]:

$$\begin{aligned} 2u/\sigma = (2a/E) \{ & 2.954 - 1.960 (a/c) + 0.452 (a/c)^2 \\ & + (a/t)^2 [0.92/(a/c)^{1.2} - 0.405/(a/c)^{0.2}] \\ & + (a/t)^4 [0.091/(a/c)^{2.4}] \} \end{aligned} \quad (3.23)$$

where

$2u$  = total crack-mouth-opening displacement,

$\sigma$  = applied stress,

$E$  = Young's modulus,

$a$  = crack depth,

$c$  = half crack length, and

$t$  = plate thickness.

The accuracy and utility of this expression for small fatigue cracks was previously demonstrated by Larsen, Jira, and Weerasooriya [255], who found excellent correspondence between crack lengths calculated from compliance measurements and

optically-measured crack lengths.

### 3.3.5 Determination of Crack Closure

There are numerous approaches for determining the magnitude of crack closure from load-displacement data [139,178]. Currently the American Society for Testing and Materials is conducting a round-robin evaluation of experimental and analytical methods for assessing crack closure [179]. At present there is no consensus regarding a procedure for determination of the point of closure; however, extensive experience by the author and his colleagues on a number of materials and specimen geometries indicates that the following method provides reliable results.

For the small-crack data, the crack closure load ( $P_{cl}$ ) was determined from the break in the load-displacement curve illustrated in Fig 3.9. The differential load-displacement data that are also shown were obtained by fitting a line to the upper, linear portion of the load-displacement data and subtracting the resulting linear-elastic component of crack opening from the actual measured displacement. This was accomplished using an expression of the form:

$$\delta\text{CMOD} = \text{CMOD} - (\beta_0 + \beta_1(P)) \quad (3.24)$$

where

$\delta\text{CMOD}$  = differential crack-mouth-opening displacement,

$\text{CMOD}$  = crack-mouth-opening displacement,

$P$  = applied load, and

$\beta_0$  and  $\beta_1$  = regression parameters of the linear load-displacement data acquired during the unloading portion of the cycle.



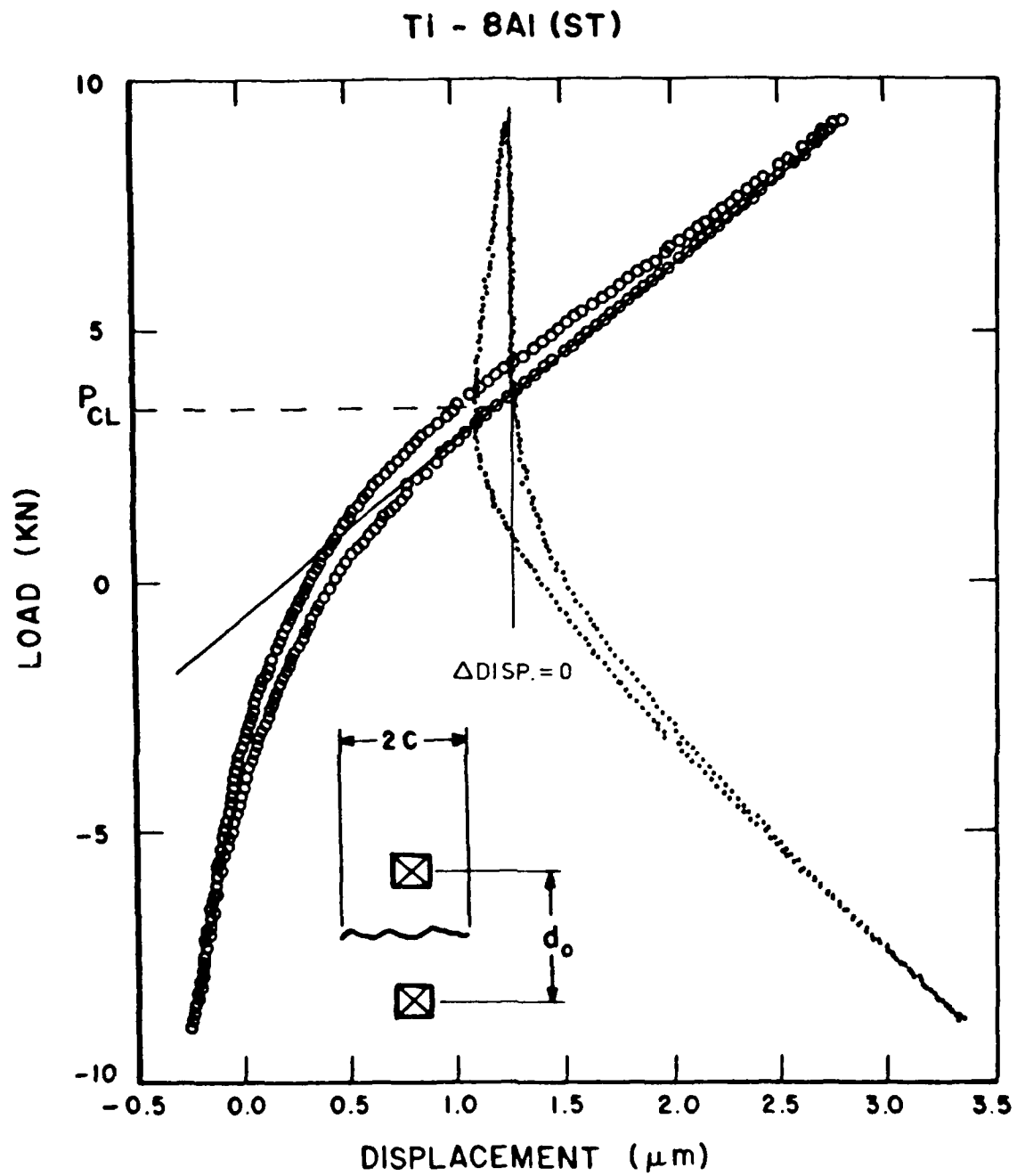


Fig. 3.9 Typical load versus crack-mouth-opening displacement data for a small surface crack. Differential load-displacement data are also shown.

Although the differential load-displacement data provided a convenient visual aid for estimating the point of closure, the actual determination of closure load ( $P_{Cl}$ ) in the small-crack tests was performed automatically using a simple computer algorithm, which is outlined as follows. The variability of the load-displacement data was quantified by a calculation of the standard error of the regression (SER) of the linear region of the unloading, load-displacement data:

$$SER = (\sum_i [CMOD_i - (\beta_0 + \beta_1(P_i))]^2 / (n - 2))^{0.5} \quad (3.25)$$

where

$i$  = data-point counter and

$n$  = total number of data points regressed.

The standard error of the regression is essentially the standard deviation of the differences between the individual raw data points and the regressed line. The algorithm to determine  $P_{Cl}$  located the crack closure load at the point where the difference between a 9-point sliding average of the measured displacement and the fitted straight line exceeded two times the standard error of the regression. Thus closure was indicated if

$$(\sum_{i=-4 \text{ to } 4} [CMOD_i - (\beta_0 + \beta_1(P_i))]) / 9 > 2(SER) \quad (3.26)$$

where

$CMOD_0$  = midpoint of the summation,

$i$  = data-point counter relative to local summation midpoint, and

the other variables are as defined earlier.

The value of 2 times SER was selected based on extensive studies on a number of materials. It was found that closure loads that were determined using this value were not significantly influenced by random variability in the load-displacement data. Furthermore, based on inspection of the plotted data, the use of 2 times SER in the algorithm produced a visually satisfying assessment of closure.

### **3.4 Fractography**

#### **3.4.1 Scanning Electron Microscopy**

Fractographic examination was performed using an ETEC Corporation Autoscan, scanning electron microscope. Fractographic specimens were prepared for examination by a four-step procedure in which failed samples were cleaned sequentially in ultrasonically-agitated solutions of acetone, methanol, ethanol, and freon. The intent of the SEM fractography was to characterize the fracture surfaces of the three materials and identify any crack-size dependent changes in the mechanism of crack propagation.

#### **3.4.2 Quantitative Fractography**

As a complement to the SEM characterization of the fracture surfaces, the crack profiles of the large- and small-crack specimens were documented by light microscopy, and quantitative analysis of fracture-surface topography was performed. The primary objective of this activity was to obtain direct measurements of fracture-surface attributes that could be related to the slip character of each of the Ti-Al alloys as well as to the measured levels of crack closure in both the large- and small-crack specimens.

Light micrographs were taken perpendicular to the free surface of the failed compact-type, C(T), specimens to document the crack profile in the large-crack specimens. In conformance with the SEM fractography, photographs were acquired from areas of the specimen corresponding to growth rates in the near-threshold ( $da/dN = 10^{-10}$  m/cycle ) and lower Paris-law ( $da/dN = 10^{-8}$  m/cycle) regions. The micrographs were taken at a magnification of 200X, and a computer digitizing tablet was used to generate the coordinates of a series of approximately equally spaced points (spacing  $\approx 7$   $\mu\text{m}$ ) along the fracture-surface profile. The resolution of the individual points was approximately 1  $\mu\text{m}$ . The crack-profile data were analyzed to obtain a number of descriptive topographical and statistical parameters that quantify the fracture surface roughness.

The 35 mm photographic record acquired during the small-crack tests was used in the quantitative fractographic analysis of the small cracks. The negative photographic images of the small cracks were projected directly onto a computer digitizing tablet to obtain a series of points describing the crack profile. The spacing and resolution of the data points were equivalent to those acquired from the C(T) specimens.

## CHAPTER 4

### RESULTS

#### 4.1 Microstructural Characterization

The titanium-aluminum alloys that were investigated were characterized microstructurally by light metallography and transmission electron microscopy, and crystallographic texture was quantified by construction of a series of X-ray diffraction pole figures. Each of these efforts is discussed below.

##### 4.1.1 Light Metallography

The microstructures of Ti-4Al and Ti-8Al(s) are pictured in Figs. 4.1 through 4.3. Although both materials generally had a fully recrystallized, equiaxed,  $\alpha$ -phase microstructure, some isolated unrecrystallized grains were observed in the Ti-4Al as shown in Fig. 4.2. These unrecrystallized grains were aligned parallel to the rolling direction of the original plate material and appeared only in the midthickness of the plate where rolling deformation is a minimum. Measurements of the equiaxed grain size revealed a slightly larger grain diameter in the Ti-8Al, as indicated in Table 4.1



Fig. 4.1 Equiaxed, recrystallized microstructure of Ti-4Al.

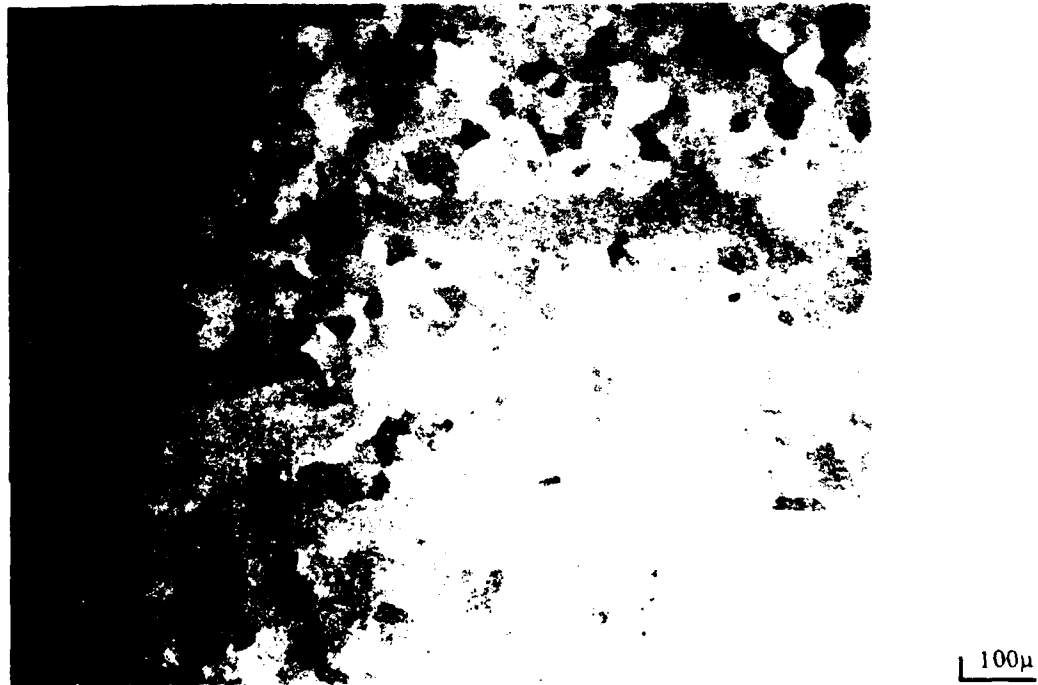


Fig. 4.2 Example of isolated unrecrystallized grains occasionally observed near the midthickness of the rolled Ti-4Al plate. The unrecrystallized grains are elongated along the rolling direction.



Fig. 4.3 Equiaxed, recrystallized microstructure of Ti-8Al.

Table 4.1: Ti-Al Alloy Grain-Size Measurements

	$\bar{l}^*$ ( $\mu\text{m}$ )	$\bar{d}^\dagger$ ( $\mu\text{m}$ )
Ti-4Al	60	101
Ti-8Al	82	138

\*  $\bar{l}$  = mean linear intercept distance between grain boundaries on an arbitrary metallographic section determined using the three-circle method [242].

†  $\bar{d}$  = mean corrected grain diameter [243].

#### 4.1.2 Transmission Electron Microscopy

The size and morphology of the  $\alpha_2$  precipitates in the Ti-8Al alloy were characterized by transmission electron microscopy. As expected, no precipitates were observed in the solution-treated and quenched material, while the aged Ti-8Al contained a uniform distribution of spherical precipitates. Micrographs showing the precipitates imaged under both bright- and dark-field conditions are presented in Fig. 4.4. The precipitates were of diameters ranging approximately from 5 to 10 nm.

#### 4.1.3 Characterization of Rolling Texture

The degree of crystallographic texture produced during hot rolling was documented by construction of X-ray diffraction pole figures of both the Ti-4Al and the Ti-8Al(s). Basal (0002), prism ( $10\bar{1}0$ ), and pyramidal ( $10\bar{1}1$ ) pole figures for both of the alloys are presented in Figs. 4.5-4.10. The Ti-4Al (0002) pole figure presented in Fig. 4.5 shows a moderately developed basal texture, wherein the polycrystalline structure was preferentially reoriented such that a predominance of grains had their basal planes aligned approximately parallel to the rolling plane. Within the rolling plane, however, there was a negligible secondary texture, as indicated by the approximately random intensity distribution shown in the prism and pyramidal pole figures (Figs. 4.6 and 4.7).



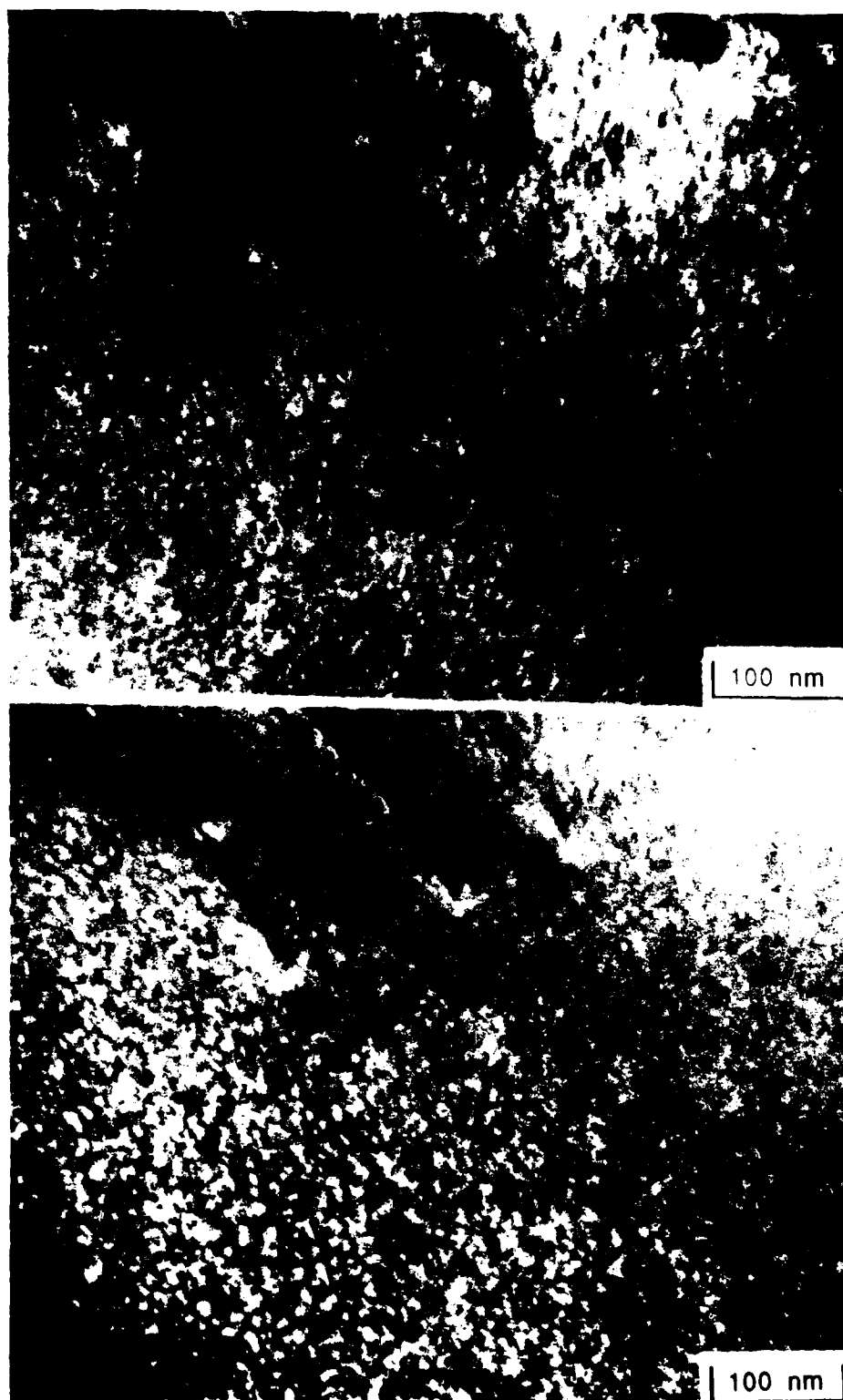


Fig. 4.4 Bright- and dark-field TEM micrographs of precipitate structure in the aged Ti-8Al alloy.

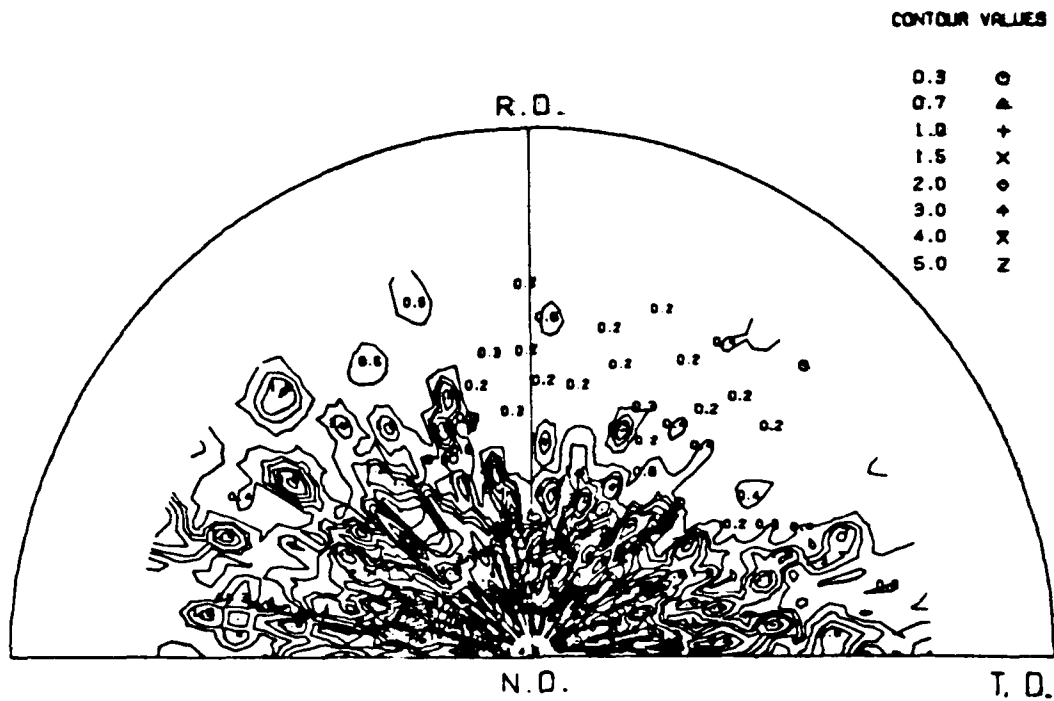
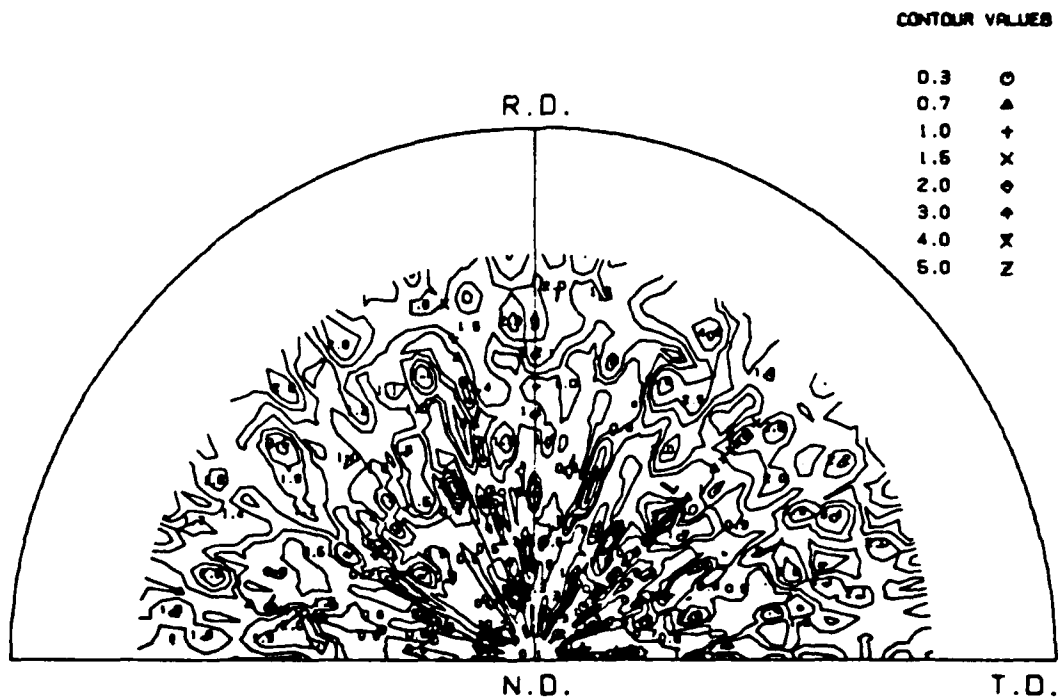


Fig. 4.5 Ti-4Al basal (0002) pole figure.

Fig. 4.6 Ti-4Al prism ( $10\bar{1}0$ ) pole figure.

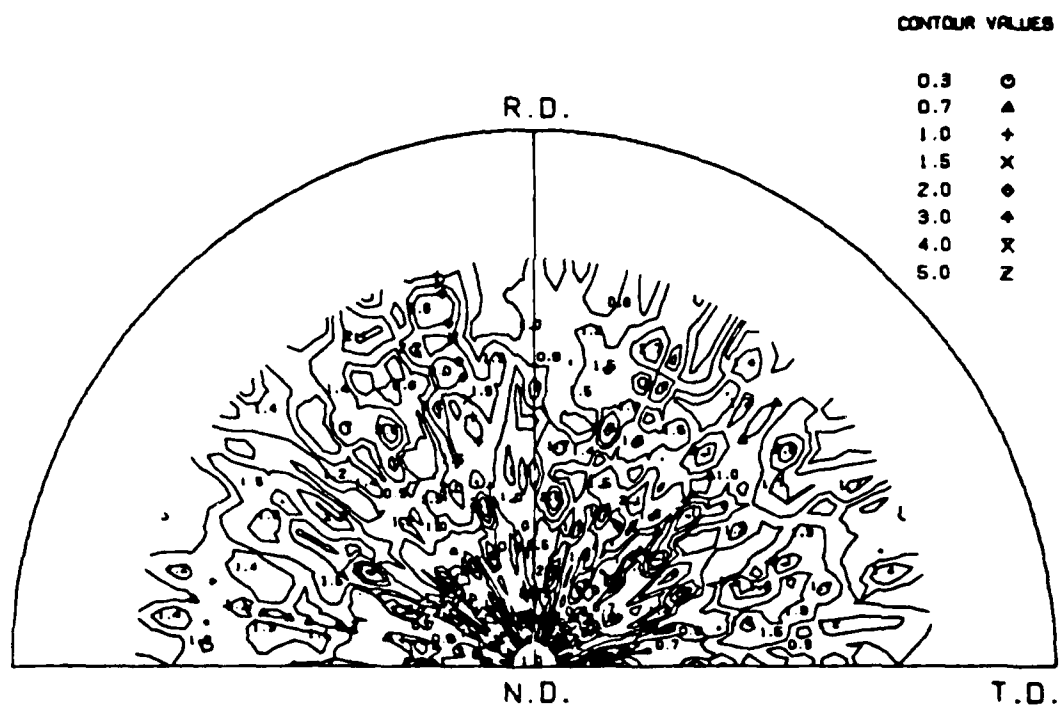
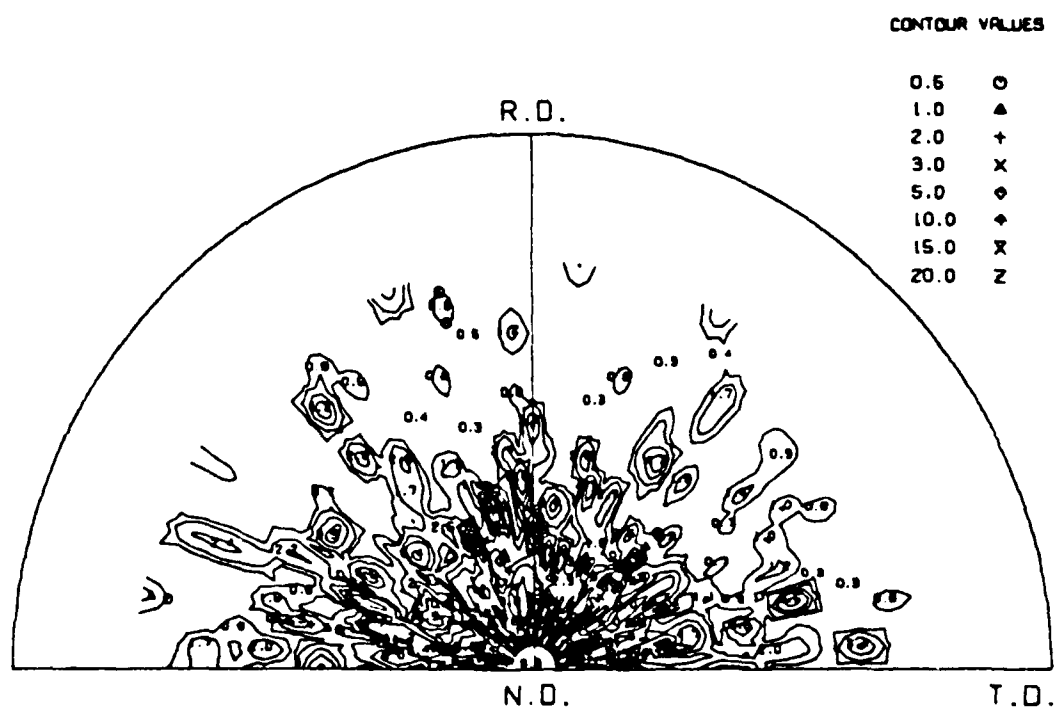
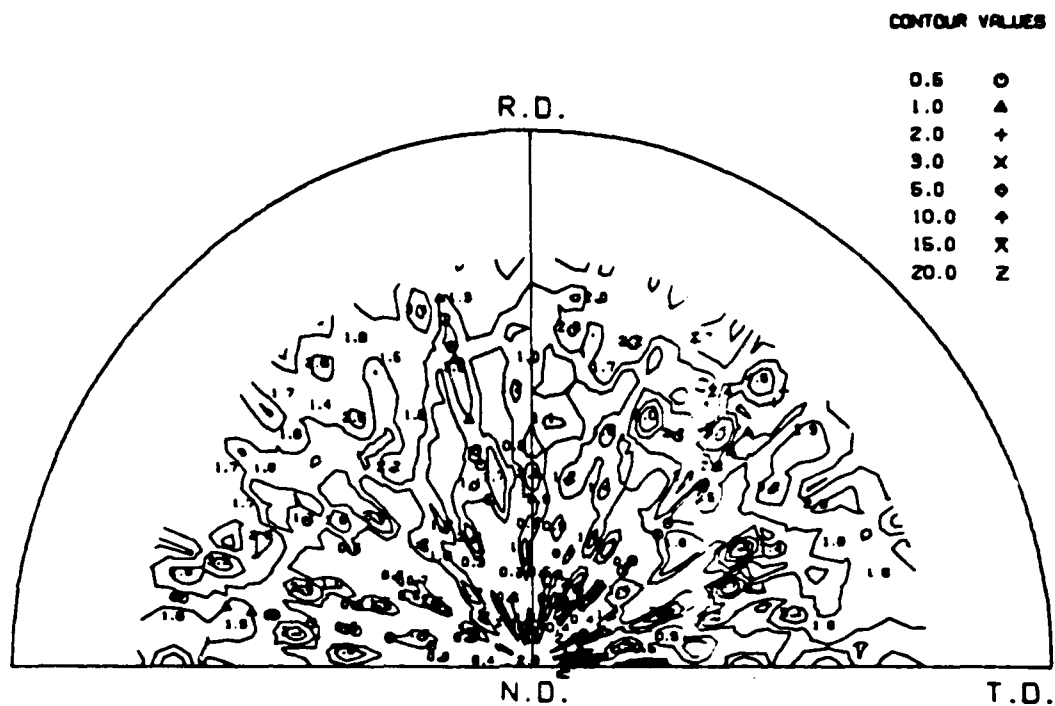
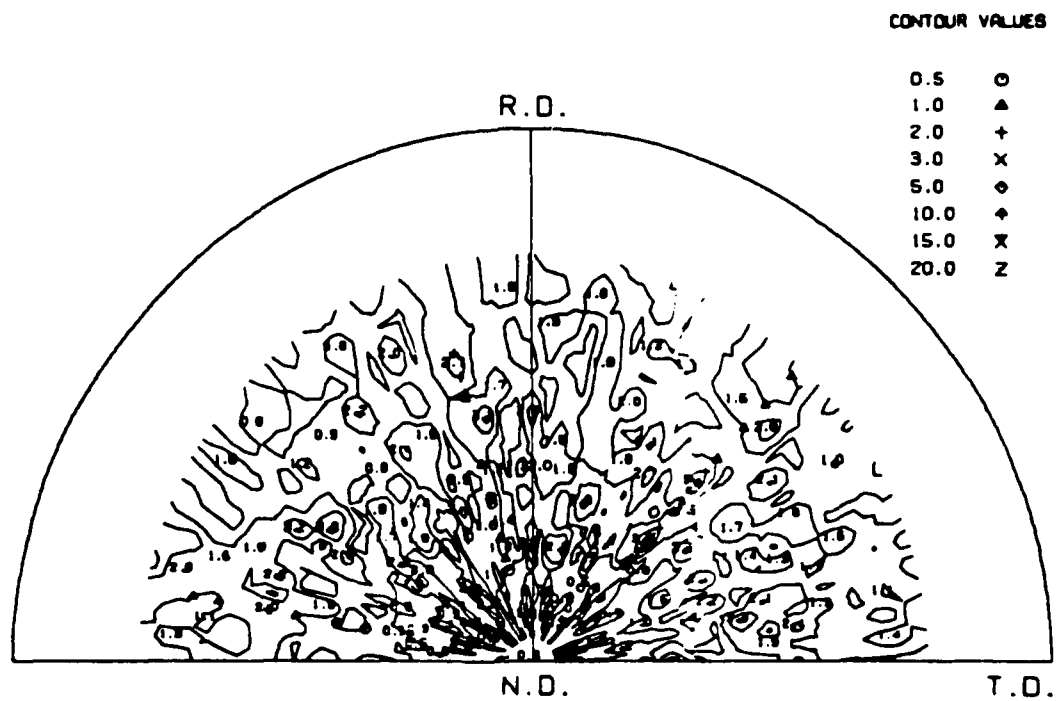
Fig. 4.7 Ti-4Al pyramidal ( $10\bar{1}1$ ) pole figure.

Fig. 4.8 Ti-8Al basal (0002) pole figure.

Fig. 4.9 Ti-8Al prism ( $10\bar{1}0$ ) pole figure.Fig. 4.10 Ti-8Al pyramidal ( $10\bar{1}1$ ) pole figure.

The Ti-8Al(s) pole figures, presented in Figs. 4.8-4.10, were qualitatively similar to those for the Ti-4Al, but the basal texture was more well defined. Thus, the material would be expected to exhibit in-plane isotropy, while mechanical properties in the short-transverse direction should differ from the equivalent in-plane measurements. As will be discussed later, this expectation was confirmed by results of mechanical property tests. Pole figures of the Ti-8Al(a) were not constructed since low-temperature aging of this material should have no effect on the existing texture of the  $\alpha$ -phase matrix.

## 4.2 Characterization of Mechanical Properties

### 4.2.1 Tensile Testing

Table 4.2 presents the results of standard tensile tests that were performed on each of the three alloy conditions. The effect of solid-solution strengthening is evident in yield-strength difference between Ti-4Al and Ti-8Al(s), and strengthening produced by  $\alpha_2$  precipitation in the aged Ti-8Al alloy is also clearly observed in the measurements of yield strength. The aging had a negligible influence on the ultimate tensile strength of the Ti-8Al. Variation in the level of solid-solution strengthening had little effect on tensile ductility and elongation, but the formation of precipitates in the Ti-8Al led to a significant reduction in the same measures of ductility. Moreover, as represented by the ratio of  $\sigma_U/\sigma_Y$ , the mild work hardening observed in the solution-treated materials was essentially nonexistent in the aged Ti-8Al. These findings were in good correspondence with similar measurements reported in the literature.

Table 4.2: Tensile Properties of Ti-Al Alloys

	$\sigma_y$ (MPa)	$\sigma_u$ (MPa)	$\sigma_u/\sigma_y$	E (GPa)	Elong. (%)	R. A. (%)	Tests
Ti-4Al	548 (11.7) <sup>†</sup>	625 (15.6)	1.14	105 (3.9)	16.8 (0.5)	26.4 (2.8)	2
Ti-8Al(s)	673 (2.5)	759 (4.5)	1.13	109 (3.9)	16.2 (1.0)	27.0 (4.3)	2
Ti-8Al(a)	753 (15.6)	769 (14.8)	1.02	100 (9.0)	7.3 (0.6)	14.0 (4.3)	3

$\sigma_y$  = 0.2% offset tensile yield strength.

$\sigma_u$  = ultimate tensile strength.

E = Young's modulus.

Elong. = % elongation in a standard 25.4 mm gage length.

R. A. = % reduction of specimen cross-sectional area.

(<sup>†</sup> = Standard deviation of measurements)

The tensile properties reported in the table represent averages of tests of tensile specimens oriented both parallel and perpendicular to the rolling direction of the plate. The data from the two orientations were combined, since within the limits of experimental error, there was no discernible orientation dependence. The absence of an orientation effect in the rolling plane of both the Ti-4Al and Ti-8Al plate was expected based on the symmetric, in-plane basal texture indicated by the pole figures of both materials.

A qualitative measure of plastic anisotropy due to the basal texture was provided indirectly by the results of the tensile tests. Since a basal texture tends to orient the (0002) planes normal to the rolling plane, slip along [0001] should be relatively restricted, resulting in limited deformation in the short-transverse direction. Alternatively, within the plane of a basal-textured plate, the abundance of both prism and basal planes that are favorably oriented for a slip should enhance deformation in the rolling plane. Based on this scenario, necking of the gage of a tensile specimen should produce an oval cross section at fracture, with deformation minimized in the

short-transverse direction and maximized along the in-plane direction. This trend was not observed in the Ti-4Al (i.e., the failed specimens had circular cross sections), suggesting that the magnitude of the texture in this material was mild. In the Ti-8Al(s), however, the oval distortion of the cross sections of the failed specimens was significant; the length of the major axis of the elliptical fracture surface was approximately 1.26 times the dimension of the minor axis. The severity of the basal texture in this material clearly produced anisotropic deformation. The aspect ratio of the oval fracture surface of the Ti-8Al(a) specimens was 1.07. Although apparently less severe than in the Ti-8Al(s), the magnitude of the oval distortion in the Ti-8Al(a) was probably governed by the limited tensile ductility in this material. While aging might be expected to alter the propensity for slip on basal versus prism planes slightly,  $c+a$  slip should remain much more difficult, and the basic influence of the basal texture on deformation should be essentially unchanged. Thus, overall, the findings of the tensile tests strongly support the character of texture documented by the pole figures.

#### 4.2.2 High-Cycle-Fatigue Testing

High-cycle-fatigue tests were performed to characterize the  $10^7$ -cycle fatigue strength of each of the Ti-Al alloy conditions. All tests were conducted under  $R = -1.0$  loading, and specimens were oriented such that the axis of loading was perpendicular (transverse) to the plate rolling direction. Figures 4.11-4.13 plot the results of the tests in terms of the maximum applied stress normalized by the respective material's yield strength (i.e.,  $\sigma_{\max}/\sigma_y$ ). The data points plotted at  $10^7$  cycles represent unfailed (run-out) specimens. In these terms, the normalized, long-life fatigue strength,  $\sigma_e/\sigma_y$ , is approximately independent of alloy condition. The specific fatigue strength of each material is listed in Table 4.3.

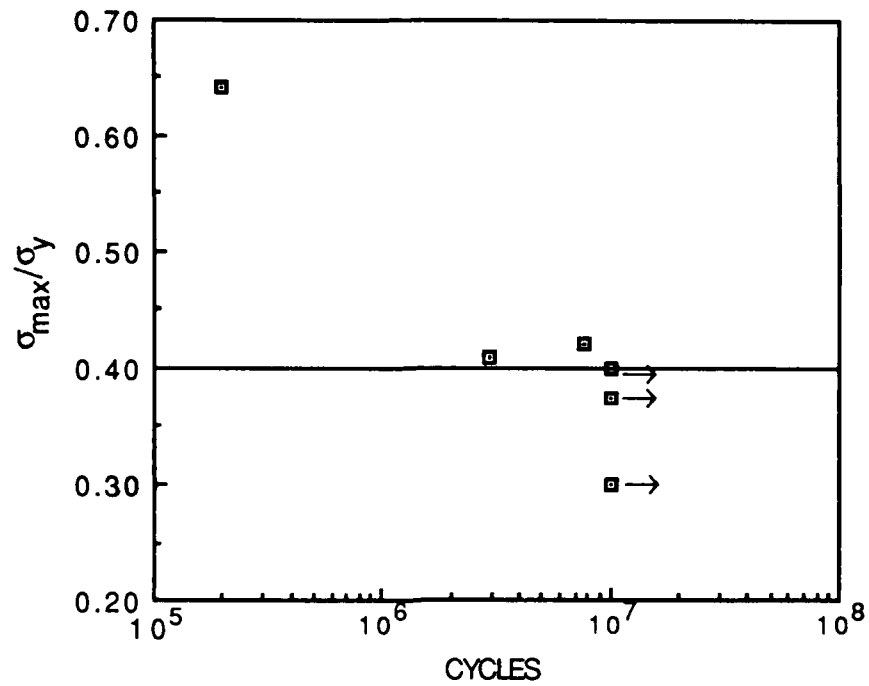


Fig. 4.11 Stress versus life (S-N) data for Ti-4Al tested under  $R = -1.0$  fatigue.

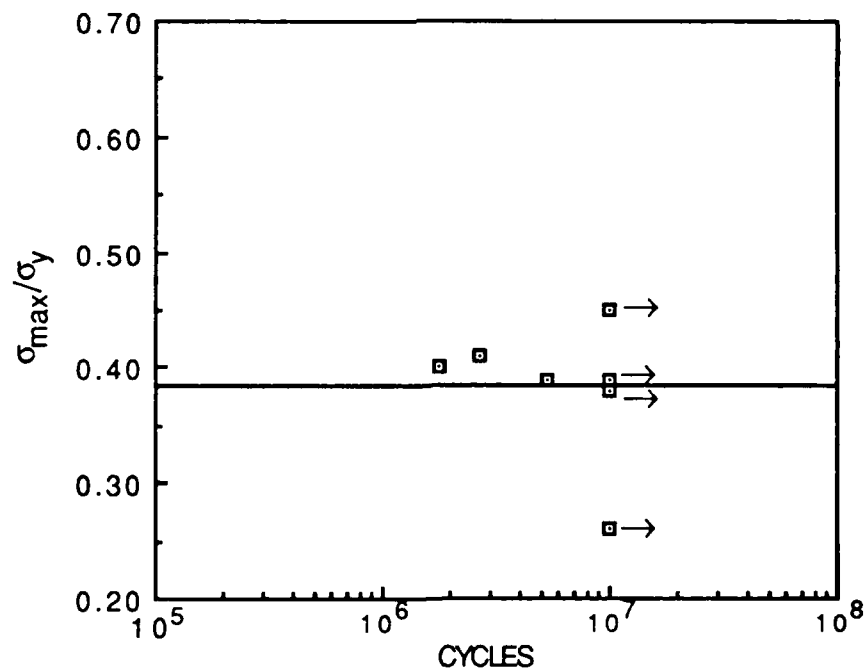


Fig. 4.12 Stress versus life (S-N) data for Ti-8Al(s) tested under  $R = -1.0$  fatigue.



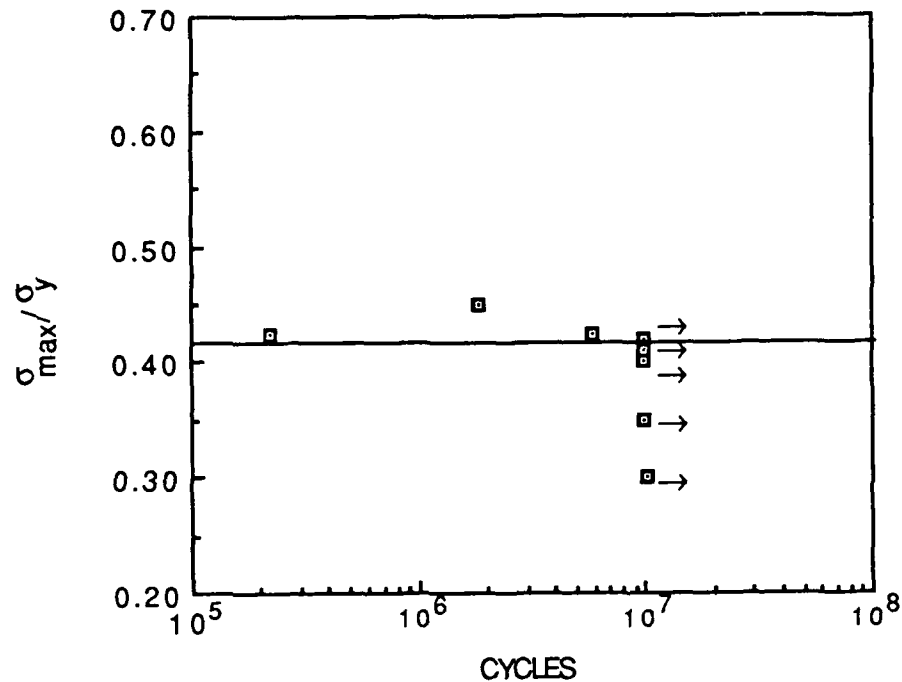


Fig. 4.13 Stress versus life (S-N) data for Ti-8Al(a) tested under  $R = -1.0$  fatigue.

Table 4.3: Fatigue Strength of Ti-Al Alloys

	$\sigma_e$ (MPa)	$\sigma_e/\sigma_y$	$\sigma_e/\sigma_u$
Ti-4Al	219	0.400	0.351
Ti-8Al(s)	260	0.386	0.342
Ti-8Al(a)	316	0.420	0.411

$\sigma_e = \sigma_{\max}$  required to cause failure in  $10^7$  cycles under  $R = -1.0$  fatigue.

#### 4.2.3 Large-Crack Fatigue Testing

A matrix of tests was performed using compact-type, C(T), specimens to establish the growth-rate behavior of large fatigue cracks in each of the materials under cycling at  $R = 0.1$  and  $0.5$ . Following precracking, load shedding was used to achieve a crack growth

threshold  $\Delta K$  (defined operationally at  $da/dN = 10^{-10}$  m/cycle), and the tests were subsequently completed under constant load-amplitude (constant  $\Delta P$ ) fatigue. In a few cases, the load shedding appeared to have produced a history effect, which influenced the level of crack closure (and the associated crack growth rate) during the decreasing- $\Delta K$  portion of the test. To eliminate the confounding effect of load history, with one exception, only the constant- $\Delta P$  (increasing- $\Delta K$ ) data will be used. The single exception to this practice is the data generated in Ti-8Al(s) under  $R = 0.5$  fatigue. Only the decreasing- $\Delta K$  data from this particular test are available due to difficulty with control of the testing machine. It should be noted, however, that a minimal crack-closure history effect is expected under  $R = 0.5$  loading.

The constant load-amplitude crack growth data for the three materials are presented in Fig. 4.14 for  $R = 0.1$ . As illustrated, the effect of alloy condition is substantial, particularly in the low growth-rate region. The most crack growth resistant material is the Ti-8Al(s), followed by the aged alloy, and finally by the Ti-4Al. Figure 4.15 presents the crack growth data for the three materials under  $R = 0.5$  fatigue, and the difference between the Ti-8Al(s) and the Ti-8Al(a) is much less than under  $R = 0.1$ . The Ti-4Al continues to exhibit appreciably higher crack growth rates than the other two alloy conditions at an equivalent  $\Delta K$ . To fully illustrate the effect of stress ratio, the  $R = 0.1$  and  $0.5$  long-crack data are presented again for the three separate materials in Figs. 4.16-4.18. The effect of  $R$  is clearly most pronounced in the Ti-8Al(s).

During each test, curves of crack-mouth-opening displacement versus applied load were periodically acquired to allow crack closure to be measured. Figure 4.19 presents the closure data for the  $R = 0.1$  tests plotted as  $K_{cl}/K_{max}$  (which is equal to  $P_{cl}/P_{max}$ ) versus  $K_{max}$ , and the three materials exhibit distinctly different behavior. For each data set, the minimum  $K_{max}$  value plotted corresponds to  $\Delta K_{th}$ . As expected,  $K_{cl}/K_{max}$

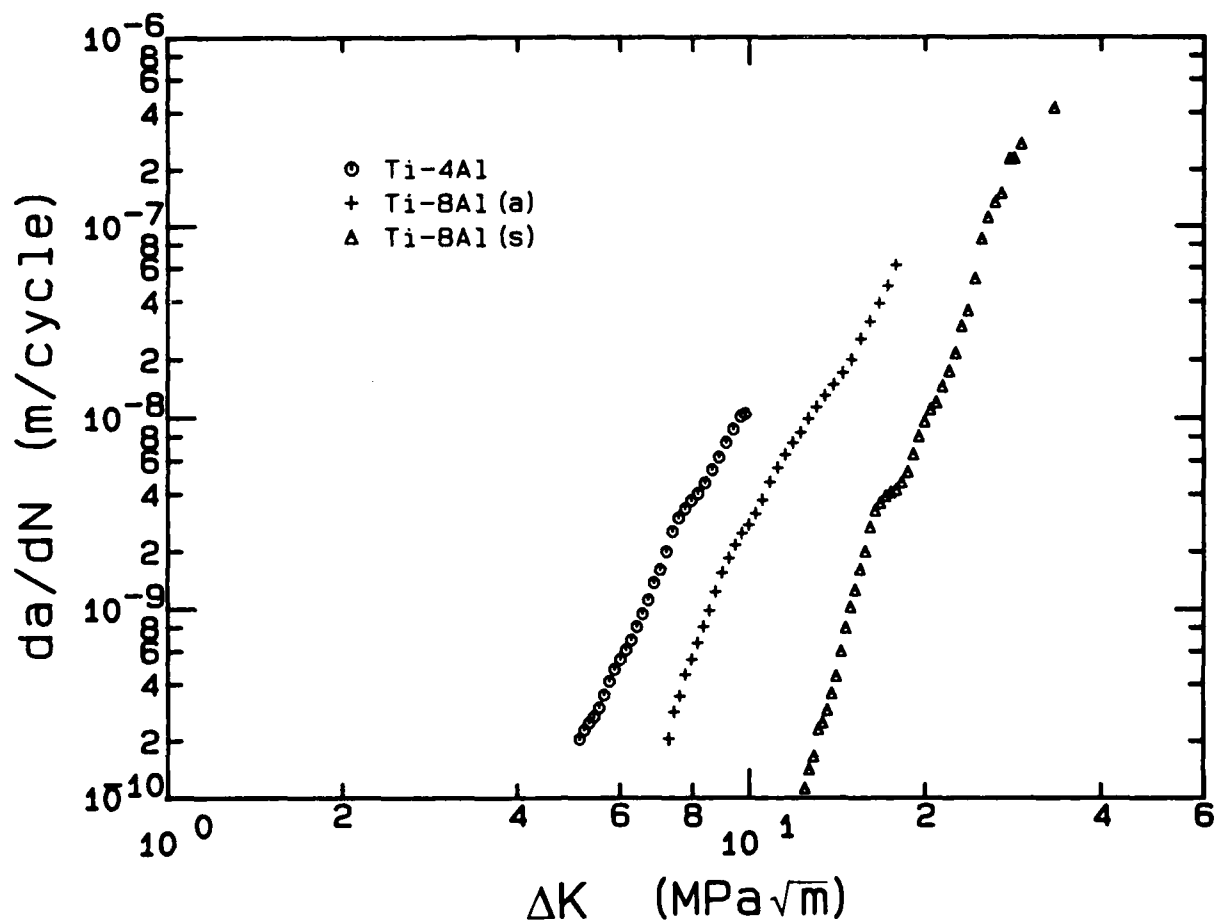


Fig. 4.14 Crack propagation data for large cracks in C(T) specimens tested under  $R = 0.1$ , constant load-amplitude fatigue.

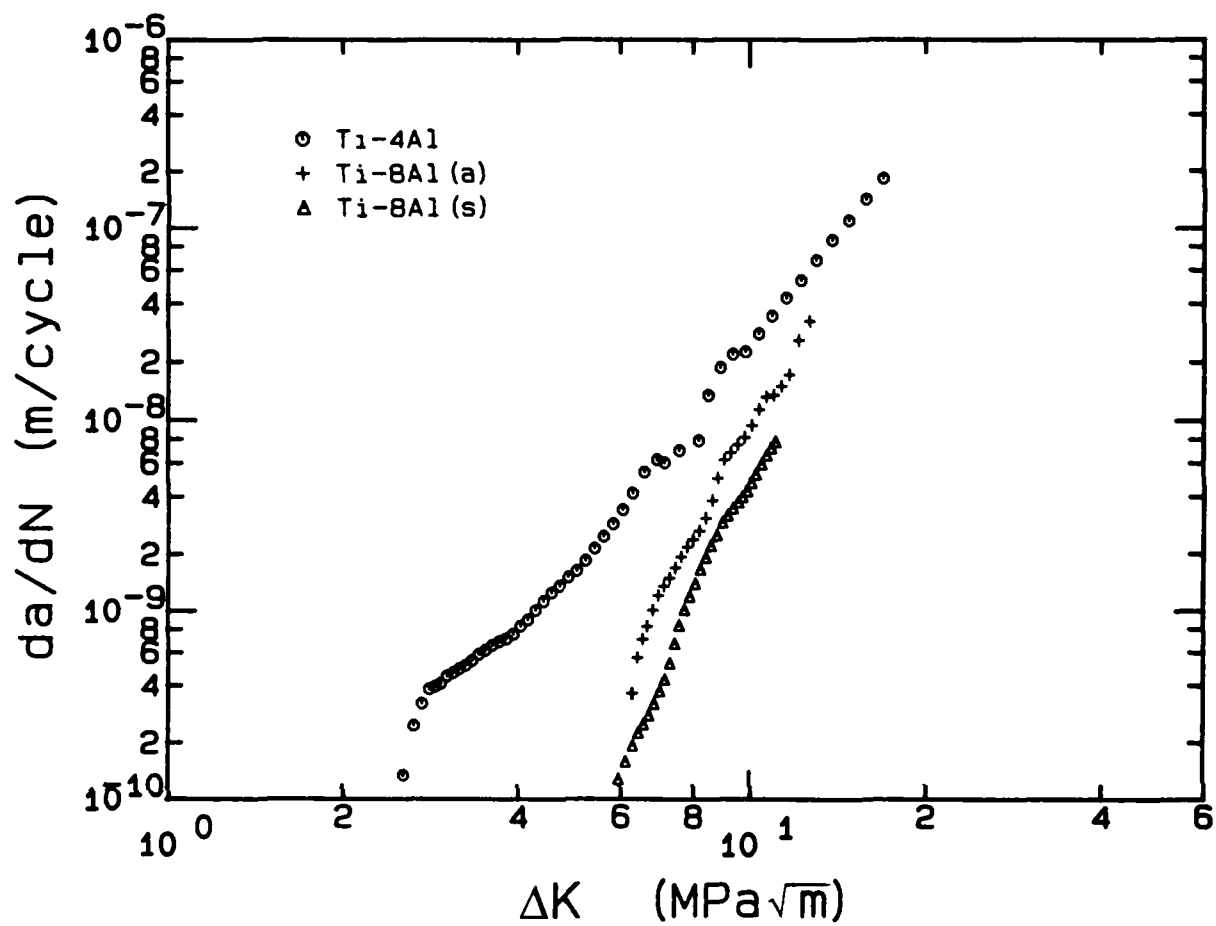


Fig. 4.15 Crack propagation data for large cracks in C(T) specimens tested under  $R = 0.5$ , constant load-amplitude fatigue.

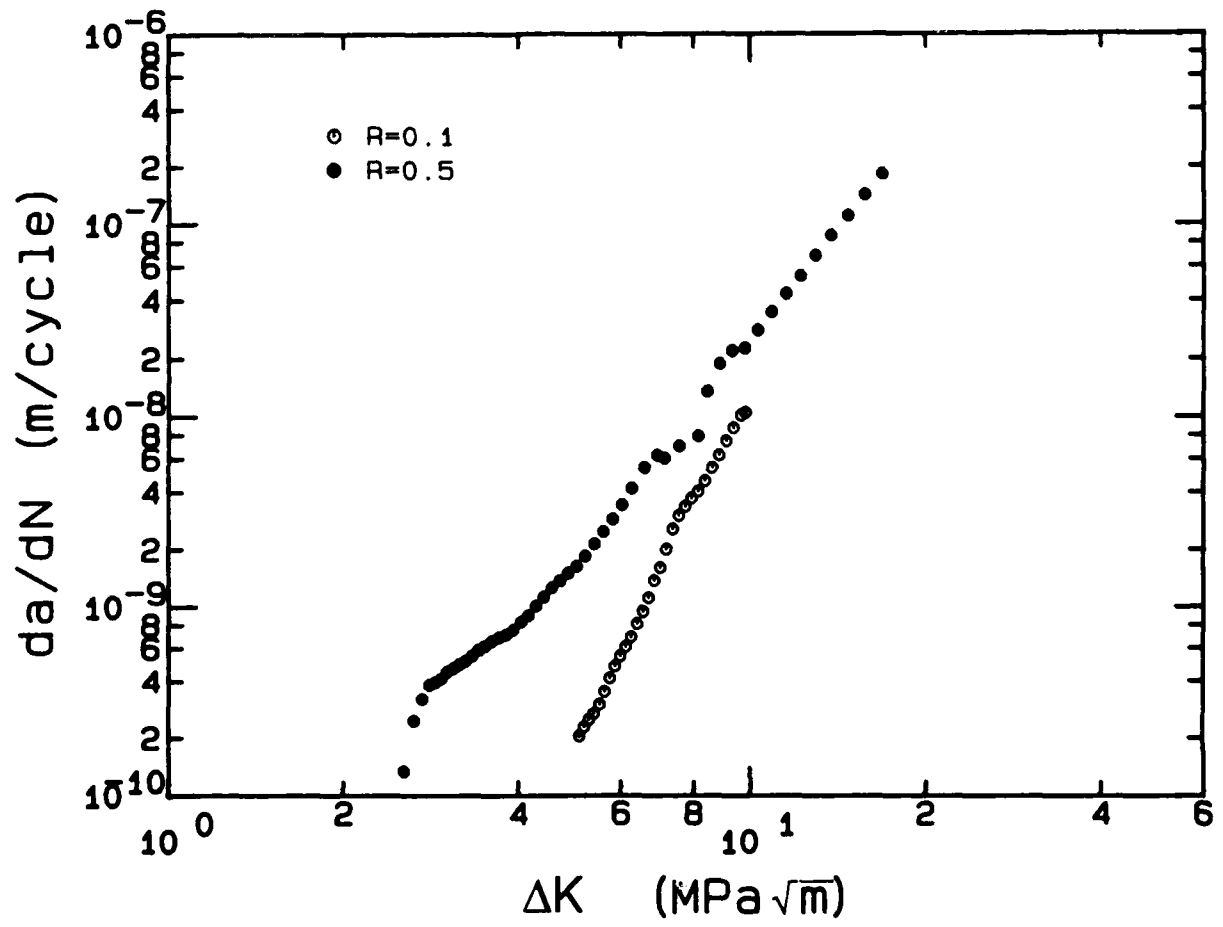


Fig. 4.16 Effect of stress ratio on the propagation of large cracks in Ti-4Al.

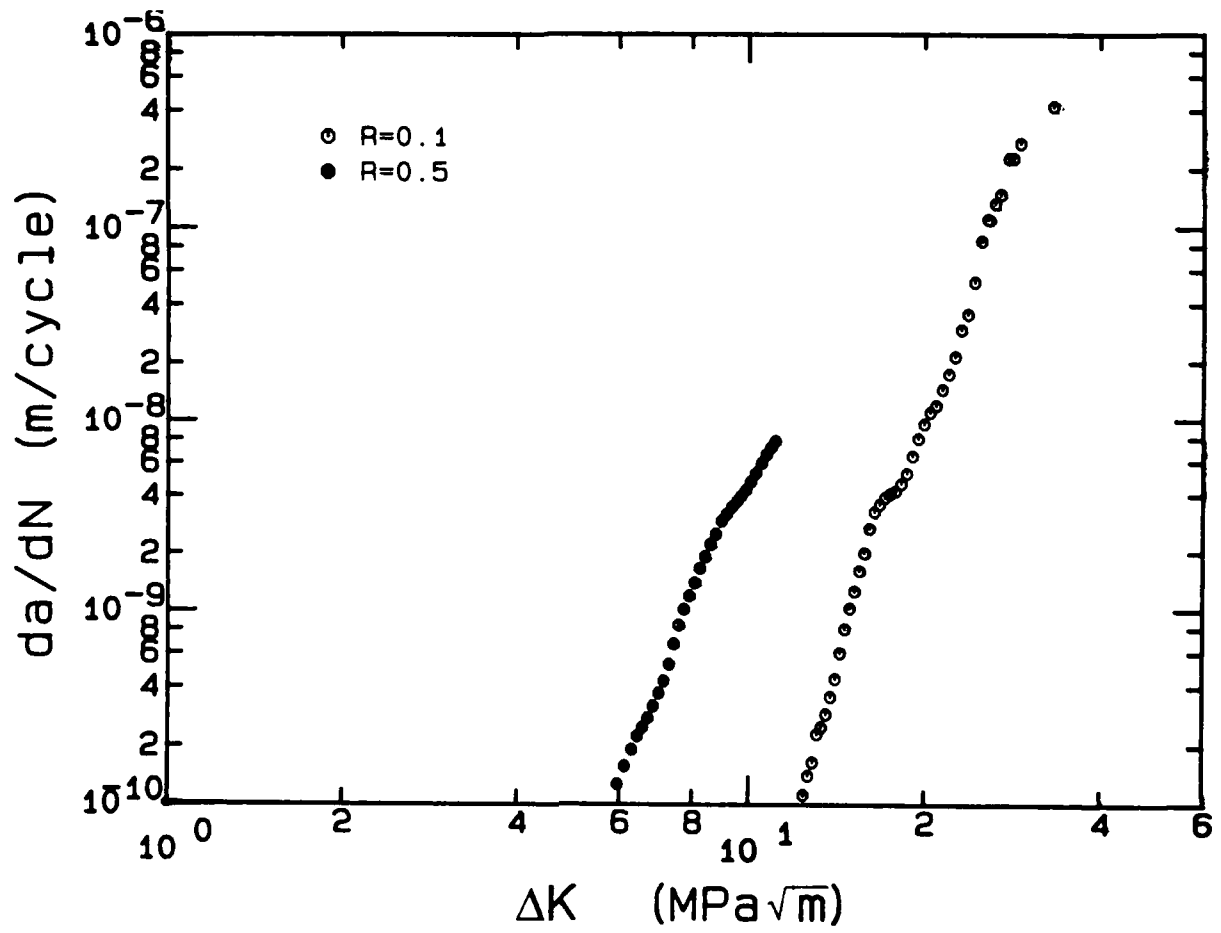


Fig. 4.17 Effect of stress ratio on the propagation of large cracks in Ti-8Al(s).

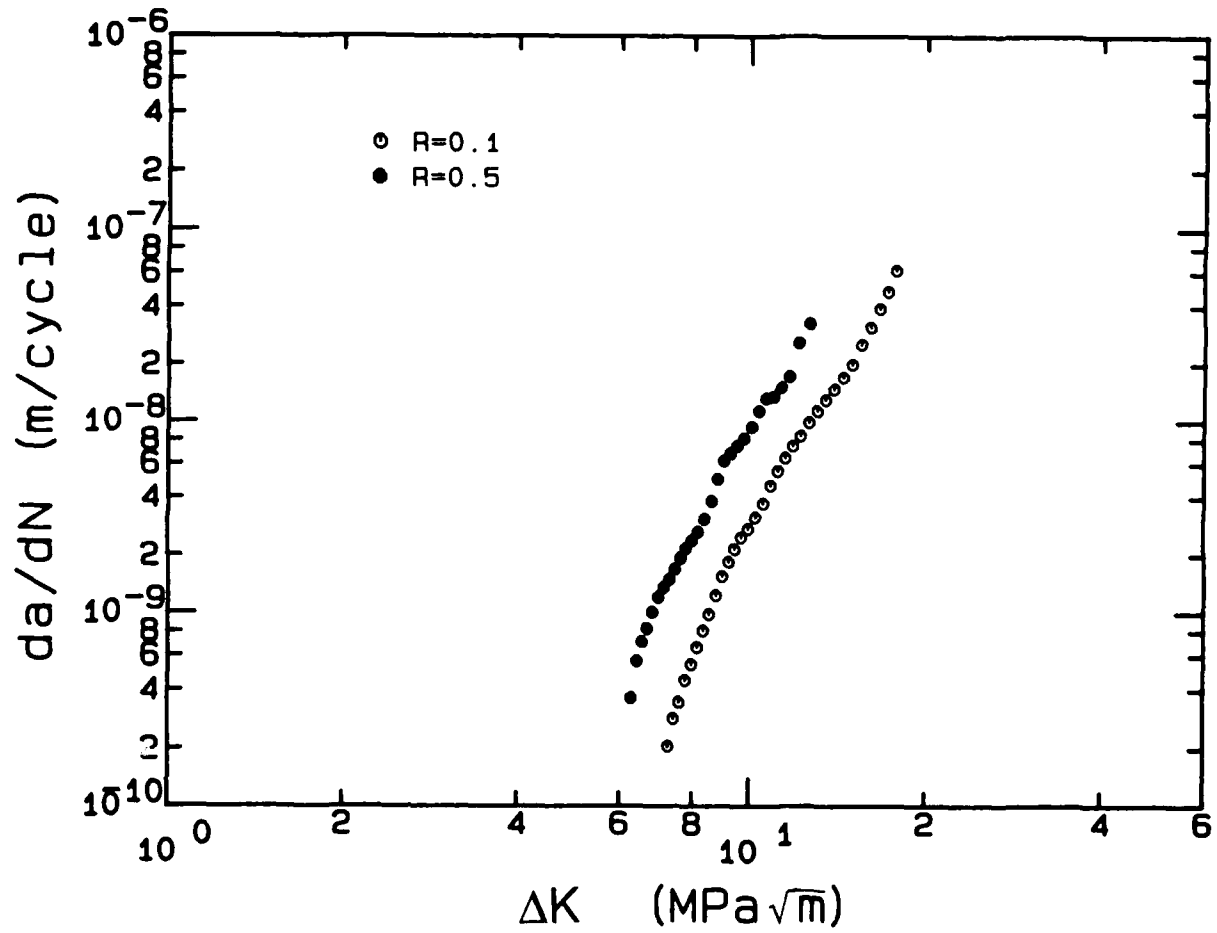


Fig. 4.18 Effect of stress ratio on the propagation of large cracks in Ti-8Al(a).

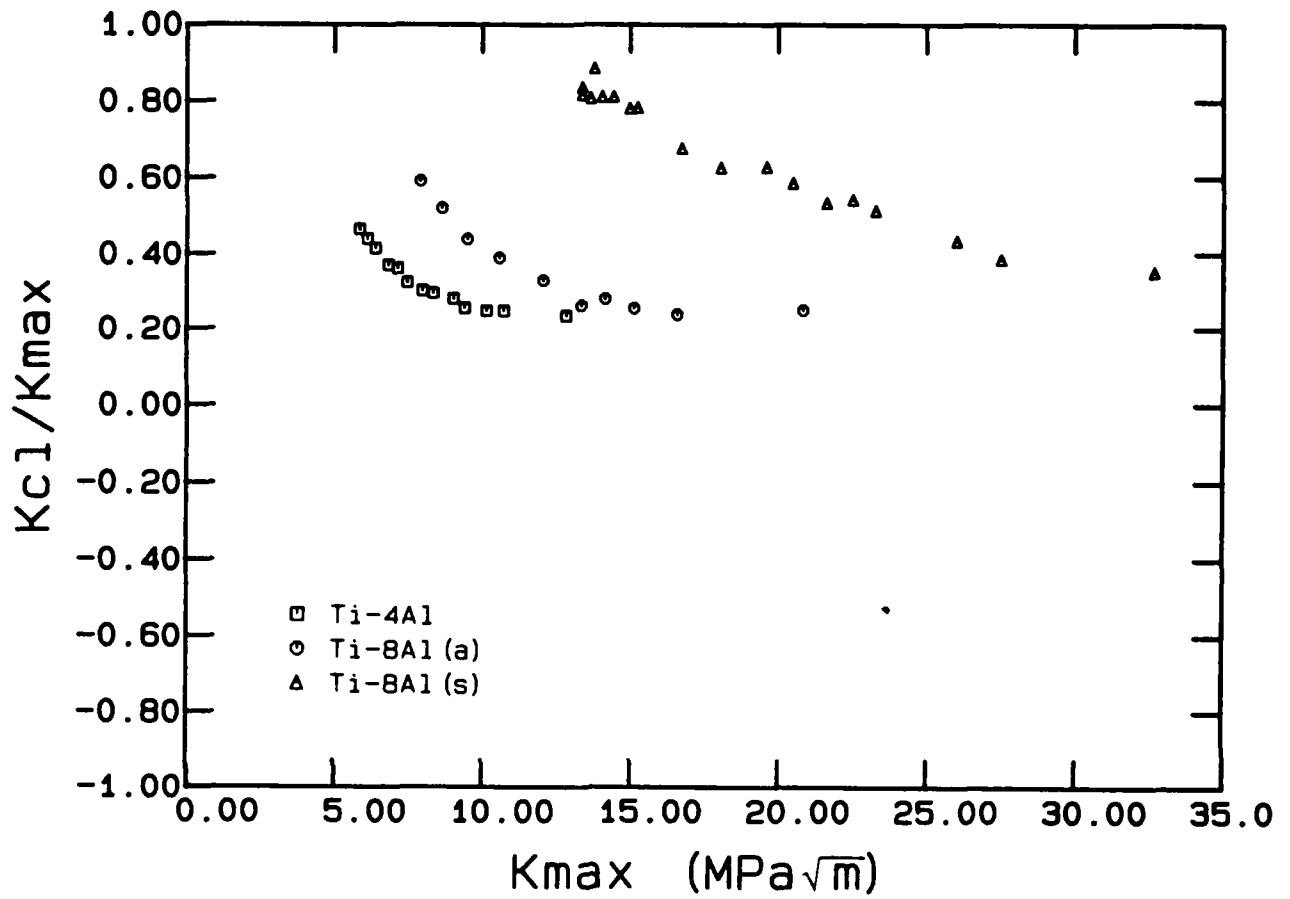


Fig. 4.19 Normalized crack-closure levels for Ti-Al alloys tested under  $R=0.1$  fatigue.



approaches a maximum as  $\Delta K$  approaches  $\Delta K_{th}$  — an effect which clearly increases with increasing closure level. For example, under  $R = 0.1$  in Ti-8Al(s),  $K_{Cl}$  approaches 90% of  $K_{max}$  at  $\Delta K_{th}$ .

Figure 4.20 presents the normalized closure data for the  $R = 0.5$  tests. The Ti-4Al data indicate that  $K_{Cl} \leq K_{min}$  for most of the range of this test. The data from both the Ti-8Al heat treatments are essentially equivalent, with  $K_{Cl}$  approaching 90% of  $K_{max}$  at  $\Delta K_{th}$ . At the higher values of  $K_{max}$ ,  $K_{Cl}$  was less than  $K_{min}$ . The similarity between the two Ti-8Al alloy data sets is in contrast to the findings for  $R = 0.1$  shown in Fig. 4.19. In Ti-8Al(a) the  $R = 0.5$  closure levels are significantly greater than the  $R = 0.1$  data from this material, while in the Ti-8Al(s) alloy, the  $R = 0.5$  closure levels are similar to the corresponding  $R = 0.1$  data.

Replotting the crack closure data in the form of  $K_{Cl}$  versus  $K_{max}$  reveals important features of the data at both stress ratios. As shown in Fig. 4.21, the values of  $K_{Cl}$  for the three alloy conditions tested at  $R = 0.1$  are approximately independent of  $K_{max}$  over the full range of the data. Note that if  $K_{Cl}$  is independent of  $K_{max}$ ,  $K_{Cl}$  must also be independent of crack length. Considering the  $R = 0.5$  data shown in Fig. 4.22, since  $K_{Cl}$  was generally less than  $K_{min}$  in Ti-4Al, the indicated  $K_{Cl}$  increases linearly with  $K_{max}$  throughout the test. Both of the Ti-8Al heat treatments exhibit approximately equivalent values of  $K_{Cl}$ , which are initially independent of  $K_{max}$ . Eventually  $K_{min}$  of these tests becomes greater than  $K_{Cl}$  and the data assume a slope of  $R = K_{min}/K_{max} = 0.5$ .

Thus, in general,  $K_{Cl}$  was largely independent of  $K_{max}$  (and crack length) in the large-crack specimens. Under  $R = 0.1$  fatigue,  $K_{Cl}$  was very dependent on alloy condition, with the Ti-8Al(s) exhibiting the highest closure, followed by Ti-8Al(a), and finally by the Ti-4Al. Under  $R = 0.5$  cycling, the Ti-8Al(a) closure level was anomalously high,

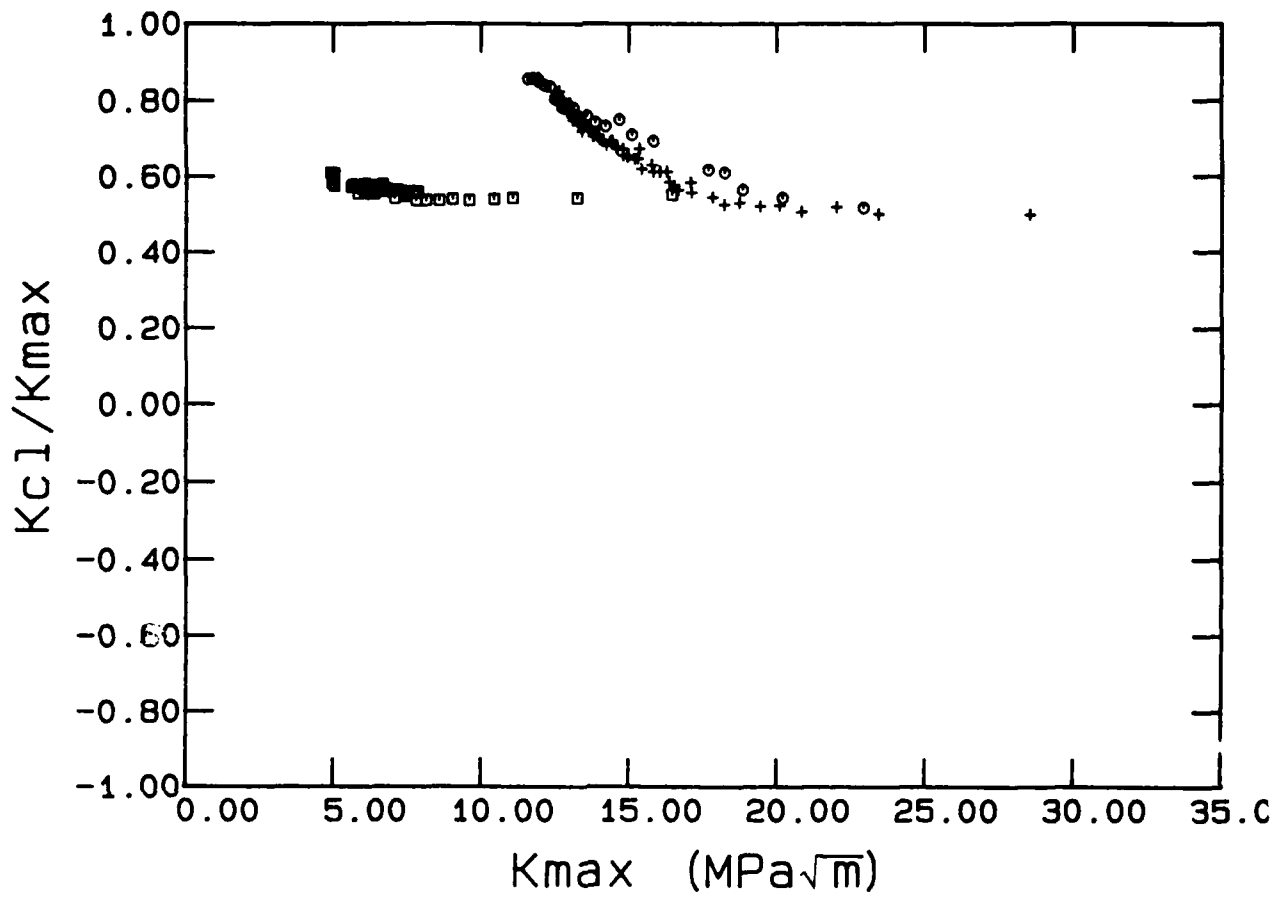


Fig. 4.20 Normalized crack-closure levels for Ti-Al alloys tested under  $R=0.5$  fatigue.

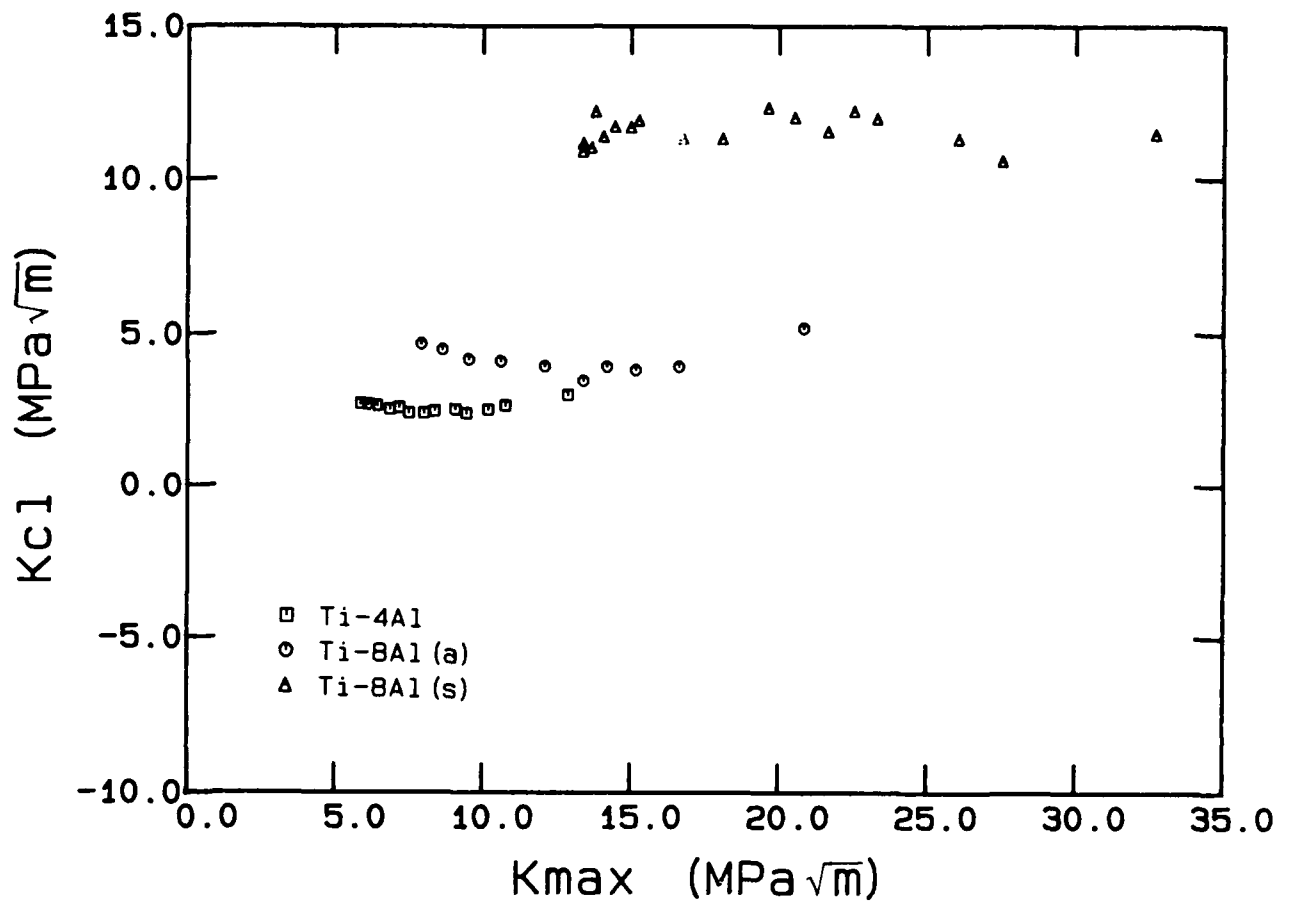


Fig. 4.21 Absolute crack-closure levels for Ti-Al alloys tested under  $R=0.1$  fatigue.

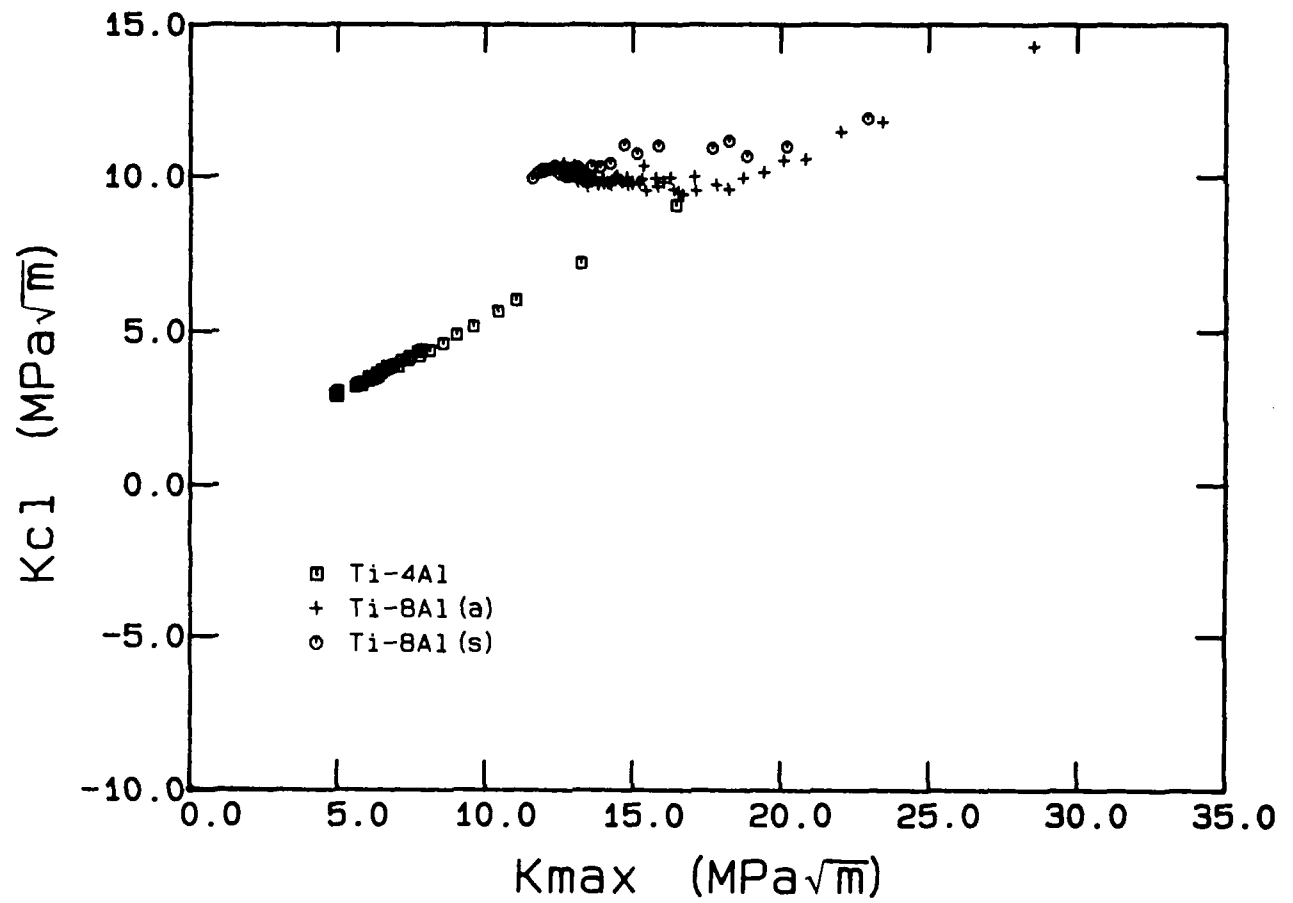


Fig. 4.22 Absolute crack-closure levels for Ti-Al alloys tested under  $R=0.5$  fatigue.

while the closure levels observed in the other alloy conditions were consistent with the  $R = 0.1$  measurements. The  $R = 0.1$  findings agree qualitatively with the earlier findings of Allison and Williams [122]. There are no known data available for comparison with the  $R = 0.5$  findings.

The large-crack growth rate data under the two stress ratios are replotted in Figs. 4.23 and 4.24 as a function of  $\Delta K_{eff}$ , which was calculated using the measured values of  $K_{cl}$ . As shown in the first figure, the  $R = 0.1$  data from the three alloy conditions are consolidated into a narrow band when plotted against  $\Delta K_{eff}$ . At the higher stress ratio ( $R = 0.5$ , Fig. 4.24),  $\Delta K_{eff}$  is able to consolidate the data into a relatively narrow band, although some separation between the data remains. Considering the utility of  $\Delta K_{eff}$ , particularly under  $R = 0.1$  fatigue, it appears that most of the differences in crack growth behavior among the three alloy conditions may be attributed to differences in crack closure behavior.

Comparisons of the  $da/dN$ - $\Delta K_{eff}$  data at  $R = 0.1$  and  $0.5$  are presented for each of the three materials in Figs. 4.25-4.27. The data from the Ti-4Al (Fig. 4.25) and the Ti-8Al(a) (Fig. 4.27) show a slightly faster crack growth rate (as much as a factor of 4) under  $R = 0.5$  cycling than under  $R = 0.1$ . As shown in Fig. 4.26, however, the data from the Ti-8Al(s) were tightly consolidated into a single band when plotted versus  $\Delta K_{eff}$ . This is particularly noteworthy, since the  $da/dN$  data at the two stress ratios differed by approximately two orders of magnitude when plotted against  $\Delta K$ . Although the ability of  $\Delta K_{eff}$  to correlate the crack growth rate data in the other two alloy conditions was less dramatic, the data from all the materials were correlated significantly better by  $\Delta K_{eff}$  than by  $\Delta K$ . This general finding suggests that crack closure effects were largely responsible for the influence of mean stress on crack propagation in the tests.

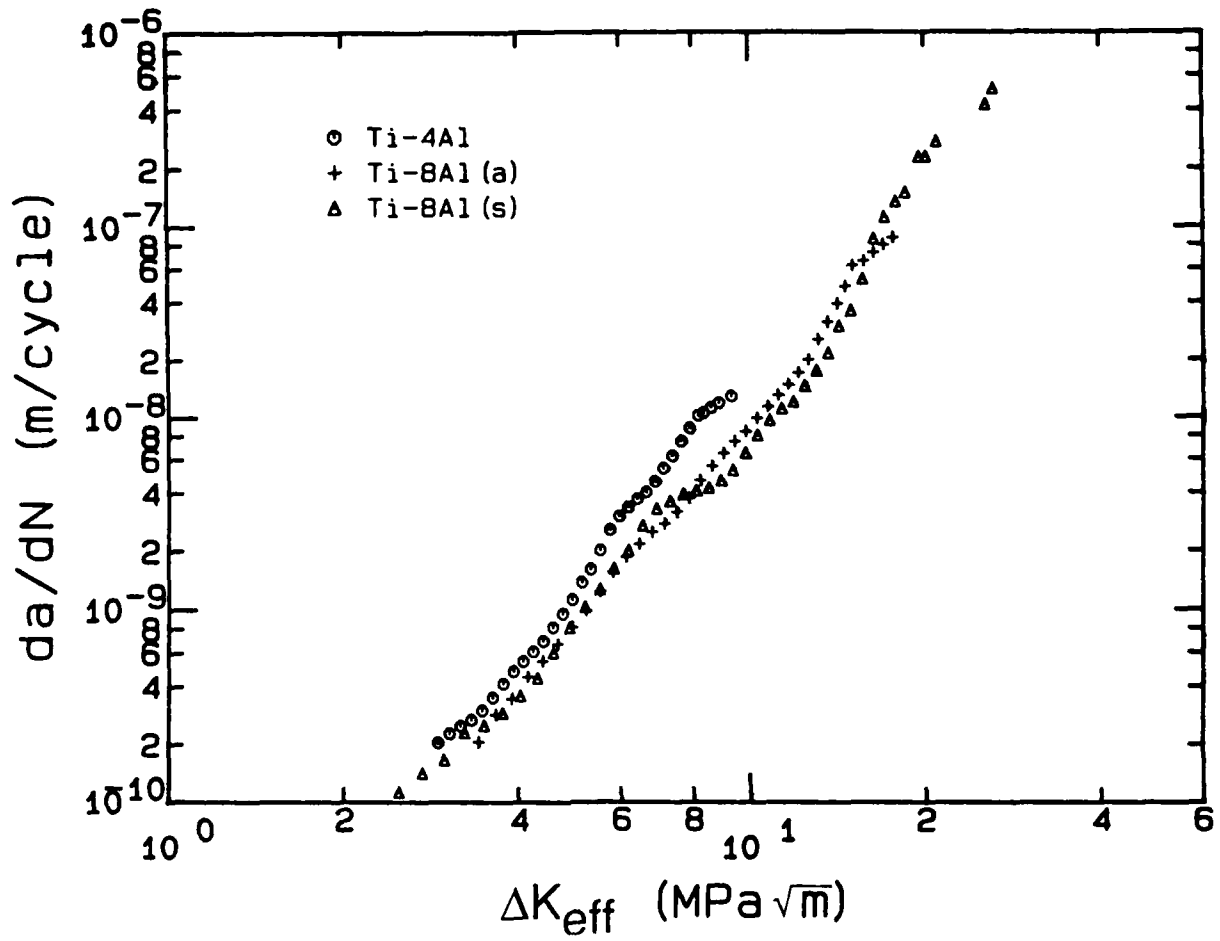


Fig. 4.23 Crack propagation data for large cracks in C(T) specimens tested under  $R = 0.1$  fatigue. Data plotted as  $da/dN$  versus  $\Delta K_{eff}$ .

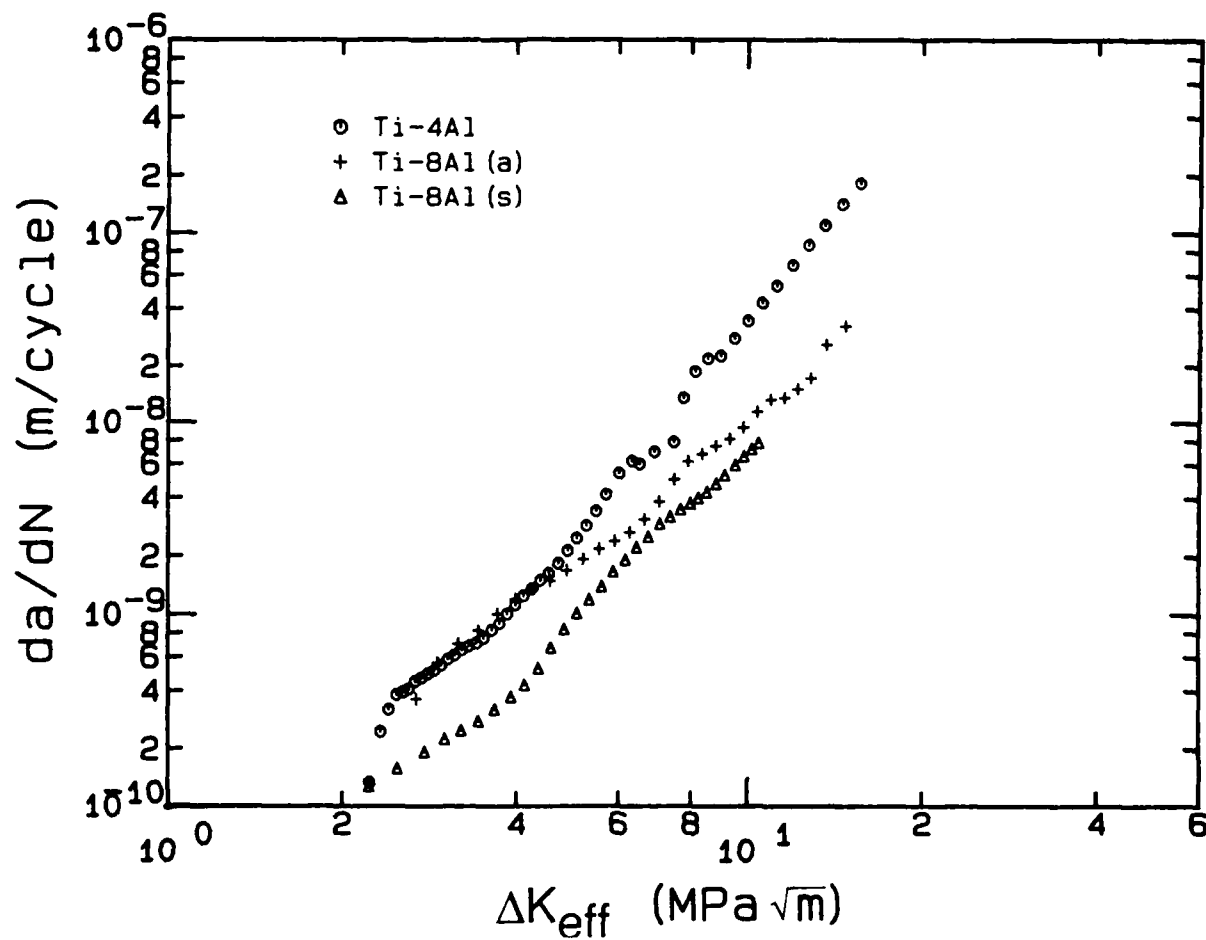


Fig. 4.24 Crack propagation data for large cracks in C(T) specimens tested under  $R = 0.5$  fatigue. Data plotted as  $da/dN$  versus  $\Delta K_{eff}$ .

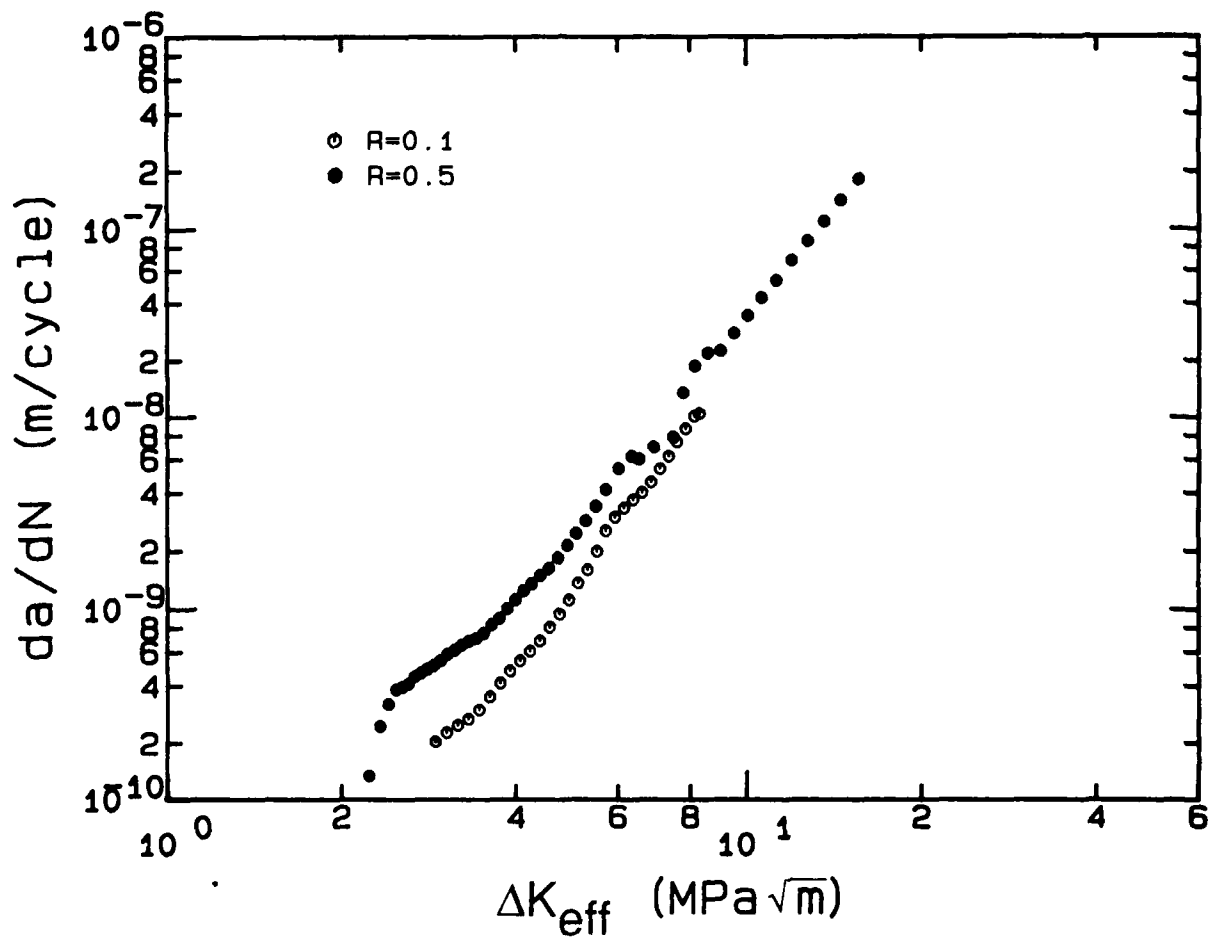


Fig. 4.25 Effect of stress ratio on the propagation of large cracks in Ti-4Al. Data plotted as  $da/dN$  versus  $\Delta K_{eff}$ .



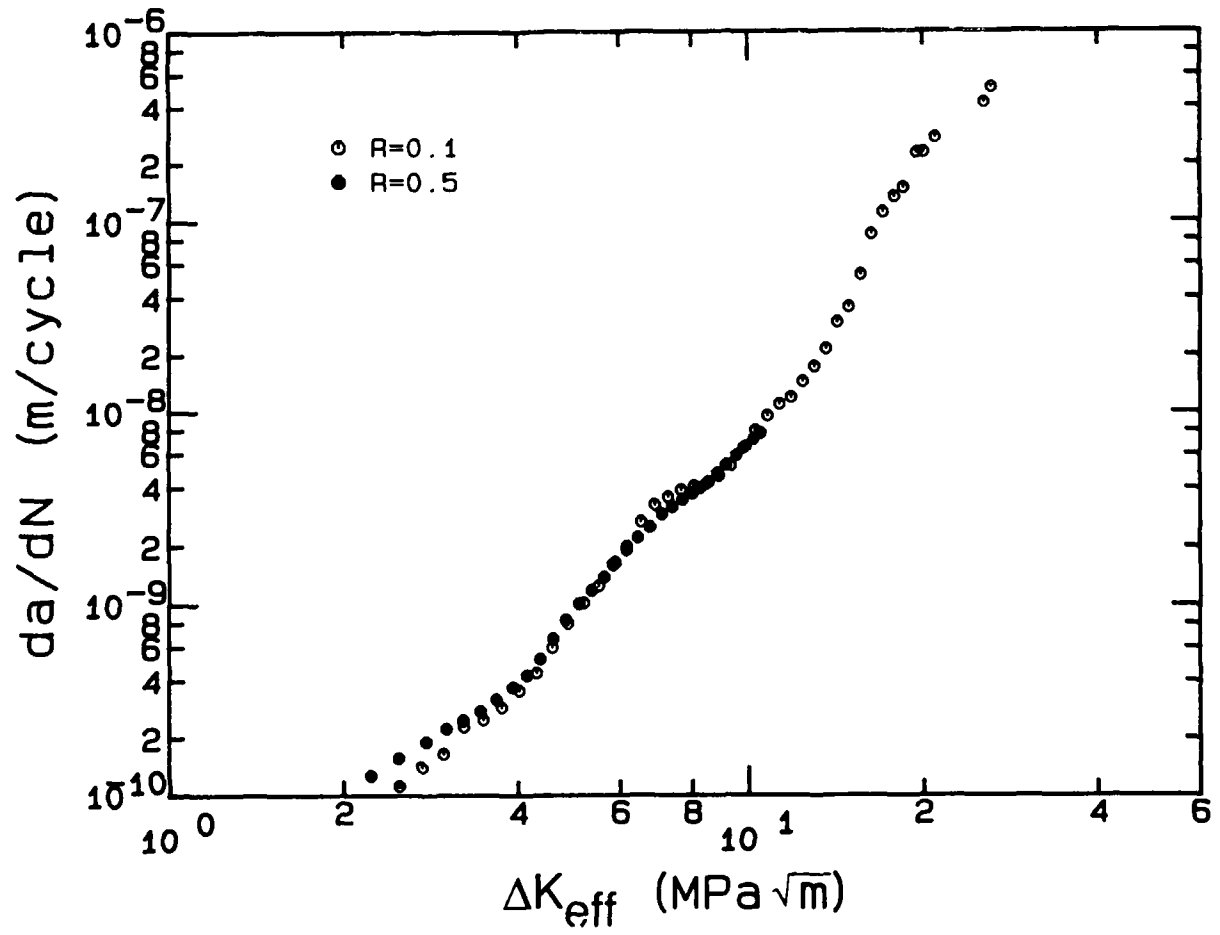


Fig. 4.26 Effect of stress ratio on the propagation of large cracks in Ti-8Al(s). Data plotted as  $da/dN$  versus  $\Delta K_{eff}$ .

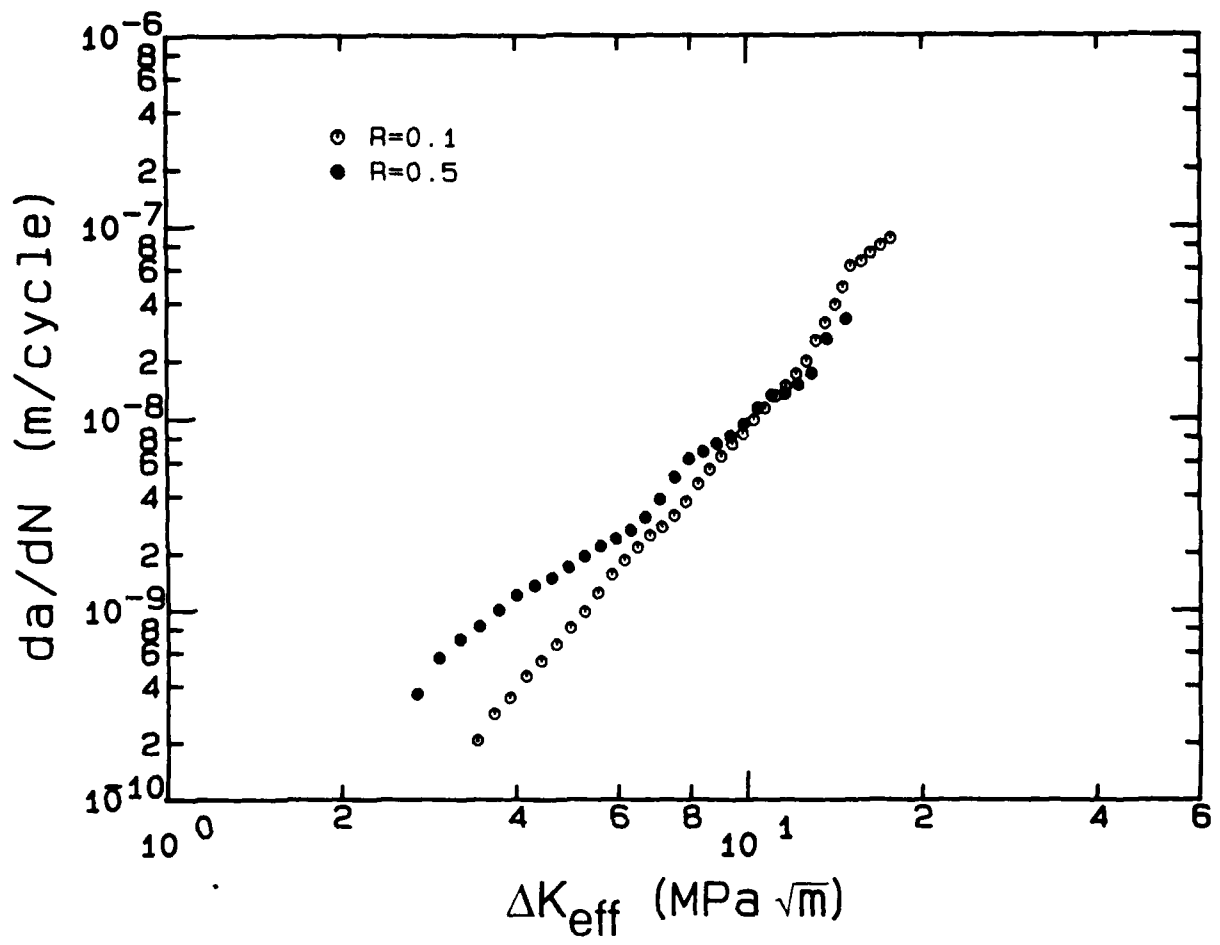


Fig. 4.27 Effect of stress ratio on the propagation of large cracks in Ti-8Al(a). Data plotted as  $da/dN$  versus  $\Delta K_{eff}$ .

For the majority of the large-crack tests, the slope of the  $da/dN - \Delta K_{eff}$  data remained approximately constant for growth rates as low as  $10^{-10}$  m/cycle. Although  $10^{-10}$  m/cycle is conventionally used as an operational definition of a threshold crack growth rate corresponding to  $\Delta K_{th}$ , this definition appears to lead to an overestimate of the true threshold condition in the present materials. Recognizing this limitation, the applied and effective values of  $\Delta K_{th}$  have been tabulated in Table 4.4 as a function of material and R. Also tabulated is the corresponding value of  $K_{cl}$ . As indicated in the table, the dramatically different values of  $\Delta K_{th}$  for the three alloy conditions are explained almost completely by crack closure. In other words, after accounting for the differences in the component of  $\Delta K_{th}$  that was due to closure, the effective resistance of the three materials to crack propagation,  $\Delta K_{eff(th)}$ , is essentially independent of alloy condition. Thus, the differences in slip character in these material are manifested almost completely through crack closure. As indicated by the  $R = 0.1$ , Ti-8Al(s) data, after accounting for closure, the remaining component of  $\Delta K_{th}$  accounts for as little as 17% of the material's total resistance to threshold crack growth.

Table 4.4: Threshold Stress Intensity Factor Ranges

		$\Delta K_{th}$ (MPa $\sqrt{m}$ )	$\Delta K_{eff(th)}$ (MPa $\sqrt{m}$ )	$K_{cl}$ (MPa $\sqrt{m}$ )
Ti-4Al	R = 0.1	4.50	2.09 (46%)	2.91
	R = 0.5	2.46	2.11 (86%)	2.81
Ti-8Al(s)	R = 0.1	12.26	2.05 (17%)	11.57
	R = 0.5	5.85	2.26 (39%)	9.44
Ti-8Al(a)	R = 0.1	6.71	2.61 (39%)	4.85
	R = 0.5	5.67	1.55 (27%)	9.77

- $\Delta K_{th}$  and its components,  $\Delta K_{eff(th)}$  and  $K_{cl}$ , are defined operationally at a crack growth rate of  $da/dN = 10^{-10}$  m/cycle.
- Percentages in parentheses are % of  $\Delta K_{th}$ .

#### 4.2.4 Anticipated Small-Crack Behavior

An assessment of the potential behavior of small fatigue cracks in the Ti-Al alloys was performed by constructing a "Kitagawa" diagram such as that shown schematically in Fig. 2.2 and discussed in section 2.1. A Goodman relationship [244] was used to adjust the  $R = -1.0$  fatigue-strength data to obtain the effective fatigue-strength stress range for  $R = 0.1$  cycling. Assuming  $a/c = 1$  and using the surface-crack stress intensity factor solution [127,128],  $\Delta K_{th}$  and  $\Delta K_{eff(th)}$  values were used to construct the lines describing the condition for threshold crack growth. The pertinent data are listed in Table 4.5, and the plot is presented in Fig. 4.28.

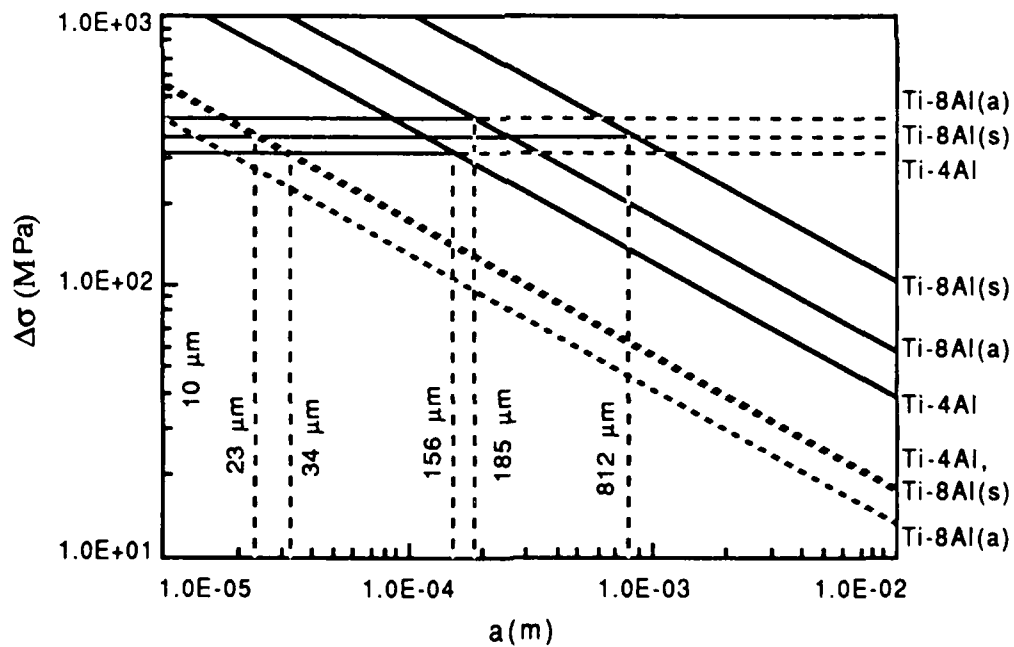


Fig. 4.28 "Kitagawa" diagram constructed for the three Ti-Al alloy both  $\Delta K_{th}$  and  $\Delta K_{eff(th)}$ .

As shown in the figure, the intersection of the fatigue-strength and the  $\Delta K_{th}$  lines (which defines the crack size  $a_0$ ) occurs over a substantial range in crack size for the three materials, ranging from 156  $\mu\text{m}$  in Ti-4Al to 812  $\mu\text{m}$  in Ti-8Al(s). However, the  $a_{0(eff)}$  crack sizes, which are defined using  $\Delta K_{eff(th)}$  for the three materials, are much smaller and show relatively limited variation, ranging from 10 to 34  $\mu\text{m}$  for the three materials.

Assuming that  $a_0$  provides a rough approximation of the crack size below which  $\Delta K_{th}$  loses its utility, the data "predict" that differences between large- and small-crack behavior in the three alloys will be substantially different when plotted against  $\Delta K$ . This difference is expected to be significantly less when  $\Delta K_{eff}$  is used to correlate the crack growth rates. The estimates provided by the construction of the figure, however, give little insight into the underlying physics and mechanics that pertain to the behavior of small and large cracks.

Table 4.5: Experimental Data and Calculated Parameters Used in Constructing Fig. 4.28

Material	$\sigma_e$ (R=-1.0) (MPa)	$\sigma_e$ (R=0.1) (MPa)	$\Delta K_{th}$ (MPa $\sqrt{\text{m}}$ )	$\Delta K_{eff(th)}$ (MPa $\sqrt{\text{m}}$ )	$a_0$ ( $\mu\text{m}$ )	$a_{0(eff)}$ ( $\mu\text{m}$ )
Ti-4Al	219	307	4.50	2.09	156	34
Ti-8Al(s)	260	367	12.26	2.05	812	23
Ti-8Al(a)	316	421	6.71	1.55	185	10

## 4.2.5 Small-Crack Fatigue Testing

### 4.2.5.1 Initiation of Small Cracks

As shown previously by Kim et al [119,120], variations in slip character in Ti-Al alloys have a dramatic effect on the initiation of fatigue cracks under low-cycle fatigue. Although crack initiation was not the primary focus of the present investigation, any transient crack growth behavior associated with the mode or mechanism of crack initiation was of interest. Therefore, as discussed earlier, fatigue cracks were initiated naturally to simulate most accurately the actual fatigue process and avoid any potentially misleading effects that might be caused by using an artificial crack starter.

In the Ti-4Al alloy, which exhibited finely distributed wavy slip, crack initiation commonly occurred at grain boundaries and grain-boundary triple points, and the cracks in this material underwent a relatively quick transition from stage I to stage II crack growth. In contrast, crack initiation in the Ti-8Al(s) occurred primarily along planar slip bands, and crack extension tended to be much more crystallographic, generally following slip bands. A similar cracking behavior was observed in the aged Ti-8Al. In this material, the extreme strain localization brought on by precipitate shearing produced a few very well defined crack initiation sites, and crack extension was also very crystallographic.

In the majority of the small-crack specimens, initiation of the dominant crack occurred at the base of the mild notch (i.e., at the minimum specimen thickness) at a location that was well removed from the specimen edge. The few specimens that formed dominant cracks at or near a specimen corner were not considered in the present investigation. Only data from small, semielliptical surface flaws were used, and testing

was terminated if a small crack approached the specimen corner or another crack.

#### 4.2.5.2 Characterization of Crack Shape

Measurements were made to determine the shape of a number of small cracks that had been heat tinted to discolor the fracture surface. The resulting data of crack depth ( $a$ ) versus surface crack half-length ( $c$ ) are presented in Fig. 4.29. As shown for all three materials, there was little variability in the measured crack shape, and the average crack aspect ratio was  $a/c = 0.9$ . This crack-shape value was in good agreement with observations reported by numerous other investigators [e.g., 30] and was identical to the finding of Gerdes et al [112] on aged Ti-8.6Al. Moreover, a stable value of  $a/c \approx 0.9$  is predicted by the Newman and Raju surface-flaw stress intensity factor solution. The accuracy of this aspect ratio was experimentally verified further by the consistently good agreement between surface crack length measurements made from photographs and crack lengths calculated from compliance assuming  $a/c = 0.9$ . Therefore, this crack shape was adopted for use in calculations of stress intensity factor. As will be demonstrated later,  $K$  calculations are only mildly sensitive to moderate variations in  $a/c$ .

#### 4.2.5.3 Measurement of Small Cracks

As discussed previously, the propagation of small cracks was tracked both photographically and by compliance measurements. The photographic measurements, provided an accurate measurement of surface crack length, as well as direct documentation of crack path. The photographic observations will be discussed in detail later. Within the present discussion, however, the benefit of the photographic measurements was associated primarily with the availability of an independent measurement of crack length. In reducing the photographic data, surface crack lengths were obtained by measuring the

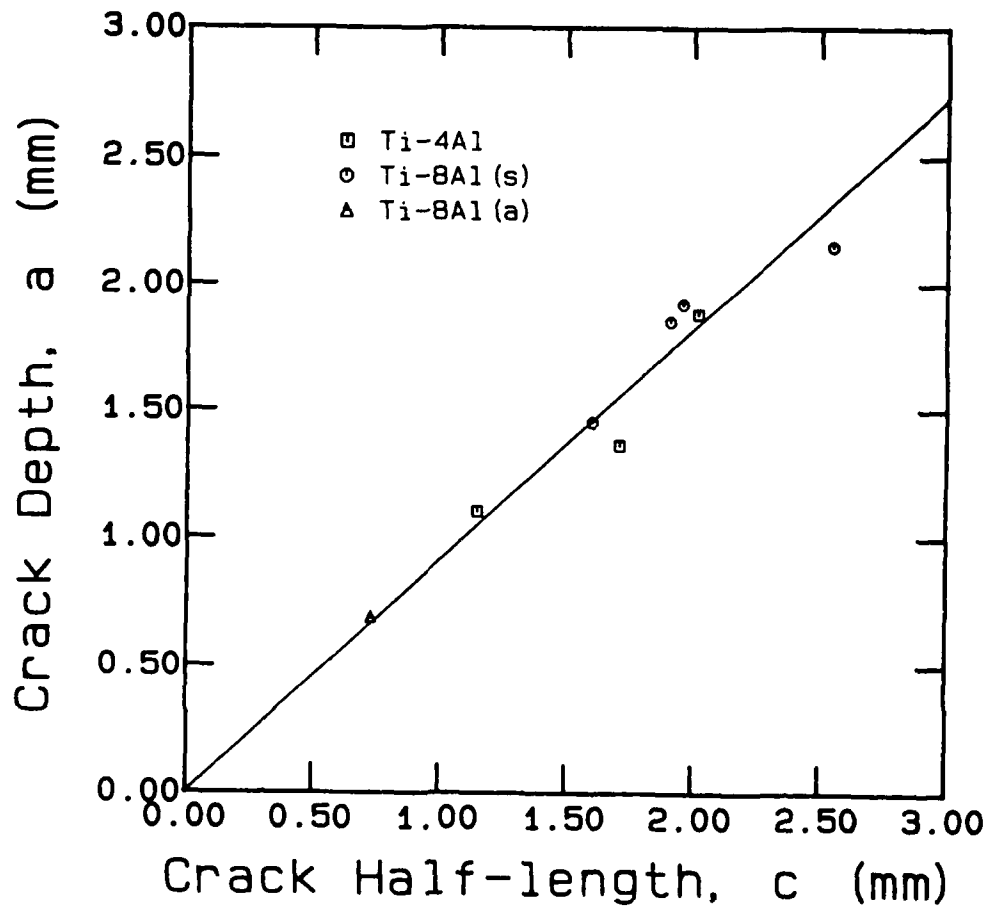


Fig. 4.29 Crack-shape data obtained from measurements of heat-tinted fracture surfaces.



length of the crack as projected onto a plane normal to the axis of loading. These measurements were generally in excellent agreement with the effective crack length determined from the compliance measurements made using the interferometric system. The excellent agreement between photographic and compliance measurements of crack length had been demonstrated previously in small-crack testing of Ti-6Al-2Sn-4Zr-6Mo [255] and was reconfirmed within the present study by data such as those illustrated in Fig. 4.30, which are from a test of Ti-8Al(s) with  $R = 0.1$  and  $\sigma_{\max}/\sigma_y = 0.6$ .

The effect on crack growth rate calculations of using photographic versus compliance measurements of crack length is illustrated in Figs. 4.31 and 4.32, respectively. These data correspond to those in Fig. 4.30. Since the photographic measurements of crack propagation represent crack length at the specimen surface, the calculated values of  $da/dN$  shown in Fig. 4.31 are very sensitive to local variations in crack growth behavior. Alternatively, the crack growth rate calculations from compliance measurements of crack length, shown in Fig. 4.32, suggest a much more continuous crack growth process, because these data represent average behavior along the entire, semielliptical crack front. As also shown in Fig. 4.32, however, the mean crack growth rate behavior appears essentially independent of the method of crack length measurement. Moreover, as discussed in Appendix 1, the variability of  $da/dN$  data is strongly dependent on the numerical method used to process the data, but the total fatigue life depends only on the average crack growth rate. To facilitate meaningful interpretation of the crack growth results, without introducing the complexities associated with variability in crack growth rate observed only at the specimen surface, the crack growth rate data to be presented were taken from the photographically-verified compliance measurements of crack length.

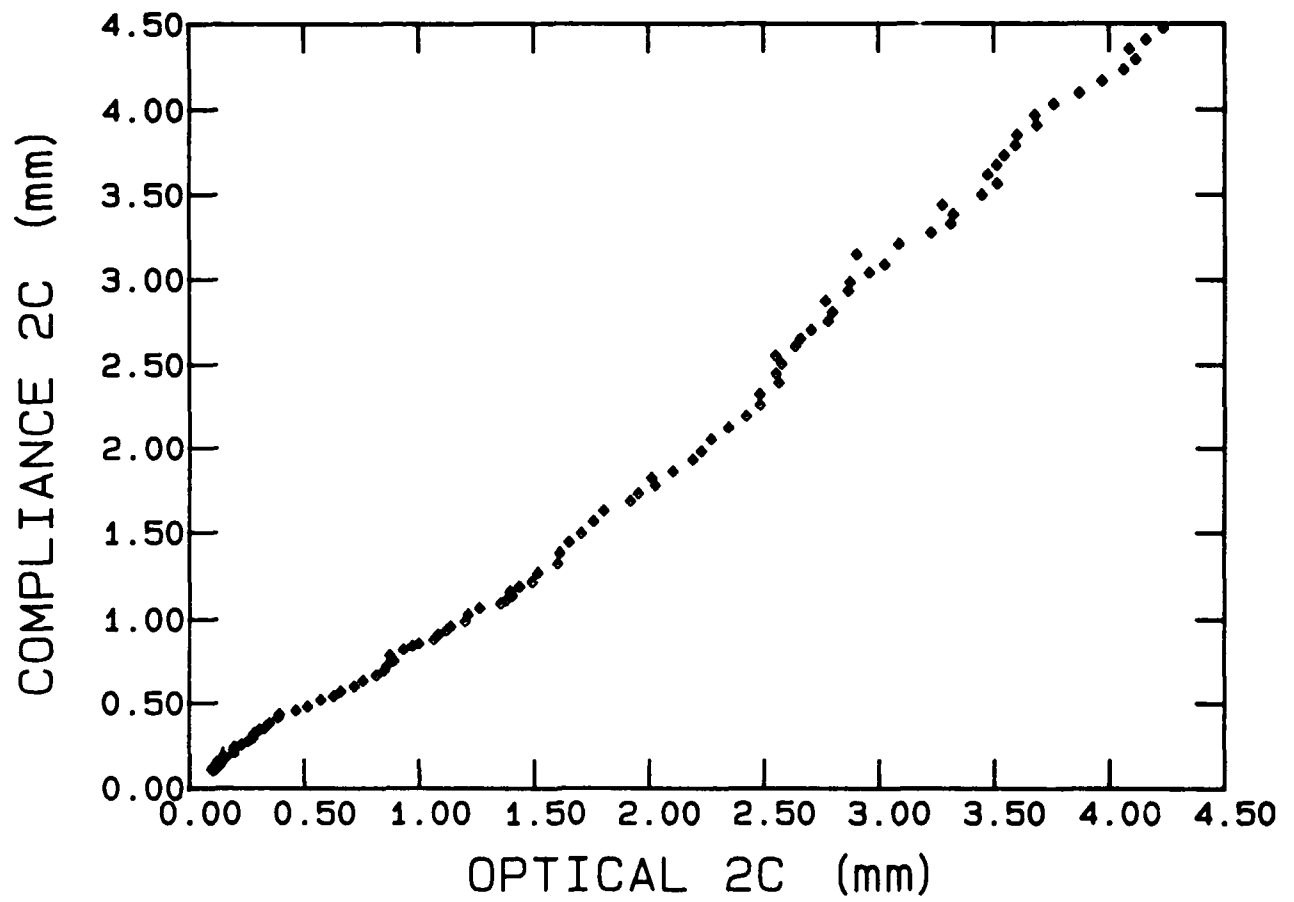


Fig. 4.30 Typical data showing the correspondence between crack length measurements obtained photographically and from compliance (Ti-8Al(s),  $R = 0.1$ ,  $\sigma_{\max}/\sigma_y = 0.6$ ).

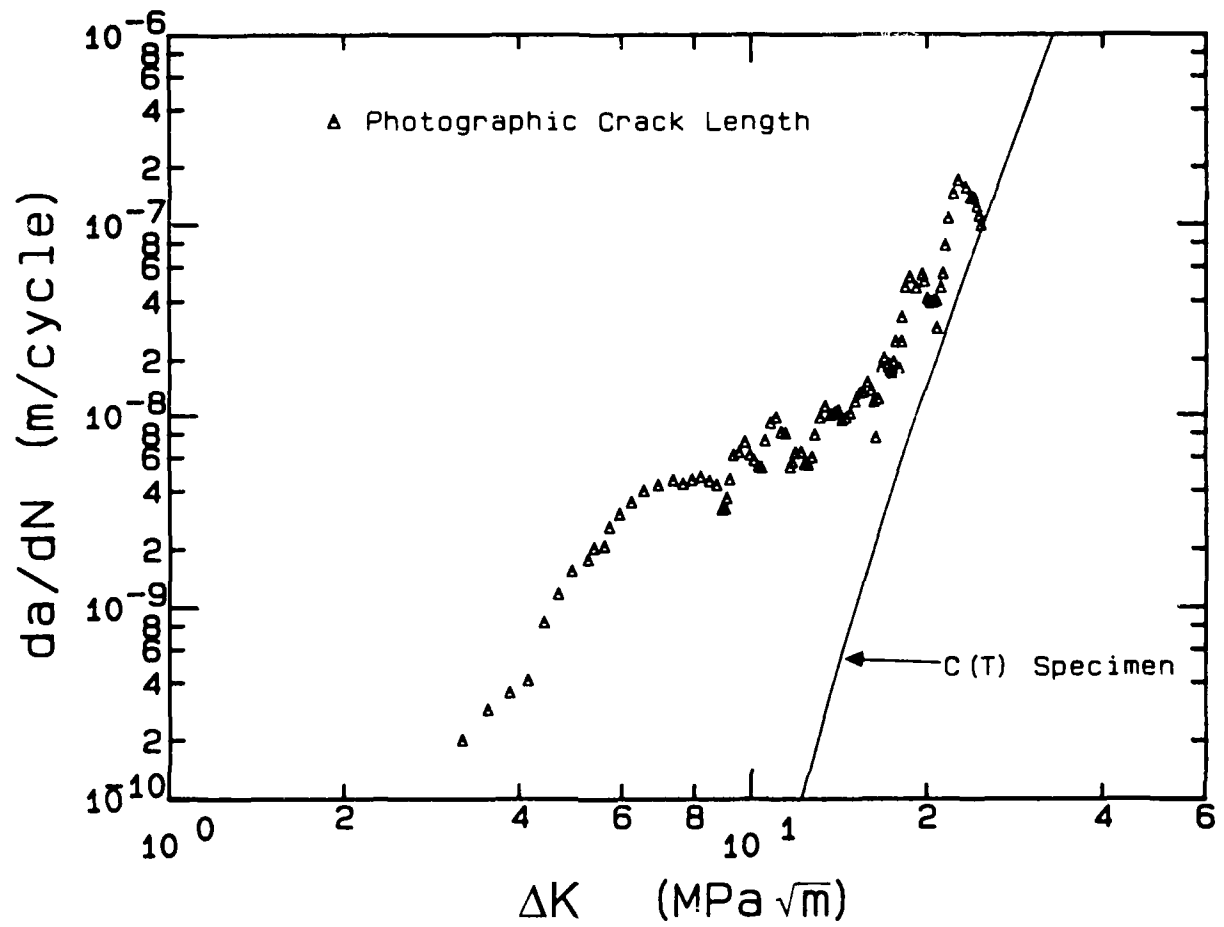


Fig. 4.31 Crack growth rate data reduced from photographic measurements of the length of a small fatigue crack in the alloy Ti-8Al(s);  $R = 0.1$ ,  $\sigma_{\max}/\sigma_y = 0.6$ .

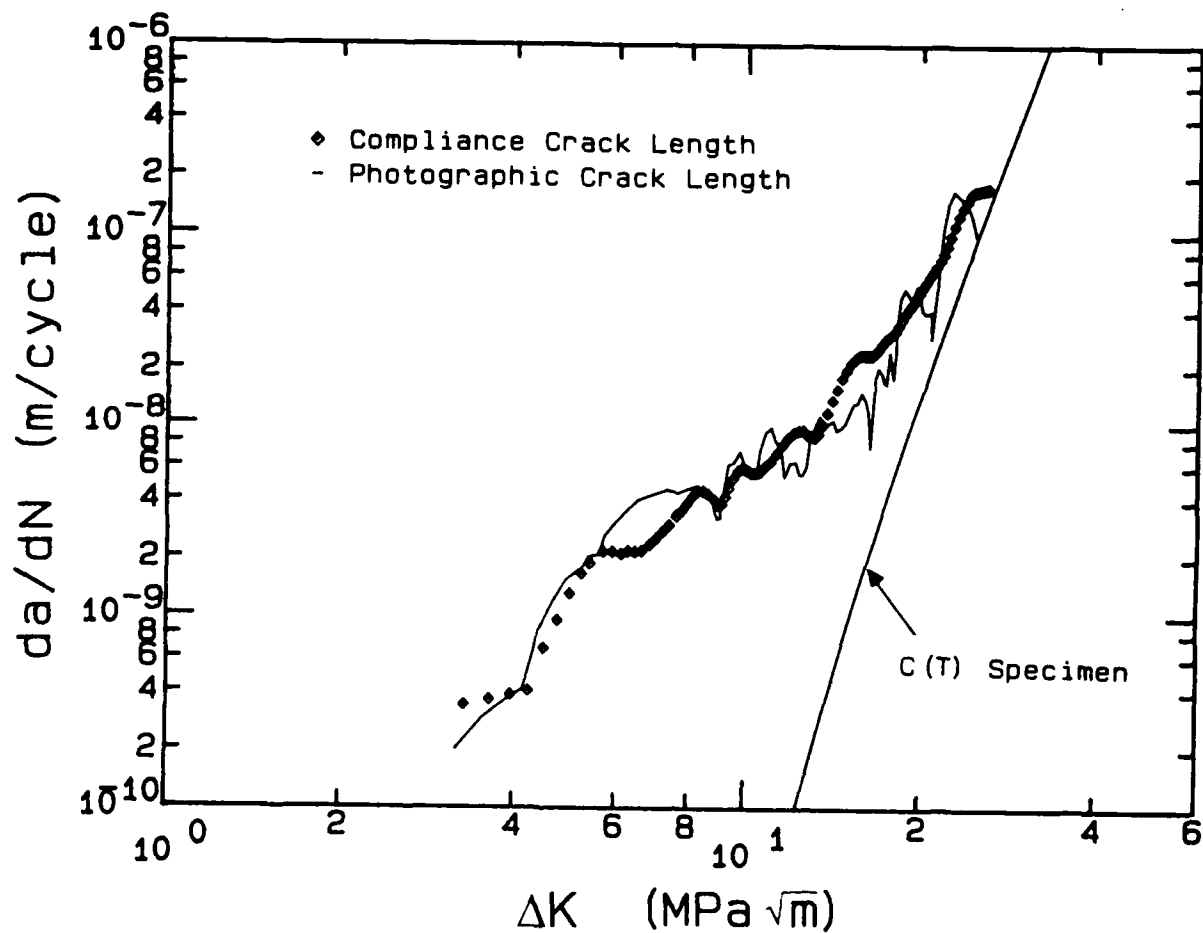


Fig. 4.32 Crack growth rate data reduced from compliance measurements of the length of a small fatigue crack in the alloy Ti-8Al(s);  $R = 0.1$ ,  $\sigma_{\max}/\sigma_y = 0.6$ . The superimposed solid line represents the corresponding data from photographic measurements shown in Fig. 4.31.

#### 4.2.5.4 Propagation of Small Cracks

Table 4.6 summarizes the range of conditions for the small-crack tests that were performed. The specific test conditions that are outlined were chosen to provide an assessment of the effects of alloy condition (slip character), stress level, and stress ratio on the growth of small cracks. The examination of these variables was intended to reveal independently the influences of alloy slip character and closure on the growth of small cracks. The Ti-8Al(s) alloy was tested under all loading conditions, since this material exhibited the highest closure levels in large-crack testing and was expected to display the most extreme small-crack behavior.

Table 4.6: Small-Crack Test Conditions

$\sigma_{\max}/\sigma_y$	R	Ti-4Al	Ti-8Al(s)	Ti-8Al(a)
0.6	-1.0		X	
0.6	0.1	X	X	X
0.6	0.5		X	
0.9	-1.0		X	
0.9	0.1	X	X	X
0.9	0.5		X	

Assuming that the crack aspect ratio remained constant at  $a/c = 0.9$ , the crack length data obtained from compliance measurements were reduced to the form of  $dc/dN$  versus  $\Delta K$  using the surface-crack stress-intensity-factor solution of Newman and Raju [127,128] and a modified-incremental-polynomial method [252, Appendix 1]. All of the data will be presented subsequently; however, a number of general trends observed in most of the tests are exemplified by the results that were presented in Fig. 4.32. These data were acquired from an individual small crack in the Ti-8Al(s) alloy tested at  $R = 0.1$

and having  $\sigma_{\max} = 0.6 \sigma_y$ . The solid line represents the large-crack growth rate trend for a 7.5 mm thick C(T) specimen also tested under  $R = 0.1$  fatigue. Clearly,  $\Delta K$  does not consolidate the large- and small-crack data, and the small crack data do not exhibit the conventional long-crack threshold stress intensity factor,  $\Delta K_{th}$ . Eventually, the small- and large-crack data merge. The small-crack data shown in the figure were taken from a crack that had initiated in the center of the test specimen, allowing crack propagation to be followed over a large distance. Some of the data to be presented subsequently were taken from less ideally located cracks, and data at the larger crack sizes (higher  $\Delta K$  values) were eliminated due to interaction with secondary cracks or the impending formation of a corner crack.

The broad range of test conditions examined, combined with the large number of data acquired, complicate the effective presentation of the small-crack results. To facilitate meaningful interpretation of the data, the experimental results will be presented in a series of plots that systematically isolate effects of the various test variables.

#### 4.2.5.4.1 Effect of Stress Level

The effect of stress level on the propagation of small cracks grown under  $R = 0.1$  fatigue is illustrated in Figs. 4.33-4.35 for the three alloy conditions. The data are presented as a function of nominally applied  $\Delta K$ , and the solid line in each figure represents the equivalent data obtained from C(T) specimens tested at  $R = 0.1$ . The small-crack data presented in the figures were acquired under testing with  $\sigma_{\max}/\sigma_y = 0.6$  and  $0.9$ . Under both stress levels in all three materials, the growth rates of the small cracks were consistently faster than indicated by the large-crack data, and the small cracks routinely propagated at stress intensity ranges that were well below the large-crack  $\Delta K_{th}$ . This effect was most accentuated in the Ti-8Al(s). There appeared to

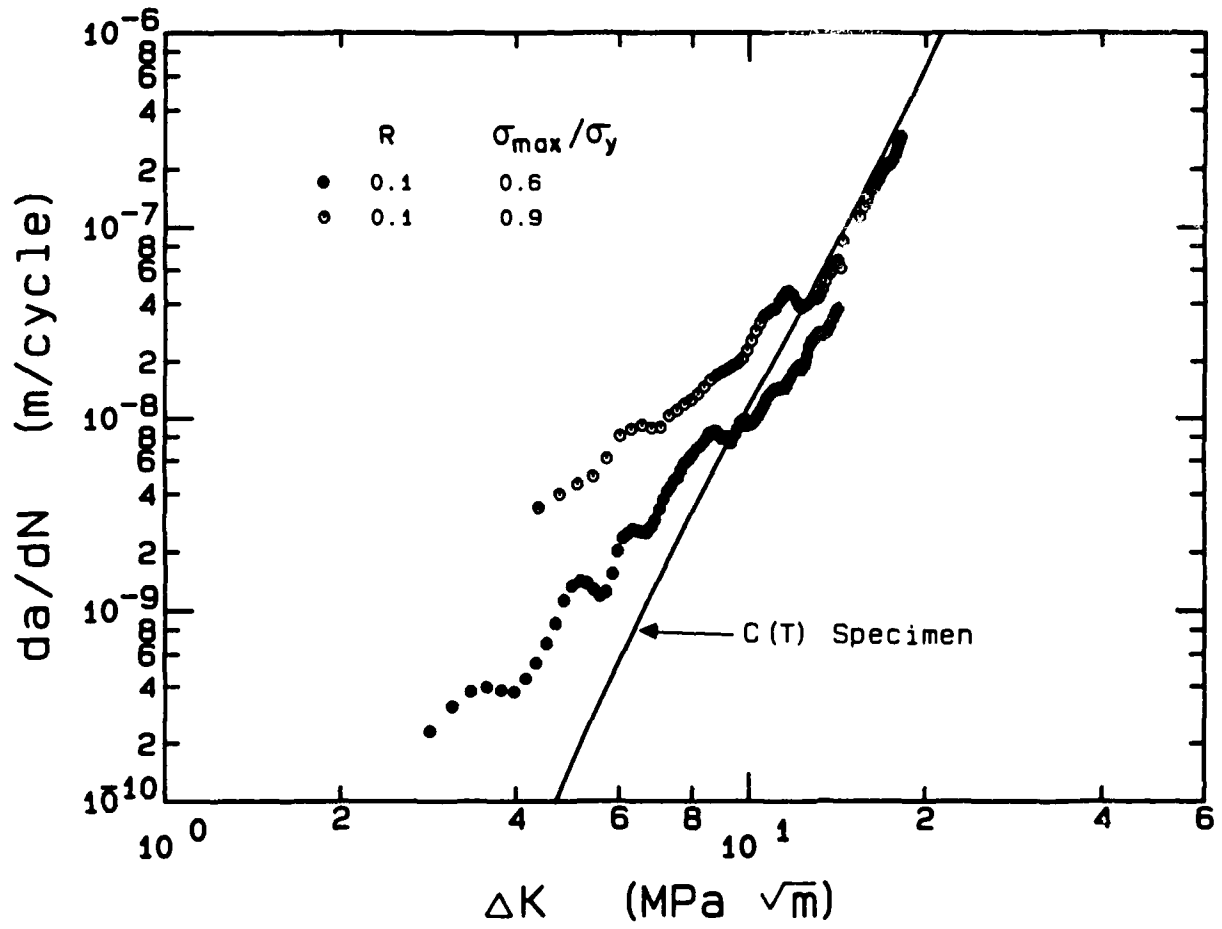


Fig. 4.33 Plot of  $da/dN$ - $\Delta K$  illustrating the effect of stress level on the growth of small cracks in Ti-4Al fatigued at  $R = 0.1$ .

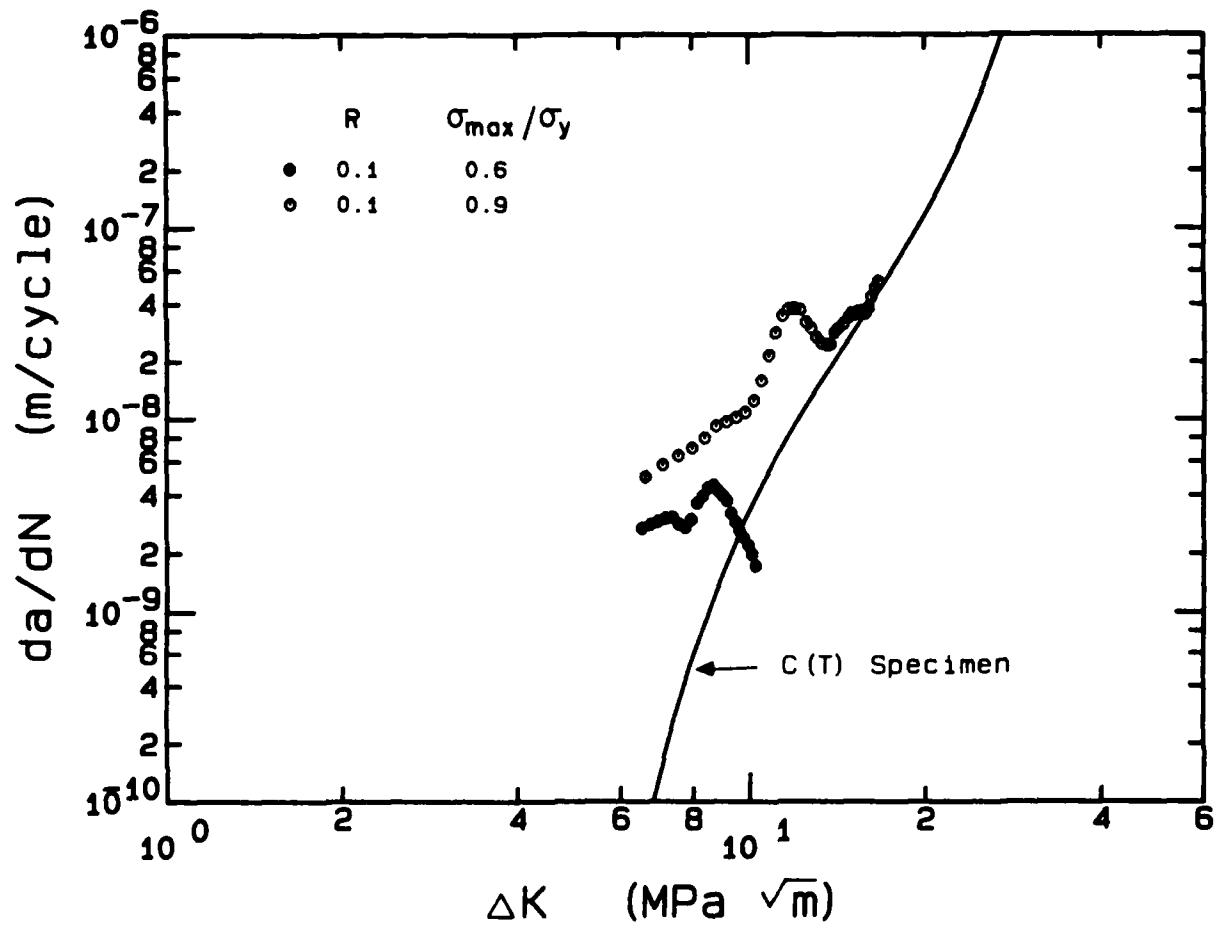


Fig. 4.34 Plot of  $da/dN$ - $\Delta K$  illustrating the effect of stress level on the growth of small cracks in Ti-8Al(a) fatigued at  $R = 0.1$ .



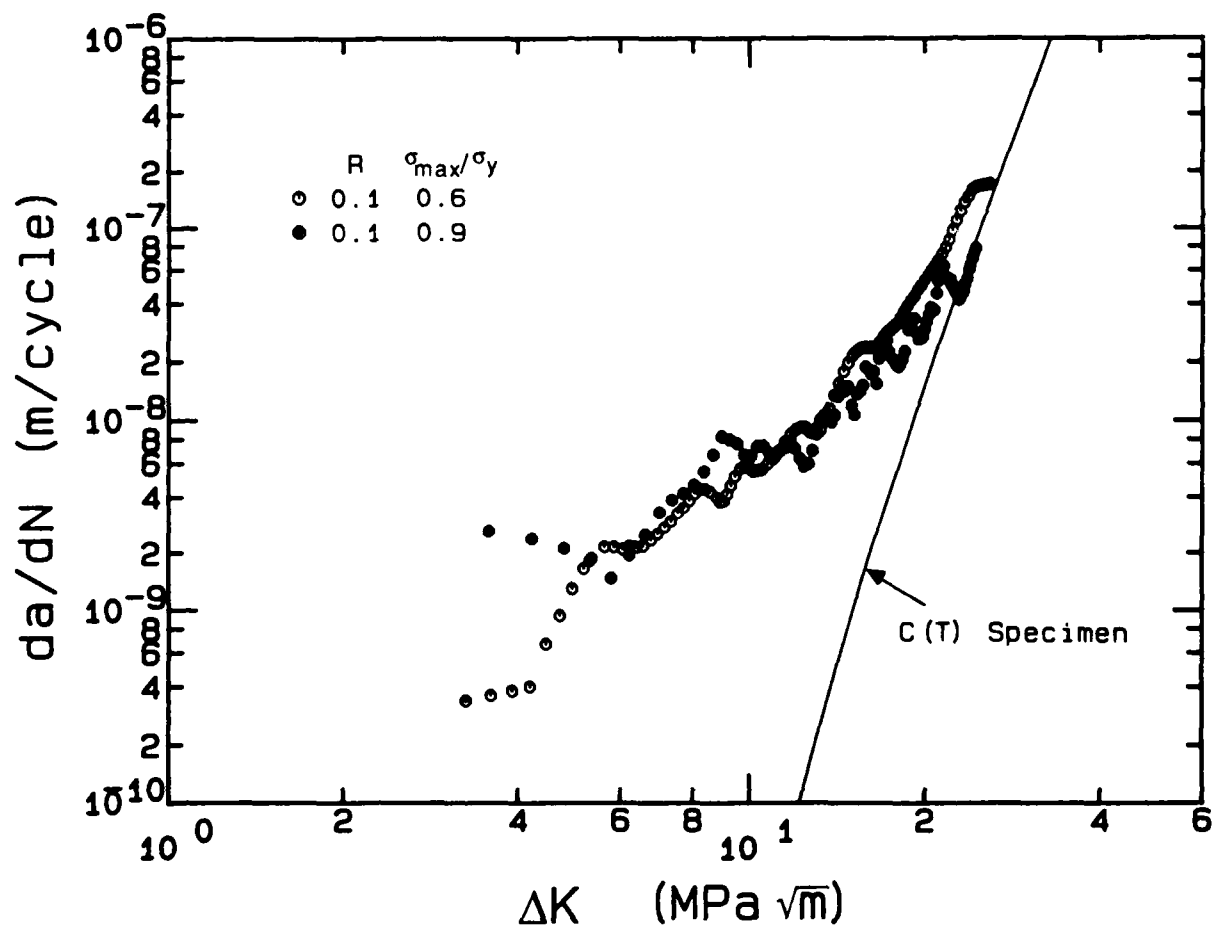


Fig. 4.35 Plot of  $da/dN$ - $\Delta K$  illustrating the effect of stress level on the growth of small cracks in Ti-8Al(s) fatigued at  $R = 0.1$ .

be a modest effect of stress level in Ti-4Al and Ti-8Al(a), although the growth of small cracks in Ti-8Al(s) appears to be independent of stress level.

The effect of stress level on the growth of small cracks in Ti-8Al(s) tested under  $R = -1.0$  and  $R = 0.5$  is shown in Figs. 4.36 and 4.37, respectively. Under  $R = -1.0$  testing, small-crack growth at the two stress levels differed by as much as a factor of 10 over much of the range in  $\Delta K$ . In contrast, as shown in Fig. 4.37, the stress effect under  $R = 0.5$  cycling was observed only at the shorter crack lengths.

Thus, the effect of varying stress level from  $\sigma_{\max}/\sigma_y = 0.6$  to 0.9 appeared to have a moderate, but inconsistent, effect on the growth of small surface cracks. Small cracks at the higher stress level often, but not exclusively, propagated faster than at the lower stress level. The stress effect was not observed in the Ti-8Al(s),  $R = 0.1$  data but was most significant in  $R = -1.0$  tests of the same material. Although test-to-test variability may have accounted for some of the inconsistencies, the general trends suggest a moderate effect of stress level that depends in a secondary way on stress ratio and alloy condition.

#### 4.2.5.4.2 Effect of Stress Ratio

The Ti-8Al(s) alloy condition was tested under three stress ratios:  $R = -1.0$ , 0.1, and 0.5. Crack growth rate data demonstrating the effect of  $R$  in this material are presented in Figs. 4.38 and 4.39 for tests at the two stress levels. The solid line in each figure represents the  $R = 0.1$ , C(T) specimen data. For the  $R = -1.0$  tests,  $\Delta K$  was calculated using only the positive stress range (i.e.,  $\Delta K = K_{\max}$ ). Using this convention, the growth rates of small cracks tested at  $\sigma_{\max}/\sigma_y = 0.6$  are largely independent of stress ratio, although the  $R = -1.0$   $da/dN$  data at the lowest  $\Delta K$  values (smallest crack lengths) appear somewhat faster than at the higher stress ratios. For tests at  $\sigma_{\max}/\sigma_y = 0.9$ , the

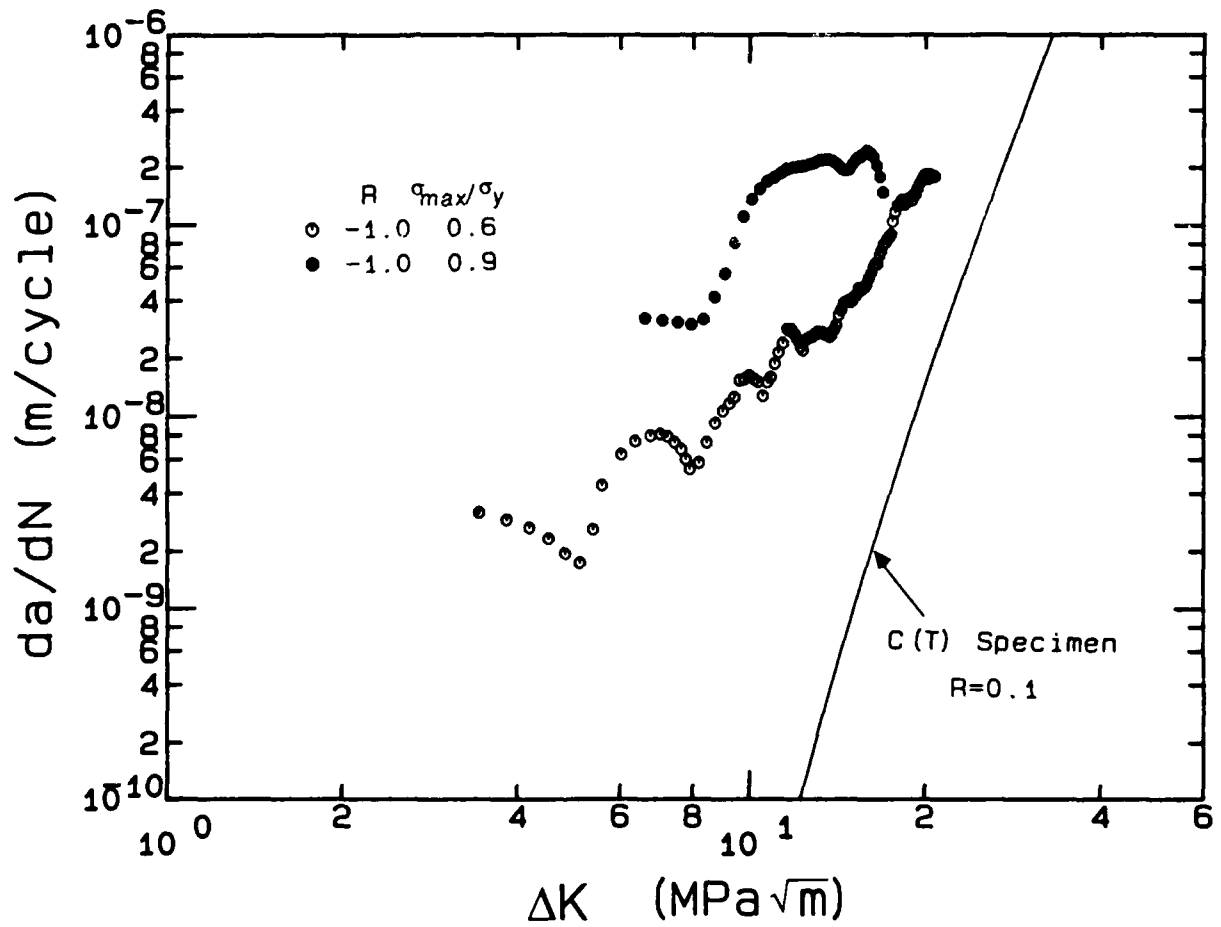


Fig. 4.36 Plot of  $da/dN$ - $\Delta K$  illustrating the effect of stress level on the growth of small cracks in Ti-8Al(s) fatigued at  $R = -1.0$ .

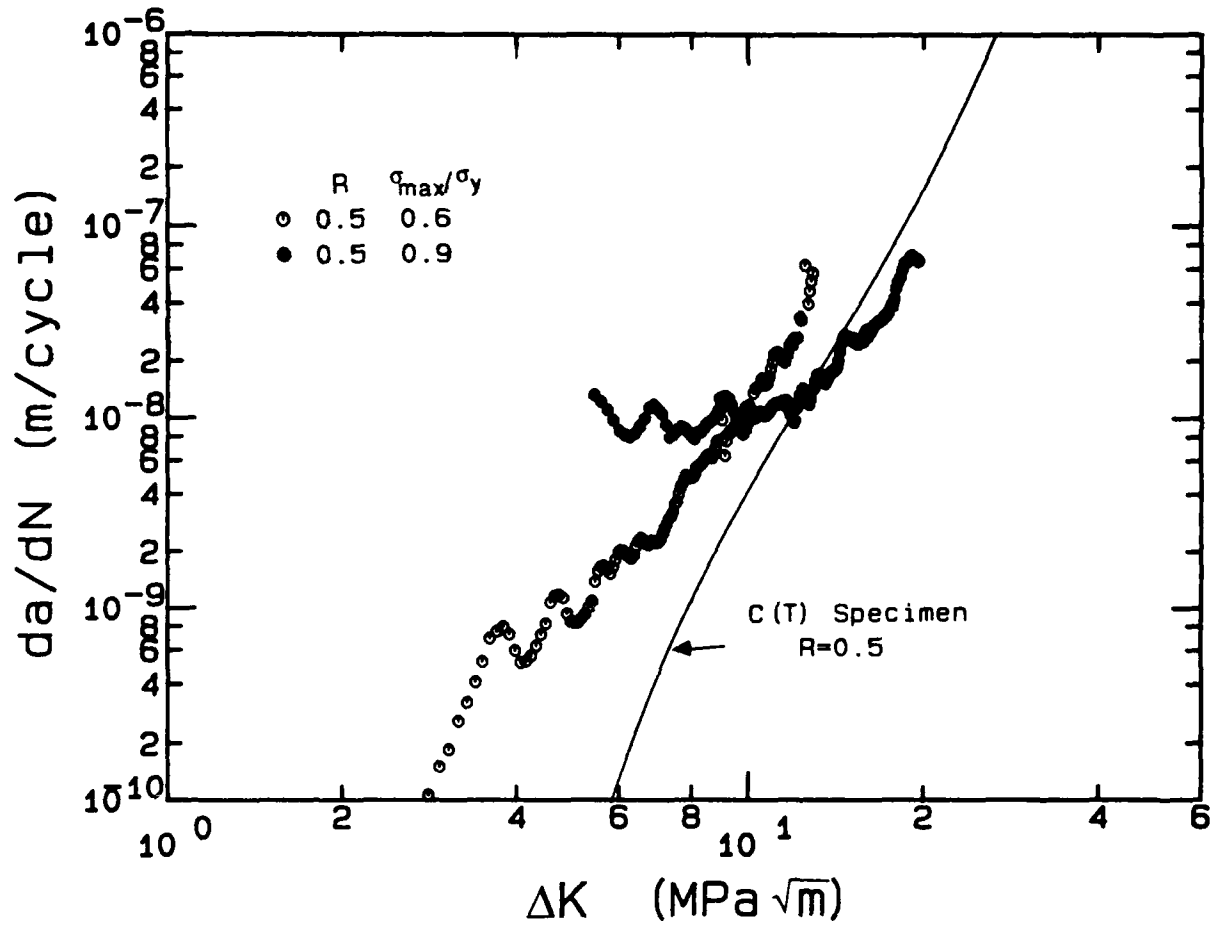


Fig. 4.37 Plot of  $da/dN$ - $\Delta K$  illustrating the effect of stress level on the growth of small cracks in Ti-8Al(s) fatigued at  $R = 0.5$ .

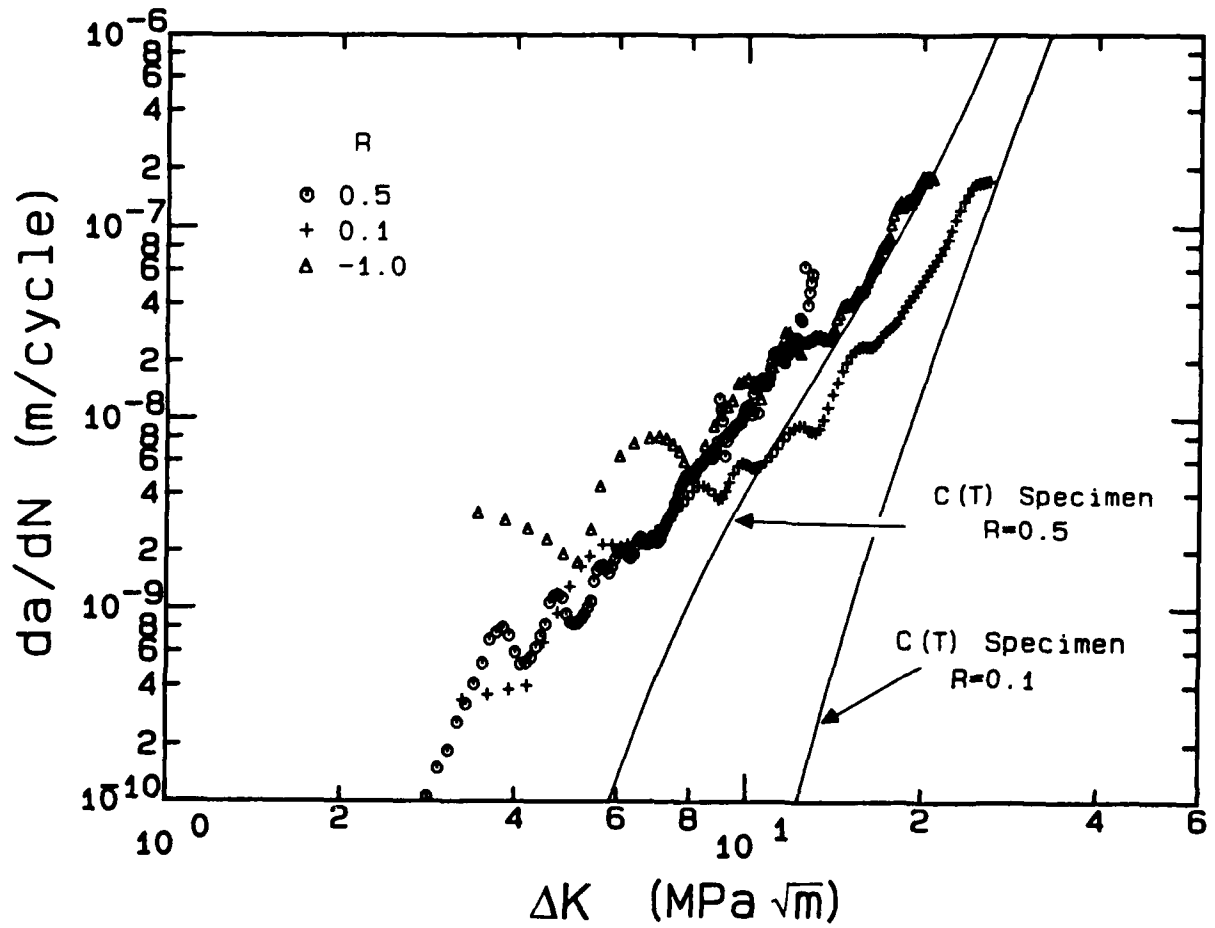


Fig. 4.38 Plot of  $da/dN$ - $\Delta K$  illustrating the effect of stress ratio ( $R$ ) on the growth of small cracks in Ti-8Al(s) tested with  $\sigma_{\max}/\sigma_y = 0.6$ .

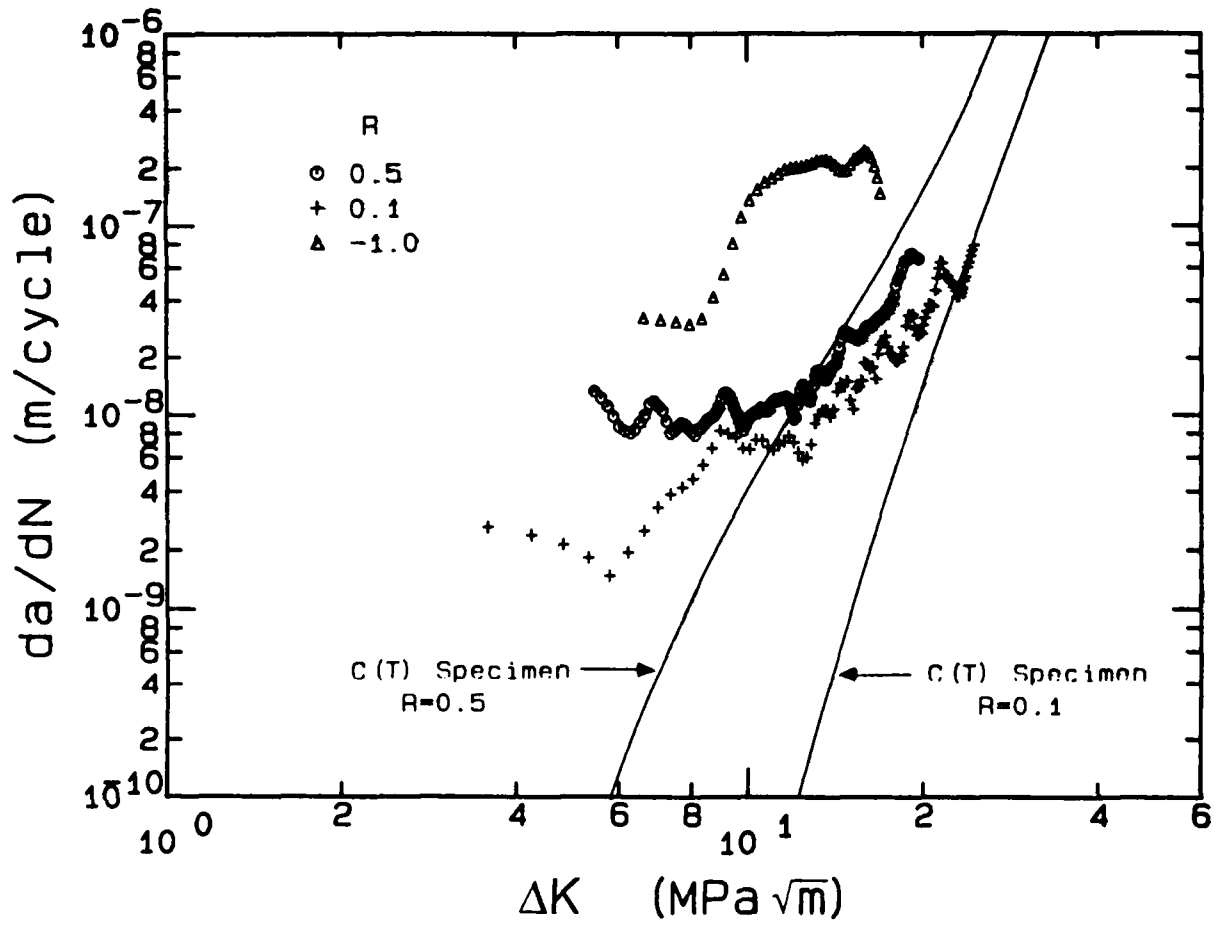


Fig. 4.39 Plot of  $da/dN$ - $\Delta K$  illustrating the effect of stress ratio ( $R$ ) on the growth of small cracks in Ti-8Al(s) tested with  $\sigma_{\max}/\sigma_y = 0.9$ .

small-crack  $da/dN$  tends to decrease as  $R$  goes from 0.5 to 0.1, and increases significantly for  $R = -1.0$ . Consistent with the discussion above, the effect of  $R$  appears to be enhanced at the higher stress level.

#### 4.2.5.4.3 Effect of Alloy Condition (Slip Character)

Small-crack data from each of the three alloy conditions tested under  $R = 0.1$  fatigue are presented in Figs. 4.40 and 4.41 for  $\sigma_{\max}/\sigma_y = 0.6$  and 0.9 respectively. Each of the corresponding C(T) specimen trend lines is also shown. At the lower stress level, Fig. 4.40, the small-crack growth rates in the three materials are quite similar over an appreciable range in  $\Delta K$  and corresponding crack size. The small-crack data are coincident in the lower region of  $\Delta K$  (smallest crack sizes) and begin to separate only after significant crack extension. At the higher stress level, Fig. 4.41, the growth rates in the three materials vary by an order of magnitude at a given  $\Delta K$ , with the growth rates being rank-ordered in correspondence with the large-crack trends. For the smallest cracks, the range in  $da/dN$  for a given  $\Delta K$  is approximately a factor of five, but as the cracks lengthen, they eventually assume the large-crack growth rates. The small cracks clearly do not obey the large-crack  $\Delta K_{th}$ . At  $\Delta K = \Delta K_{th}$  for Ti-8Al(s) large cracks, the small-crack growth rates differ by a factor of ten, while the corresponding difference in large-crack  $da/dN$  is almost three orders of magnitude.

Thus, although the three alloy conditions exhibit widely differing crack growth rates in large-crack specimens, the growth rates of the smallest cracks in the same materials are equivalent at  $\sigma_{\max}/\sigma_y = 0.6$  and only modestly different under fatigue at  $\sigma_{\max}/\sigma_y = 0.9$ . The influence of alloy condition and the associated variation in slip character on fatigue crack propagation is, therefore, strongly crack-size dependent.

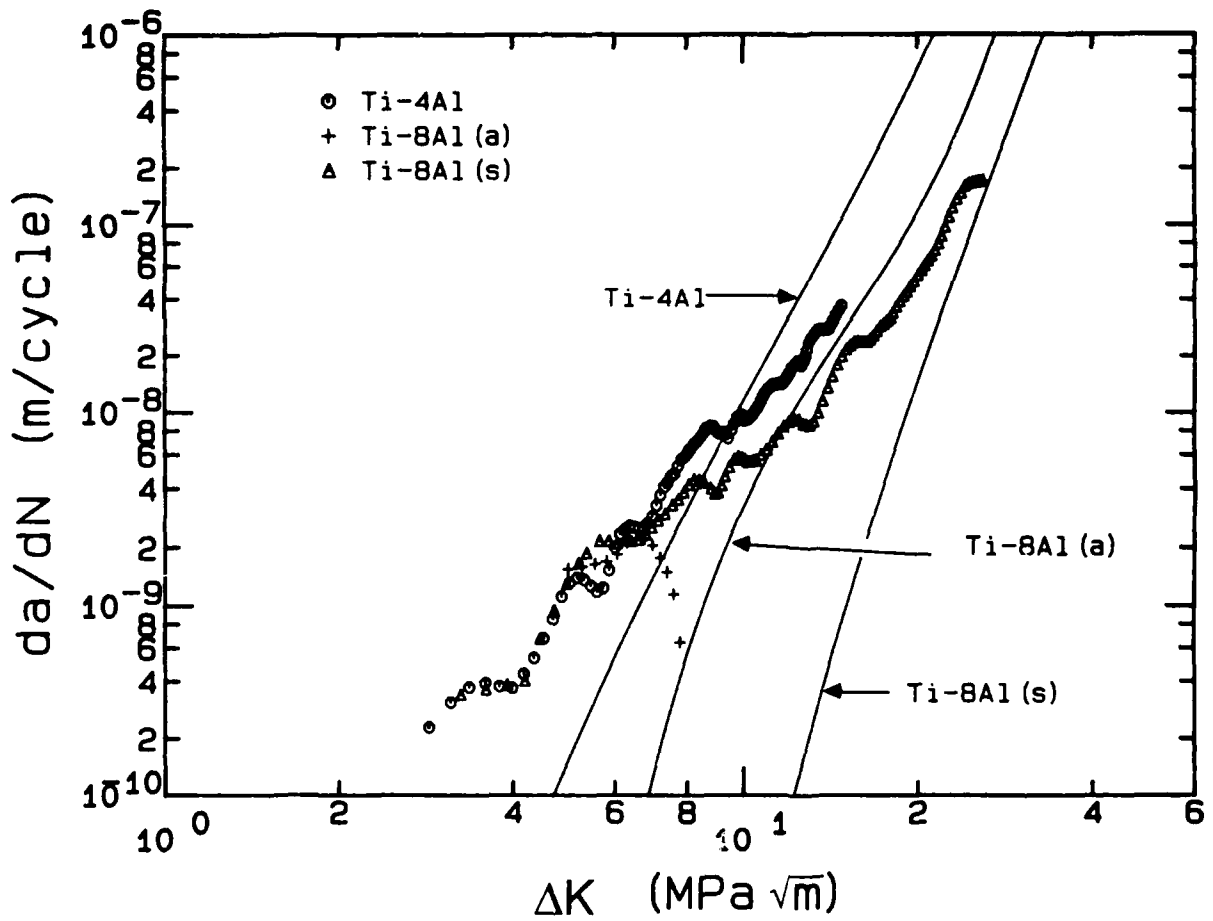


Fig. 4.40 Plot of  $da/dN$ - $\Delta K$  illustrating the effect of alloy condition on the growth of small cracks propagated under  $R = 0.1$  fatigue with  $\sigma_{\max}/\sigma_y = 0.6$ .



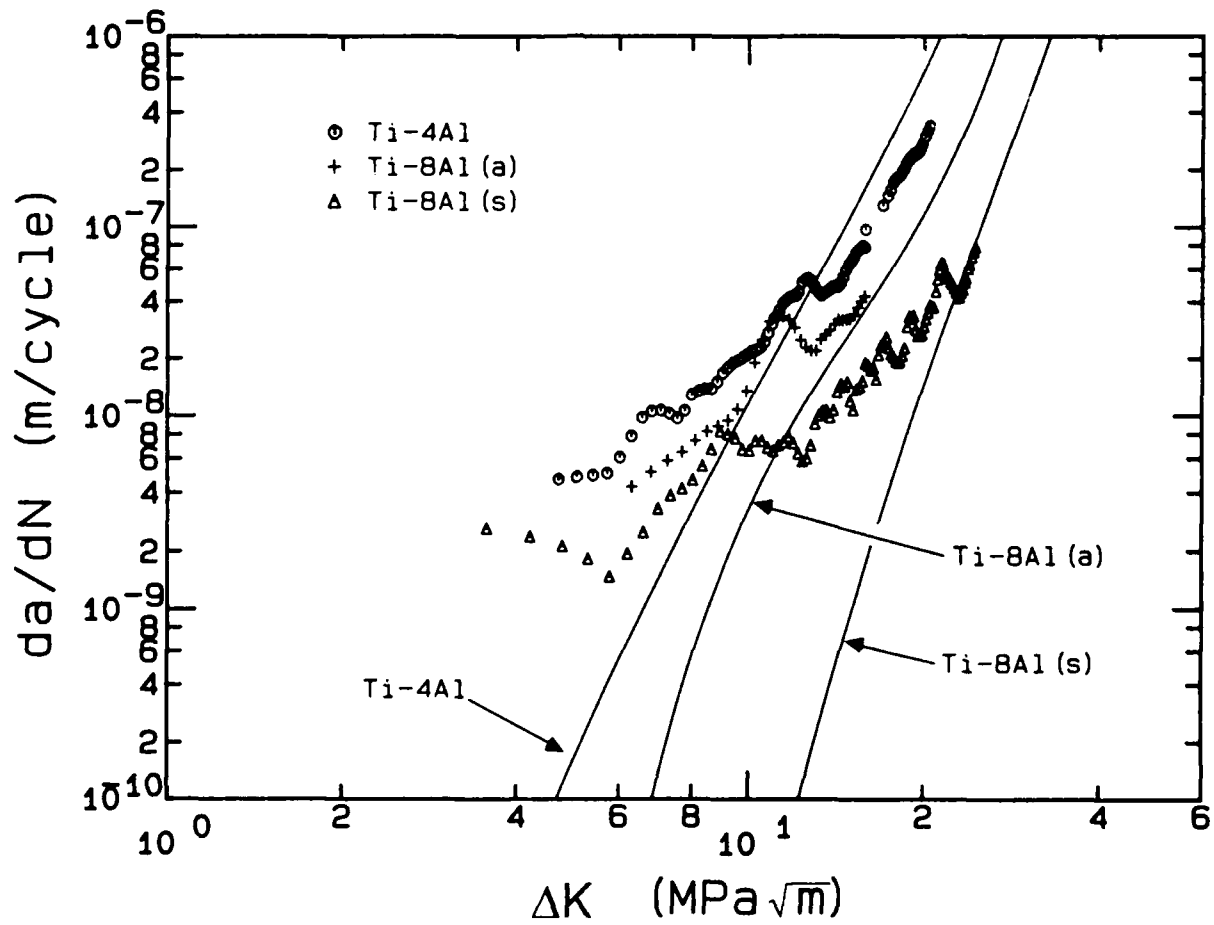


Fig. 4.41 Plot of  $da/dN$ - $\Delta K$  illustrating the effect of alloy condition on the growth of small cracks propagated under  $R = 0.1$  fatigue with  $\sigma_{\max}/\sigma_y = 0.9$ .

#### 4.2.5.5 Measurement of Closure of Small Cracks

Crack closure behavior was monitored throughout the small-crack tests using the interferometric displacement gage. Figures 4.42 through 4.45 present the data plotted in normalized form ( $K_{cl}/K_{max}$  versus  $K_{max}$ ). The first two figures illustrate the effect of alloy condition on the measured closure in small cracks tested at  $R = 0.1$  and having  $\sigma_{max}/\sigma_y = 0.6$  and  $0.9$ , respectively. At the lower stress level,  $K_{cl}/K_{max}$  quickly develops to a value which is approximately equivalent for all three materials and appears to be independent of  $K_{max}$ . For  $\sigma_{max}/\sigma_y = 0.9$ , Fig. 4.43,  $K_{cl}/K_{max}$  increases in an approximately linear fashion with  $K_{max}$  until assuming an approximately constant level. The closure behavior at both stress levels is in striking contrast to the behavior of large cracks shown in Fig. 4.19, where  $K_{cl}/K_{max}$  continually decreased with increasing  $K_{max}$ .

Figures 4.44 and 4.45 illustrate the effect of stress ratio on the small-crack closure in Ti-8Al(s) at  $\sigma_{max}/\sigma_y = 0.6$  and  $0.9$ , respectively. At the lower stress level, the data from both the  $R = -1.0$  and  $0.1$  tests show an increasing normalized closure level, which again stabilizes at an approximately constant value. As expected, the data for  $R = 0.5$  are approximately constant over the entire range of  $K_{max}$ , since the minimum possible closure level for these data is limited by  $K_{min}$ . As shown in Fig. 4.45, the small-crack closure behavior at  $\sigma_{max}/\sigma_y = 0.9$  is qualitatively similar to that observed at the lower stress level, with the exception of the  $R = -1.0$  test. Under the fully reversed loading, crack closure decreases initially and stabilizes at an approximately constant, negative value. The behavior is essentially the reverse of the trend found for  $\sigma_{max}/\sigma_y = 0.6$ .

The small-crack closure data are replotted in absolute terms ( $K_{cl}$  versus  $K_{max}$ ) in Figs. 4.46 through 4.49. In contrast to the uniform levels of crack closure observed in

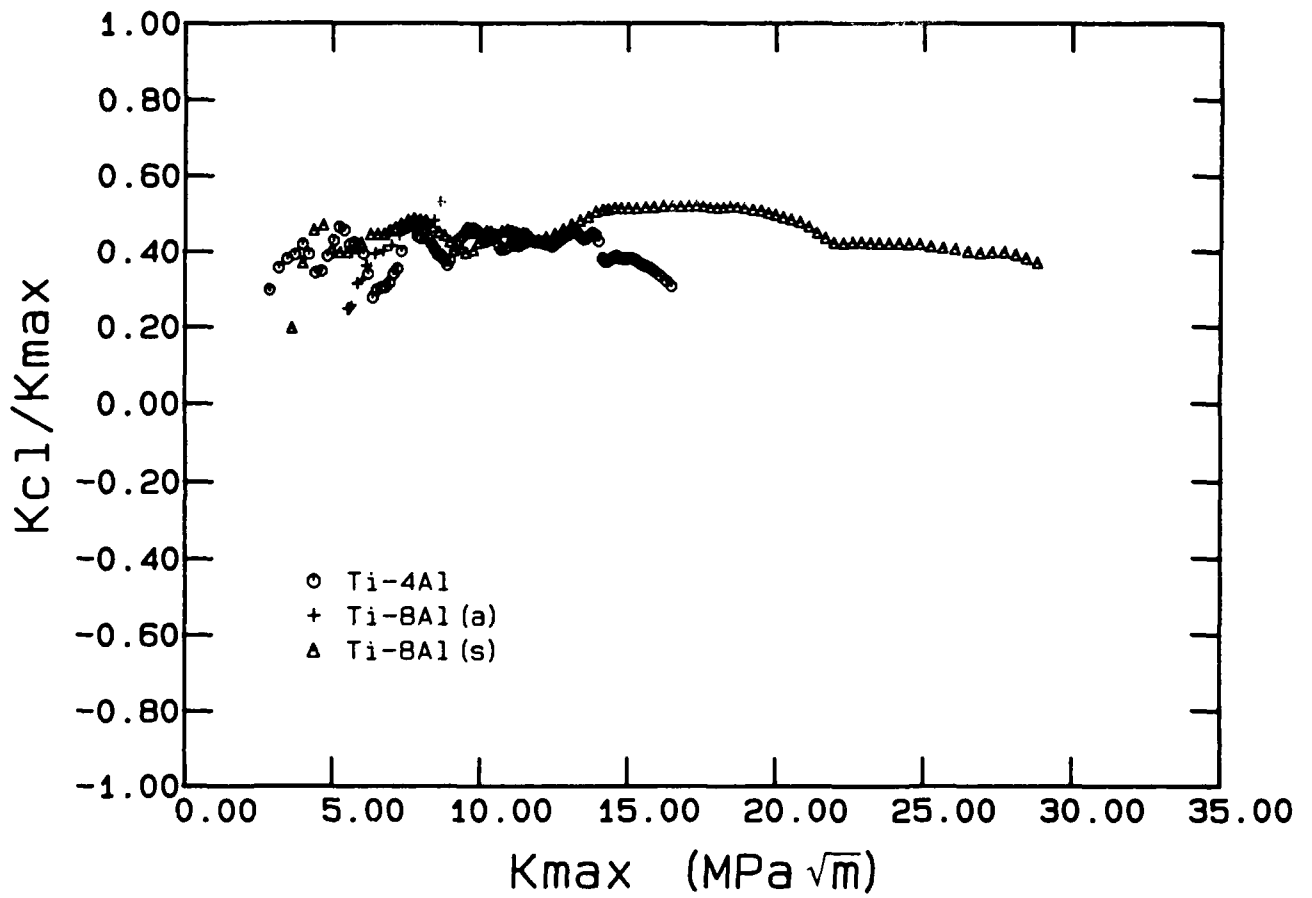


Fig. 4.42 Normalized small-crack closure behavior observed in each of the three alloy conditions tested under  $R = 0.1$  fatigue ( $\sigma_{max}/\sigma_y = 0.6$ ).

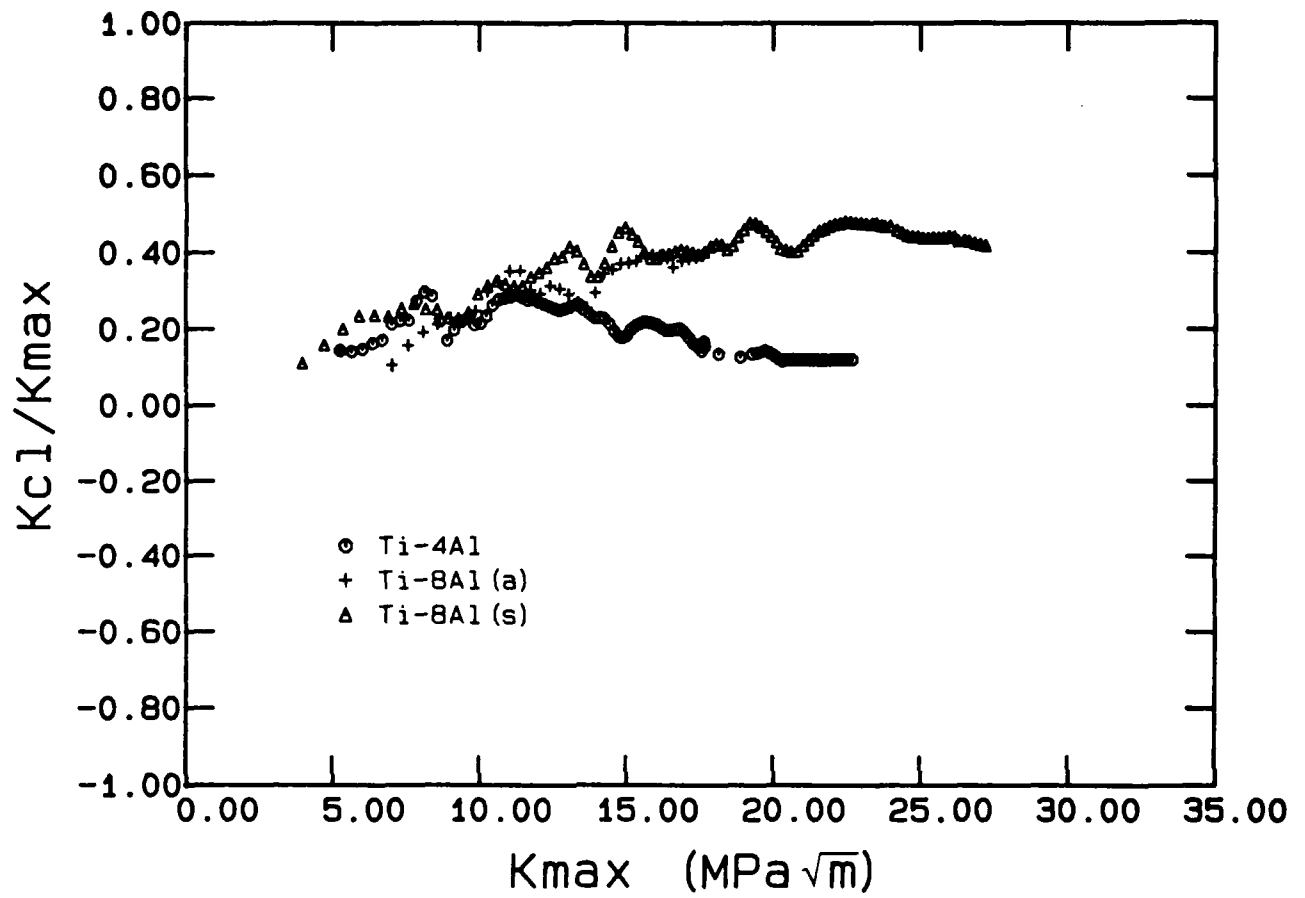


Fig. 4.43 Normalized small-crack closure behavior observed in each of the three alloy conditions tested under  $R = 0.1$  fatigue ( $\sigma_{max}/\sigma_y = 0.9$ ).

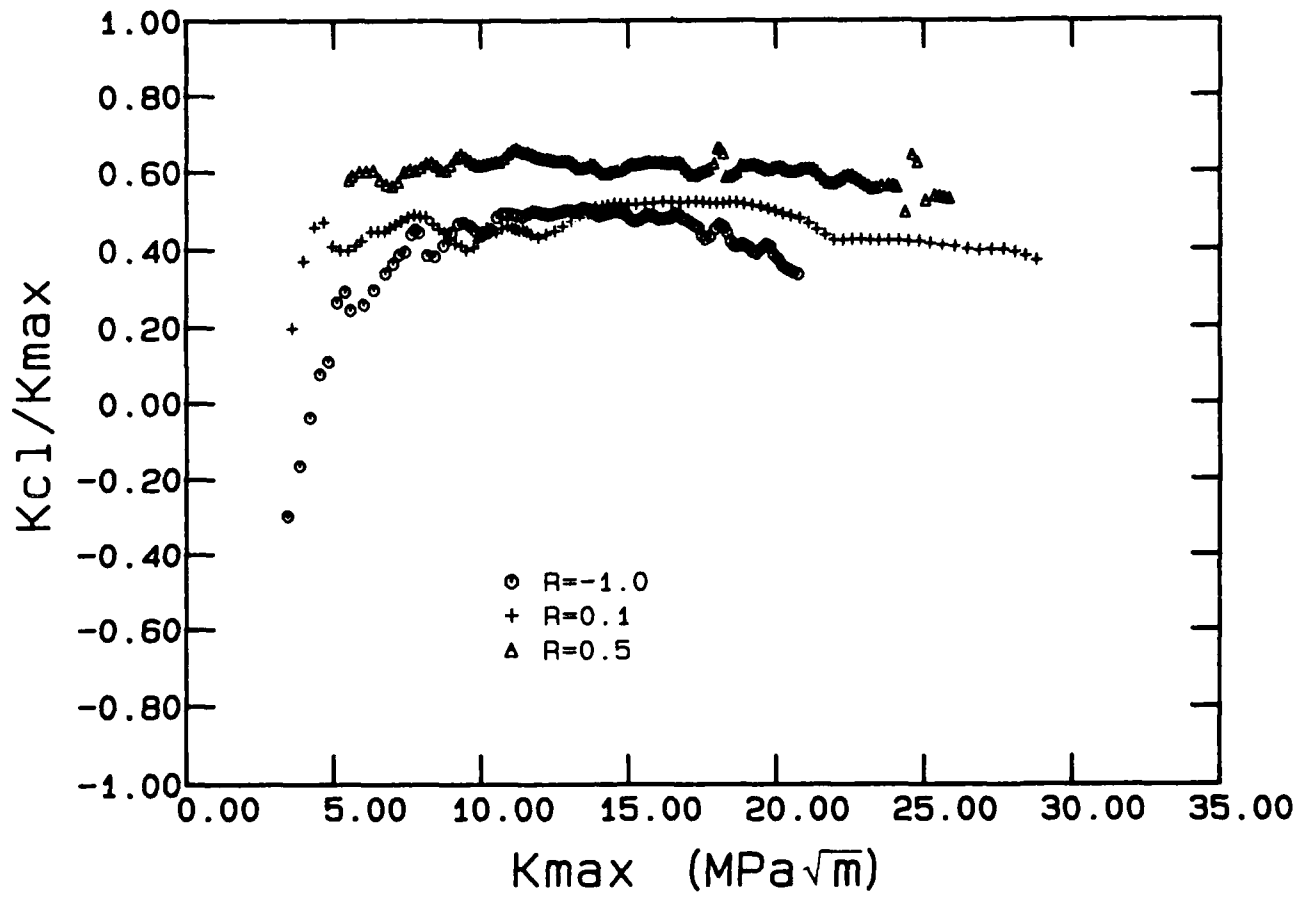


Fig. 4.44 The effect of stress ratio on normalized small-crack closure behavior in Ti-8Al(s) ( $\sigma_{max}/\sigma_y = 0.6$ ).

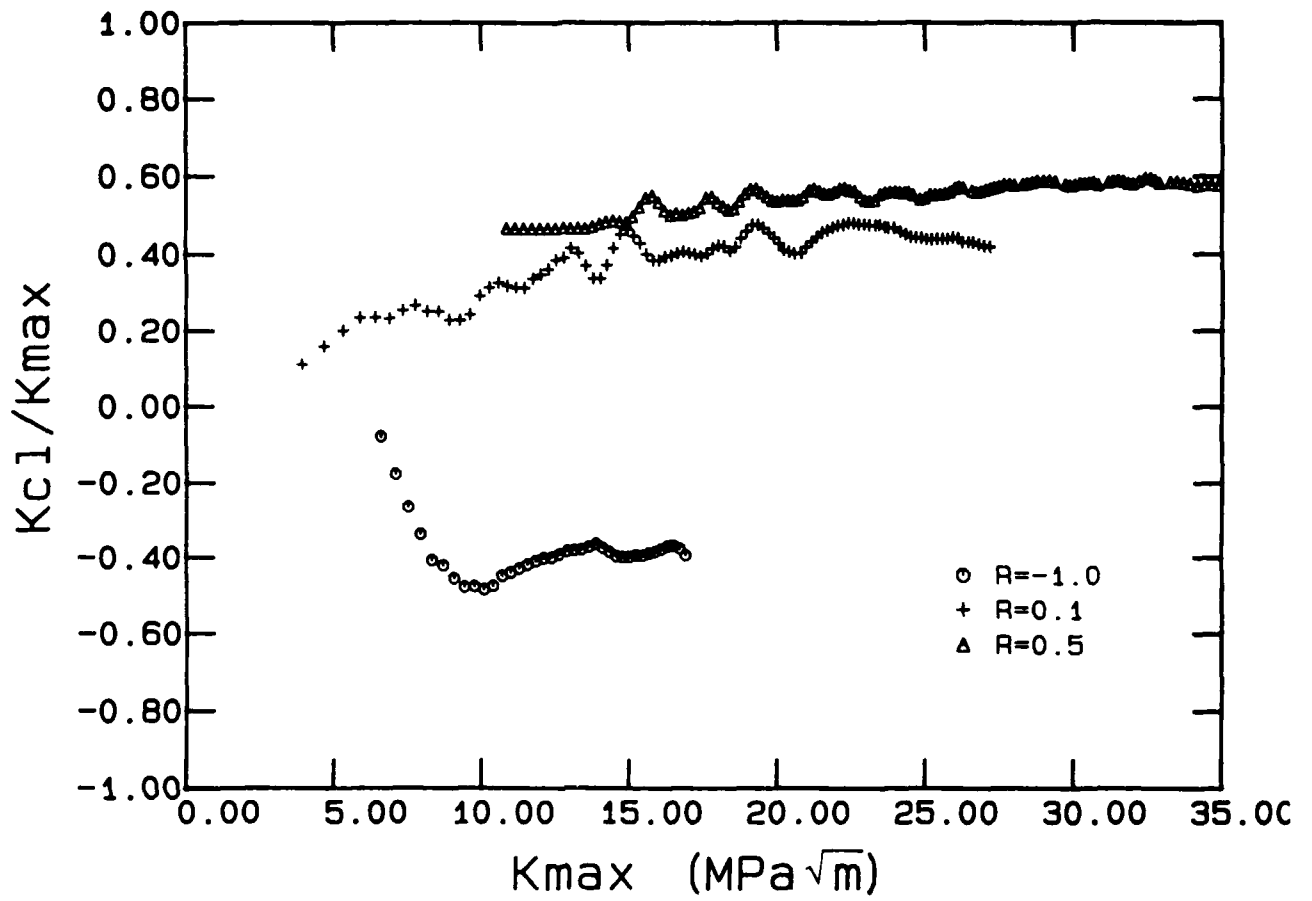


Fig. 4.45 The effect of stress ratio on normalized small-crack closure behavior in Ti-8Al(s) ( $\sigma_{max}/\sigma_y = 0.9$ ).

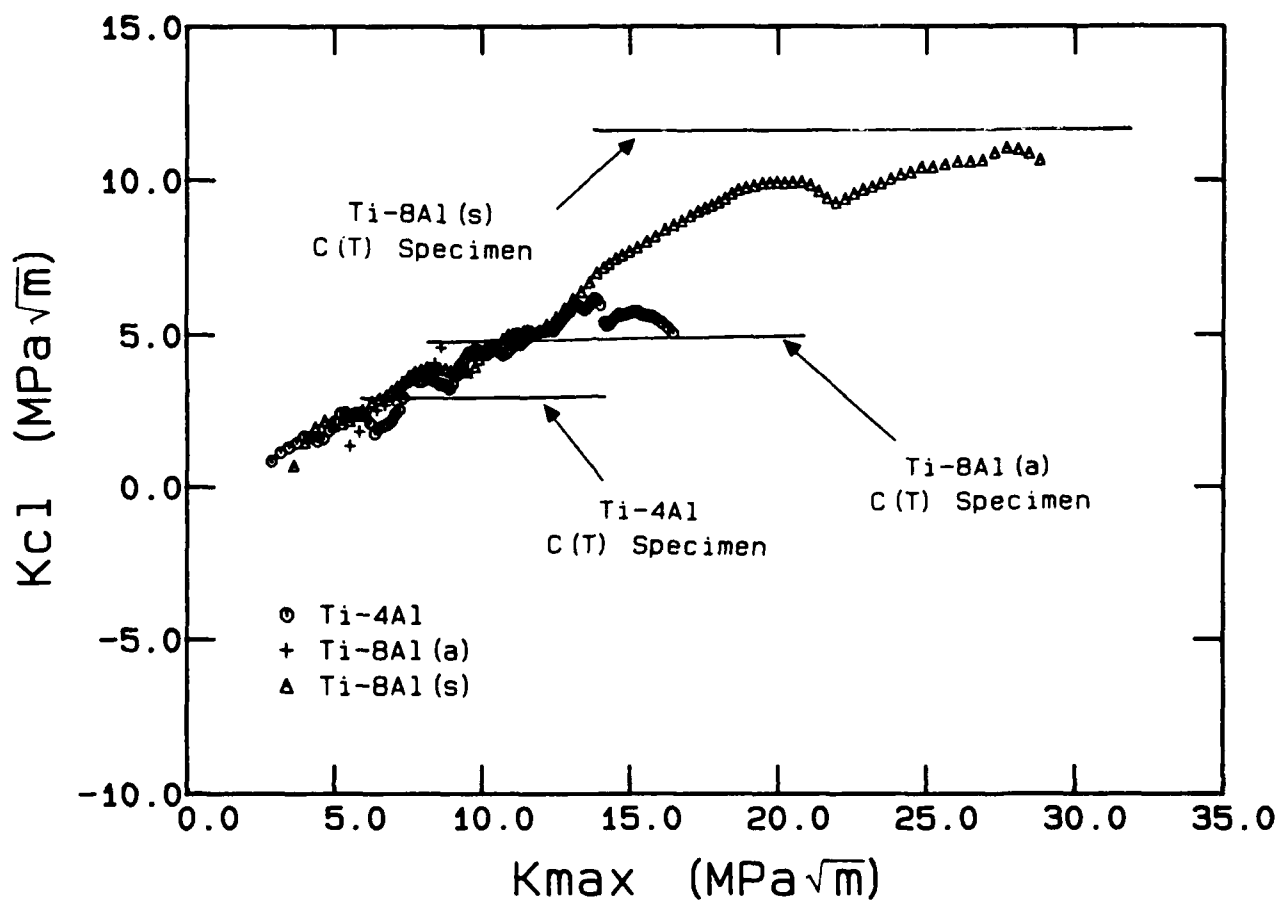


Fig. 4.46 Absolute small-crack closure behavior observed in each of the three alloy conditions tested under  $R = 0.1$  fatigue ( $\sigma_{max}/\sigma_y = 0.6$ ).

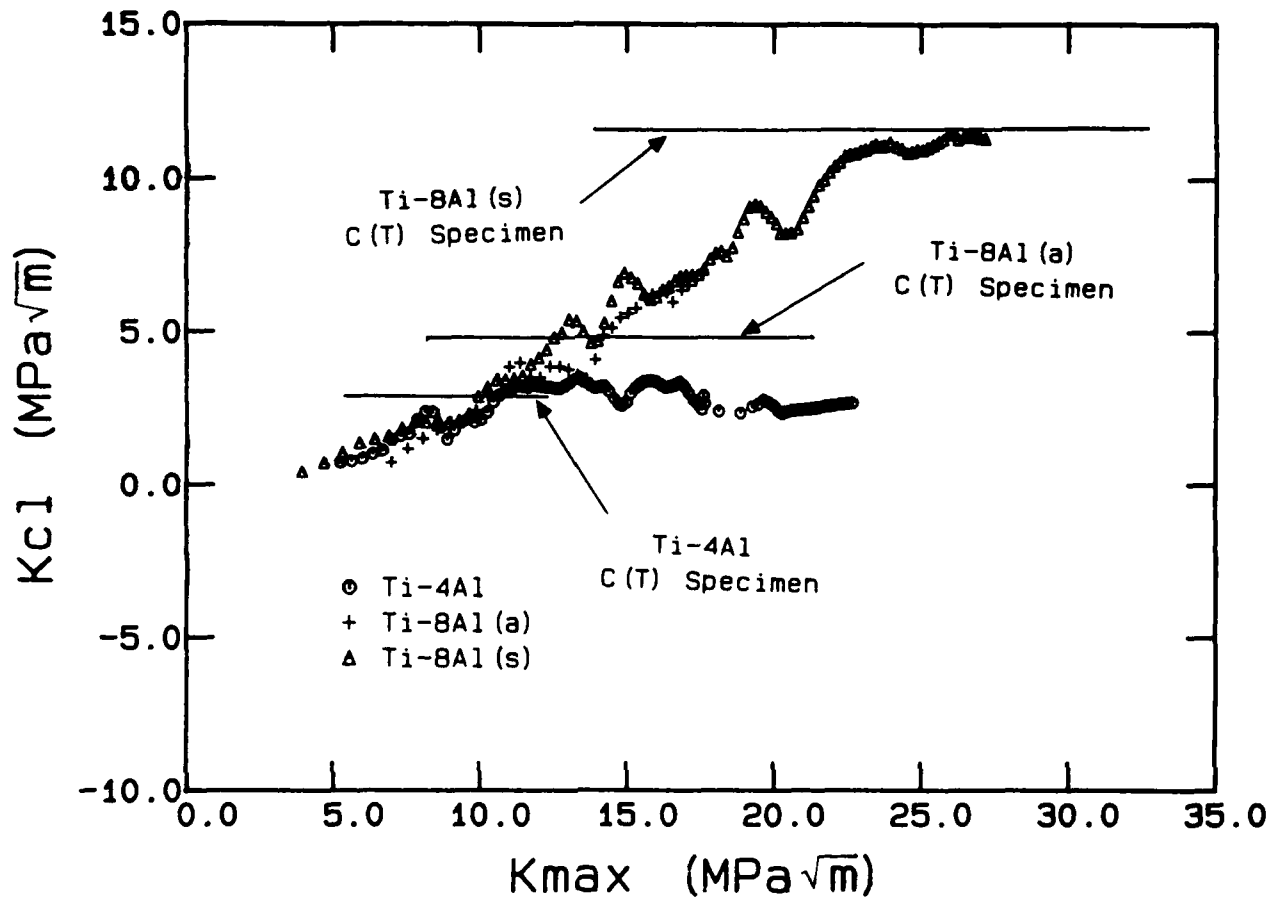


Fig. 4.47 Absolute small-crack closure behavior observed in each of the three alloy conditions tested under  $R = 0.1$  fatigue ( $\sigma_{max}/\sigma_y = 0.9$ ).



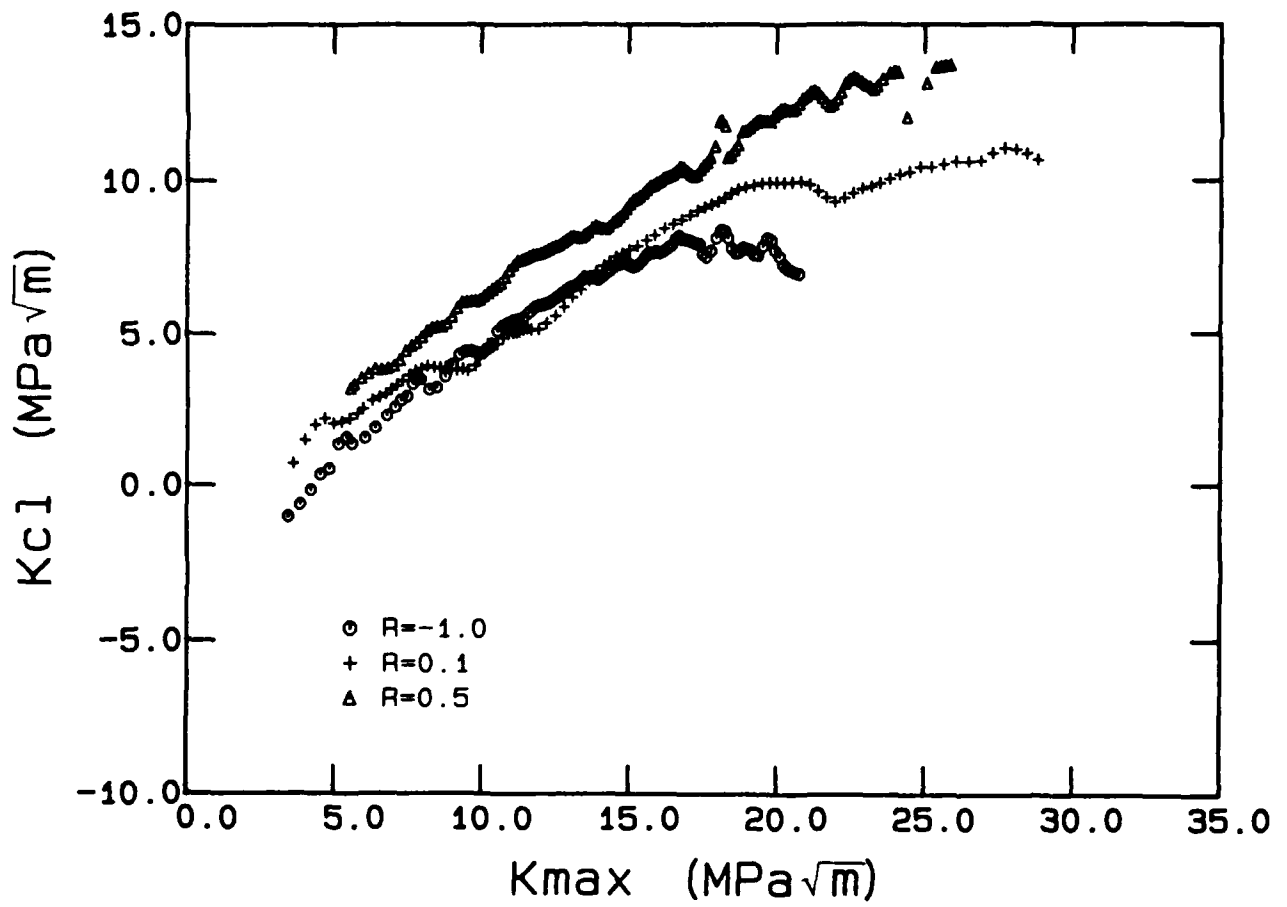


Fig. 4.48 The effect of stress ratio on absolute small-crack closure behavior in Ti-8Al(s) ( $\sigma_{max}/\sigma_y = 0.6$ ).

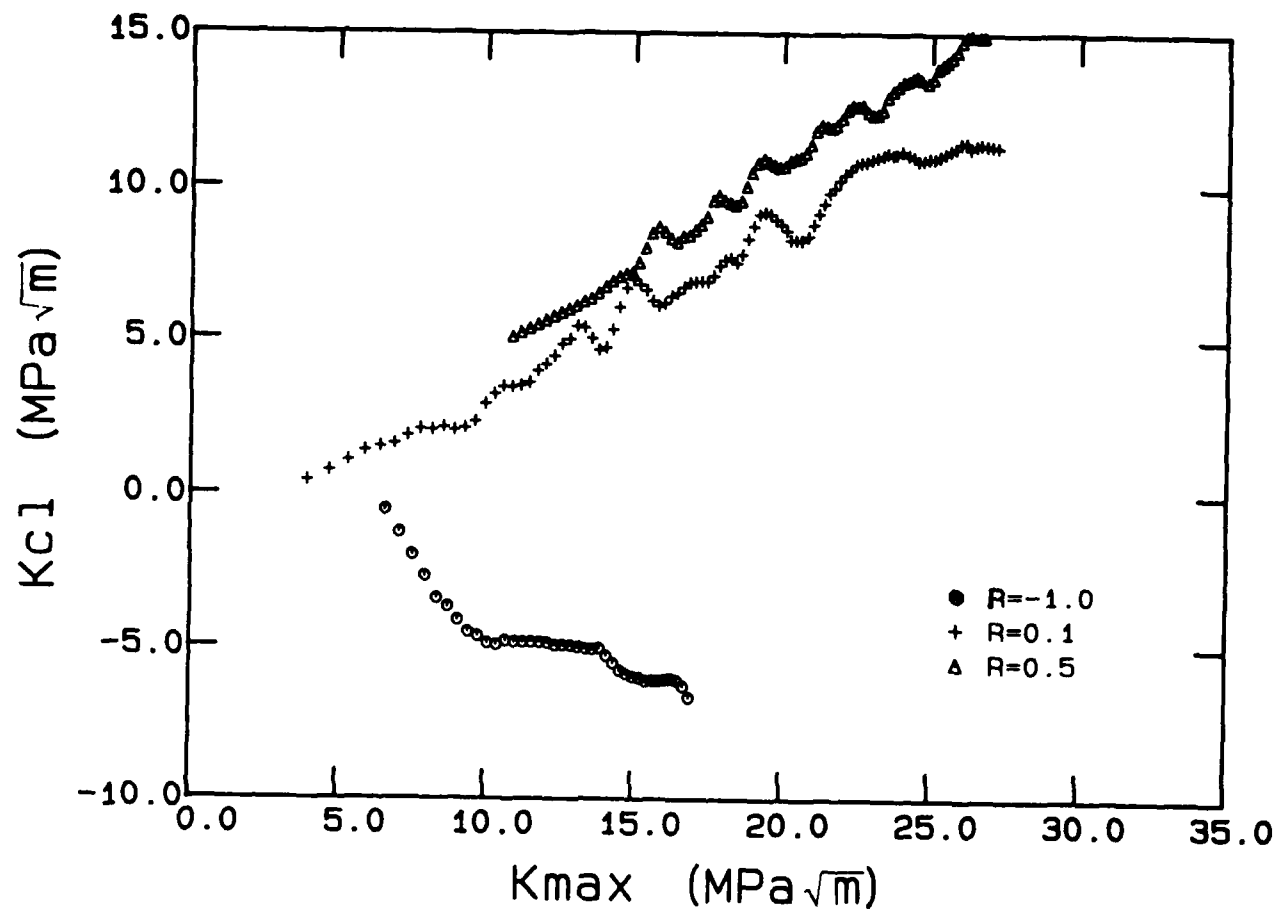


Fig. 4.49 The effect of stress ratio on absolute small-crack closure behavior in Ti-8Al(s) ( $\sigma_{max}/\sigma_y = 0.9$ ).

tests of large cracks, the small-crack closure levels display a clear dependence on crack length. As shown in Figs. 4.46 and 4.47 ( $\sigma_{\max}/\sigma_y = 0.6$  and  $0.9$ , respectively), plotting the data in this fashion results in the consolidation of the data from all three alloy conditions at the lower stress intensities (shorter crack lengths). For the small cracks that attained sufficient length, the measured value of  $K_{Cl}$  eventually became approximately independent of  $K_{\max}$ , consistent with the behavior observed in the large through cracks in C(T) specimens. Thus it appears that crack closure in the three materials developed at a nearly equivalent rate, while the maximum  $K_{Cl}$  that developed was strongly material dependent. Since the rate of development of crack closure was independent of material, while the maximum closure level that was achieved was material dependent, the crack length over which closure developed was also material dependent and was proportional to the maximum, or large-crack, closure level. Thus, crack closure developed relatively quickly in the Ti-4Al, while the Ti-8Al(s) required the greatest crack extension in order to achieve the approximate large-crack closure level.

The effect of stress ratio on the development of small-crack closure in Ti-8Al(s) is illustrated in Figs. 4.48 and 4.49 for  $\sigma_{\max}/\sigma_y = 0.6$  and  $0.9$ , respectively. At the lower stress level, crack closure develops equivalently for  $R = -1.0$  and  $R = 0.1$ , while the data for  $R = 0.5$  shows a slightly higher closure level over the same range in  $K_{\max}$ . With the exception of the  $R = -1.0$  condition, the data at the higher stress, Fig. 4.49, are essentially equivalent to the  $\sigma_{\max}/\sigma_y = 0.6$  data shown in Fig. 4.48. At both stress levels the  $R = 0.5$  data lie slightly above the  $R = 0.1$  data. Although the indicated closure level for the  $R = 0.5$  tests cannot fall below  $0.5K_{\max}$ , many of the measurements show closure to be greater than this minimum value.

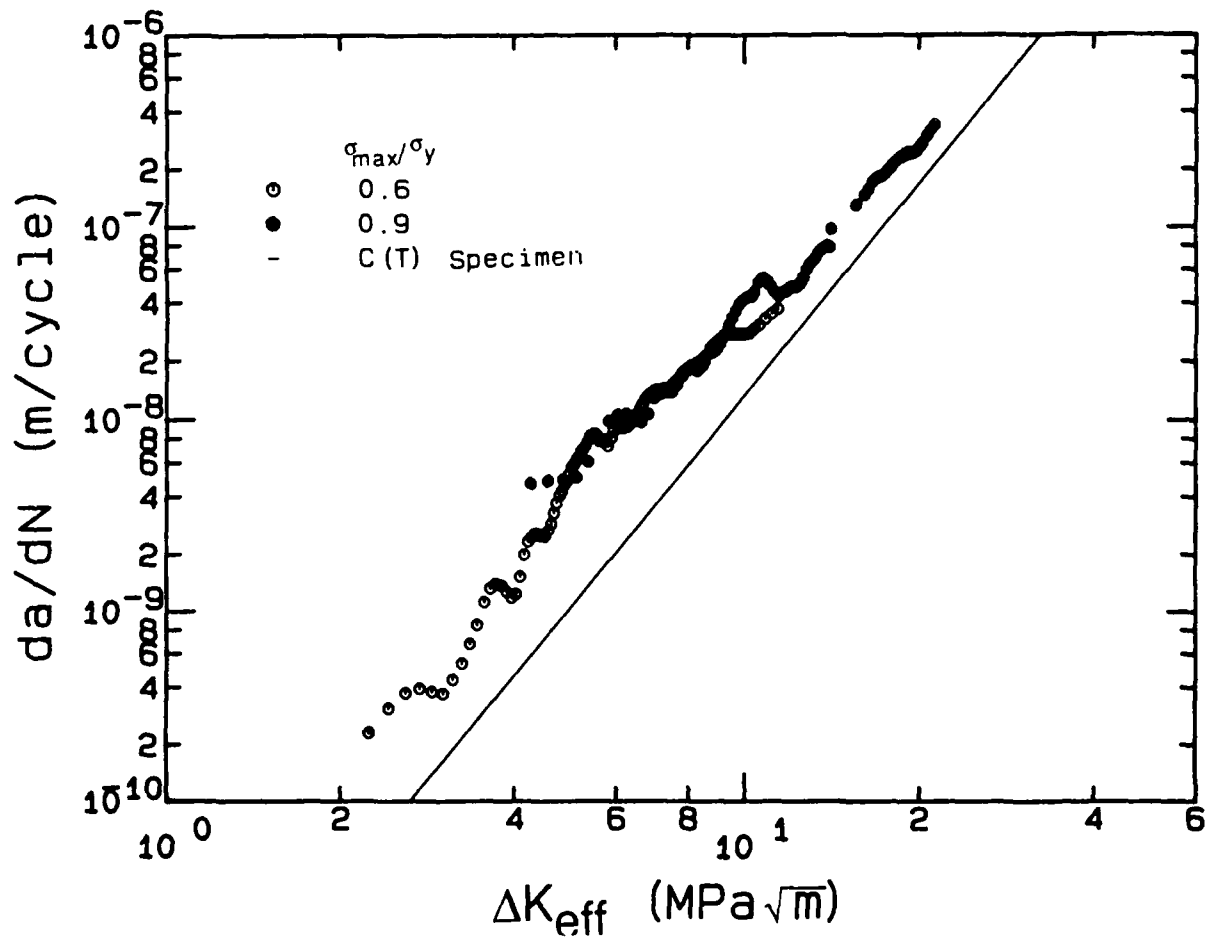
#### 4.2.5.6 The Utility of $\Delta K_{eff}$

The measured closure loads were used to compute  $\Delta K_{eff}$  for each of the small-crack tests. In correspondence with the earlier plots of  $da/dN$  versus  $\Delta K$  (Figs. 4.33 through 4.41), the  $da/dN$  versus  $\Delta K_{eff}$  data are presented in Figs 4.50 through 4.58. Each of the plots also includes a solid line that represents the appropriate  $da/dN$ - $\Delta K_{eff}$ , C(T)-specimen data.

##### 4.2.5.6.1 Effect of Stress Level

Figures 4.50 through 4.52 plot the  $R = 0.1$  small-crack data from each of the three alloy conditions tested at the two stress levels ( $\sigma_{max}/\sigma_y = 0.6$  and  $0.9$ ). For each of the materials, the effect of stress level on the growth of small cracks is essentially eliminated when the data are plotted against  $\Delta K_{eff}$ . Although as shown in Fig. 4.50, the Ti-4Al small-crack data fall slightly above the corresponding large-crack line (independent of crack size), the agreement between the large- and small-crack data is greatly improved over the corresponding  $da/dN$ - $\Delta K$  plot. The improvement in correlation offered by  $\Delta K_{eff}$  is even more dramatic in the Ti-8Al(s) shown in Fig. 4.52. These small-crack data previously lay approximately two orders of magnitude above the large-crack curve.

The use of  $\Delta K_{eff}$  as a correlating parameter also greatly reduces the apparent effect of stress level on the growth of small cracks in Ti-8Al(s) tested at  $R = -1.0$  and  $0.5$ . In comparison with Fig. 4.36, where large- and small-crack growth rates differed by two to three orders of magnitude when plotted versus  $\Delta K$ , plotting the data against  $\Delta K_{eff}$  reduces this difference to a factor of ten or less, as shown in Fig. 4.53. The most dramatic improvement in the consolidation of the data is for the  $R = -1.0$ ,  $\sigma_{max}/\sigma_y = 0.9$  test. At this condition, when plotted versus  $\Delta K$ , the small- and large-crack  $da/dN$  data differed by



F 4.50 Plot of  $da/dN$ - $\Delta K_{eff}$  illustrating the effect of stress level on the growth of small cracks in Ti-4Al fatigued at  $R = 0.1$ .

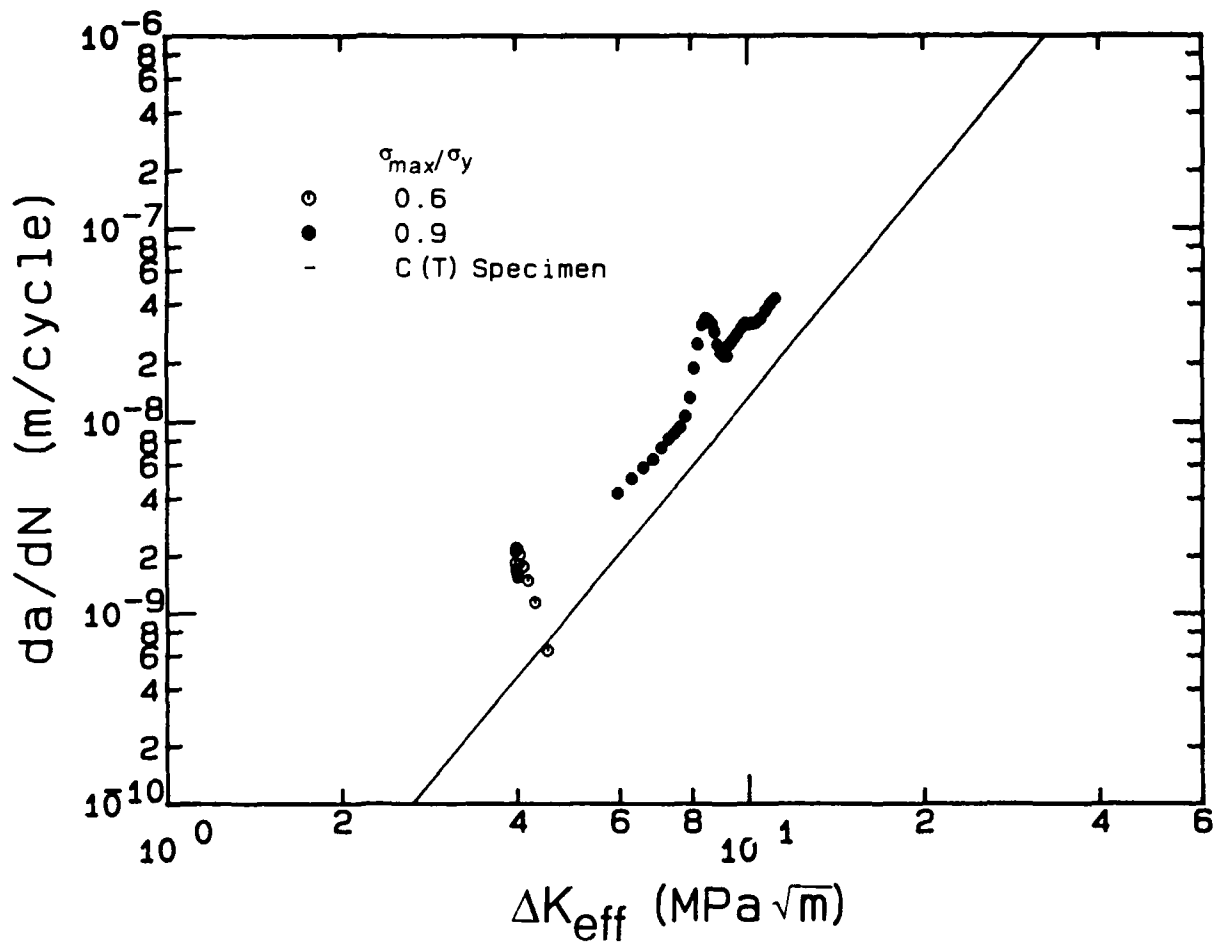


Fig. 4.51 Plot of  $da/dN$ - $\Delta K_{eff}$  illustrating the effect of stress level on the growth of small cracks in Ti-8Al(a) fatigued at  $R = 0.1$ .

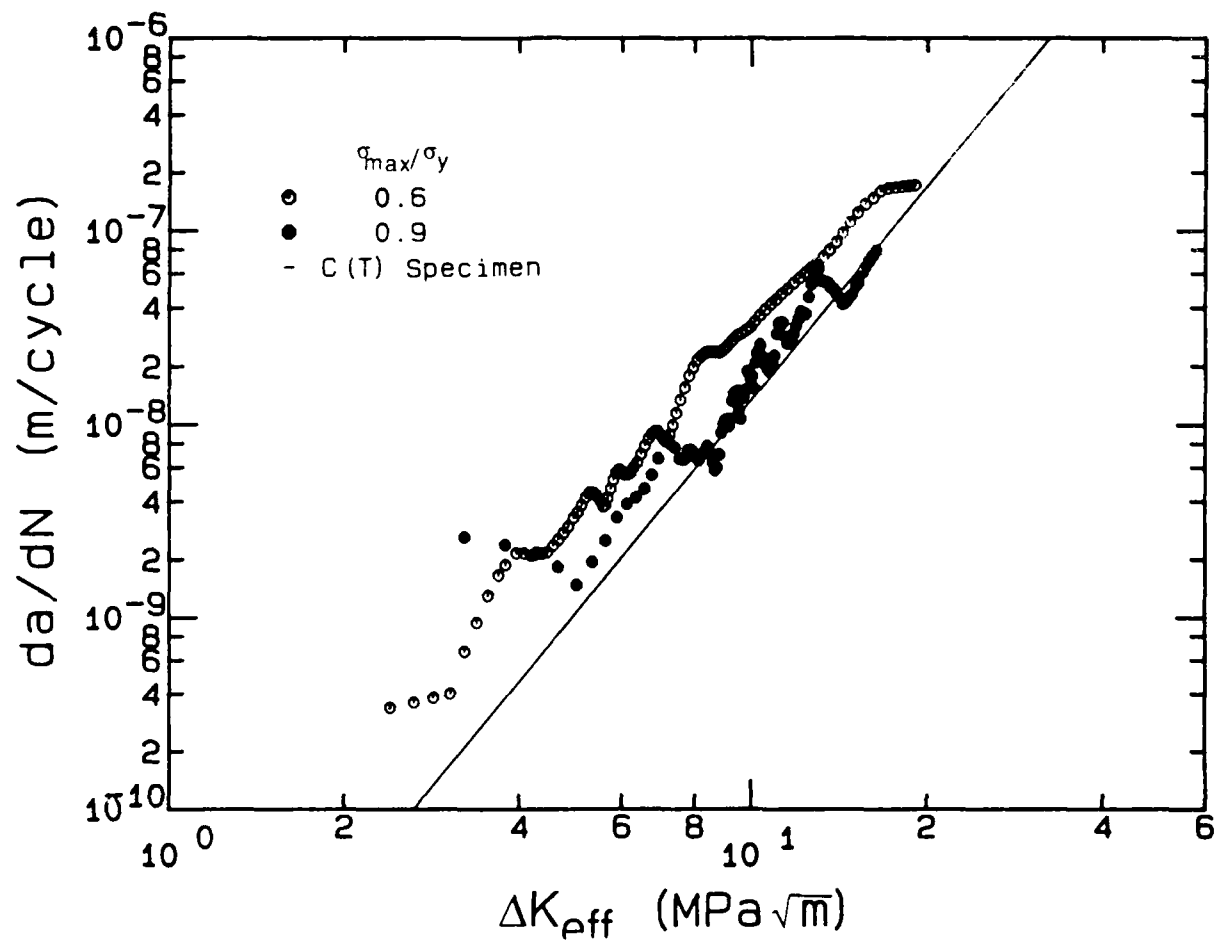


Fig. 4.52 Plot of  $da/dN$ - $\Delta K_{eff}$  illustrating the effect of stress level on the growth of small cracks in Ti-8Al(s) fatigued at  $R = 0.1$ .

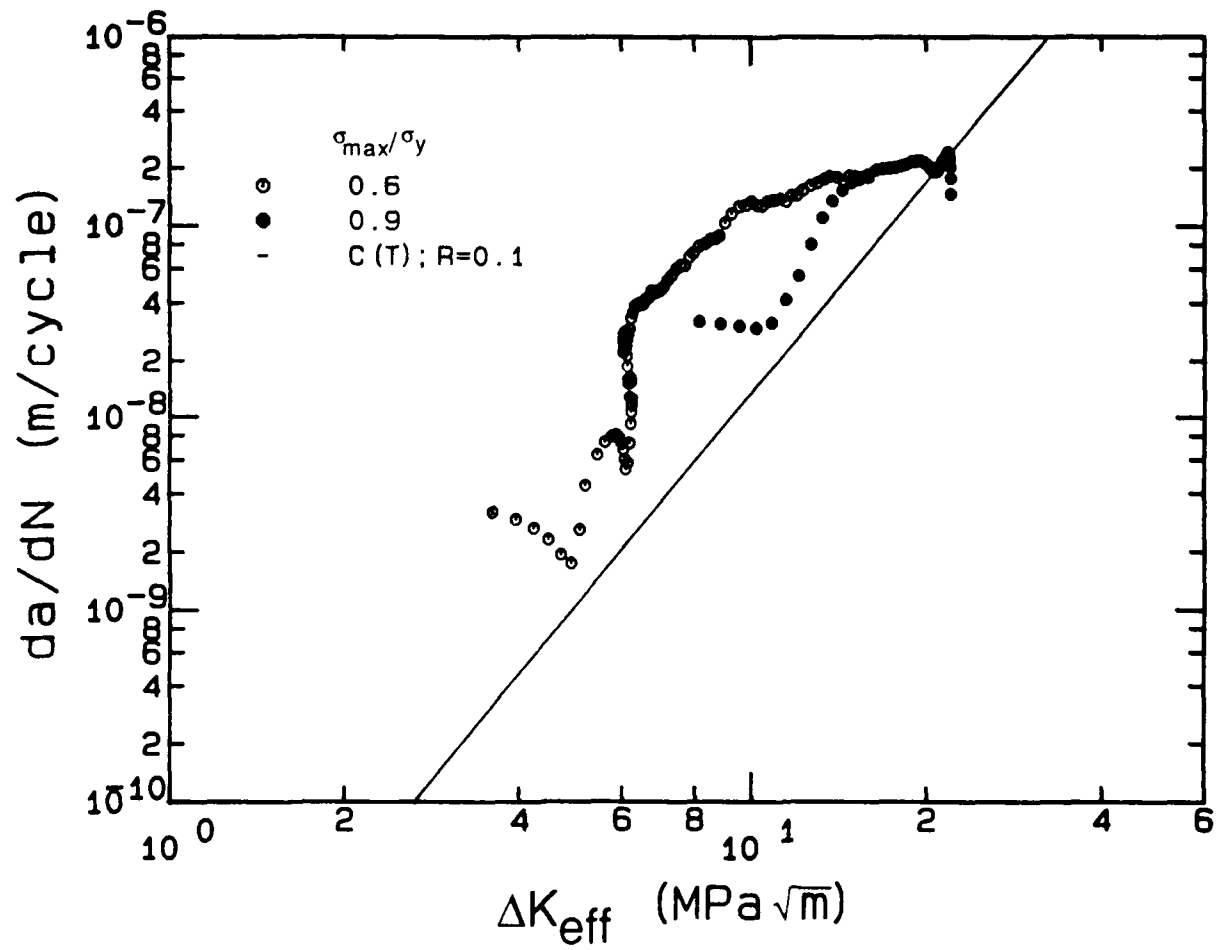


Fig. 4.53 Plot of  $da/dN$ - $\Delta K_{eff}$  illustrating the effect of stress level on the growth of small cracks in Ti-8Al(s) fatigued at  $R = -1.0$ .



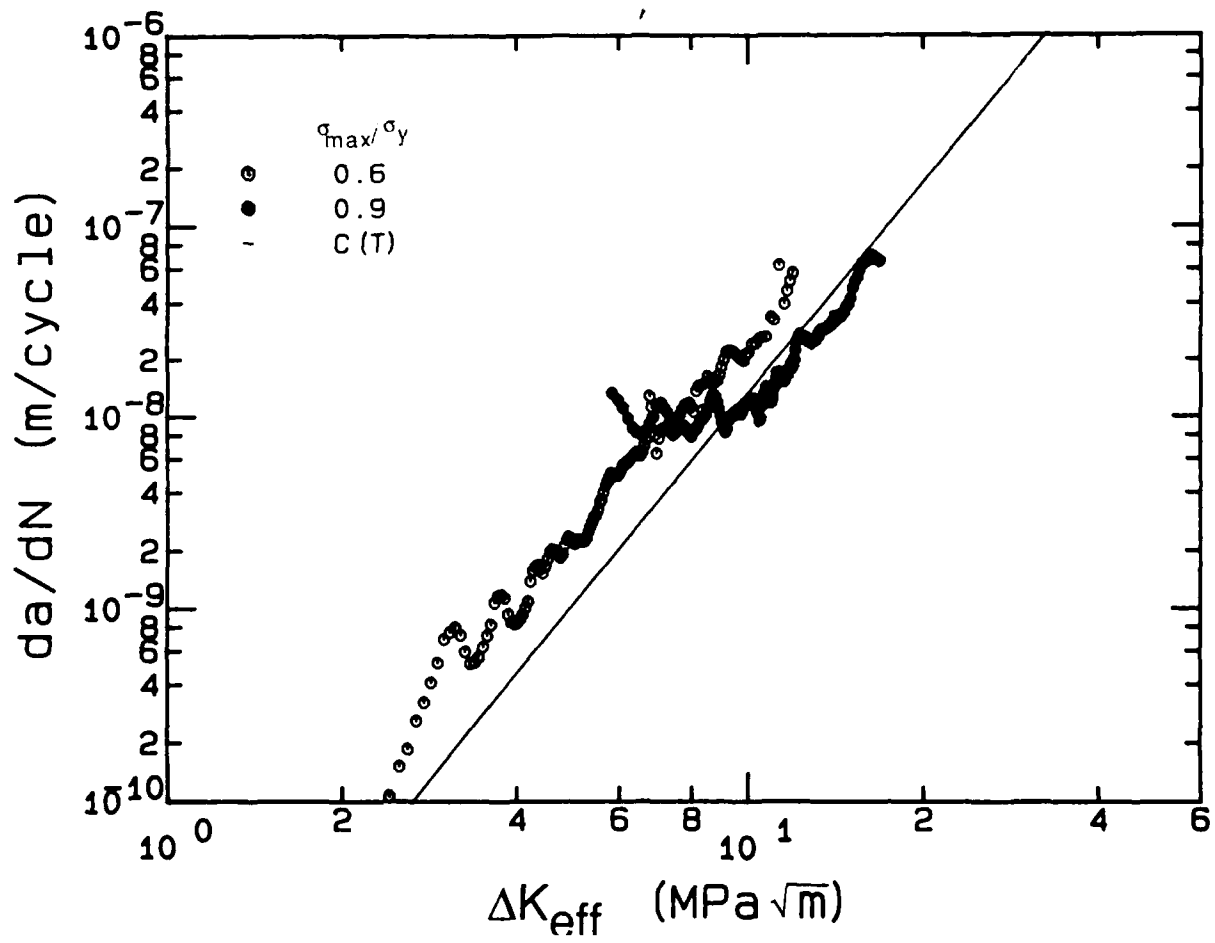


Fig. 4.54 Plot of  $da/dN$ - $\Delta K_{eff}$  illustrating the effect of stress level on the growth of small cracks in Ti-8Al(s) fatigued at  $R = 0.5$ .

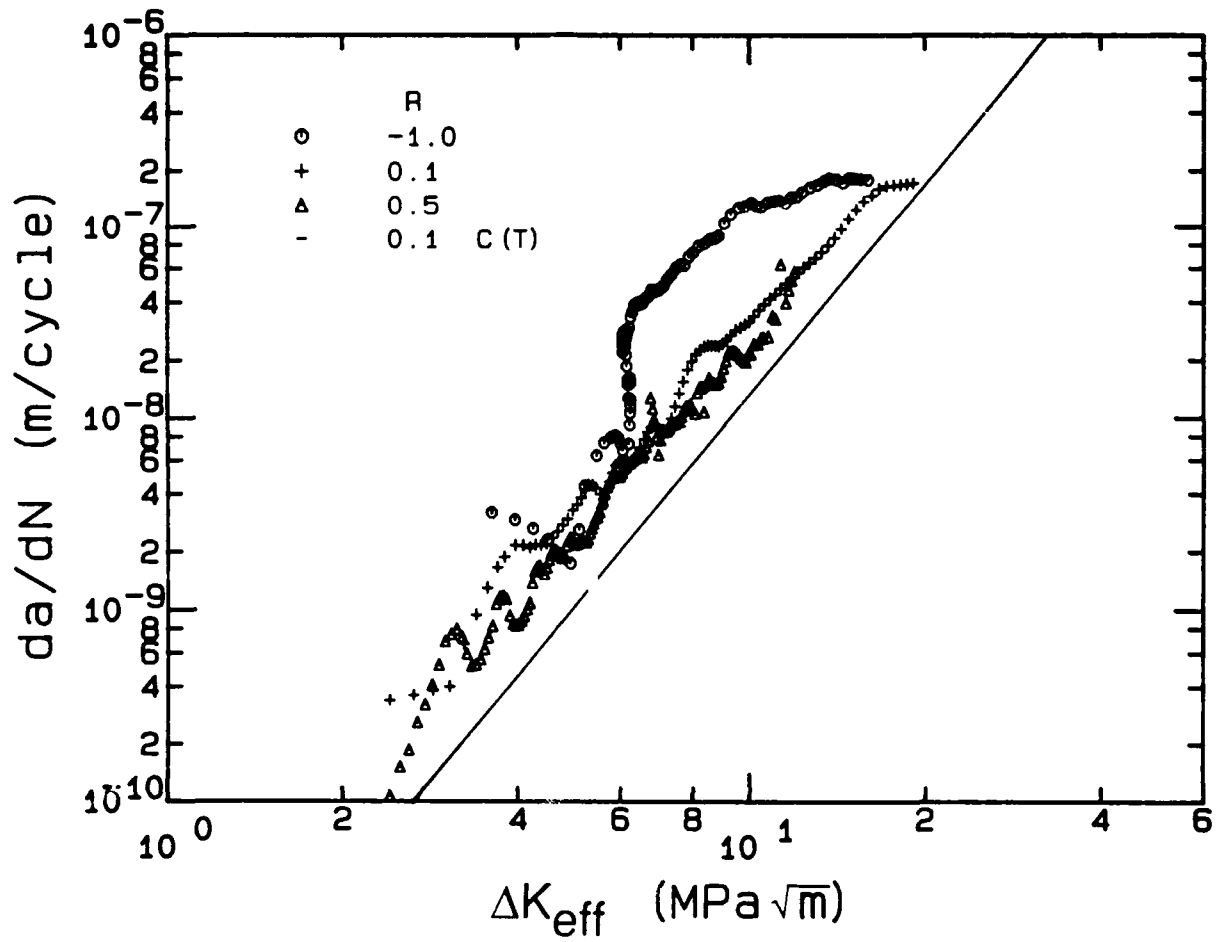


Fig. 4.55 Plot of  $da/dN$ - $\Delta K_{eff}$  illustrating the effect of stress ratio ( $R$ ) on the growth of small cracks in Ti-8Al(s) tested with  $\sigma_{max}/\sigma_y = 0.6$ .

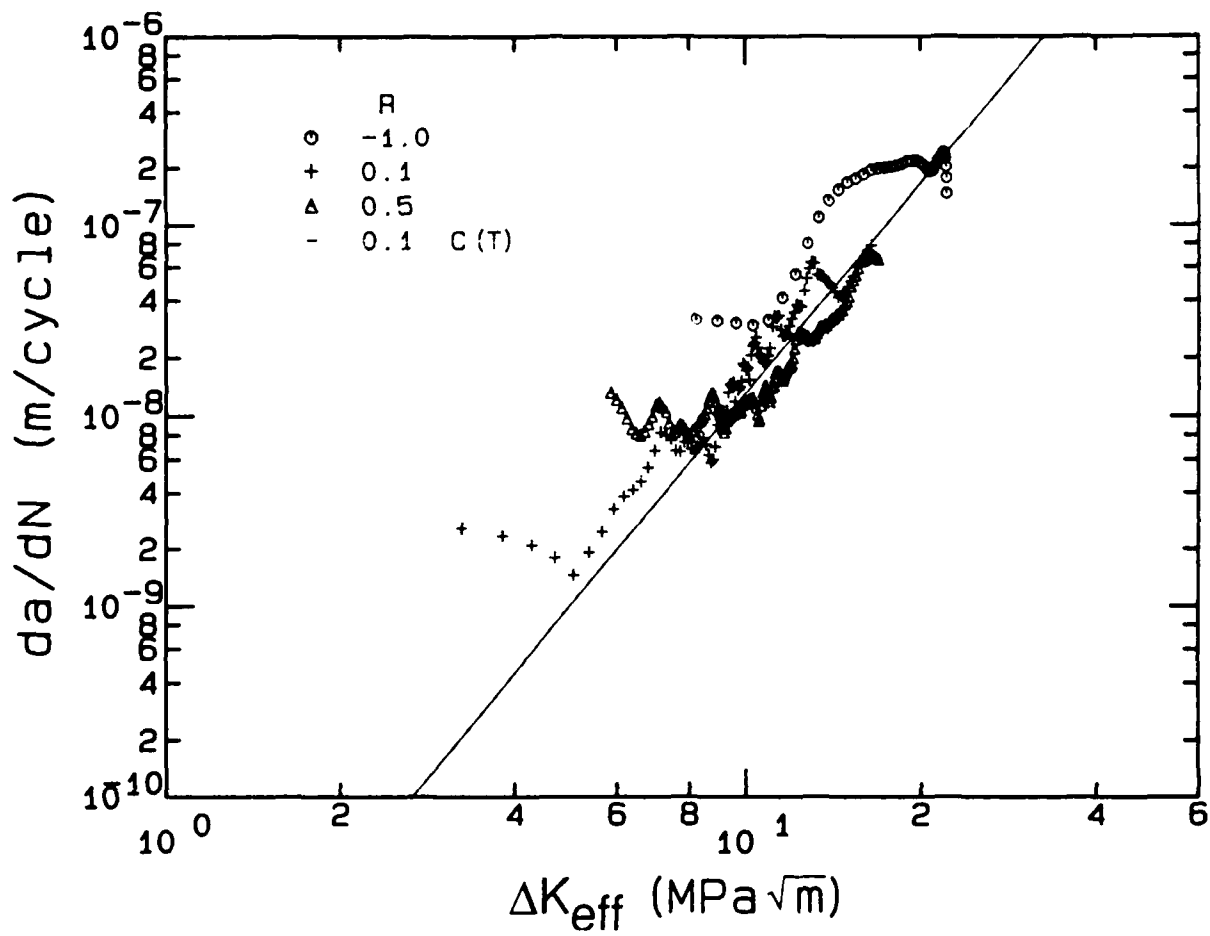


Fig. 4.56 Plot of  $da/dN$ - $\Delta K_{eff}$  illustrating the effect of stress ratio ( $R$ ) on the growth of small cracks in Ti-8Al(s) tested with  $\sigma_{max}/\sigma_y = 0.9$ .

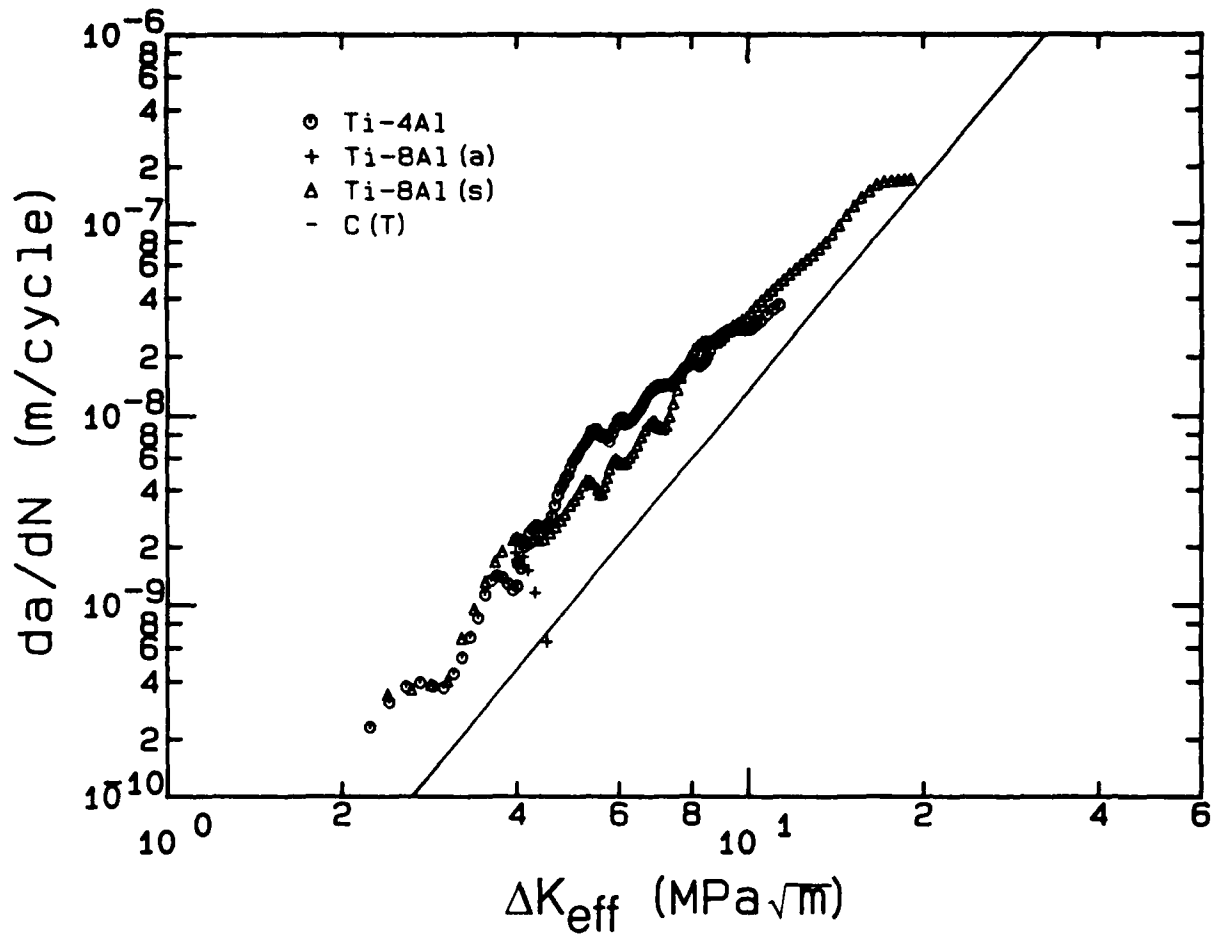


Fig. 4.57 Plot of  $da/dN$ - $\Delta K_{eff}$  illustrating the effect of alloy condition on the growth of small cracks propagated under  $R = 0.1$  fatigue with  $\sigma_{max}/\sigma_y = 0.6$ .

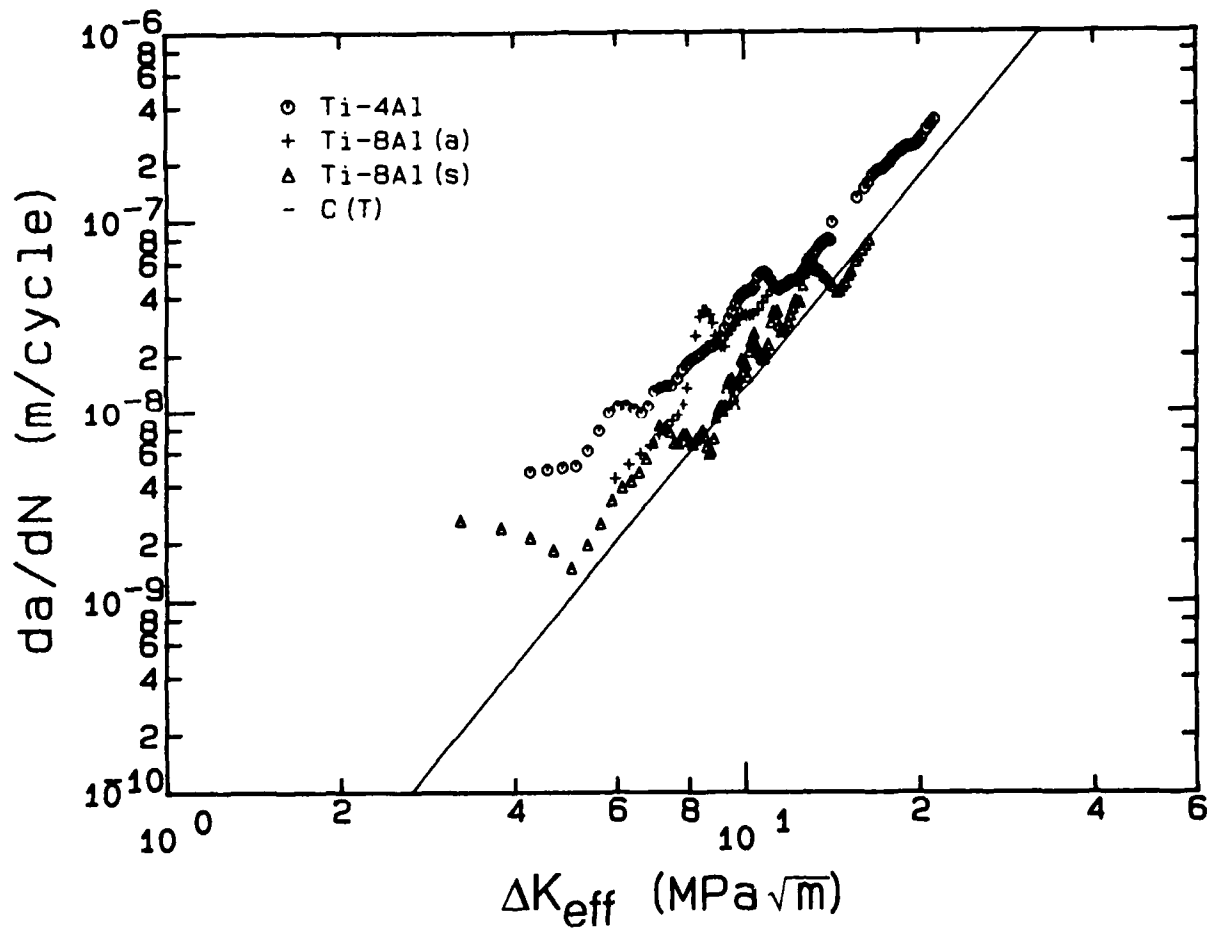


Fig. 4.58 Plot of  $da/dN$ - $\Delta K_{eff}$  illustrating the effect of alloy condition on the growth of small cracks propagated under  $R = 0.1$  fatigue with  $\sigma_{max}/\sigma_y = 0.9$ .

a factor of approximately 2000, while use of  $\Delta K_{\text{eff}}$  has reduced this difference to a factor of 5 or less. The data at the lower stress level in this figure are unusual. Although the crack growth rates at the lowest values of  $\Delta K_{\text{eff}}$  (shortest crack lengths) fall relatively near the large-crack curve, the separation between the small- and large-crack data increases abruptly in the region of  $\Delta K_{\text{eff}} \approx 6.5 \text{ MPa}\sqrt{\text{m}}$  and approaches the large-crack curve only after appreciable additional growth. This behavior, which was not observed in any other small-crack test, was the result of an unusually rapid development of the small-crack closure level.

The  $R = 0.5$  data are also well correlated by  $\Delta K_{\text{eff}}$ , as shown in Fig. 4.54. These small-crack data, which were as much as three orders of magnitude faster than the large-crack  $da/dN$ - $\Delta K$  data (Fig. 4.37), now fall within approximately a factor of 5 or less of the large-crack crack curve.

#### 4.2.5.6.2 Effect of Stress Ratio

$\Delta K_{\text{eff}}$  also correlates the small-crack data obtained at the three stress ratios ( $R = -1.0, 0.1, \text{ and } 0.5$ ) for both of the stress levels ( $\sigma_{\text{max}}/\sigma_y = 0.6 \text{ and } 0.9$ ), as shown respectively in Figs. 4.55 and 4.56 (the companion  $da/dN$ - $\Delta K$  data are shown in Figs. 4.38 and 4.39). For  $\sigma_{\text{max}}/\sigma_y = 0.6$ , most of the small-crack data fall within a factor of four of the large-crack curve, although the  $R = -1.0$  data are somewhat anomalous as stated earlier. At the higher stress level (Fig. 4.56), the small- and large-crack data are well consolidated when plotted against  $\Delta K_{\text{eff}}$ . Notably, at the shortest crack lengths, each of these data sets shows a tendency to deviate from the large-crack trend — a behavior that was also observed in a few of the other tests.

#### 4.2.5.6.3 Effect of Alloy Condition (Slip Character)

Figures 4.57 and 4.58 present the small- and large-crack  $da/dN-\Delta K_{eff}$  data from each of the three alloy conditions fatigued under  $R = 0.1$  cycling with  $\sigma_{max}/\sigma_y = 0.6$  and  $0.9$  respectively (see Figs. 4.40 and 4.41 for  $da/dN-\Delta K$  comparison). The first figure shows no influence of alloy condition on the growth of small surface cracks over the full range examined ( $2c \approx 50 \mu m$  to  $4 mm$ ). The collection of small-crack data lie at a growth rate approximately a factor of three higher than the large-crack trend. The small-crack data at the higher stress (Fig. 4.58) are also well consolidated by  $\Delta K_{eff}$ , but a small effect of material is demonstrated by a small spread in the small-crack growth rates for a given  $\Delta K_{eff}$ . Note that the very limited dependency of small-crack growth rate on material is consistent with the large-crack  $da/dN-\Delta K$  data; i.e., the small-crack growth rates tend to order in the same manner as did the large-crack data. This observation may be fortuitous, however, since all of these small-crack data fall within approximately a factor of five of the large-crack trend. Thus, after accounting for crack closure, there is little evidence to suggest that the various alloy conditions and their associated differences in slip character have an appreciable influence on the growth rates of very small fatigue cracks.

### 4.3 Fractography

Fracture surfaces of both the large- and small-crack specimens were examined to determine the mechanisms of crack propagation and to document any crack-size dependent differences in crack growth mechanism. The fractographic investigation considered a number of test and geometric variables which included: stress level, stress intensity factor range, crack geometry, crack size, and stress state. The fractographs were obtained using scanning electron microscopy, and light micrographs taken along the specimen surface were used to record the crack paths for subsequent quantitative interpretation.

### 4.3.1 Scanning Electron Microscopy

#### 4.3.1.1 Large-Crack Specimens

Fractographs of the large-crack specimens were obtained from two different regions of the  $da/dN$ - $\Delta K$  curve: the near-threshold region ( $da/dN \approx 10^{-10}$  m/cycle) and the lower portion of the "Paris-law" region ( $da/dN \approx 10^{-8}$  m/cycle). Taking the micrographs at these two growth rates facilitated an assessment of the dependence of crack growth mechanism on  $da/dN$  and provided a basis for comparison of the C(T)-specimen fracture surfaces with those from the small-crack specimens. The fractographs at the higher growth rate are believed to be best suited for the purpose of comparison with small-crack fractographs, since much of the small-crack growth-rate data falls in a range near  $10^{-8}$  m/cycle. Because the small cracks were inherently confined to the near-surface region of the specimen, the corresponding large-crack fractographs were taken from regions near the free surface of the C(T) specimens. This action was further justified by the absence of distinguishable differences between fractographs from the near-surface versus interior regions of the fracture surface. In other words, effects of stress state (plane stress versus plane strain) on the crack growth mechanism were not discernible in the SEM fractographs.

The format for presentation of the large-crack fractographs will be as follows. All fractographs are from tests of C(T) specimens fatigued at  $R = 0.1$ , and for a given location on the fracture surface, a series of four fractographs of increasing magnification will be presented. In each fractograph, the direction of crack propagation is from right to left, and the free surface of the specimen is near the bottom edge of the fractograph.



Fractographs of Ti-4Al taken at  $da/dN = 10^{-10}$  and  $10^{-8}$  m/cycle are shown in Figs. 4.59 and 4.60, respectively. At the lower growth rate (Fig. 4.59) the crack growth is transgranular, and numerous locations on the surface are flat and relatively featureless. The featureless regions were probably produced by abrasion of the opposing fracture surfaces during repeated fatigue crack closure at the near-threshold growth rate. In regions where such contact did not occur, fine crystallographic steps are occasionally evident, as shown at the highest magnification. In contrast, at the higher growth rate of  $10^{-8}$  m/cycle, the fracture surface shown in Fig. 4.60 shows little evidence of fracture-surface abrasion, and a number of larger regions of apparently crystallographic crack growth are evident. Some of the large crystallographic appearing regions are of grain-size dimensions (from Table 4.1: Ti-4Al average grain diameter  $\approx 100 \mu\text{m}$ ).

Fractographs of Ti-8Al(s), presented in Figs. 4.61 and 4.62, show the apparently much more crystallographic nature of crack propagation in this material. In the near-threshold region, Fig. 4.61, the large crystallographic-looking facets make up approximately 27% of the projected surface area, as determined by a random point count at a magnification of 200X. The facets are believed to be primarily of (0001) orientation [237], and may be interconnected by prism-plane steps. At the higher growth rate, Fig. 4.62, the fracture surface appears even more crystallographic, with the crystallographic features accounting for approximately 50% of the projected surface area. At higher magnifications, however, areas that appear macroscopically crystallographic are seen to exhibit extensive microplasticity, which often develops in parallel crystallographic steps. Although the step-like features have a dimension as small as  $10^{-7}$  m (as compared to the growth rate of  $10^{-8}$  m/cycle), these steps are not believed to be fatigue striations. Rather, they appear to be slip line markings [216] that form along the crack path.

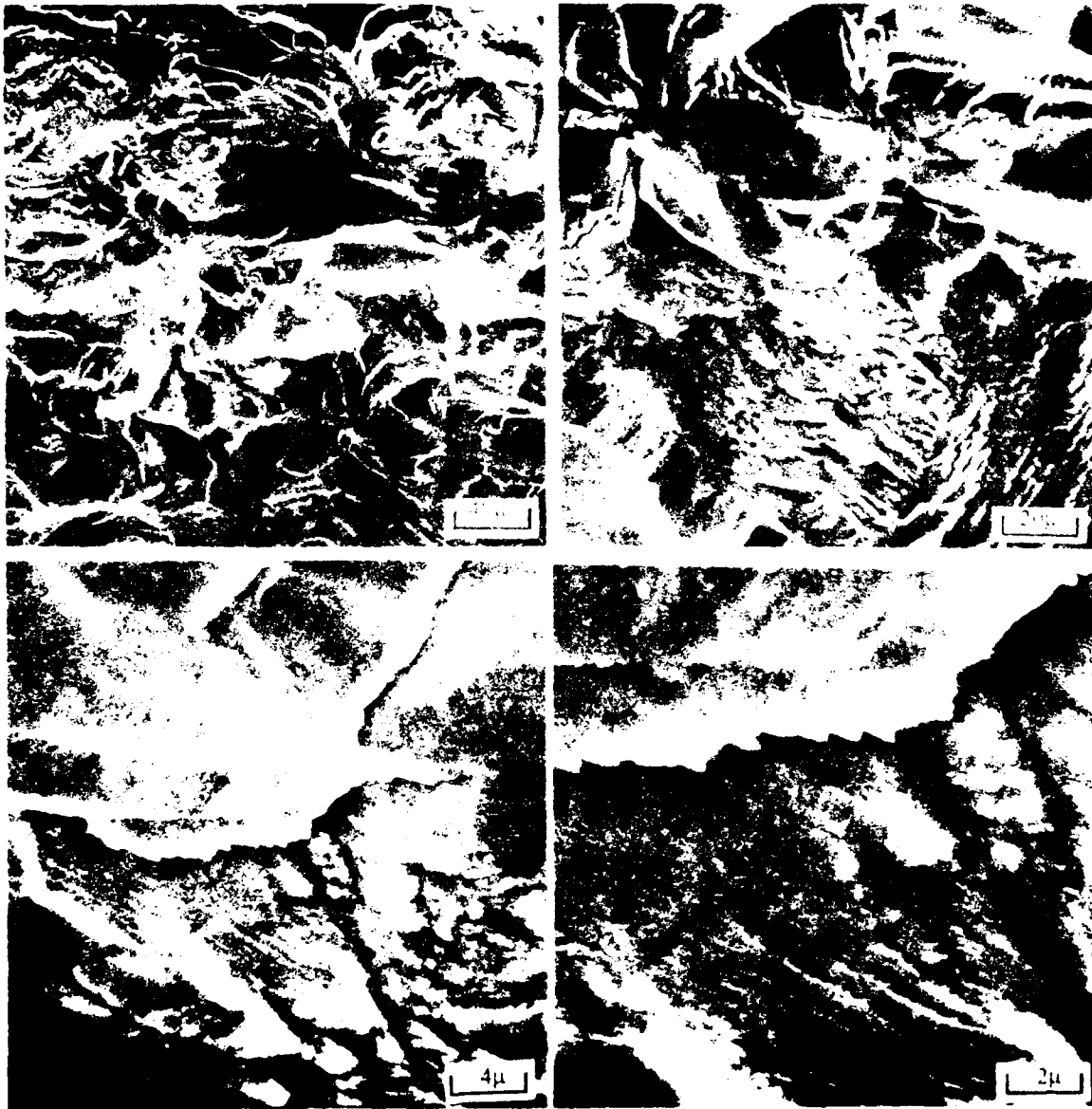


Fig. 4.59 Fracture surface of a Ti-4Al C(T) specimen fatigued at  $R = 0.1$ ;  $\Delta K = 5.1 \text{ MPa}\sqrt{\text{m}}$  and  $da/dN = 10^{-10} \text{ m/cycle}$ .

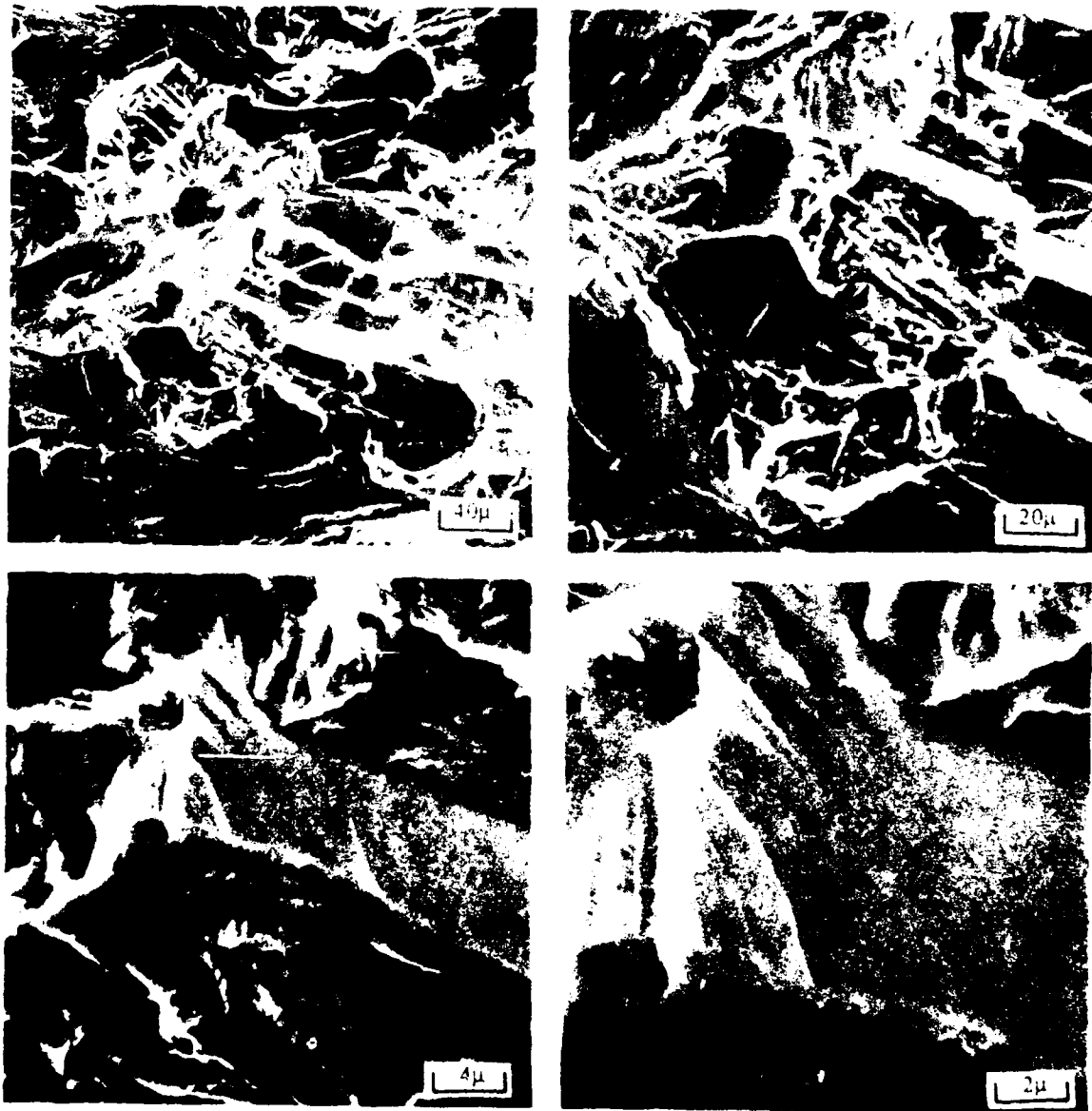


Fig. 4.60 Fracture surface of a Ti-4Al C(T) specimen fatigued at  $R = 0.1$ ;  $\Delta K = 9.7 \text{ MPa}\sqrt{\text{m}}$  and  $da/dN = 10^{-8} \text{ m/cycle}$ .

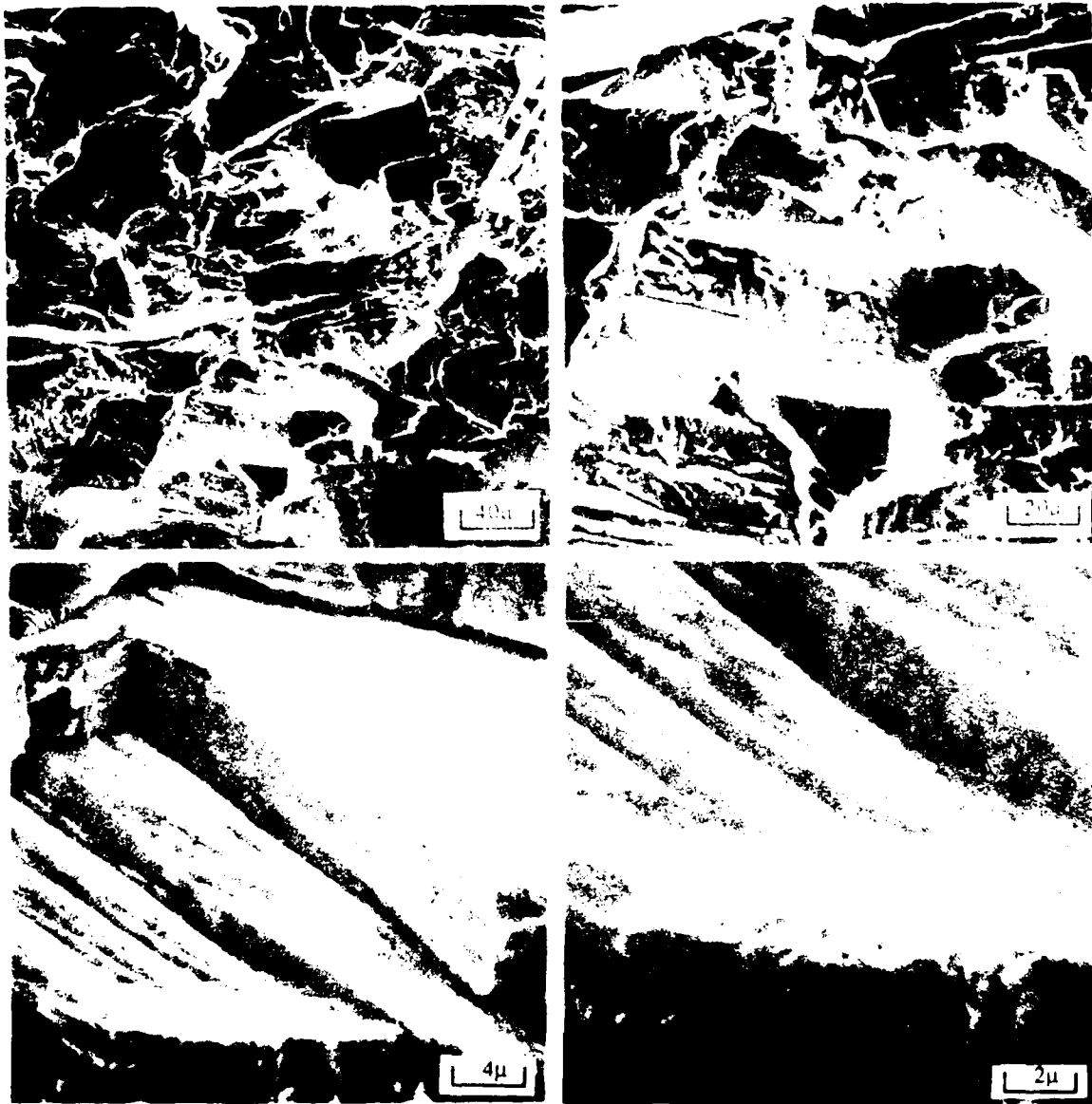


Fig. 4.61 Fracture surface of a Ti-8Al(s) C(T) specimen fatigued at  $R = 0.1$ :  $\Delta K = 12.4 \text{ MPa}\sqrt{\text{m}}$  and  $da/dN = 10^{-10} \text{ m/cycle}$ .

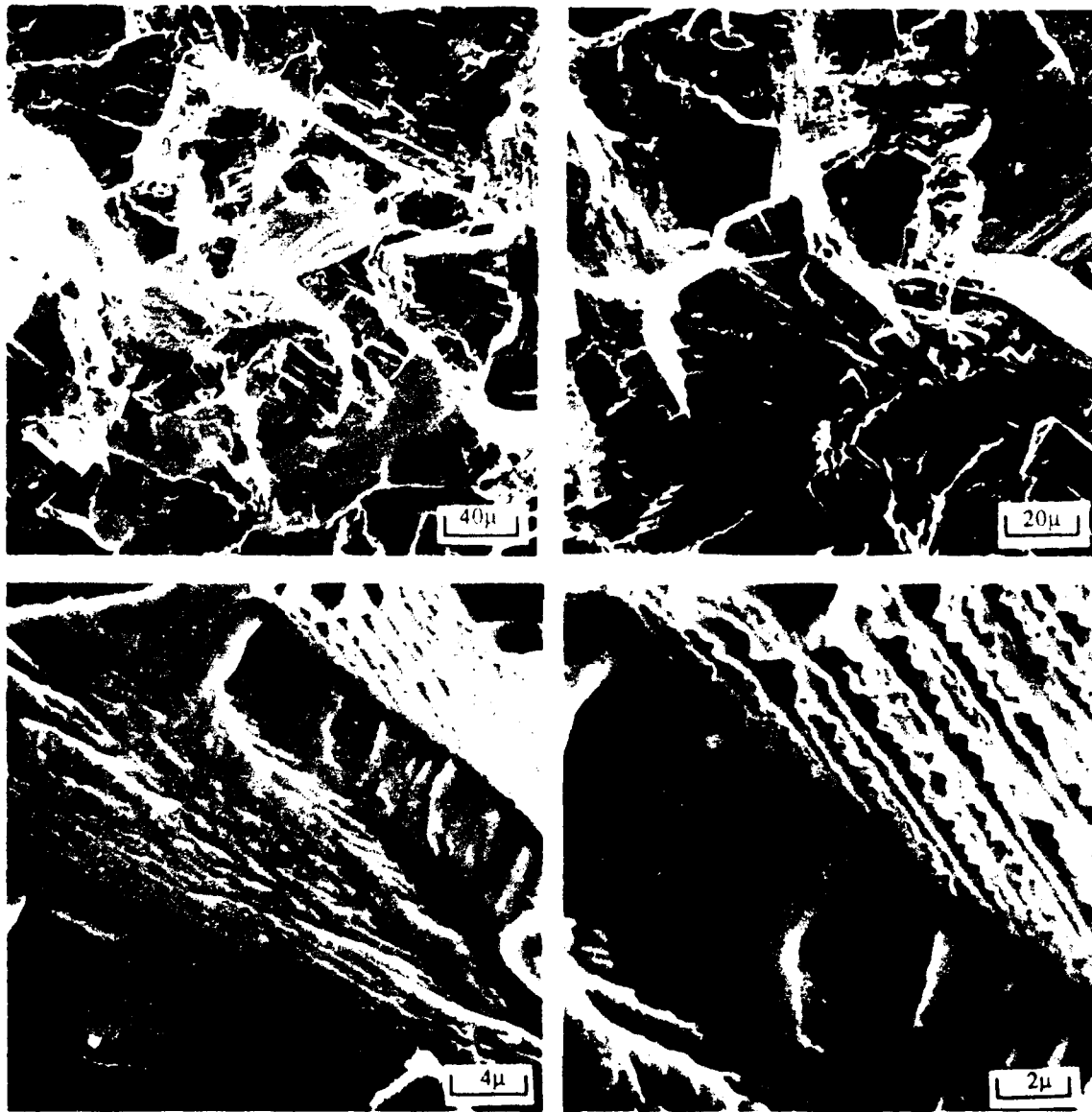


Fig. 4.62 Fracture surface of a Ti-8Al(s) C(T) specimen fatigued at  $R = 0.1$ ;  $\Delta K = 20.4 \text{ MPa}\sqrt{\text{m}}$  and  $da/dN = 10^{-8} \text{ m/cycle}$ .

Representative fracture surfaces from the aged Ti-8Al are shown in Figs. 4.63 and 4.64, which respectively have  $da/dN = 10^{-10}$  and  $10^{-8}$  m/cycle. Both figures show that the mechanism of crack growth maintains a large apparently crystallographic component, with approximately 45% of the projected fracture surface exhibiting crystallographic facets. The crystallographic fracture features in this material appear to be more sharply defined than in either of the other alloy conditions. As shown in the higher magnification fractographs in Fig. 4.63, some of the protruding features appear to have been abraded at the near-threshold crack growth rate. Such abrasion is again less evident in the fractographs shown in Fig. 4.64, which were taken from a region of propagation at  $10^{-8}$  m/cycle. Here again the fracture surface is highly crystallographic in appearance (approximately 50% of the projected area), and some very well defined, fine crystallographic steps are present.

In general, the large-crack fractographic observations are well correlated with the slip character of each alloy. The finely distributed wavy slip exhibited by the Ti-4Al most easily accommodated the deformation associated with crack growth, and this material correspondingly had the flattest, most featureless fracture surface. The increased aluminum content and associated increase in slip planarity of the Ti-8Al(s) strongly promoted crystallographic crack propagation in this material, leading to a much more tortuous crack path. Further restricting slip by aging the Ti-8Al resulted in the most crystallographic fracture surface. Although the area fraction of crystallographic facets formed in this material was approximately equivalent to that observed in the Ti-8Al(s), the crystallographic features of the Ti-8Al(a) were more sharply defined, consistent with the more extremely restricted slip in this material.

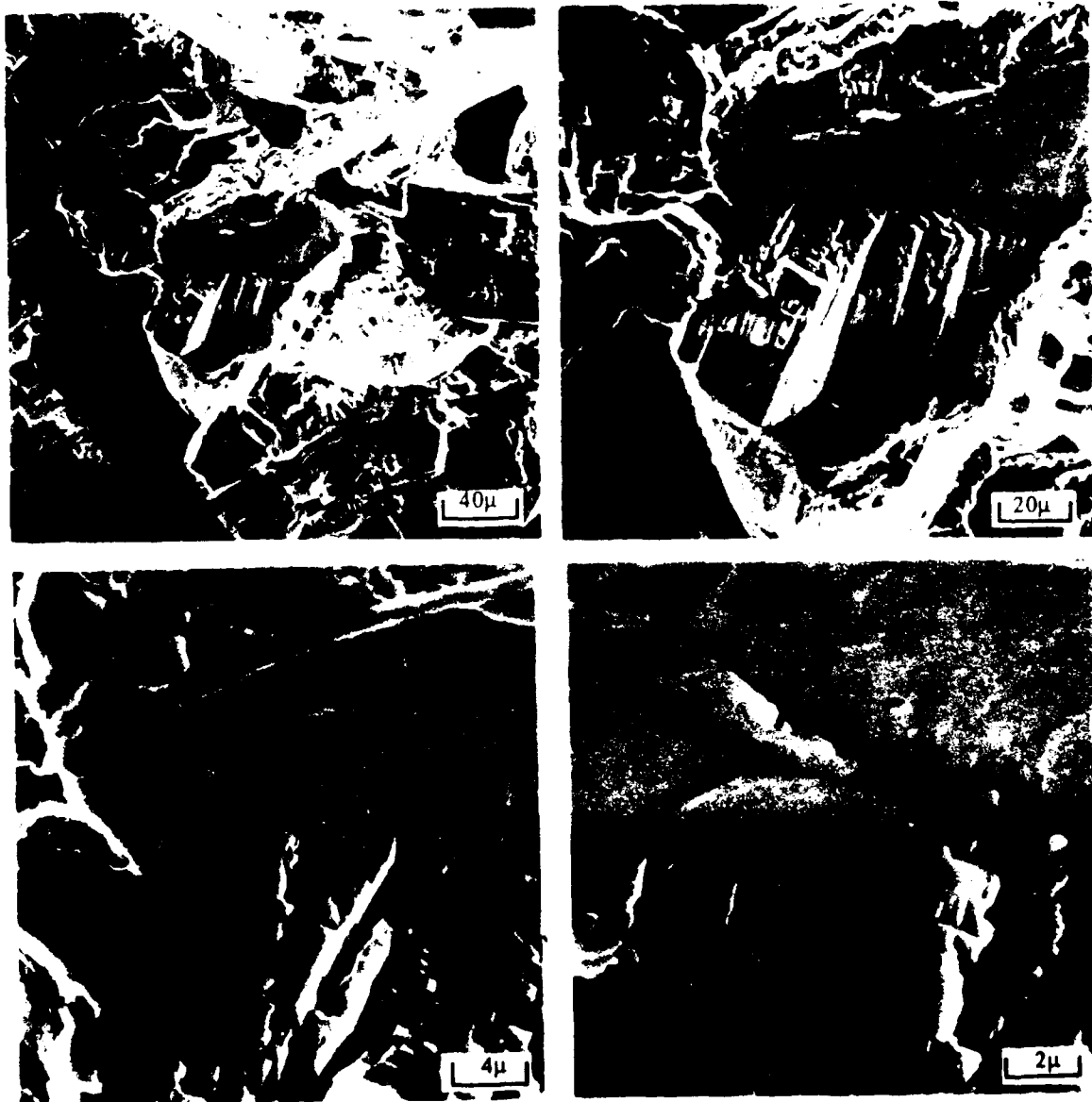


Fig. 4.63 Fracture surface of a Ti-8Al(a) C(T) specimen fatigued at  $R = 0.1$ ;  $\Delta K = 7.2 \text{ MPa}\sqrt{\text{m}}$  and  $da/dN = 10^{-10} \text{ m/cycle}$ .

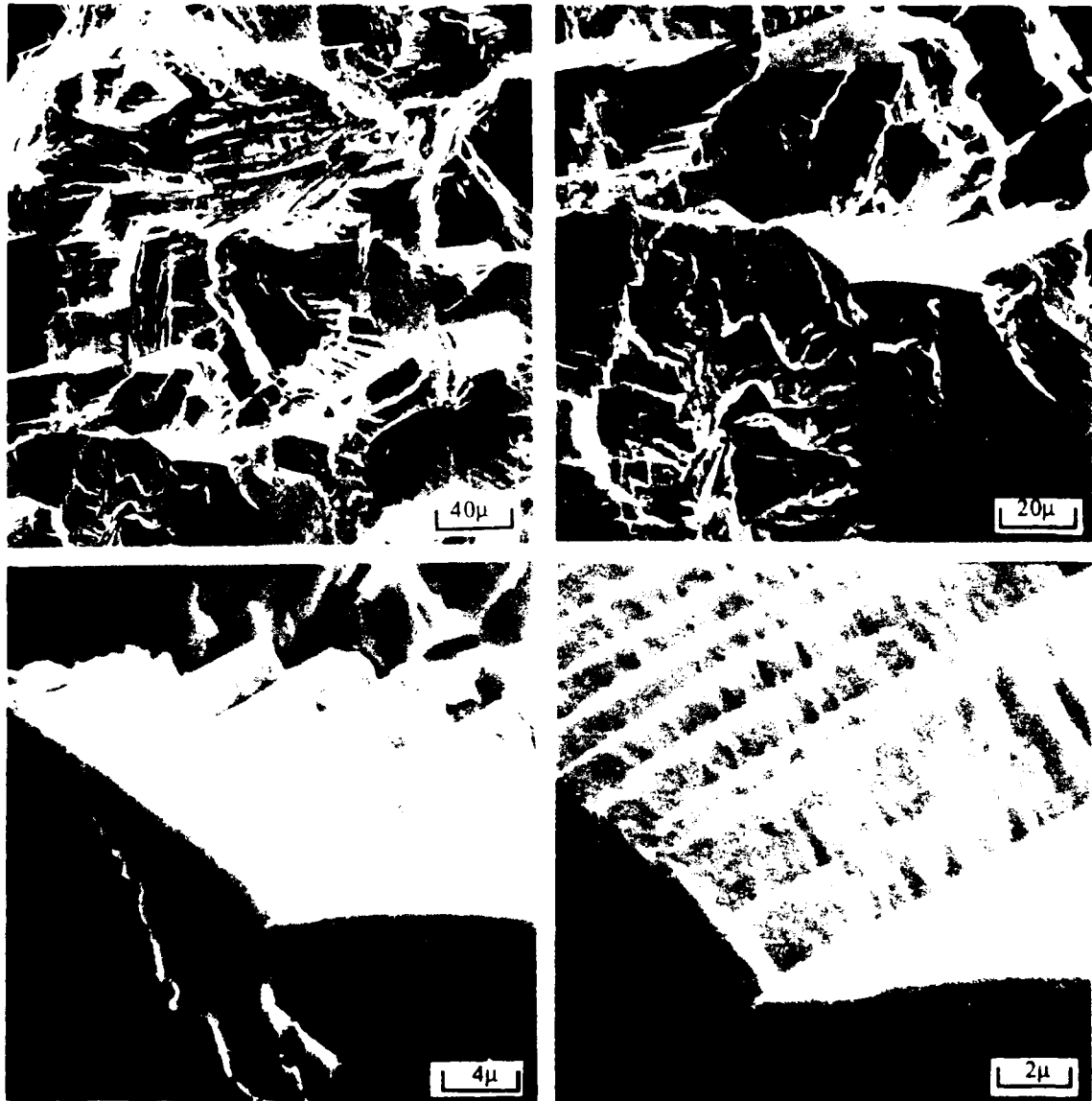


Fig. 4.64 Fracture surface of a Ti-8Al(a) C(T) specimen fatigued at  $R = 0.1$ ;  $\Delta K = 13.0 \text{ MPa}\sqrt{\text{m}}$  and  $da/dN = 10^{-8} \text{ m/cycle}$ .



#### 4.3.1.2 Small-Crack Specimens

The fracture surfaces of the small-crack specimens were examined in the scanning electron microscope to determine the mechanisms of crack propagation and characterize any dependence of crack-growth mechanism on crack size. The findings of the investigation as a whole are well represented by fractography from a few specimens. Therefore, typical fractographs from small-crack specimens of each of the three alloy conditions will be presented along with examples of less common fractographic features.

Figure 4.65 presents a series of fractographs from a Ti-4Al small-crack specimen {84-650; specimen numbers identified in Appendix 2} that was tested at  $R = 0.1$  with  $\sigma_{\max}/\sigma_y = 0.6$ . Before final fracture, this particular crack attained a length of  $2c = 4.04$  mm. The origin of the crack is located at the center of the specimen and is on the lower edge of the fracture surface as pictured. The nearly semicircular shape of the critical crack ( $a/c = 0.93$ , determined from heat-tint measurements) is evident in the fractograph at the lowest magnification. Inspection of the series of fractographs presented in the figure reveals a mildly crystallographic fracture surface similar to the equivalent large-crack fracture surface previously shown in Fig. 4.60. Note that it is probably more appropriate to compare the large-crack fracture surface from the region having a growth rate of  $10^{-8}$  m/cycle, since much of the small-crack data fall in this range. The fracture surface of the small-crack specimen shows no obvious change in crack-growth mechanism, and the surface appears essentially indistinguishable from the corresponding large-crack surface. Even at the site of the crack's initiation, which is located directly above the Vickers indentation shown on the side of the specimen, there is only minimal evidence of a transition from stage I to stage II crack growth.

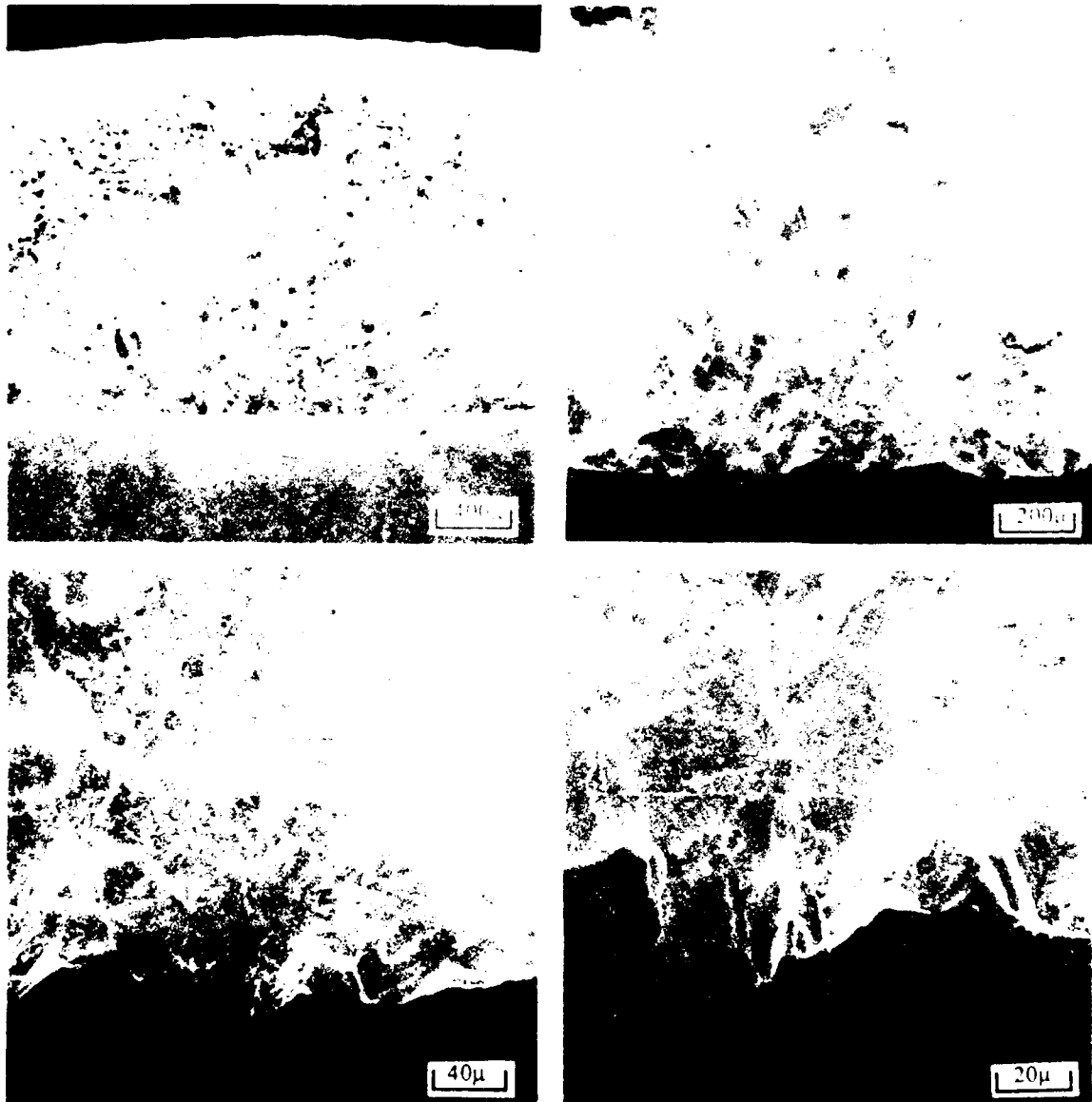


Fig. 4.65 Fracture surface of a Ti-4Al small-crack specimen fatigued at  $R = 0.1$  and having  $\sigma_{\max}/\sigma_y = 0.6$ .

Figure 4.66 presents fractographs of a similar small crack {84-620} in Ti-8Al(s) propagated under  $R = 0.1$  fatigue with  $\sigma_{\max}/\sigma_y = 0.9$ . This crack also initiated at the center of the specimen and attained a critical crack size of  $2c = 3.92$  mm with a final aspect ratio of  $a/c = 0.98$ . The overall fracture surface appears equivalent to the corresponding large-crack fracture surface (Fig. 4.62), although the crack initiation site, which is again located above the Vickers indentation, is clearly more crystallographic than the remainder of the surface. The width of this stage I region appears to be approximately three grains, and its approximate depth is 1.5 grains. The geometry of the features at the initiation site suggest that the crack initially developed along combination of basal and prism slip planes and began stage II growth after achieving a size greater than approximately 2 to 3 intersected grain diameters.

The fracture surface of a small crack in Ti-8Al(a) is shown in Fig. 4.67 {84-706}. This specimen, tested with  $\sigma_{\max}/\sigma_y = 0.6$  and  $R = 0.1$ , generally exhibits the well-defined crystallographic fatigue crack growth surface previously found for the equivalent large crack shown in Fig. 4.64. At the initiation site, however, there is an extensive region of crystallographic cracking, which appears to have dimensions of depth and width that are both approximately 5 times the average grain size of the materials. The crystallographic nature of the early crack growth is very evident along the free surface of the specimen, which exhibits a number of sharp steps as the crack lengthens. In this specimen, crack initiation occurred within an abnormally large grain. The small crack apparently propagated along a slip band within this grain until encountering the surrounding microstructure, which was of the normal grain size. At this point, the crack changed from stage I to stage II growth, and as shown by the lower data set in Fig. 4.34, experienced a corresponding decrease in growth rate. Due to its proximity to the corner of the specimen, it was necessary to terminate this test early. The specimen was failed under monotonic loading, which probably accounts for the significant deformation

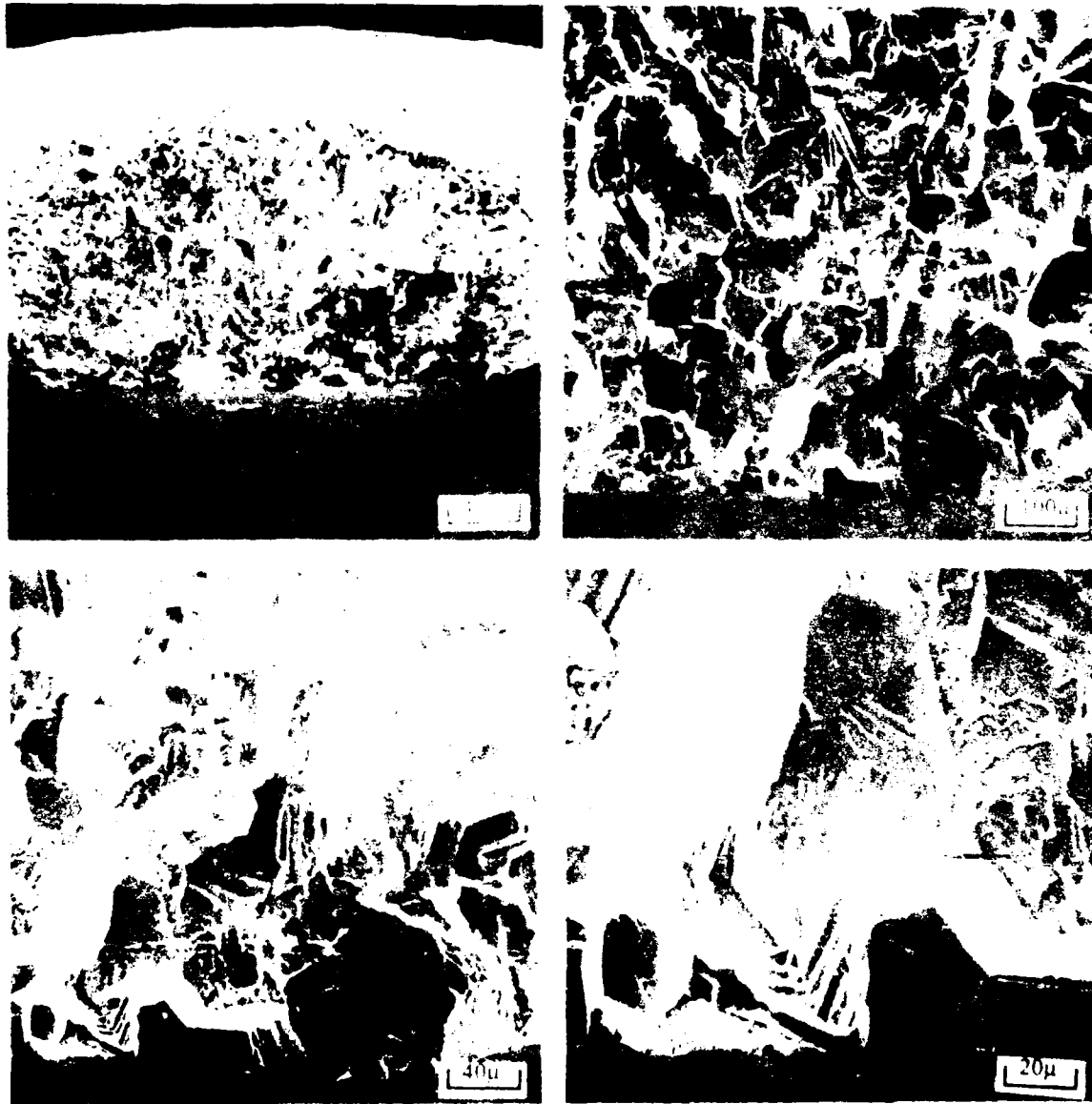


Fig. 4.66 Fracture surface of a Ti-8Al-6Sn-2Zr-0.5B small-crack specimen fatigued at  $R = 0.1$  and having  $\sigma_{max}/\sigma_y = 0.9$ .

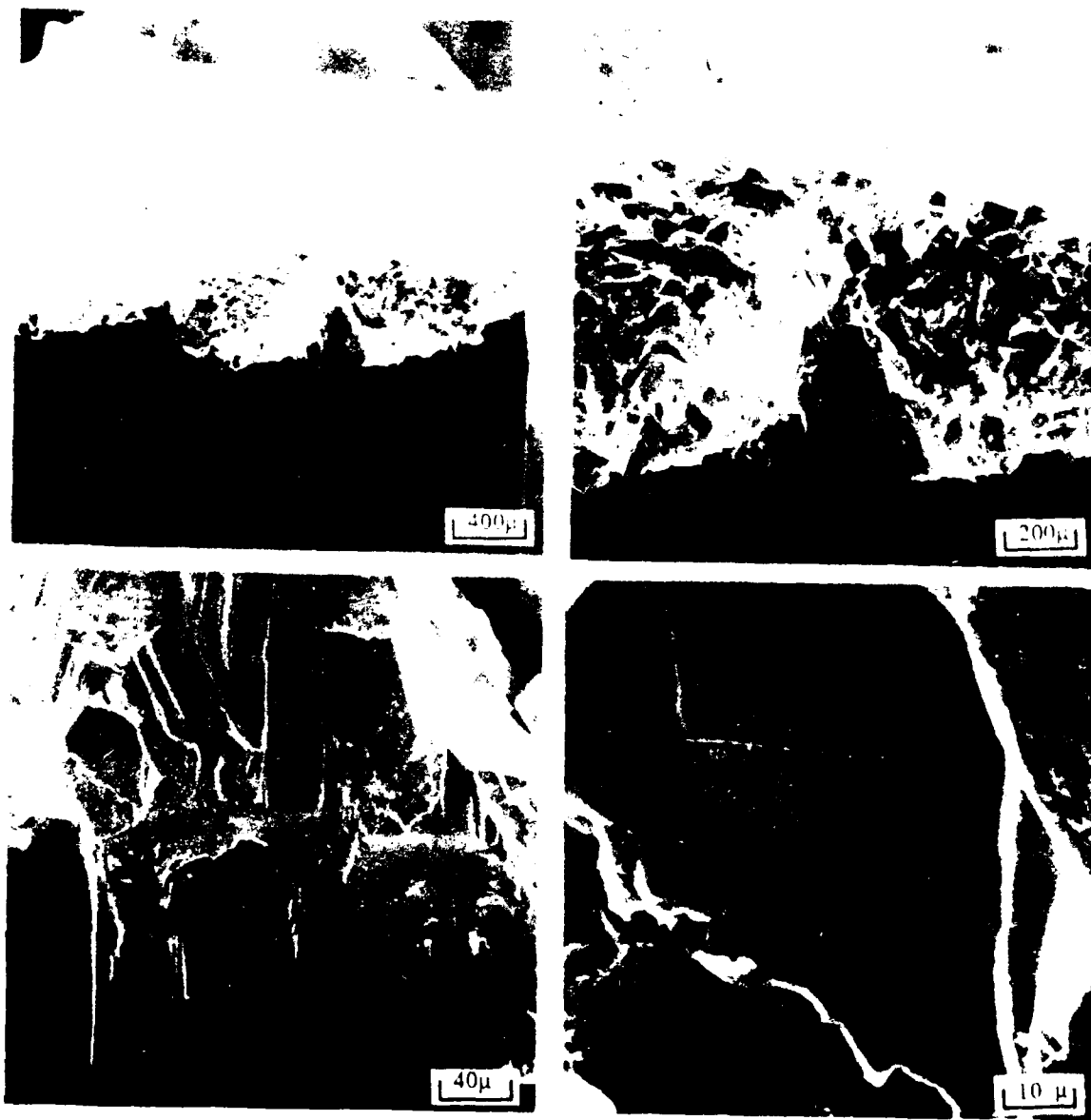


Fig. 4.67 Fracture surface of a Ti-8Al(a) small-crack specimen fatigued at  $R = 0.1$  and having  $\sigma_{\max}/\sigma_y = 0.6$ .

surrounding the small fatigue crack.

A few of the small cracks exhibited unusual fractographic features that were of microstructural interest but which did not noticeably affect the crack propagation behavior. That is, although the small cracks propagated faster than their counterpart large cracks, the peculiarities of the individual cracks to be discussed did not appear to influence their basic crack growth trends.

The most prominent microstructural/fractographic irregularity was the formation of a crack at a large, unrecrystallized grain such those identified in the Ti-4Al metallography (Fig. 4.3). Figure 4.68 shows the fracture surface of the Ti-4Al small-crack specimen {84-651} tested under  $R = 0.1$  fatigue with  $\sigma_{\max}/\sigma_y = 0.9$ . The small crack pictured achieved a final size of  $2c = 2.30$  mm with  $a/c = 0.96$  and was centered about an elongated, unrecrystallized grain whose length was several times the average grain size of the material. Consistent with the earlier metallographic observations, the major axis of this grain is oriented in along the rolling direction of the original alloy plate. Although the mechanics of crack initiation would suggest that this grain would form the first crack, the location of the Vickers indentation shows that the first indication of crack initiation on the specimen surface was at a location adjacent to the large grain. Apparently local compatibility requirements surrounding this grain led to initiation. Following initiation, the small crack apparently maintained an approximately semicircular shape and remained centered on its original initiation site, which was slightly to the left of the elongated grain as pictured. The suggestion of a semicircular crack shape is based on measurements on the heat-tinted fracture surface as well as the combination of photographic and compliance crack length measurements from which crack shape could be calculated. The  $da/dN-\Delta K$  data from this specimen are presented in Fig. 4.33 ( $\sigma_{\max}/\sigma_y = 0.9$ ), and although these data fall above the  $\sigma_{\max}/\sigma_y = 0.6$  data, this

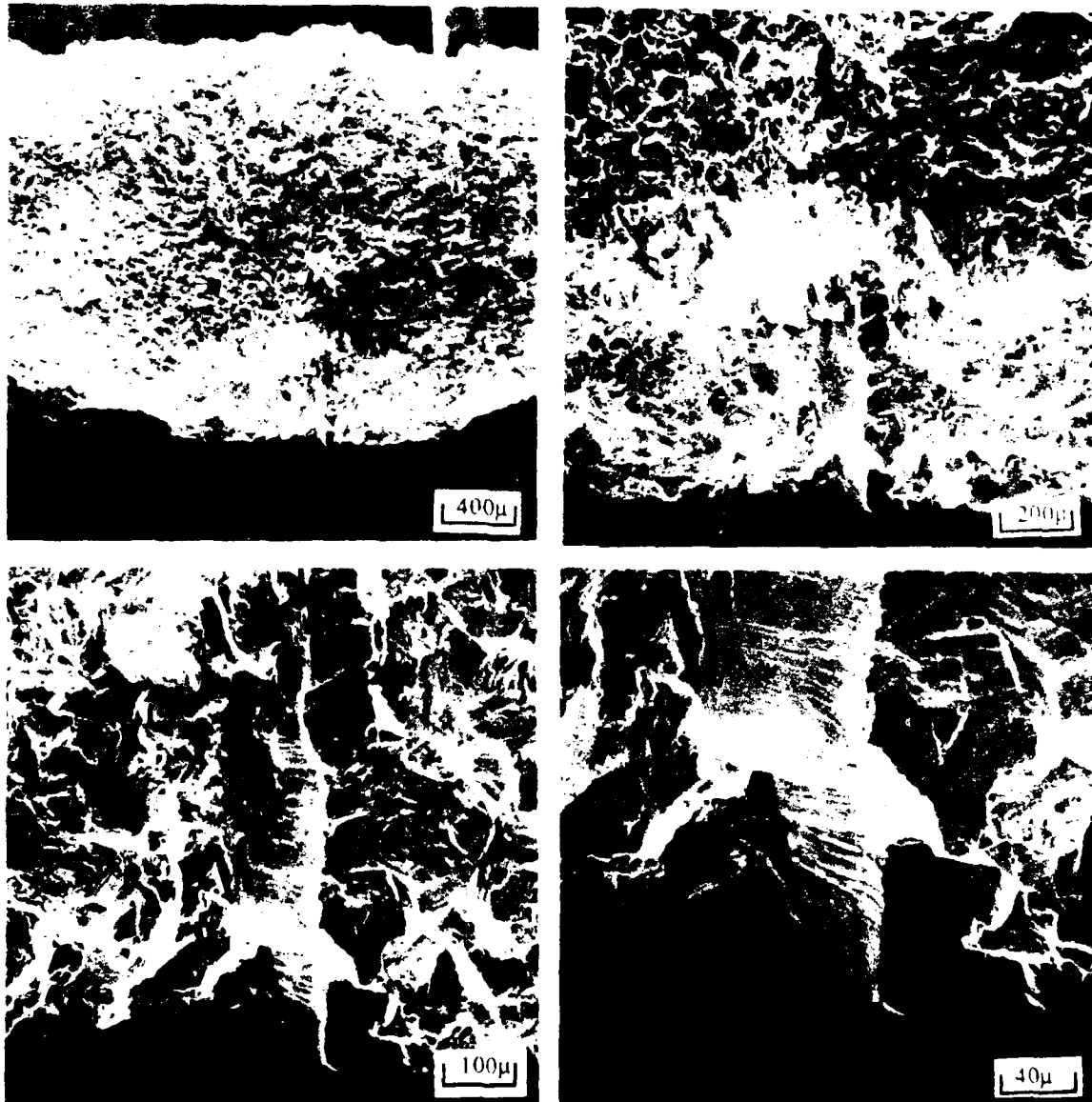


Fig. 4.68 Fracture surface of a Ti-4Al small-crack specimen fatigued at  $R = 0.1$  and having  $\sigma_{\max}/\sigma_y = 0.9$ . A large unrecrystallized grain is shown near the site of crack initiation, which is located above the Vickers indentation.

difference in  $da/dN$  is completely eliminated when plotted against  $\Delta K_{eff}$  (Fig. 4.50).

Thus, although the large grain apparently dictated the site of crack initiation, it appeared to have little influence on the material's inherent resistance to small-crack growth.

Figure 4.69 presents a series of fractographs of a Ti-8Al(s) small-crack specimen {84-698} that was tested under  $R = 0.5$  fatigue with  $\sigma_{max}/\sigma_y = 0.6$ . The critical crack size in this case was  $2c = 5.10$  mm, and the corresponding aspect ratio was  $a/c = 0.85$ . As shown in the higher magnification fractographs, this crack had an extremely crystallographic initiation site, which is located above the Vickers indentation visible on the specimen surface. The location of the indentation, which was placed at the center of the newly initiated small crack, indicates that the crack formed primarily on a single facet and subsequently intersected a grain boundary. The crack appears to have followed the grain boundary until achieving a surface length of  $2c \approx 100$   $\mu\text{m}$ . Subsequently it assumed a transgranular, often crystallographic, crack propagation behavior similar to that observed on the corresponding large-crack specimen shown in Fig. 4.62.

A number of general observations emerge from the SEM fractographic investigation. Aside from the presence of a few large unrecrystallized grains, there is little evidence of significant differences in crack growth mechanism between the large cracks grown in C(T) specimens and the small surface cracks. Under normal circumstances, such as those shown in Figs. 4.65, 4.66, and 4.69, local anisotropy only appeared to influence the mechanism of crack growth for cracks of radius less than approximately 1.5 times the average grain size. In the presence of isolated larger grains, such as those shown in Figs. 4.67 and 4.68, the crack appeared to assume stage II growth once its radius achieved a dimension approximately equal to the minimum dimension of the large grain. Beyond this crack size, there appeared to be no direct effect of the large grain on the growth of small cracks.



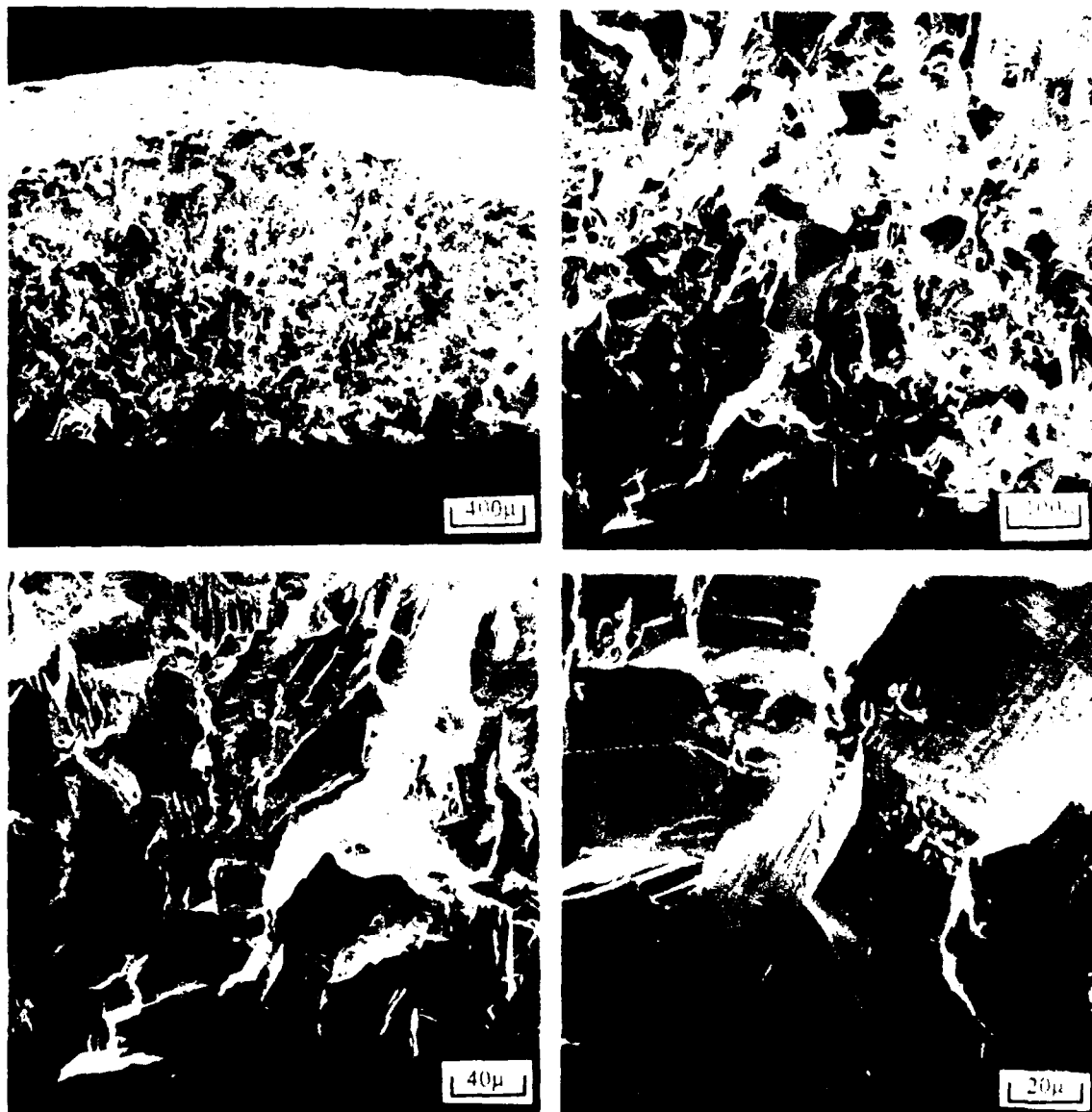


Fig. 4.69 Fracture surface of a Ti-8Al(a) small-crack specimen fatigued at  $R = 0.5$  and having  $\sigma_{\max}/\sigma_y = 0.6$ . The crack initiation site is located above the Vickers indentation, which is visible on the surface of the specimen.

### 4.3.2 Quantitative Fractography

Fracture-surface profiles were digitized from light micrographs taken along the free surfaces of the large- and small-crack specimens. This was done to provide an objective measure of fracture-surface similitude between the small and large cracks and to facilitate a quantitative assessment of the relationship between fracture-surface features and the development of closure in small cracks. Since the small cracks have a very significant free-surface component, the quantitative fractography was performed using crack profiles from the surface of the small- and large-crack specimens. Crack profiles from the surface have been shown to correspond closely to profiles obtained from the specimen interior [263].

A detailed computer analysis of the fracture surface profiles was performed. Topological parameters examined included: lineal roughness ( $R_L$ )  $\equiv$  profile crack length divided by the crack length projected normal to the load axis; local lineal roughness  $\equiv R_L$  measured incrementally along a given crack profile;  $H \equiv$  maximum deviation of the crack profile from its mean path; and local fracture plane orientation  $\equiv$  angular orientation of normal to the fracture profile (tracked incrementally and analyzed statistically). All of the quantitative parameters produced essentially equivalent relative measures of fracture surface topography. Therefore, to simplify the following discussion, the quantitative fractographic analysis will be presented only in terms of the nondimensional lineal roughness parameter,  $R_L$ .

#### 4.3.2.1 Large-Crack Specimens

Light micrographs taken along the free surface of the failed C(T) specimens were used to document the crack profile of the large-crack specimens. In conformance with the

SEM fractography, photographs were taken in regions of the specimen corresponding to near-threshold growth rates ( $da/dN = 10^{-10}$  m/cycle) and in the lower Paris-law region ( $10^{-8}$  m/cycle). Examples of the fracture surface profiles are shown in Fig. 4.70, and Fig. 4.71 presents a comparison of the corresponding measurements of lineal roughness. The data are also listed in Table 4.7. In all cases the fracture surface from the  $10^{-8}$  m/cycle region was of significantly greater roughness than was the  $10^{-10}$  m/cycle region. This was an unexpected result, since crack growth at near- $\Delta K_{th}$  stress intensity levels is normally accompanied by very restrictive crack tip deformation, and the mechanism of crack extension tends to be more crystallographic than at higher values of  $\Delta K$ . Corresponding to the change from fine wavy slip (Ti-4Al) to coarse planar slip (Ti-8Al(s)), there is a dramatic increase in lineal roughness. The fracture surface roughness of the aged Ti-8Al, however, is slightly reduced.

Table 4.7: C(T) Specimen Fracture Surface Roughness Measurements

<u>Material</u>	<u>R</u>	<u>da/dN</u> (m/cycle)	<u>R<sub>L</sub></u>
Ti-4Al	0.1	$10^{-10}$	1.110
Ti-4Al	0.1	$10^{-8}$	1.287
Ti-8Al(s)	0.1	$10^{-10}$	1.335
Ti-8Al(s)	0.1	$10^{-8}$	1.452
Ti-8Al(a)	0.1	$10^{-10}$	1.236
Ti-8Al(a)	0.1	$10^{-8}$	1.409

$R_L \equiv \text{lineal roughness} \equiv \text{profile length/projected length}$

There is an inconsistent relationship between fracture surface roughness, as quantified by  $R_L$ , and crack closure,  $K_{Cl}$ . As shown by Fig. 4.21,  $K_{Cl}$  was approximately constant for each of the three materials, independent of  $K_{max}$  and  $\Delta K$ . However, the

da/dN $10^{-10}$  m/cycle $10^{-8}$  m/cycle

Ti-4Al

500  $\mu$ m $10^{-10}$  m/cycle $10^{-8}$  m/cycle

Ti-8Al(s)

 $10^{-10}$  m/cycle $10^{-8}$  m/cycle

Ti-8Al(a)

Fig. 4.70 C(T) specimen fracture surface profiles obtained from regions of two different growth rates in the each of the three Ti-Al alloy conditions.

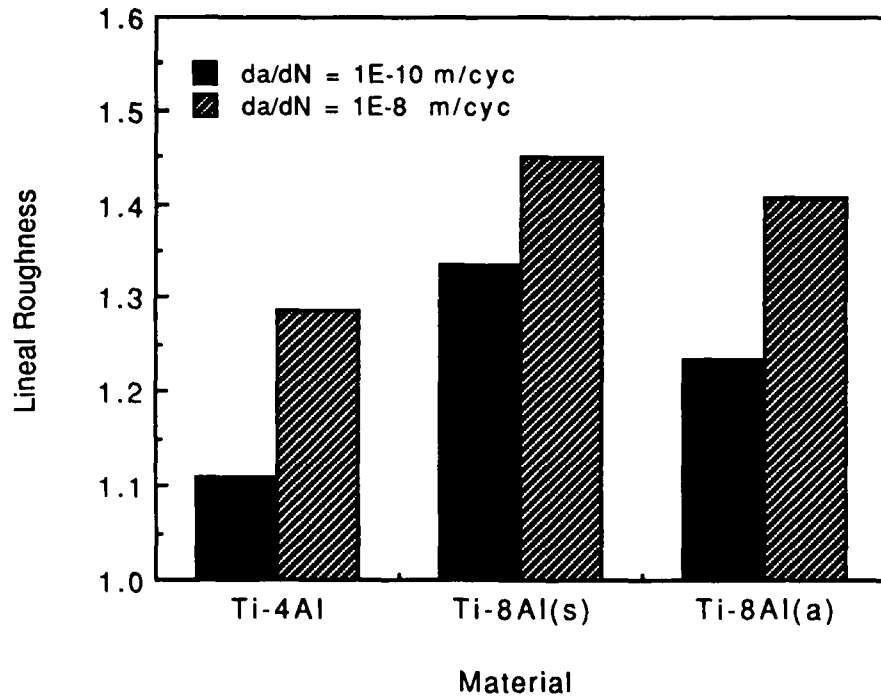


Fig. 4.71 Measured lineal roughness of the fracture surface profiles illustrated in Fig. 4.63.

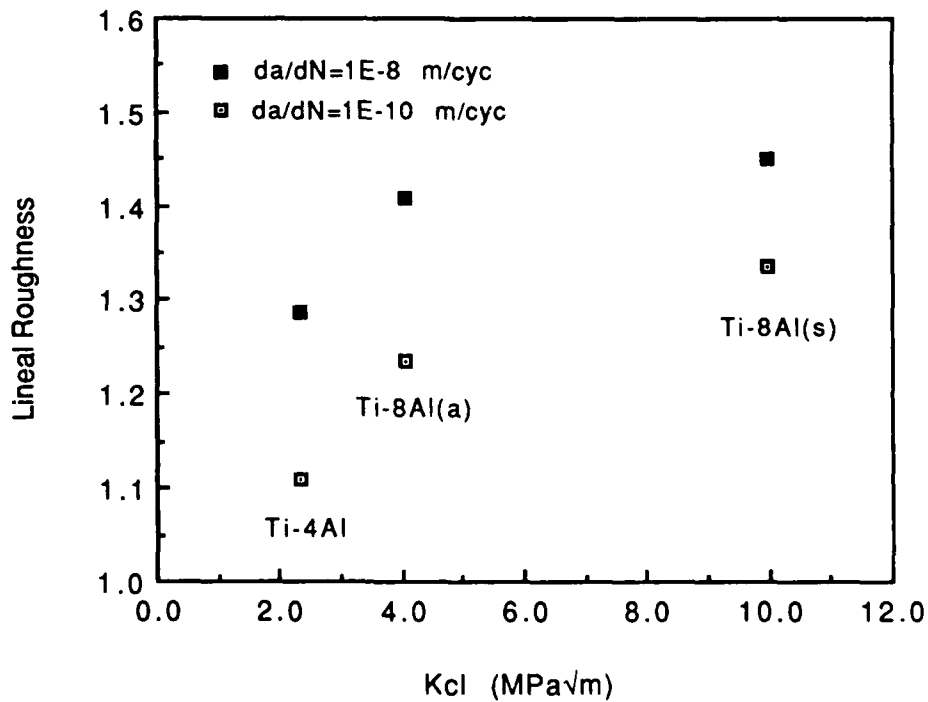


Fig. 4.72 Measured lineal roughness of the fracture surface profiles illustrated in Fig. 4.63 plotted against the corresponding measurement of  $K_{Ic}$ .

measurements of lineal roughness from growth-rate regions of  $10^{-10}$  and  $10^{-8}$  m/cycle are significantly different, as illustrated in Fig. 4.72. Thus, there does not appear to be unique relationship between fracture surface roughness, as quantified by lineal roughness (as well as other similar topographic parameters) and the magnitude of measurements of closure of large cracks in C(T) specimens.

#### 4.3.2.2 Small-Crack Specimens

The digitized profiles of each of the small cracks are presented in Fig. 4.73, and the corresponding measurements of lineal roughness are listed in Table 4.8. For the reasons discussed earlier, only the large-crack measurements from the  $10^{-8}$  m/cycle regions will be used in the present comparison. The small-crack measurements generally compare well with each material's respective large-crack roughness measurements from the  $10^{-8}$  m/cycle regions. In Ti-4Al the large- and small-crack lineal roughness measurements are nearly equivalent. The small-crack,  $\sigma_{\max}/\sigma_y = 0.6$  roughness measurement in Ti-8Al(a) is similar to the large crack value, but the corresponding measurement from the  $\sigma_{\max}/\sigma_y = 0.9$  small-crack test is much higher than the other two. Most of the values of  $R_L$  obtained from the Ti-8Al(s) small-crack specimens compare well with the large-crack measurements. Of the six small-crack roughness measurements, the extreme values occur for testing under  $R = 0.5$  fatigue at the two different stress levels. Although this might appear to suggest an effect of stress level, this trend in  $R_L$  is reversed for both the  $R = -1.0$  and  $0.1$  tests of this material. A multiple regression analysis of the data indicated that the small-crack lineal roughness measurements were correlated only with the alloy condition; effects of stress level and  $R$  effects were insignificant.

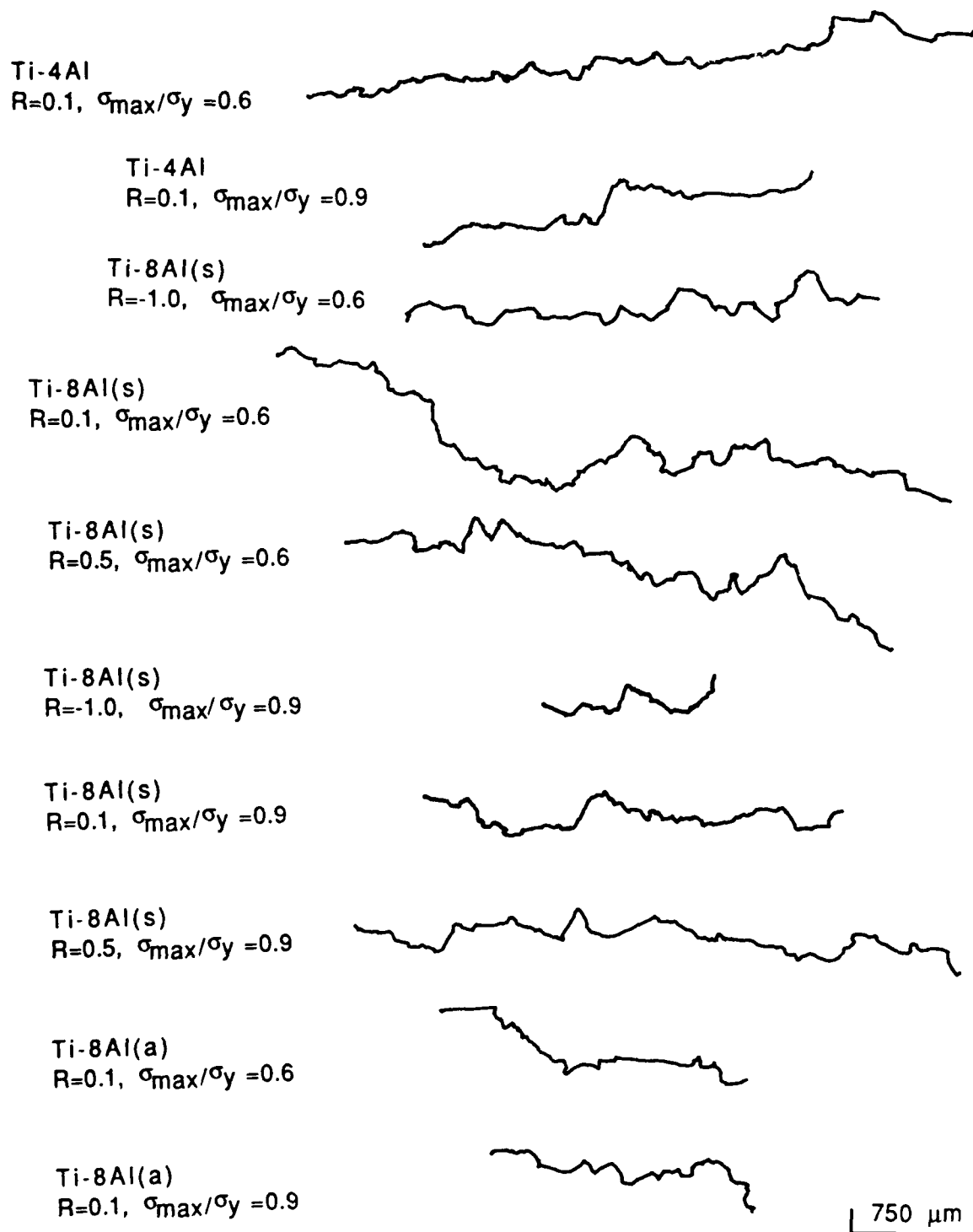


Fig. 4.73 Fracture surface profiles obtained from each of the small-crack specimens.

Table 4.8: Small-Crack Fracture Surface Roughness Measurements

<u>Material</u>	<u>B</u>	<u><math>\sigma_{\max}/\sigma_y</math></u>	<u><math>R_L</math></u>
Ti-4Al	0.1	0.60	1.305
Ti-4Al	0.1	0.90	1.299
Ti-8Al(s)	-1.0	0.60	1.437
Ti-8Al(s)	0.1	0.60	1.478
Ti-8Al(s)	0.5	0.60	1.589
Ti-8Al(s)	-1.0	0.90	1.488
Ti-8Al(s)	0.1	0.90	1.509
Ti-8Al(s)	0.5	0.90	1.315
Ti-8Al(a)	0.1	0.60	1.372
Ti-8Al(a)	0.1	0.90	1.501

To characterize the dependence of fracture surface roughness on crack length, an incremental evaluation of lineal roughness was performed using successive 100  $\mu\text{m}$  increments along the crack profile. By plotting these local measurements of  $R_L$  as a function of position along the crack, it was possible to determine if fracture surface roughness varied as the crack extended. For one of the small cracks for which crack initiation occurred within an abnormally large grain, the local lineal roughness was substantially greater than the average value for this crack. This behavior, however, was confined to the single large grain, and once the crack extended into adjacent grains, the local lineal roughness assumed values consistent with the remaining fracture surface. The remaining small cracks did not exhibit significantly different measurements of local roughness as the crack grew from its original initiation site.

Summarizing the results of the quantitative fractography, the measurements of fracture surface roughness on the C(T) specimens showed a significant effect of alloy condition. For a given specimen, fracture surface roughness was significantly less in



regions having  $da/dN = 10^{-10}$  than for regions with a  $10^{-8}$  m/cycle growth rate. There was no indication of a significant difference between the fracture surface roughness of the small- versus large-crack specimens, and for a given small crack, fracture surface roughness appeared to be independent of crack length.

## **CHAPTER 5**

### **DISCUSSION**

The design of the experimental program purposefully minimized the influence of a number of the key factors cited earlier as possible causes of the anomalous behavior of small fatigue cracks. This was done to facilitate a focused study of the interrelated effects on small-crack growth of slip character and crack closure, with secondary emphasis of the role on crack-tip plasticity. Although these factors were the principal experimental variables, effects of the other three factors (multiple-crack interactions, crack shape, and environment) were also of possible limited influence. In the discussion of the effects of the various experimental variables, the role of each of the lesser variables will be discussed prior to consideration of the three primary variables. Although all six variables may potentially influence crack growth in general, within the context of the present investigation, it is of central importance to characterize the crack-size-dependent influence of the experimental variables.

#### **5.1 Secondary Experimental Variables**

##### **5.1.1 Multiple-Crack Effects**

To avoid the confounding influence of multiple-crack interactions, the small-crack data presented were taken only from isolated small cracks. Data from any cracks that approached a secondary crack were eliminated. Thus, the effect of multiple-crack interactions was not an experimental variable and will not be discussed.

### 5.1.2 Differences in Local Crack-Tip Environment

The literature reporting the behavior of chemically-small cracks generally attributes the rapid growth of small cracks to a crack-size dependence of crack-tip electrochemical processes in corrosive liquids. Such considerations should not pertain to the present findings, since both the large- and small-crack experiments were conducted in room-temperature laboratory air of an approximate relative humidity ranging from 40 to 60%.

Although large cracks in Ti-Al alloys are known to propagate faster in air than in vacuum [e.g., 82], this effect is believed to be due to a combination of two effects: (i) the availability of hydrogen in moist air, which accelerates fatigue crack propagation due to local embrittlement, and (ii) the rewelding of discrete regions of the fracture surface in vacuum tests, which resists crack growth. Since both the large- and small-crack experiments were performed in air, only the hydrogen-embrittlement mechanism is applicable to the present results. However, there is no reason to believe that the kinetics of hydrogen embrittlement in moist air are dependent on crack size. For the present experimental results, therefore, the effect of environment on the crack-size dependence of  $da/dN$  is believed to be negligible.

### 5.1.3 Crack-shape Effects

#### 5.1.3.1 Initiation from Inherent Material Defects

As discussed in the review of the literature, transients in measured surface-crack growth rate may be associated with the formation of a small crack at an initial defect

[131,132] or with crack initiation within a slip band [113]. Considering the present experimental results, the findings of the fractographic examination of small-crack specimens revealed no intrinsic material defects at the origin of crack initiation, indicating that the first crack-shape effect was not a factor in the experiments.

#### 5.1.3.2 Initiation from Persistent Slip Bands

The findings of Wagner et al [113] should apply directly to the present research on Ti-8Al(a). As discussed in section 2.6, serial removal of surface layers of fatigue specimens of aged Ti-8.6Al indicated that very shallow small cracks formed along slip bands and that an approximately semicircular crack shape was achieved for surface crack lengths,  $2c$ , greater than approximately five times the mean-linear-intercept grain size. These findings may differ from the present results, however, since the Ti-8.6Al data were acquired from the population of all initiated small cracks, while the current data were acquired only from dominant, rapidly propagating (worst-case) cracks.

As shown in Fig. 4.29, the crack-shape data acquired within the present research program indicated that  $a/c \approx 0.9$ , independent of crack size and material. However, the heat-tinting procedure that was used was of insufficient resolution to provide crack-shape measurements of cracks as small as those reported for the Ti-8.6Al. A second, indirect, assessment of the shapes of the small cracks was provided by the simultaneous determination of cracks length from photographic versus compliance measurements. The photographic data gave a direct measure of the surface crack length, while the compliance measurements gave an effective surface crack length, which was based on an assumed crack aspect ratio of  $a/c = 0.9$ . Although crack-opening compliance is relatively insensitive to variations in crack shape, comparison of the measured surface crack length from photographic versus compliance data did not suggest the existence of

very shallow small cracks in any of the experiments. It is speculated that the absence of crack-shape effects similar to those reported for the Ti-8.6Al may be attributed to the enhanced ability to differentiate slip bands from small cracks that was provided by observing the cracks under an applied load in the current experiments.

In general, it appears that the initial development of very shallow, small cracks was not a significant feature of the present data. It should be noted that many of the small-crack data presented are for surface cracks of length greater than five times the grain size, where a stable crack shape would be expected. In addition, the tendency for development of shallow surface cracks is believed to be successively less significant in Ti-8al(s) and Ti-4Al due to the increased dispersal of slip in these materials and the concomitant change in the mode of crack initiation. Thus, although crack-shape effects may account for certain irregularities in  $dc/dN$  at the smallest crack sizes in coarse, planar-slip materials such as aged Ti-8.6Al, the present small-crack results do not appear to exhibit an appreciable influence of this factor.

#### **5.1.3.3 Crack-Shape Effects on the Stress Intensity Factor**

The finite element calculations of Newman and Raju [127,128] describe the dependence of the stress intensity factor on position along the front of a semielliptical surface crack. This solution is normalized with respect to specimen dimensions and is independent of absolute crack size. Since, for an arbitrary shape,  $K$  varies along the crack front, a single value of this parameter cannot describe the driving force for crack propagation. However, as confirmed by the tendency of small surface cracks to achieve an approximately semicircular shape, a stable crack aspect ratio quickly develops as the crack extends from its initiation site. The reason for this stability in crack shape is illustrated in Fig. 5.1, which gives dimensionless stress intensity factor as a function of

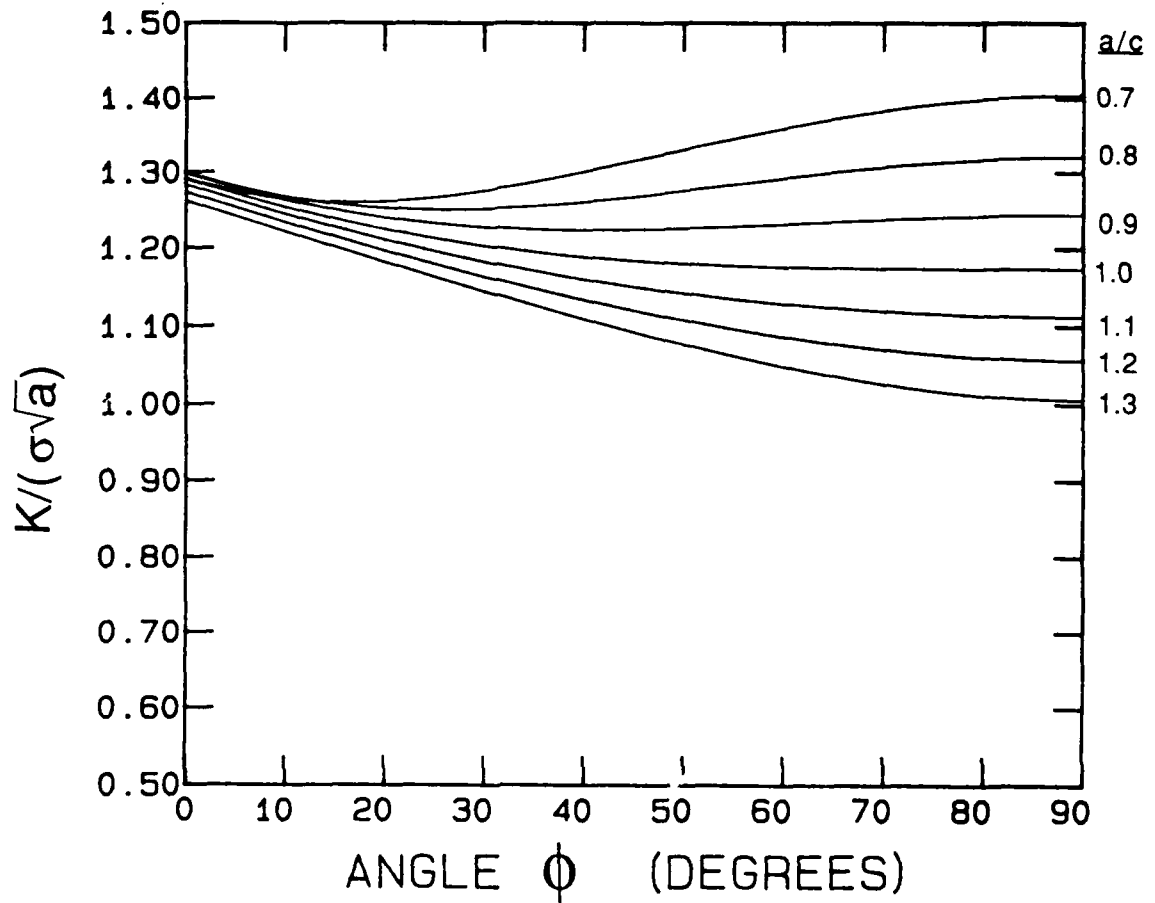


Fig. 5.1 Dimensionless stress intensity factor as a function of the parametric angle  $\phi$  (see Fig. 3.5) for a range in aspect ratios ( $a/c$ ), assuming that  $a$  and  $c \ll$  specimen dimensions. The figure shows that the surface-crack stress intensity factor solution is only mildly sensitive to variations in  $a/c$ .

the parametric angle  $\phi$  (see Fig. 3.5) for a range in aspect ratios ( $a/c$ ), assuming that both  $a$  and  $c \ll$  specimen dimensions. The curves show that the stress intensity factor at the specimen surface ( $K_c$ ) is approximately equal to the stress intensity factor at the crack depth ( $K_a$ ) when  $a/c \approx 0.85$  — similar to the 0.9 value observed in the present experiments. To simulate the actual experimental measurements, the figure was generated assuming that the surface crack length,  $2c$ , was accurately measured and that variations in  $a/c$  were due to variations in crack depth. The series of curves show that  $K$  at any location along the crack front is a relatively insensitive function of crack shape. For example, for  $0.8 \leq a/c \leq 1.2$  the maximum variation in  $K_a$  is approximately  $\pm 11\%$ , and there is an almost negligible variation in  $K_c$ . Since the experimentally determined aspect ratio of  $a/c \approx 0.9$  gives a value of  $K$  that is approximately independent of the angle  $\phi$  (and  $K$  is insensitive to small variations in  $a/c$ ),  $K$  for the small cracks is reasonably represented by a single value at a given set of conditions. Because there is a small numerical uncertainty in the calculation of  $K_c$  due to free surface effects [127],  $K_a$  appears to be a more stable single parameter to represent the surface-crack driving force. Therefore, all of the stress intensity calculations presented in the present work are based on  $K_a$ . This appears to be a reasonable approach, since variations in  $a/c$  due to interactions with microstructural features are not expected to influence  $K$  (and  $da/dN$ ) dramatically, and any irregularities in crack shape should be quickly overcome as the crack attempts to stabilize its shape.

Summarizing the effects of the secondary experimental variables, the contribution of multiple-crack interactions and environment to the rapid growth of small cracks in the present experiments was held to a negligible level, and the possible contribution of crack-shape effect is believed to be minimal, possibly being an issue only for the very smallest crack sizes and limited primarily to the Ti-8Al(a). Otherwise, variations in the semielliptical shape of the small cracks were extremely limited and were consistent with

the pertinent stress intensity factor solution, which itself is only a mild function of crack shape. Having eliminated the possible contribution of the secondary experimental variables, it appears that the remaining three variables were the principal factors contributing to the "anomalous" small-crack growth rates observed in the present results. Each of these will now be discussed in detail.

## 5.2 Primary Experimental Variables

### 5.2.1 Effects of Crack-Tip Plasticity

Although the experimental program was conducted to avoid bulk and notch plasticity, the maximum stress levels of 60 and 90 percent of  $\sigma_y$  were selected to allow an assessment of the contribution of crack-tip plasticity effects to the rapid growth of small cracks (when correlated with  $K$ ) under nominally elastic loading. The basic objective in this regard was not to verify the worthiness of the various existing elastic-plastic fracture mechanics parameters, but rather to investigate the useful limits of the linear elastic fracture mechanics parameter,  $K$ . In fatigue, this assessment obviously considered both nominally applied  $\Delta K$  and  $\Delta K_{eff}$ . The appeal of the continued use of  $K$  was based largely on the general utility of this parameter in the characterization of fatigue crack growth and the very extensive large-crack  $da/dN$ - $\Delta K$  data base that exists for a wide range of materials. Therefore, the only crack-driving-force parameter that will be addressed in this discussion is the stress intensity factor, considering various possible modifications for crack-tip plasticity and crack closure.

As stated earlier, the small-scale yielding assumption, which is a theoretically necessary condition for the generality of  $K$ , requires that the crack-tip plastic zone size ( $r_p$ ) be small in comparison with the crack length and all specimen dimensions. In the



present small-crack experiments,  $r_p$  was small relative to specimen dimensions, but under some circumstances the extent of the plastic zone was a significant fraction of the crack size.

Since  $K$  is approximately proportional to  $\sigma(a)^{0.5}$  for most geometries, fatigue crack propagation tests of conventional large-crack specimens are necessarily conducted at relatively low stress levels and the ratio of the plastic zone size to crack length ( $r_p/a$ ) is small. Conversely, to achieve equivalent values of  $\Delta K$  in small-crack tests requires a much higher stress, and  $r_p/a$  may become large, violating small-scale yielding. To assess the significance of crack-tip plasticity, the commonly used Irwin estimate of the plastic zone size given in Eq. 2.5 ( $r_p = \alpha(K/\sigma_y)^2$ ) may be combined with the stress intensity factor solution for the appropriate crack geometry to estimate  $r_p/a$ . For example, assuming a semicircular surface crack that is much smaller than the specimen dimensions, the Newman and Raju solution for the stress intensity factor at the specimen surface,  $K_C$ , may be reduced to the simple expression:

$$K_C = F \sigma(c)^{0.5} \quad (5.1)$$

where  $F$  is a geometrical factor that depends only on the angle  $\phi$ , which defines angular position along the crack front (Fig. 3.5). Substituting Eq. 5.1 into the expression for the plastic zone size (Eq. 2.5) gives

$$r_p/a = \alpha F^2 (\sigma/\sigma_y)^2, \quad (5.2)$$

indicating that  $r_p/a$  is independent of crack length.

Equation 2.5, however, suffers a basic limitation as  $\sigma$  approaches  $\sigma_y$ . For example, considering a small semicircular crack and assuming plane stress constraint ( $\alpha = 1/\pi$ ), at the specimen surface  $F = 1.29$  and Eq. 2.5 becomes

$$r_p/a = 0.53 (\sigma/\sigma_y)^2, \quad (5.3)$$

indicating that  $r_p/a$  achieves the unlikely value of 0.53 when the net-section stress equals the yield strength.

To correct for this inconsistency, it is necessary to use a more general crack-tip stress-field solution. One such estimate [264] gives

$$r_p/a = 1/(1-(\sigma/\sigma_y)^2)^{0.5} - 1 \quad (5.4)$$

This equation, which is also independent of crack length, provides a more satisfying result:  $r_p/a \rightarrow \infty$  as  $\sigma/\sigma_y \rightarrow 1$ . Furthermore, the expression has been found by Lankford et al [63] to correspond well with the experimentally measured plastic zone size of small cracks in the aluminum alloy 7075-T651.

For the present test conditions, the various calculations of the normalized plane-stress plastic zone size for a semicircular surface crack are given in Table 5.1. Along with the estimates of the monotonic plastic zone size, a calculation of the cyclic plastic zone size based on Eq. 2.6 is presented. As shown, particularly by Eq. 5.4,  $r_p/a$  for the different stress levels varies dramatically, approximately satisfying the small-scale yielding criterion for  $\sigma_{\max}/\sigma_y = 0.6$ , while significantly violating the same assumption when  $\sigma_{\max}/\sigma_y = 0.9$ . Since all of the calculations are independent of crack length, however, violation of the small-scale yielding assumption does not appear to

explain the rapid growth of small cracks. The evidence gathered under the current project clearly shows that small cracks, which initially grow rapidly, eventually achieve growth rates that are consistent with the large-crack trend, but the calculations show that  $r_p/a$  for the small cracks has remained constant.

Table 5.1: Normalized Plastic Zone Size Calculations

$\sigma_{max}/\sigma_y$	Eq. 5.3 $r_p/a$	Eq. 5.4 $r_p/a$	Cyclic $r_p/a$
0.6	0.19	0.25	0.05
0.9	0.43	1.29	0.11

Among the shortcomings of all of the plastic-zone estimates is the failure to consider influence of slip character on the form of the crack-tip plastic zone. As discussed in section 4.2.5.4.1, a relatively consistent effect of stress level on small cracks was observed in Ti-4Al and Ti-8Al(a) (Figs. 4.26 and 4.28, respectively), but the crack growth rate data for Ti-8Al(s) tested under similar conditions (Fig. 4.27) showed no significant effect of stress level. This apparent inconsistency might suggest a slip-character dependence of the effect of crack-tip plasticity on the propagation of small fatigue cracks. However, as shown in Figs. 4.43-4.45, the data from each of the three materials at both stress levels are collapsed into a single band when plotted against  $\Delta K_{eff}$ . Although in some cases the small-crack data fall above the large-crack  $da/dN-\Delta K_{eff}$  trend, the small-crack data consistently fall along a single band, independent of stress level. Thus, after accounting for crack closure, the large difference in the extent of crack-tip plasticity associated with the two stress levels appears to have a negligible influence on crack growth rate under the nominally elastic loading conditions used in the test program.

This finding is in contrast with the analytical predictions and suggests that the small-scale yielding assumption is significantly less stringent than previously believed. It should be noted that the utility of  $\Delta K$  and  $\Delta K_{\text{eff}}$  for small cracks in Ti-6Al-2Sn-4Zr-6Mo (which exhibits much lower levels of crack closure than the present Ti-Al alloys) has been demonstrated by Larsen et al [255] in similar tests over a range of stress ratios and the same relative stress levels ( $\sigma_{\text{max}}/\sigma_y = 0.6$  and  $0.9$ ).

### 5.2.2 Local Microstructural Effects

Although the principal microstructurally-controlled variable in the Ti-Al alloys was slip character, a number of other potential, minor microstructural effects on crack growth existed in the experimental program. Some of the microstructural effects directly influence crack propagation, while many are more subtle, being largely manifested through their influence on crack closure. Because of the close interrelationship between microstructure and crack closure in Ti-Al alloys, the discussion of these factors will be necessarily intertwined, although their discussion will be divided roughly into separate sections. In considering the influence of both microstructure and crack closure, it is particularly important to identify effects that differ for large and small cracks.

#### 5.2.2.1 Effects of Grain Boundaries

As discussed in the Chapter 2, grain-boundary interactions with small cracks may differ from those of large cracks. From a statistical point of view, crack initiation should occur at the most favorable location, based on factors that include preexisting material or surface-finish defects, local stress level, orientation of a critical slip system, grain size, and local elastic and plastic constraint. Although a crack may form at a "weak" location in the microstructure, subsequent propagation depends on the favorable orientation of

adjacent grains, and lacking such, nonpropagating cracks may be expected to occur. The critical small cracks, however, are those that have adjacent grains favorably oriented for continued crack propagation and which do not experience significant resistance to crack growth at the first grain boundary.

The experimental approach used for the present Ti-Al small-crack experiments attempted selectively to identify the specific small crack that would eventually fail the specimen. Often this was possible, but in a few instances the specimen failed from one or more separate crack(s). Clearly, within the life of several of the individual small-crack specimens, nonpropagating cracks appeared to exist. It was impossible, however, to distinguish between apparently nonpropagating cracks and very slowly growing cracks, since the specimen quickly failed from the rapidly propagating small crack. In this regard, it should be recognized that the small-crack data presented here represent the biased population of critical small cracks, while excluding the more benign (slower growing) cracks. Thus, the grain boundary interactions that were observed should also be biased. Such bias is significant, however, in that it corresponds to the cracks that govern a material's fatigue capability.

The influence of grain structure on small cracks was routinely observed in the photographic measurements of surface crack length as shown by the  $dc/dN-\Delta K$  data of Fig. 4.31. Close inspection of the photographic record of the propagation of the small cracks, particularly in the Ti-8Al(s) and Ti-8Al(a), revealed an intermittent pattern of growth that was well correlated with grain boundary position. Since the photographs were taken while the specimen was held under 75% of the maximum fatigue load, the small cracks were held open, and it was relatively easy to distinguish a crack from a slip band. Consistent with the findings on aged Ti-8.6Al [112,113], small cracks were commonly observed to propagate along planar slip bands and to deflect at grain boundaries in order

follow the most favorably oriented slip system. Slip-band formation in the grain immediately ahead of the crack tip routinely required an extended period, but there was no visual evidence of an open crack until after a very well-defined slip band had developed. At this point, the photographic images indicated that the period required to transform the slip band into an open crack corresponded to a very small number of cycles, often occurring between successive photographs. This intermittent pattern of crack growth often resulted in periodic variations in  $dc/dN$  that corresponded roughly with the grain size.

It should be recognized that the discontinuous nature of small-crack propagation across grain boundaries is consistent with the behavior of large cracks. The extremely high measurement precision (of the order of  $1\ \mu\text{m}$ ) that is necessarily used to track the advance of small cracks is much greater than for techniques typically used for large cracks. Coupled with the fact that the majority of the small-crack data reported in the literature are from crack length measurements on the specimen surface, significant interactions of the crack front with distinct microstructural features should be expected.

If the measurement of the size of a small surface crack were averaged along the entire crack front (for example, using the IDG compliance measurements), a much more continuous crack advance would be indicated. Rather than observing crack/grain-boundary interactions only on the specimen surface, three-dimensional measurement techniques effectively monitor crack advance over a crack front of length  $\pi(a)$ , and this length quickly encompasses many grains. Moreover, if the small-crack data were reduced to the form of  $da/dN-\Delta K$  in a manner similar to that used for large cracks (ASTM standard E647 recommends a minimum crack extension of  $254\ \mu\text{m}$  between data points), the variability in small-crack growth rate would be extremely reduced. However, such a data reduction procedure is not realistic for small cracks because of their

size. Thus, the experience provided by the current experimental program suggests that interactions of small cracks with grain boundaries are not fundamentally different from large cracks (although the interactions may be more selective).

#### 5.2.2.2 Effects of Grain Size

It is well known that the reduction in slip length that accompanies a reduction in grain size normally results in increased yield strength, and with a few exceptions [e.g., 89,90; see Section 2.5.2], fatigue strength is also increased with decreasing grain size. Conversely, decreasing grain size often leads to faster fatigue crack growth rates, particularly in the near-threshold regime.

Although grain size was not varied in the present experiments, crack growth data at  $R = 0.1$  are available from research by Allison on two separate heats each of Ti-4Al and Ti-8Al; the Ti-8Al was tested in the solution-treated and quenched as well as the aged condition. As a simple measure of the effect of grain size effect on crack growth, a comparison of the measured values of  $\Delta K$ ,  $K_{cl}$ , and  $\Delta K_{eff(th)}$  is presented in Table 5.2. A measure of test-to-test variability is provided by the very similar results found when comparing the current Ti-4Al data with those of Allison's Ti-4Al (heat 2), which is exactly the same material — heat treated and machined separately. Considering the current test results, however, there is no clear effect of grain size. Although data from Allison's Ti-8Al(s) indicate a significant effect of grain size on  $\Delta K_{th}$ , these data are not consistent with the present results. In the Ti-8Al(a), the reported values of  $\Delta K_{th}$  are both higher than the current results, particularly for an approximately equivalent grain size. Considering only the Allison data, there is a much more significant effect of grain size on Ti-8Al(s) than in Ti-8Al(a). Thus, the available data demonstrate no clear effect of grain size on either  $\Delta K_{th}$  or  $K_{cl}$ .

One notable result emerges from the collective data of Table 5.2. The values  $\Delta K_{\text{eff(th)}}$  for the various tests and heats of all three materials are remarkably consistent; the standard deviation of the six  $\Delta K_{\text{eff(th)}}$  values is 0.28 MPa $\sqrt{\text{m}}$  compared with a standard deviation of 4.48 MPa $\sqrt{\text{m}}$  for  $\Delta K_{\text{th}}$ . Thus, although the available data do not define a clear effect of grain size on the growth of large cracks, the variability that exists appears to be directly related to the influence of the microstructure on  $K_{\text{cl}}$ , and after accounting for crack closure, there is a negligible effect of grain size on the threshold crack growth behavior of large cracks.

Table 5.2: Effect of Grain Size on Threshold Stress Intensity Factor Range and Crack Closure Stress Intensity Factor for Tests Conducted at  $R = 0.1$

<u>Material</u>	<u>Grain Size<sup>*</sup></u> <u>(<math>\mu\text{m}</math>)</u>	<u><math>\Delta K_{\text{th}}</math></u> <u>(MPa<math>\sqrt{\text{m}}</math>)</u>	<u><math>K_{\text{cl}}</math></u> <u>(MPa<math>\sqrt{\text{m}}</math>)</u>	<u><math>\Delta K_{\text{eff(th)}}</math></u> <u>(MPa<math>\sqrt{\text{m}}</math>)</u>
Ti-4Al <sup>1</sup>	60	4.50	2.91	2.09
Ti-4Al <sup>2</sup> Heat 1	40	5.5	---	---
Ti-4Al <sup>2</sup> Heat 2	70	4.3	1.6	2.7
Ti-8Al(s) <sup>1</sup>	80	12.26	11.57	2.05
Ti-8Al(s) <sup>2</sup> Heat 1	40	12.5	---	---
Ti-8Al(s) <sup>2</sup> Heat 2	70	16.8	14.7	2.1
Ti-8Al(a) <sup>1</sup>	80	6.71	4.85	2.61
Ti-8Al(a) <sup>2</sup> Heat 1	40	7.5	---	---
Ti-8Al(a) <sup>2</sup> Heat 2	70	8.9	6.6	2.3

\* Grain size defined by mean-linear-intercept.

1. Data from current experiments.

2. Data from Ref. [122].

In the present small-crack experiments, grain size was not a test variable. The only existing data on the effect of grain size on the growth of small cracks in Ti-Al alloys are those of Gerdes et al [112], which are shown in Fig. 2.10 and discussed in section 2.5.2. These data, which were generated in vacuum, show that increasing grain size from 20 to 100  $\mu\text{m}$  significantly improves the material's resistance to the propagation of large



fatigue cracks but has a slightly opposite effect on small cracks. Although crack closure was not measured in these experiments, the grain-size effect on large cracks was argued to be partially produced by closure differences. Conversely, it was suggested that the small cracks did not experience crack closure and that the higher density of grain boundaries in the the small grain-size alloy was responsible for the improved resistance to small-crack growth in this material. These assertions appear consistent with the experience acquired from the present test program, although the Ti-8.6Al behavior might be somewhat different for tests performed in air instead of vacuum.

As discussed in Chapter 2, the size of the key microstructural unit has been argued to be the factor that defines the crack-size limit of linear elastic fracture mechanics. Implicit in the use of the stress-intensity factor to correlate crack growth rate data is the continuum assumption of solid mechanics. This assumption is violated when the crack length approaches the scale of key microstructural dimensions in materials that exhibit crystallographic elastic and plastic anisotropy such as the present  $\alpha$ -phase titanium alloys. In the Ti-Al alloys, grain size is the primary dimension of interest. Although the Ti-8Al(a) alloy contains second-phase precipitates, their diameter of approximately  $0.01\ \mu\text{m}$  is insufficient to disturb the crack-tip stress field appreciably on a macroscale. Considering the collective small-crack test results, six of the cracks achieved a crack size sufficient for the small-crack data to converge with the data from large cracks in C(T) specimens. The pertinent data for these tests are presented in Table 5.3. All of these experiments were performed under  $R = 0.1$  fatigue, and data from both stress levels and all three materials are reported. The surface crack half-length,  $C$ , where the crack growth rate data became crack-size independent is indicated for each material along with the mean-linear-intercept grain size,  $\bar{l}$ . The indicated crack size is clearly much larger than the size of the critical microstructural unit – a finding that is consistent with results reported by Daeubler and Thompson on 1080 pearlitic steel [118]. For the tests of the

three materials at the lower stress level, the ratio  $C/\bar{l}$  varies by as much as a factor of 3.8 for the Ti-8Al(s) versus the Ti-8Al(a) – materials which have an identical grain size. Thus, the tabulated data suggest that, at best, the crack-size limit for applicability of  $\Delta K$  is only roughly related to the grain size. Obviously there are other important factors.

Table 5.3: Crack Size at Which Small and Large-Crack Data Converge When Plotted Versus Nominally Applied  $\Delta K$

Material	R	$\sigma_{max}/\sigma_y$	C ( $\mu\text{m}$ )	$\bar{l}^*$ ( $\mu\text{m}$ )	$C/\bar{l}$
Ti-4Al	0.1	0.6	660	60	11.0
Ti-4Al	0.1	0.9	540	60	9.0
Ti-8Al(s)	0.1	0.6	1500	80	18.8
Ti-8Al(s)	0.1	0.9	1060	80	13.3
Ti-8Al(a)	0.1	0.6	400	80	5.0
Ti-8Al(a)	0.1	0.9	480	80	6.0

\*  $\bar{l}$  = mean grain boundary intercept distance.

### 5.2.2.3 Effects of Crystallographic Texture

As shown earlier, a mild basal texture existed in the Ti-4Al alloy plate, while a more significant basal texture was observed in the Ti-8Al. This tendency is consistent with the availability of twinning as a deformation mode in addition to  $a$  and  $c+a$  slip in Ti-4Al, while twinning is suppressed in the more aluminum-rich Ti-8Al [119].

Although the critical resolved shear stress for  $c+a$  slip is significantly higher than  $a$  slip in both alloys, deformation having a  $c$  component could be accommodated by slip plus twinning in Ti-4Al, while only slip was available in the Ti-8Al. Thus, due to the more restrictive deformation in Ti-8Al, this material should develop the basal texture more readily.

As expected theoretically and confirmed by the tensile tests, both of the Ti-Al alloy compositions exhibited elastic and plastic planar isotropy. The early work of Allison [122] on C(T) specimens of similarly textured Ti-Al alloys indicated that fatigue crack growth rates were also independent of orientation within the rolling plane. Although all of the crack propagation experiments performed within the present investigation were of a single orientation (T-L; the normal to the crack plane oriented in the transverse direction and a longitudinal direction of crack propagation), the small-crack tests provided an indirect assessment of the effect of texture on crack growth. The surface cracks in these tests were oriented such that the crack depth ( $a$ ) advanced along the plate rolling direction, while the surface crack extension ( $c$ ) was in a direction normal to the original rolling plane. In spite of this difference, the aspect ratio of the small surface cracks remained  $a/c \approx 0.9$ , consistent with experimental results on untextured material and with the theoretically stable crack shape. The 0.9 aspect ratio was independent of material and, therefore, independent of the difference in texture observed between the Ti-4Al and the Ti-8Al. It is likely that this crack shape would have been altered if moderate levels of texture had a significant effect on the growth of small cracks. Thus it appears that, for the magnitude of the basal texture developed in the present alloys, the effect of texture on the propagation of small fatigue cracks is not appreciable in the present experimental results.

#### 5.2.2.4 Differences in Crack Growth Mechanism

Although differences in crack growth mechanism is an appealing explanation for the differences in the propagation behavior of small and large cracks (when plotted against  $\Delta K$ ), there is little evidence from the present investigation to support this idea. Neither the SEM fractographic investigation nor the quantitative analysis of crack profiles indicated any significant differences between the mechanisms of propagation between the large and small cracks. At the very smallest crack sizes ( $2c < 3$  times the

mean-linear-intercept grain size, approximately), there was an indication of enhanced crystallographic cracking in a small number of cases. At these very small crack sizes,  $\Delta K_{\text{eff}}$  was less able to consolidate the small- and large-crack  $da/dN$  data (see Figs. 4.32 and 4.49). This trend is believed to be associated with a microstructural effect, which may be partially a change in crack growth mechanism. Other microstructural effects that are believed to contribute to the rapid growth of cracks of length ( $2c$ ) less than approximately 3 times the grain size are: (i) crack growth transients associated with crack initiation at a preexisting defect or within a favorably oriented grain and (ii) the ultimate breakdown in the applicability of  $K$  due to local anisotropy.

#### 5.2.2.5 Effects of Alloy Slip Character

In face-centered-cubic alloys, increases in slip planarity are promoted by factors that decrease stacking-fault energy, inhibiting cross slip and encouraging continued dislocation activity on the active slip plane. Alternatively, slip planarity of hexagonal-close-packed materials such as  $\alpha$ -phase titanium-aluminum alloys is promoted by factors that reduce the resistance to dislocation motion on the active slip plane. For example, disruption of short-range order in titanium-aluminum alloys is believed to be responsible for the observed increased slip planarity which develops primarily in the range of 4 to 6 percent aluminum [119]. In aged alloys containing more than approximately 6% Al, slip planarity is further enhanced by shearing of the coherent, ordered  $\text{Ti}_3\text{Al}$  precipitates, resulting in intense strain localization.

The three Ti-Al alloy conditions examined under the current project exhibit the full range in slip character, as illustrated by the typical dislocation structures developed under cyclic loading of each materials shown in Fig. 2.20 from the work of Kim [119]. Short-range-ordering and precipitation effects are absent in the Ti-4Al, and as shown,

this material exhibits fine, weakly developed, cellular arrays of dislocations, primarily of a type on prism planes [119]. The rate of quenching of solution-treated Ti-8Al is apparently insufficient to suppress the development of short-range order, and fatigue damage in this material takes the form of coarse planar arrays of a dislocations, often extending across the full width of individual grains. As revealed by inspection of the Ti-Al phase diagram (Fig. 2.19), aging of solution-treated and quenched Ti-8Al results in the formation of  $\alpha_2$  precipitates, while partially depleting the matrix of aluminum. Since the present Ti-8Al alloy had an oxygen concentration similar to that of the Namboodhiri et al material [229], the modified  $\alpha/\alpha_2$  phase boundary shown in the figure should describe the behavior of the present Ti-8Al(a) material. Thus, assuming that the 550°C aging treatment approached equilibrium conditions, the composition of the  $\alpha$ -phase matrix should be approximately Ti-6Al. As reported by Kim [119], the transition from fine, wavy slip to coarse, planar slip in Ti-Al alloys occurs primarily in the range of 4 to 6 percent aluminum. Thus, although aging produces in a leaner  $\alpha$  phase, the slip in this matrix phase should tend to be similar to that of Ti-8Al(s), modified by the shearing of the  $\alpha_2$  precipitates. As shown in Fig. 2.20, slip character of Ti-8Al(a) results in the formation of the extremely coarse, widely separated, bands of dislocations.

As shown by the results of the tensile tests of the solution-treated alloys presented in Table 4.2, increasing the aluminum content from 4 to 8% increases yield and ultimate tensile strength, while having little influence on ductility or the extent of work hardening. Aging the Ti-8Al moderately increases yield strength but essentially eliminates work hardening, and ductility is significantly reduced. In low cycle fatigue, Kim [119] found that the increasing slip planarity and concentration of slip that is observed in the three alloy conditions produced a reduction in fatigue capability under high-strain conditions. However, in Ti-8Al the aging slightly improved the LCF performance under low plastic strain ranges.

The present high-cycle-fatigue results for the three Ti-Al alloys (outlined in Table 4.3 and shown in Figs. 4.11-4.13) show that the  $10^7$ -cycle fatigue strength correlates roughly with each material's yield strength, which should correlate approximately with critical resolved shear strength. Apparently the concentration of slip associated with the increase in slip planarity in these materials has a much less significant effect on HCF capability than does the increased strength. This observation is consistent with high-cycle-fatigue results in aged Ti-8.6Al, where it was reported that the beneficial strengthening effect of precipitation more than offset the detrimental effect of strain localization caused by precipitate shearing [82].

#### 5.2.2.5.1 Effects of Alloy Slip Character on Fatigue Crack Propagation

The differences in slip character exhibited by the three materials influence a range of properties pertinent to crack propagation. Of potential importance are the effects of slip character on slip reversibility, crack tortuosity and deflection, and crack closure. As discussed earlier, increases in slip reversibility have been suggested to improve crack growth resistance by reducing the rate of damage accumulation [121]. Increases in crack tortuosity are said to increase the energy required for crack extension by increasing the area of the fracture surface, while crack deflection has been argued to reduce the magnitude of the local stress intensity factor. Finally, for fatigue at low stress ratios, crack closure may reduce crack growth rates by reducing the effective stress intensity factor range.

Considering the large-crack  $da/dN-\Delta K$  ( $R = 0.1$ ) data for the three alloy conditions presented in Fig. 4.14, a significant effect of material is evident, consistent with the earlier findings of Allison [112] and the present  $R = 0.5$  data, which are shown in Fig. 4.15. The trend in the data, however, is contrary to the high-cycle-fatigue results

(Table 4.3), since the fatigue crack growth performance of the three materials is ordered in the sequence of decreasing cracks growth rates (higher values of  $\Delta K_{th}$ ) as: Ti-4Al, Ti-8Al(a), Ti-8Al(s). The Ti-8Al(a) had the highest high-cycle-fatigue strength.

Obviously the factors that control HCF behavior in the two Ti-8Al alloys have a much different effect on the growth of large cracks in these materials. Since the three materials have a nearly equivalent, equiaxed grain size (Table 4.1), the crack growth trends cannot have been produced by variations in the size of this primary microstructural feature. The three materials differ moderately in yield and tensile strength (Table 4.2), but the ordering of the crack growth trends is inconsistent with the measured strengths. Moreover, fatigue crack growth rates are not generally related to monotonic strength.

Recognizing that increased slip planarity has been reported to lead to increased slip reversibility in fatigue of Ti-Al alloys [119], it would be expected that the Ti-8Al(a) crack growth performance would be superior to that for Ti-8Al(s). Since the aging has the opposite effect, the influence of slip reversibility on the growth of large cracks in Ti-Al alloys does not appear to be significant.

Recalling the findings of the quantitative fractography, which indicated that the large-crack paths in Ti-8Al(s) and Ti-8Al(a) were very similar in terms of roughness, it appears that effects of crack tortuosity and crack deflection are unable to account for the significant differences in crack growth behavior. Although there is some correlation between the measured roughness and the rates of crack propagation in the Ti-4Al and Ti-8Al(s), this is not believed to be associated appreciably with either crack tortuosity or crack deflection effects, considering the complete lack of correlation for the two Ti-8Al alloys.

When the large-crack propagation data are plotted against  $\Delta K_{eff}$  as shown in Figs.

4.23 and 4.24 for  $R = 0.1$  and  $0.5$  fatigue, respectively, the effect of alloy condition is largely eliminated (all of the data fall within the range of normal experimental error). Clearly differences in crack closure are primarily responsible for the differences in crack growth rates when the data are plotted versus  $\Delta K$ . Since the experimentally measured crack closure so completely accounts for the differences in large-crack propagation behavior, the data strongly confirm the earlier assertions of minimal influences of slip reversibility, crack tortuosity, and crack deflection effects in the Ti-Al alloys. Note that an increase in any of these three factors tends to decrease the macroscopic, mode I, crack growth rate. Therefore, it is not possible for opposing effects of these factors to cancel mutually.

As shown by the  $da/dN$ - $\Delta K$  plot in Fig. 4.40 ( $R = 0.1$ ,  $\sigma_{\max}/\sigma_y = 0.6$ ), the effect of alloy condition on the growth of small fatigue cracks was minimal, and only after appreciable crack growth did the small-crack data fall into agreement with the corresponding large-crack data. In complete contrast with the large-crack results, the small crack data from the three materials were essentially indistinguishable at the lowest  $\Delta K$  values, whereas the large-crack data exhibited three distinctly different values of  $\Delta K_{th}$ . Thus, unless the factors of slip reversibility, crack tortuosity and deflection, and crack closure had offsetting effects, none of these factors influenced propagation of the smallest surface cracks. This is true in spite of the dramatic differences in deformation characteristics as well as differences in fracture surface topography of the three materials. As shown in Fig. 4.57, the small-crack data are collapsed into a very narrow band when plotted against  $\Delta K_{eff}$ .

In contrast to the data at  $\sigma_{\max}/\sigma_y = 0.6$ , the  $da/dN$ - $\Delta K$  small-crack data presented in Fig. 4.41 having  $\sigma_{\max}/\sigma_y = 0.9$  display a limited effect of alloy condition at the smallest crack sizes. This influence of slip character at the smallest crack sizes persists



when the data are plotted against  $\Delta K_{\text{eff}}$  (Fig. 4.58). As the cracks extend beyond their initial sizes, however, the growth rate data from the three materials are consolidated into a single band. The differences in  $da/dN$  for the smallest cracks may be due to differences in crack-tip deformation produced by the various slip characters of the three materials.

The findings of the quantitative fractography indicated that the fracture surfaces of the small cracks were essentially equivalent to those of the corresponding large cracks at a similar growth rate. Although the characters of the fracture surfaces were dependent on material, they were not crack-size dependent, and the concluded absence of an appreciable effect of crack tortuosity and crack deflection on large-crack growth should also apply to small cracks.

#### 5.2.2.6 Effects of Crack Closure

From the collection of fatigue crack growth experiments it is clear that crack closure exerts a very significant influence on the growth of both large and small cracks. As had been speculated [e.g. 37], the beneficial crack-tip-shielding effect of crack closure on the growth of large cracks is minimal for small cracks and only becomes significant after appreciable crack extension. In the Ti-Al alloys, variations in slip character are associated with large differences in crack closure which develop at remarkably similar rates. The following discussion will attempt to identify the underlying reasons for the observed small-crack behavior.

Although they operate simultaneously, the relative contributions of the mechanisms of oxide-, plasticity-, and roughness-induced crack closure appear to be very different. As stated earlier, viscous fluid-induced and phase transformation-induced crack closure are not applicable to the present results. Oxide-induced closure should only become

significant if the thickness of the oxide wedge is of the order of the crack-tip-opening displacement (CTOD), which for large cracks is given approximately by [265]

$$\text{CTOD} = 0.49 (K^2/(\sigma_y E)). \quad (5.5)$$

Although oxide thickness measurements on the Ti-Al alloys were not made, Allison [122] reported measurements showing that the thickness of fracture surface oxides that form during room temperature threshold fatigue crack growth testing of Ti-8Al(s) was approximately 5 nm. This thickness is negligible compared to CTOD for any of the three materials and is consistent with the fact that, in air, titanium alloys normally do not exhibit fretting, which is generally required to develop appreciable levels of oxide-induced closure. The assertion that oxide-induced closure does not achieve significant levels is supported indirectly by the large-crack  $K_{CI}$  measurements, which are approximately independent of  $\Delta K$ . If oxide-induced crack closure, which is believed to operate primarily at near-threshold growth rates, was significant then the measurements of  $K_{CI}$  should have been higher near  $\Delta K_{th}$ .

As shown in Fig. 2.15 [156], numerical computations of plasticity-induced crack closure indicate that  $\sigma_{op}/\sigma_{max}$  is a function of normalized stress level ( $\sigma_{max}/\sigma_o$ ;  $\sigma_o$  = flow stress), stress ratio, and three-dimensional constraint. Holding these factors fixed,  $\sigma_{op}/\sigma_{max}$  (which is equal to  $K_{op}/K_{max}$ ) is a constant, indicating that  $K_{op}$  is a linearly increasing function of  $K_{max}$ . This trend is supported by the independent computations by Nicholas et al [266] for small cracks, although  $K_{op}/K_{max}$  was indicated to depend on stress level. The present large-crack closure measurements (Figs. 4.19 and 4.20) show that  $K_{op}/K_{max}$  is clearly not a constant but depends significantly on material and on  $K_{max}$ . Near  $\Delta K_{th}$ ,  $K_{op}/K_{max}$  for the three materials ranges approximately from 0.5 to 0.9 and decreases as  $K_{max}$  increases. At the highest values of  $K_{max}$ ,  $K_{op}/K_{max}$  appears to

assume an approximately constant value of 0.25 under  $R = 0.1$  fatigue (Fig. 4.19). This value is in very good agreement with the numerical prediction for the appropriate plane-strain constraint (see Fig. 2.15), although  $K_{op}/K_{max}$  may decrease slightly as constraint becomes more completely plane-strain as  $K_{max}$  decreases. Thus, it appears that the contribution of plasticity-induced crack closure in the Ti-Al alloys is reasonably described by  $K_{op}/K_{max} \approx 0.25$  and that other mechanisms are responsible for the closure levels greater than this. The large differences in  $K_{op}/K_{max}$  for the three materials strongly support the contention that factors in addition to plasticity make important contributions to crack closure in the Ti-Al alloys.

The functional dependence of roughness-induced crack differs from that of plasticity-induced closure. Although much more complete formulations may be appropriate for specific asperity and specimen geometries, Eq. 5.5 may be used to illustrate the general form of the dependence. This equation shows that  $K$  is proportional to  $(CTOD)^{0.5}$ , and assuming that contact of the fracture surfaces occurs immediately behind the crack tip,  $K_{cl} \propto (CTOD_{cl})^{0.5}$ . Assuming that the height of the load-carrying asperities is a constant, then  $CTOD_{cl}$  and  $K_{cl}$  are constants. If  $K \propto \sigma\sqrt{a}$ , then  $K_{cl}/K_{max} \propto 1/(\sqrt{a})$  for a constant load-amplitude fatigue test. Summing the contributions of plasticity- and roughness-induced crack closure results in a form similar to the observed large-crack behavior shown in Fig. 4.19, indicating that roughness-induced crack closure plays a significant role in determining the near-threshold crack growth behavior of the Ti-Al alloys.

The large differences in  $K_{cl}/K_{max}$  for the three Ti-Al alloys point to the significant influence of slip character on crack closure. The experimental evidence from the two Ti-8Al alloy conditions is particularly compelling, since these materials have identical compositions and similar strengths, while exhibiting dramatically different levels of

crack closure. The manner in which the microstructural differences are manifested is, however, unclear. As shown by the quantitative fractography, no direct relationship between fracture surface roughness and  $K_{CI}$  appears to exist. It is possible that the quantitative fractography was of insufficient resolution to characterize the critical topological features that control the level of roughness-induced closure, or fracture surface profiles from the plane-strain region of the specimen may have been more revealing. It is speculated, however, that neither of these factors was primarily responsible for the failure to identify controlling topological features. Rather, it is believed that the primary sources of the roughness-induced crack closure were features that cannot be quantified by crack profile analysis on a single fracture surface. Factors that require characterization of the mating of fracture surface mating include: the effect of asperity pullout [139] along with the effect of mode II displacements on crack closure. Close inspection of the small-crack specimens prior to fracture revealed that contact of the fracture surfaces due to surface roughness occurred primarily at discrete asperities. Presumably, this mechanism contributed to closure in the C(T) specimens.

It is well known that appreciable, local mode II deformation accompanies the macroscopic, mode I deformation that occurs during stage II crack growth. These mode II deformations are believed to be primarily responsible for the development of roughness-induced crack closure. Such shear deformation cannot, however, be documented by examining the crack profile from a single fracture surface. Even if both surfaces of an unfractured specimen are inspected, it is very difficult to quantify residual, microscopic, mode II displacements.

Considering the respective slip characters of the three Ti-Al alloys, the following speculative explanation for the closure behavior observed in the large-crack tests is presented. The finely distributed wavy slip that occurs in the Ti-4Al (see Fig. 2.20) is

believed to promote uniform crack-tip deformation, which allows the crack to proceed along a relatively flat path having limited mode II deformation and few significant asperities. The crack closure that occurs in this material is, therefore, due primarily to plasticity, and only near  $\Delta K_{th}$  does CTOD become small enough for roughness-induced closure to contribute significantly to  $K_{cl}/K_{max}$ .

The physical processes that lead to crack closure in Ti-8Al(s) are believed to be quite different. Crack propagation in this material, which exhibits coarse planar slip, proceeds along interconnecting slip bands that often deflect markedly as the local deformation proceeds across grain boundaries. Thus, the crack path is very tortuous, and the amplitude of the crack tortuosity is controlled by the slip length, which is governed by the grain size. The mode II deformations that accompany the crack extension are probably controlled by the intensity and the breadth of the residual shear displacements parallel to the local segments of the crack. In addition, secondary slip lines adjacent to the fracture surface probably contribute to the formation of distorted asperities that do not mate well with the opposing fracture surface. The combination of a very rough fracture path characterized by appreciable local mode II residual deformations and distorted asperities, therefore, is believed to be responsible for the microstructurally controlled component of crack closure in Ti-8Al(s). When this closure component is combined with the underlying plasticity-induced closure, a very large value of  $K_{cl}$  results. In the near- $\Delta K_{th}$  region, the overall effect of the crack closure is to shield the crack tip from approximately 85% of the remotely applied  $\Delta K$  in  $R = 0.1$  fatigue.

As discussed earlier, aging the Ti-8Al results in the formation of fine, coherent, ordered,  $\alpha_2$  precipitates that are sheared by dislocations that travel in planar arrays in the matrix. Although precipitation depletes the matrix of short-range-ordered aluminum atoms, the phase diagram shown in Fig. 2.19 shows that the matrix composition does not

fall below the approximate Ti-6Al composition that is required to promote planar slip. Thus, in terms of length (which is controlled primarily by grain size) and orientation (which is controlled by crystallographic orientation and texture), the resulting slip lines that precede crack formation and growth tend to resemble those developed in Ti-8Al(s). Because the slip in the Ti-8Al(a) is extremely localized due to the cutting of the precipitates, however, the slip lines in this material tend to be much more narrow than those in the Ti-8Al(s). Therefore, although the slip within an individual slip band in Ti-8Al(a) is extremely intense, the residual mode II displacement associated with the fractured slip band is believed to be much less than in the Ti-8Al(s). Moreover, the localization of slip in the aged material probably reduces the occurrence of the three-dimensional deformation that is necessary for the formation of distorted, misfitting asperities. The component of microstructurally controlled, roughness-induced crack closure is, therefore, much less in the aged Ti-8Al than in the Ti-8Al(s). This hypothesis is supported by the relatively low values of  $K_{CI}$ , in spite of the very high measurements of fracture surface roughness.

#### 5.2.2.6.1 Closure of Small Cracks

In contrast to the approximately constant levels of  $K_{CI}$  observed in C(T) specimens, small-crack closure undergoes a period of transient development. As shown in Figs 4.46 and 4.47 ( $\sigma_{max}/\sigma_y = 0.6$  and  $0.9$ , respectively), small-crack closure develops at an essentially equivalent rate in the three Ti-Al alloys, although there is a modest effect of stress level (closure develops more slowly at the higher stress). Only as the small-crack closure levels approach the large-crack trends does  $K_{CI}$  become approximately independent of  $K_{max}$ . The point at which the small-crack  $K_{CI}$  achieves the large-crack behavior appears to agree approximately with the point at which the small- and large-crack data join when plotted against  $\Delta K$ . These crack sizes are listed in Table 5.3

for the specimens for which sufficient crack growth occurred. These data indicate that a crack length as great as  $2c = 3.0$  mm is required to fully develop closure in the small surface cracks.

A trend in the development of closure exists for most of the Ti-8Al(s) small-crack tests performed over a range of stress ratios, as shown in Figs. 4.48 and 4.49 ( $\sigma_{\max}/\sigma_y = 0.6$  and  $0.9$ , respectively). At the lower stress level, the  $R = 0.1$  and  $-1.0$  data approximately coincide, while the  $K_{Cl}$  data for  $R = 0.5$  are slightly higher. The  $R = 0.5$  values probably exceed the other measurements because this specimen never experienced a minimum stress less than  $0.5 \sigma_{\max}$ . The load-carrying asperities are believed to be partially compressed, plastically, at the minimum stress, and greater compression occurs for lower stress ratios. Apparently most of the plastic compression occurs during the tensile part of the loading cycle, since the  $R = 0.1$  and  $R = -1.0$  data are similar.

For  $R = 0.5$  and  $0.1$  fatigue, the  $\sigma_{\max}/\sigma_y = 0.9$  test results (Fig. 4.49) are similar to the data at the lower stress. The  $R = -1.0$  data, however, display a very different behavior. Following crack initiation, which was consistently performed with  $\sigma_{\max}/\sigma_y = 0.6$ , the maximum stress level was increased. During subsequent small-crack growth a nominally negative level of closure developed. On these axes, this indicates that the crack remained open at zero load, and closure only occurred under compression loading. At this high stress level a residual crack opening displacement accumulated, apparently due to cyclic ratcheting. This was the only test condition for which a negative  $K_{Cl}$  developed with increasing crack length. The  $R = -1.0$ ,  $\sigma_{\max}/\sigma_y = 0.6$   $K_{Cl}$  data shown in Fig. 4.48 were initially negative, but a positive trend quickly developed.

If  $K_{Cl}$  is proportional to  $K_{\max}$ , then  $K_{Cl}/K_{\max}$  must be a constant, independent of  $K_{\max}$  and crack length. For  $\sigma_{\max}/\sigma_y = 0.6$  testing (Fig. 4.42), this appears to be true,

approximately. At the higher stress level of  $\sigma_{\max}/\sigma_y = 0.9$  (Fig. 4.43),  $K_{cl}/K_{\max}$  appears to increase with increasing  $K_{\max}$  and crack length. The Ti-8Al(s) data for the three different stress ratios (Fig. 4.44 and 4.45) indicate that  $K_{cl}/K_{\max}$  tends to be approximately constant for  $\sigma_{\max}/\sigma_y = 0.6$  but increases slightly with increasing  $K_{\max}$  at the higher stress level. In a few instances  $K_{cl}/K_{\max}$  exhibits initial transient behavior, but quickly stabilizes.

The general trend of the development of small-crack closure appears to be as shown schematically in Fig. 5.2. The small-crack closure stress intensity increases linearly with increasing  $K_{\max}$  (where  $K_{\max} \propto \sqrt{a}$ ). The slope of this line is approximately equal

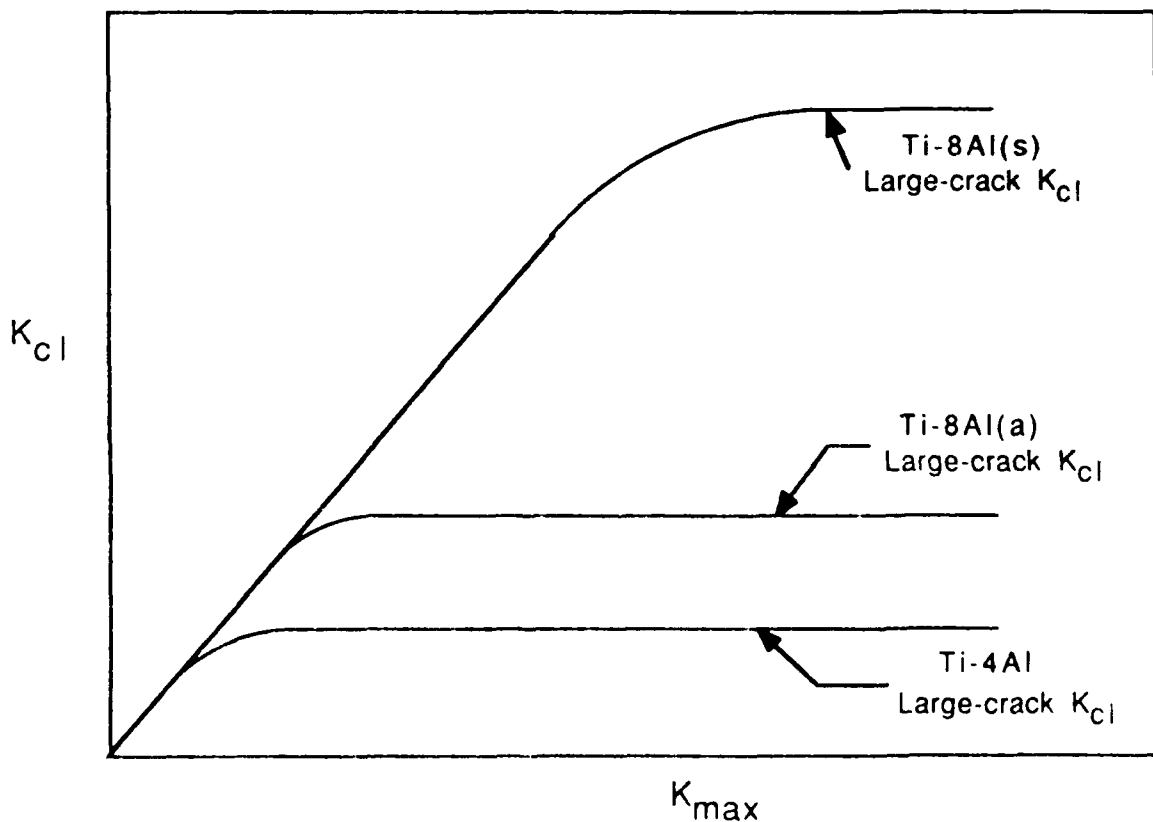


Fig. 5.2 Schematic illustration of the form of the development of small-crack closure in the three Ti-Al alloys.



to the fully developed value of  $K_{CI}/K_{max}$  for large cracks in C(T) specimens. Under some circumstances the actual  $K_{CI}$  versus  $K_{max}$  data may fall below the indicated line (e.g. during the early growth at the high stress level). Under no conditions does  $K_{CI}$  develop more rapidly than illustrated in the figure. Thus, until achieving the large-crack  $K_{CI}$ , the small-crack  $\Delta K_{eff}$  is much greater than the large-crack  $\Delta K_{eff}$ . The data indicate that  $\Delta K_{th}$  for large cracks is largely governed by roughness-induced crack closure and that most of the difference in  $da/dN-\Delta K$  between the small- and large-crack data is associated with the transient development of crack closure and the resulting absence of the conventional  $\Delta K_{th}$  for the small cracks.

The ability of  $\Delta K_{eff}$  to consolidate the large- and small-crack growth rate data into a single band, regardless of material, stress level, or stress ratio, strongly confirms that crack-closure effects are primarily responsible for the crack-size dependence of  $da/dN-\Delta K$  data in Ti-Al alloys. The experimental measurements show that small fatigue cracks undergo a transient period during which  $K_{CI}$  develops from an initially negligible value. Only after sufficient crack extension has occurred does the crack achieve the level of crack closure measured in more conventional large-crack testing. The crack size required to fully develop crack closure ranged approximately from 5 to 18 times the mean-linear-intercept grain size. This finding is significant because it indicates that much of the "anomalously" rapid growth of microstructurally small cracks may be associated with microstructurally-controlled crack-closure effects rather than effects of crystallographic anisotropy in the region of the crack tip. Previously, it had often been suggested that violation of the continuum assumption of solid mechanics was responsible for the inability of  $\Delta K$  to correlate the data of large and small cracks of microstructural dimensions. The present findings indicate that this factor is limited to cracks of approximate size,  $2c < 3$  times the mean-linear-intercept grain size.

It appears that the primary effect of slip character is to influence the topography of the fatigue fracture surface and thereby affect the level of roughness-induced crack closure. In the large-crack tests, the influence of roughness-induced closure was fully developed, while similar closure levels were only achieved in the small cracks after significant growth. After accounting for its influence on crack closure, slip character appears to have little effect on the inherent resistance of the Ti-Al alloys to crack growth. This is in sharp contrast to the effects of slip character on low-cycle-fatigue crack initiation [119].

### 5.3 Implications for Design of Damage Tolerant Alloys

The findings of this research project have particular significance with regard to design of alloys and their subsequent use as structural materials. The data suggest that there is limited potential to influence small-crack growth behavior through microstructural modifications that enhance roughness-induced crack closure. Although implementation of such alloy design philosophies may have a dramatic effect on the behavior of large fatigue cracks, the effect may be extremely misleading, since in all probability, small fatigue cracks will not be similarly affected. Moreover, total fatigue life calculations that use data generated in conventional long-crack tests may seriously underestimate the early growth of a fatigue crack, leading to a very significant error in the calculation.

## CHAPTER 6

### SUMMARY AND CONCLUSIONS

The following paragraphs summarize the findings and conclusions of the research on the propagation of small fatigue cracks in titanium-rich Ti-Al alloys — specifically, solution-treated Ti-4Al and Ti-8Al as well as aged Ti-8Al. The test program focused on the effects of microstructure and crack closure on the growth of small fatigue cracks. Other factors that may influence the behavior of small cracks were intentionally constrained. Although in many instances the generality of the findings may exceed the bounds of the research, extrapolation of the findings to other alloy systems and testing conditions should be done with appropriate caution.

1. In all three alloy conditions and for all test conditions, which included stress levels ranging from 60 to 90% of the respective material's yield strength and, for Ti-8Al(s), stress ratios of -1.0, 0.1, and 0.5, small surface cracks propagated faster than large cracks subjected to an equivalent  $\Delta K$ . The small cracks also propagated at values of nominally calculated  $\Delta K$  that were significantly below the large-crack  $\Delta K_{th}$ .
2. Small-crack  $da/dN$  data from each of the three materials at both stress levels are collapsed into a single band when plotted against  $\Delta K_{eff}$  and are in approximate agreement with similar data from tests of conventional large-crack, C(T), specimens. Furthermore, plotting  $da/dN$  versus  $\Delta K_{eff}$  largely eliminates the apparent effect of stress ratio on the growth of small cracks in Ti-8Al(s).

3. The potential contribution of multiple-crack interactions and environment to the rapid growth of small cracks in the experiments was held to a negligible level, and the possible contribution of crack-shape effects is believed to be minimal. The average aspect ratio of the small cracks was  $a/c = 0.9$ , and variations in the semielliptical shape of the small cracks were extremely limited and were consistent with the pertinent stress intensity factor solution, which itself is only a mild function of crack shape.
4. When plotted as  $da/dN$  versus  $\Delta K$ , there appeared to be a mild effect of nominally elastic stress level on the growth of small fatigue cracks. After accounting for crack closure, the large difference in the extent of crack-tip plasticity associated with stress levels equal to 60 and 90% of the respective materials' yield strength had negligible influence on crack growth rate.
5. Since, for the range of stresses examined,  $\Delta K_{eff}$  adequately correlated the small-crack data, it was unnecessary to use an elastic plastic parameter to describe the magnitude of the crack driving force.
6. Recognizing that increased slip planarity has been reported to lead to increased slip reversibility in fatigue of Ti-Al alloys [214], it might be expected that the Ti-8Al(a) crack growth performance would likely be superior to that for Ti-8Al(s). Since the aging has the opposite effect on crack growth, the influence of slip reversibility on the growth of large cracks in Ti-Al alloys does not appear to be significant. This conclusion is supported by the fact that the difference in crack growth rate between Ti-8Al(s) and Ti-8Al(a) is completely explained by crack closure effects, thereby eliminating the possibility of a significant contribution from

slip reversibility.

7. Although the character and distribution of slip in Ti-Al alloys have a dramatic influence on low-cycle-fatigue crack initiation and on the propagation behavior of large fatigue cracks in conventional specimens, this effect is minimal for small cracks. In the same materials, small surface cracks subjected to elastic loading under nominally equivalent  $\Delta K$  fatigue exhibit nearly equivalent resistance to fatigue crack growth.
8. The observed disparity between large and small fatigue crack propagation behavior is largely the result of differences in fatigue crack closure characteristics of large versus small cracks. Whereas large cracks exhibit fully developed levels of crack closure, the small cracks experience a transient period during which crack closure rises to the long-crack value. The rate of closure development was found to be approximately independent of alloy condition (slip character), stress level, and stress ratio, but the maximum level of crack closure was directly related to alloy slip character. For the available data, the crack depth required to completely develop crack closure ranged from 5 to 18 times the mean-linear-intercept grain size.
9. Crack closure arguments are only partially able to explain the behavior of small fatigue cracks. For surface cracks of length,  $2c$ , less than approximately two to three times the material's grain size, the data of large and small cracks were not consolidated by  $\Delta K_{eff}$  in some instances.
10. In general, both the small- and large-crack fractographic observations are well correlated with the slip character of each alloy. The alloy Ti-4Al, which exhibits finely distributed wavy slip, had the flattest, most featureless fracture surface. The

increased aluminum content and associated increase in slip planarity of the Ti-8Al(s) strongly promoted crystallographic crack propagation, leading to a much more tortuous crack path. Further localizing slip by aging the Ti-8Al resulted in the most crystallographic fracture surface, although the fracture surface roughness was slightly less than in Ti-8Al(s).

11. An extensive fractographic investigation using scanning electron microscopy revealed little evidence of significant differences in crack growth mechanism between the large cracks grown in C(T) specimens and the small surface cracks. Local anisotropy only appeared to influence the mechanism of crack growth for surface cracks of depth less than approximately 1.5 times the average grain size. In the presence of isolated larger grains, the crack appeared to assume stage II growth once its depth achieved a dimension approximately equal to the minimum dimension of the large grain. Beyond this crack size, there appeared to be no direct effect of the large grain on the growth of small cracks.
12. Consistent with the SEM fractographic investigation, quantitative fractographic measurements of fracture surface profiles from the C(T) specimens showed a significant effect of alloy condition on fracture surface roughness. The Ti-4Al displayed the least fracture surface roughness, while roughness levels were significantly higher, but similar, in the Ti-8Al alloy in both the solution-treated and quenched and the aged conditions. For a given material, fracture surface roughness was significantly less in regions of  $da/dN = 10^{-10}$  m/cycle than for regions with a  $10^{-8}$  m/cycle growth rate. There was no indication of a significant difference between the fracture surface roughness of the small- versus large-crack specimens, and for a given small crack, fracture surface roughness appeared to be independent of crack length.

13. There appears to be a limited potential to influence small-crack growth behavior through microstructural modifications that enhance roughness-induced crack closure. Although implementation of such alloy design philosophies may have a dramatic effect on the behavior of large fatigue cracks, the effect may be extremely misleading, since small fatigue cracks may not be similarly affected. Total fatigue life calculations that use data generated in conventional long-crack tests may seriously underestimate the early growth of a fatigue crack, leading to a very significant error in the calculation.

## CHAPTER 7

### RECOMMENDATIONS FOR FUTURE RESEARCH

Based on the findings of the present research on the propagation of small fatigue cracks in titanium-aluminum alloys, the following recommendations for future research are offered.

1. It has been shown that the development of crack closure occurs at a similar rate for materials having dramatically different slip characters but having a similar grain sizes. Small-crack experiments should be performed to determine if the rate, or form, of the development of crack closure is dependent on the absolute size of microstructural features.
2. The results of the quantitative fractography indicated that a complicated relationship exists between fracture surface roughness and crack closure. This finding, however, may have been influenced by the lack of adequate experimental techniques and analytical parameters to document the fine details of fracture surface topography. Improved fractographic methods should be developed to quantify three-dimensional fracture surface characteristics of both large and small cracks, and such measurements should be related to crack closure.
3. It appears that local mode II deformation along the fracture surface contributes significantly to the level of roughness-induced crack closure. Experimental techniques should be developed and applied to characterize these displacements, and



crack closure characteristics should be correlated with the measurements. At this time, in situ SEM techniques appear to offer the most potential for progress in this area.

4. Although large-scale plasticity due to high net-section stresses or stress concentration at a notch was intentionally avoided in the present small-crack experiments, there appears to be need for research to develop or demonstrate the general capability of elastic/plastic crack-tip field parameters for describing the small-crack driving force in the presence of extensive plasticity.
5. The present findings show that slip character (manifested through crack closure) affects the growth of small and large cracks differently. Furthermore, it is known that the effects of slip character on crack initiation are different from either of effects on crack growth. To optimize the design of new alloys, a model of the relative contributions of crack initiation and the growth of both small and large cracks should be developed as a function of microstructural features and loading conditions.

## CHAPTER 8

## APPENDIX

## MODIFIED INCREMENTAL POLYNOMIAL METHOD

Use of the automated photomicroscopic system in conjunction with the interferometric displacement gage to monitor the propagation of small surface cracks provided a unique data acquisition capability. Unlike most of the other methods used to monitor the growth of small fatigue cracks, each of these techniques commonly acquired a large number of crack length measurements (occasionally more than 300). However, the large number, and unique nature, of the small-crack data necessitated the development of a nonstandard numerical method to reduce the crack growth data ( $2c$  vs.  $N$ ) to the form of  $dc/dN$  vs.  $\Delta K$ .

To study the discontinuous nature of propagation of small fatigue cracks and track unusual events, crack length measurements were taken frequently, and the resulting crack extension ( $\Delta c$ ) between successive measurements was often vanishingly small. Although this procedure provided valuable data of the instantaneous crack length, the ratio of the precision of crack length measurement to  $\Delta c$  was large, possibly leading to significant errors in the determination of  $dc/dN$ . Following guidelines set forth in the ASTM Standard Test Method for Measurement of Fatigue Crack Growth Rates (E 647-86a) [249], the data should have been edited such that  $\Delta c$  was at least ten times the crack length measurement precision. This approach, however, required that the majority of the available crack length measurements be eliminated. The elimination of data at the shortest

crack lengths was particularly disadvantageous, since this crack-length regime was the primary focus of the investigation. Therefore, an alternative data-reduction method was developed to utilize all of the available crack length data without introducing artificially large errors in the calculated values of  $dc/dN$ .

According to the ASTM standard, an incremental polynomial regression is to be performed such that each set of seven successive crack length points is fitted with a second-degree polynomial (parabola), and  $da/dN$  and  $\Delta K$  are determined at the fourth of the seven points. Since the standard specifies that the crack length data be taken at approximately equal increments of  $\Delta a$ , and that  $\Delta a$  be ten times the measurement precision, the error in  $da/dN$  is maintained approximately uniform as the crack extends. A slight modification to the ASTM incremental polynomial method provided similar control of the error in  $da/dN$ , while allowing all of the data to be used. Figure 8.1 illustrates the general approach schematically. The primary difference from the standard method lies in the choice of the data that are regressed incrementally. Under the present approach, all crack length data falling within an interval ( $\Delta a_{reg}$ ) were fitted with the second degree polynomial, and  $\Delta K$  and  $da/dN$  were calculated at the arithmetic crack-length midpoint of the interval. This process was performed repeatedly, with the sliding regression being successively incremented by an amount  $\Delta a_{inc}$ . For the small-crack data presented,  $\Delta a_{inc}$  was set equal 25  $\mu m$  (over ten times the measurement precision) and  $\Delta a_{reg}$  was taken as six times  $\Delta a_{inc}$ . The values of  $\Delta a_{inc}$  and  $\Delta a_{reg}$  were chosen to provide good definition of crack growth rate for the cracks at their smallest size, while limiting the variability in  $da/dN$  due to errors in the individual measurements. This approach to calculating  $da/dN$  was unique since an unlimited number of data points could be analyzed and the variability in  $da/dN$  due to random error in crack-length measurement was uniform, independent of crack length and  $\Delta K$ .

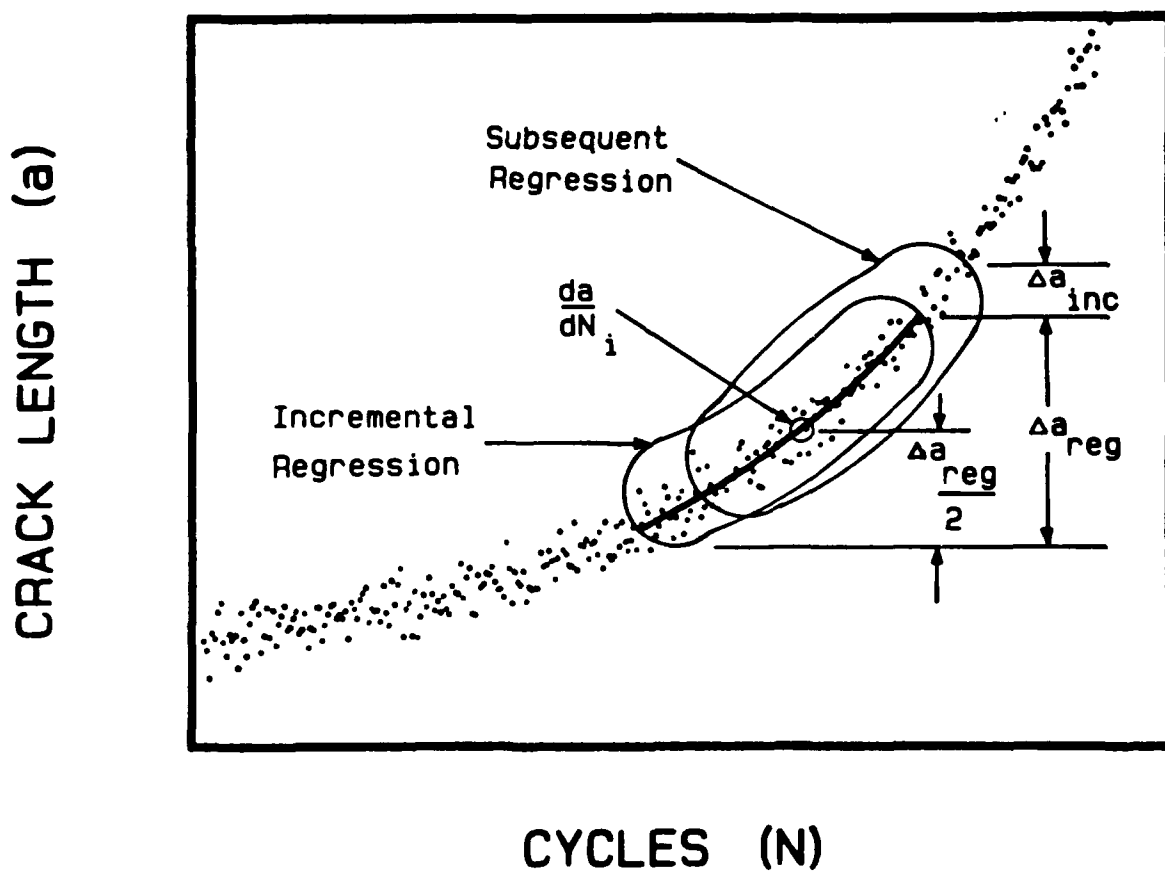


Fig. 8.1 Schematic illustrating the principles of the modified incremental method for reduction of crack growth data.

The accuracy of the modified incremental polynomial method was evaluated in a manner similar to that used by Hudak et al [250]. A random error in crack length was added to each of the points in an artificial crack growth data set ( $a$  vs.  $N$ ) that was generated from a realistic analytical expression giving  $da/dN$  as a function of  $\Delta K$ . The modified incremental polynomial method was used to reduce the artificial data to the form of  $da/dN$  versus  $\Delta K$ , and these data were compared with the original analytical expression. The reduced data and the analytical expression were found to agree excellently. Based on this success, the modified incremental polynomial method was also used to reduce crack growth data from the C(T) specimens that were tested under computer control with crack length determined by compliance measurements. For these large-crack specimens,  $\Delta a_{inc}$  was set equal to 250  $\mu m$ , while  $\Delta a_{reg}$  was six times  $\Delta a_{inc}$ . In general, the modified incremental polynomial method was found to be very effective in reducing data from a number of different types of crack growth tests. Moreover, the method provided the added benefit of using a large number of data to define the crack growth rate behavior, thereby achieving a high degree of statistical confidence in the calculations.

## CHAPTER 9

## APPENDIX 2

## SUMMARY OF CRACK PROPAGATION TESTS

Specimen Number	Alloy	Geometry	Orientation	R	Test Type
84-633	Ti-4Al	C(T)	T-L	0.10	$\Delta K_{th}$
84-632	Ti-4Al	C(T)	T-L	0.50	$\Delta K_{th}$
84-582	Ti-8Al(s)	C(T)	T-L	0.10	$\Delta K_{th}$
84-584	Ti-8Al(s)	C(T)	T-L	0.50	$\Delta K_{th}$
84-586	Ti-8Al(a)	C(T)	T-L	0.10	$\Delta K_{th}$
84-585	Ti-8Al(a)	C(T)	T-L	0.50	$\Delta K_{th}$

Specimen Number	Alloy	Geometry	Orientation	R	$\sigma_{max}/\sigma_y$
84-650	Ti-4Al	Small Crack	T-L	0.10	0.60
84-651	Ti-4Al	Small Crack	T-L	0.10	0.90
87-153	Ti-8Al(s)	Small Crack	T-L	-1.00	0.60
84-711	Ti-8Al(s)	Small Crack	T-L	0.10	0.60
84-698	Ti-8Al(s)	Small Crack	T-L	0.50	0.60
84-699	Ti-8Al(s)	Small Crack	T-L	-1.00	0.90
84-620	Ti-8Al(s)	Small Crack	T-L	0.10	0.90
84-702	Ti-8Al(s)	Small Crack	T-L	0.50	0.90
84-706	Ti-8Al(a)	Small Crack	T-L	0.10	0.60
84-703	Ti-8Al(a)	Small Crack	T-L	0.10	0.90

## CHAPTER 10

## REFERENCES

1. S. A. Sattar and C. V. Sundt, "Gas Turbine Engine Disk Cyclic Life Prediction," Journal of Aircraft, 1975, Vol. 12, pp. 360-365.
2. T. A. Cruse and T. G. Meyer, "Structural Life Prediction and Analysis Technology," Air Force Aero Propulsion Laboratory Report AFAPL-TR-78-106, Wright-Patterson AFB, OH, 1978.
3. J. M. Hyzak, W. H. Reimann, and J. E. Allison, "The Development of Quantitative NDI for Retirement-for-Cause," Air Force Materials Laboratory Report AFML-TR-78-198, Wright-Patterson AFB, OH, 1979.
4. J. A. Harris, Jr., D. L. Sims, and C. G. Annis, Jr., "Concept Definition: Retirement for Cause of F100 Rotor Components," Air Force Wright Aeronautical Laboratories Report AFWAL-TR-80-4118, Wright-Patterson AFB, OH, 1980.
5. C. G. Annis, Jr., M. C. VanWanderham, J. A. Harris, Jr., and D. L. Sims, "Gas Turbine Engine Disk Retirement-for-Cause: An Application of Fracture Mechanics and NDE," J. Eng. for Power, Trans. ASME, 1981, Vol. 103, pp. 198-200.
6. C. G. Annis, Jr., J. S. Cargill, J. A. Harris, Jr., and M. C. VanWanderham, "Engine Component Retirement-for-Cause: A Nondestructive Evaluation (NDE) and Fracture Mechanics-based Maintenance Concept," J. of Met., 1981, pp. 24-28.
7. W. D. Cowie, "Turbine Engine Structural Integrity Program (ENSIP)," Journal of Aircraft, 1975, Vol. 12, pp. 366-369.
8. United States Air Force, "Engine Structural Integrity Program," Military Standard 1783, Aeronautical Systems Division, Wright-Patterson Air Force Base, OH, 1984.
9. T. T. King, W. D. Cowie, and W. H. Reimann, "Damage Tolerant Design Concepts for Military Engines," AGARD Conference Proceedings No. 393, NATO Advisory Group for Aerospace Research and Development, 1985, pp. 3.1-3.9.
10. T. T. King, J. Hurchalla, and D. Nethaway, "United States Air Force Engine Damage Tolerance Requirements," Presented at the AIAA/ASME/SAE 21st Joint Propulsion Conference, Monterey, CA, July, 1985.

11. Engine Cyclic Durability by Analysis and Testing, AGARD Conference Proceedings No. 368, NATO Advisory Group for Aerospace Research and Development, 1984.
12. Damage Tolerance Concepts for Critical Engine Components, AGARD Conference Proceedings No. 393, NATO Advisory Group for Aerospace Research and Development, 1985.
13. J. M. Larsen and T. Nicholas, "Cumulative Damage Modeling in Turbine Engine Materials," Eng. Fract. Mech., 1985, Vol. 22, pp. 713-730.
14. T. Nicholas, J. H. Laflen, and R. H. Van Stone, "A Damage Tolerant Design Approach to Turbine Engine Life Prediction," Proceedings: Conference on Life Prediction for High-Temperature Gas Turbine Materials, Syracuse University Press, Syracuse, NY, 1986, pp. 4.1-4.61.
15. J. Lankford and S. J. Hudak, Jr., "Relevance of the Small Crack Problem to Lifetime Prediction in Gas Turbines," Proceedings: Conference on Life Prediction for High-Temperature Gas Turbine Materials, Syracuse University Press, Syracuse, NY, 1986, pp. 11.1-11.22.
16. R. H. Jeal, "Damage Tolerance Concepts for Critical Engine Components," Damage Tolerance Concepts for Critical Engine Components, AGARD Conference Proceedings No. 393, NATO Advisory Group for Aerospace Research and Development, 1985, pp. 1.1-1.12.
17. C. Howland, M. A. Hicks, and R. H. Jeal, "The Relevance of Short Crack Behavior to the Integrity of Major Rotating Aero Engine Components," Small Fatigue Cracks, R. O. Ritchie and J. Lankford, Eds., The Metallurgical Society, Inc., Warrendale, PA, 1986, pp. 607-622.
18. A. F. Blom, "Relevance of Short Fatigue Crack Growth Data for Durability and Damage Tolerance Analyses of Aircraft," Small Fatigue Cracks, R. O. Ritchie and J. Lankford, Eds., The Metallurgical Society, Inc., Warrendale, PA, 1986, pp. 623-638.
19. M. M. Rosson, "Computer Controls the Eddy Current Testing of Jet Engine Parts," Metal Progress, May 1985, pp. 27-30.
20. S. Pearson, "Initiation of Fatigue Cracks in Commercial Aluminum Alloys and The Subsequent Propagation of Very Short Cracks," Eng. Fract. Mech., 1975, Vol. 7, pp. 235-247.
21. J. Lankford, "The Growth of Small Fatigue Cracks in 7075-T6 Aluminum," Fat. Eng. Mats. Struc., 1982, Vol. 5, pp. 233-248.
22. H. Kitagawa and S. Takahashi, "Applicability of Fracture Mechanics to Very Small Cracks or the Cracks in the Early Stage," Proceedings of the Second International Conference on Mechanical Behavior of Materials, Boston, MA, 1976, pp. 627-631.



23. M. H. El Haddad, K. N. Smith, and T. H. Topper, "Fatigue Crack Propagation of Short Cracks," J. Eng. Mater. Technol. Trans. ASME, 1979, Vol. 101, pp. 42-46.
24. M. H. El Haddad, T. H. Topper, and K. N. Smith, "Prediction of Non Propagating Cracks," Eng. Fract. Mech., 1979, Vol. 11, pp. 573-584.
25. M. H. El Haddad, T. H. Topper, and I. F. C. Smith, "Fatigue Life Prediction of Welded Components Based on Fracture Mechanics," Journal of Testing and Evaluation, 1980, Vol. 8, pp. 301-307.
26. K. Tanaka, Y. Nakai, and M. Yamashita, "Fatigue Growth Threshold of Small Cracks," Int. J. Frac., 1981, Vol. 17, pp. 519-533.
27. Behavior of Short Cracks in Airframe Components, AGARD conference Proceedings No. 328, NATO Advisory Group for Aerospace Research and Development, 1982.
28. Euromech Colloquium on the Creation and Behavior of Short Fatigue Cracks, Fat. Eng. Mats. Struc., 1982, Vol. 5, pp. 303-353.
29. The Behaviour of Short Fatigue Cracks, EGF Pub. 1, K. J. Miller and E. R. de los Rios, Eds., Mechanical Engineering Publications, London, 1986.
30. Small Fatigue Cracks, R. O. Ritchie and J. Lankford, Eds., The Metallurgical Society, Inc., Warrendale, PA, 1986.
31. S. J. Hudak, Jr., "Small Crack Behavior and the Prediction of Fatigue Life," J. Eng. Mater. Technol. Trans. ASME, 1981, Vol. 103, pp. 26-35.
32. K. J. Miller, "The Short Crack Problem," Fat. Eng. Mats. Struc., 1982, Vol. 5, pp. 223-232.
33. R. O. Ritchie and S. Suresh, "Mechanics and Physics of the Growth of Small Cracks," Behavior of Short Cracks in Airframe Components, AGARD conference Proceedings No. 328, NATO Advisory Group for Aerospace Research and Development, 1982, pp. 1.1-1.14.
34. R. W. Hertzberg, Deformation and Fracture Mechanics of Engineering Materials, Second Edition, John Wiley and Sons, New York, 1983, pp. 553-562.
35. R. A. Smith, "Short Fatigue Cracks," Fatigue Mechanisms: Advances in Quantitative Measurement of Physical Damage. ASTM STP 811, J. Lankford, D. L. Davidson, W. L. Morris, and R. P. Wei, Eds., American Society for Testing and Materials, Philadelphia, PA, 1983, pp. 264-279.
36. B. N. Leis, M. F. Kanninen, A. T. Hopper, J. Ahmad, and D. Broek, "A Critical Review of the Short Crack Problem in Fatigue," Air Force Wright Aeronautical Laboratories Report AFWAL-TR-83-4019, Wright-Patterson AFB, OH, 1983.

37. S. Suresh and R. O. Ritchie, "Propagation of Short Fatigue Cracks," Int. Metals Rev., 1984, Vol. 29, pp. 445-476.
38. J. Lankford, "The Influence of Microstructure on the Growth of Small Fatigue Cracks," Fat. Eng. Mats. Struc., 1985, Vol. 8, pp. 161-175.
39. R. P. Gangloff and R. O. Ritchie, "Environmental Effects Novel to the Propagation of Short Fatigue Cracks," Fundamentals of Deformation and Fracture, B. A. Bilby and K. J. Miller, Eds., Cambridge University Press, Cambridge, England, 1984, pp. 531-558.
40. J. Lankford and D. L. Davidson, "The Role of Metallurgical Factors in Controlling the Growth of Small Fatigue Cracks," Small Fatigue Cracks, R. O. Ritchie and J. Lankford, Eds., The Metallurgical Society, Inc., Warrendale, PA, 1986, 51-71.
41. S. J. Hudak and K. S. Chan, "In Search of a Driving Force to Characterize the Kinetics of Small Crack Growth," Small Fatigue Cracks, R. O. Ritchie and J. Lankford, Eds., The Metallurgical Society, Inc., Warrendale, PA, 1986, pp. 379-405.
42. R. P. Gangloff and R. P. Wei, "Small Crack-Environment Interactions: The Hydrogen Embrittlement Perspective," Small Fatigue Cracks, R. O. Ritchie and J. Lankford, Eds., The Metallurgical Society, Inc., Warrendale, PA, 1986, pp. 239-264.
43. C. W. Brown and J. E. King, "The Relevance of Microstructural Influences in the Short Crack Regime to Overall Fatigue Resistance," Small Fatigue Cracks, R. O. Ritchie and J. Lankford, Eds., The Metallurgical Society, Inc., Warrendale, PA, 1986, pp. 73-96.
44. R. O. Ritchie and J. Lankford, "Overview of the Small Crack Problem," Small Fatigue Cracks, R. O. Ritchie and J. Lankford, Eds., The Metallurgical Society, Inc., Warrendale, PA, 1986, pp. 1-5.
45. R. O. Ritchie and J. Lankford, "Small Fatigue Cracks: A Statement of the Problem and Potential Solutions," Report Number UCB/RP/86/A1037, University of California, Berkeley CA, Feb., 1986. In press: Materials Science and Engineering.
46. A. Talug and K. Reifsnider, "Analysis and Investigation of Small Flaws," Cyclic Stress-Strain and Plastic Deformation Aspects of Fatigue Crack Growth, ASTM STP 637, American Society for Testing and Materials, Philadelphia, PA, 1977, pp. 81-96.
47. R. J. Allen and J. C. Sinclair, "The Behavior of Short Cracks," Fat. Eng. Mats. Struc., 1982, Vol. 5, pp. 343-347.
48. W. F. Brown, Jr. and J. E. Srawley, Plane Strain Crack Toughness Testing of High Strength Metallic Materials, ASTM STP 410, American Society for Testing and Materials, Philadelphia, PA, 1966, pp. 25-26.

49. Broek, D., Elementary Engineering Fracture Mechanics, Martinus Nijhoff Publishers, 1984, pp. 91-93.
50. J. R. Rice, "Mechanics of Crack Tip Deformation and Extension by Fatigue," Fatigue Crack Propagation. ASTM STP 415, American Society for Testing and Materials, Philadelphia, PA, 1967, pp. 247-309.
51. J. Lankford, D. L. Davidson, and T. S. Cook, "Fatigue Crack Tip Plasticity," Cyclic Stress-Strain and Plastic Deformation Aspects of Fatigue Crack Growth. ASTM STP 637, American Society for Testing and Materials, Philadelphia, PA, 1977, pp. 36-55.
52. J. R. Rice, "A Path Independent Integral and the Approximate Analysis of Strain Concentration by Notches and Cracks," J. Appl. Mech., Trans. ASME, 1968, pp. 379-386.
53. G. G. Trantina and H. G. deLorenzi, "Elastic-Plastic Fracture Mechanics Analysis of Small Cracks," Proceedings of the Army Symposium on Solid Mechanics, Army Materials and Mechanics Research Center report AMMRC MS 82-4, 1982, pp. 203-214.
54. W. T. Chiang and K. J. Miller, "Elastic-Plastic Finite Element Analyses of Short Cracks," Fat. Eng. Mats. Struc., 1982, Vol. 5, pp. 249-263.
55. N. E. Dowling, "Crack Growth During Low-Cycle Fatigue of Smooth Axial Specimens," Cyclic Stress-Strain and Plastic Deformation Aspects of Fatigue Crack Growth. ASTM STP 637, American Society for Testing and Materials, Philadelphia, PA, 1977, pp. 97-121.
56. M. H. El Haddad, N. E. Dowling, T. H. Topper, and K. N. Smith, "J Integral Applications for Short Fatigue Cracks at Notches," Int. J. Frac., 1980, Vol. 16, pp. 15-30.
57. M. Klesnil, J. Polak, and P. Liskutin, "Short Crack Growth Close to the Fatigue Limit in Low Carbon Steel," Scripta Met., 1984, Vol.18, pp. 1231-1234.
58. K. S. Chan, "Local Crack-Tip Field Parameters for Large and Small Cracks: Theory and Experiment," Small Fatigue Cracks, R. O. Ritchie and J. Lankford, Eds., The Metallurgical Society, Inc., Warrendale, PA, 1986, pp. 407-425.
59. K. S. Chan and J. Lankford, "A Crack-Tip Strain Model for the Growth of Small Fatigue Cracks," Scripta Met., 1983, Vol.17, pp. 529-532.
60. R. S. Vecchio and R. W. Hertzberg, "A Rationale for the "Apparent Anomalous" Growth Behavior of Short Fatigue Cracks," Eng. Fract. Mech., 1985, Vol. 22, pp. 1049-1060.
61. D. L. Davidson and J. Lankford, "Fatigue Crack Tip Strains in 7075-T6 Aluminum

- Alloy by Stereoimaging and Their Use in Crack Growth Models," Fatigue Mechanisms: Advances in Quantitative Measurement of Physical Damage. ASTM STP 811, J. Lankford, D. L. Davidson, W. L. Morris, and R. P. Wei, Eds., American Society for Testing and Materials, Philadelphia, PA, 1983, pp. 371-399.
62. D. L. Davidson and J. Lankford, "High Resolution Techniques for the Study of Small Cracks," Small Fatigue Cracks, R. O. Ritchie and J. Lankford, Eds., The Metallurgical Society, Inc., Warrendale, PA, 1986, pp. 455-470.
  63. J. Lankford, D. L. Davidson, and K. S. Chan, "The Influence of Crack Tip Plasticity in the Growth of Small Fatigue Cracks," Metall. Trans. A, 1984, Vol. 15A, pp. 1579-1588.
  64. J. Lankford and D. L. Davidson, "Near-threshold Crack Tip Strain and Crack Opening for Large and Small Fatigue Cracks," Fatigue Crack Growth Threshold Concepts, D. Davidson and S. Suresh, Eds., TMS-AIME, Warrendale, PA, 1984, pp. 447-463.
  65. B. N. Leis and T. P. Forte, "Fatigue Growth of Initially Physically Short Cracks in Notched Aluminum and Steel Plates," Fracture Mechanics: Thirteenth Conference. ASTM STP 743, R. Roberts, Ed., American Society for Testing and Materials, Philadelphia, PA, 1981, pp. 100-124.
  66. B. N. Leis, "Fatigue Crack Propagation Through Inelastic Gradient Fields," International Journal of Pressure Vessels and Piping, 1982, pp. 141-158.
  67. N. E. Dowling, "Notched Member Fatigue Life Predictions Combining Crack Initiation and Propagation," Fat. Eng. Mats. Struc., 1979, Vol. 2, pp. 129-138.
  68. J. C. Newman, Jr., "An Improved Method of Collocation for the Stress Analysis of Cracked Plates with Various Shaped Boundaries," NASA TN D-6376, National Aeronautical and Space Administration, Washington, D. C., 1971.
  69. M. M. Hammouda and K. J. Miller, "Elastic-Plastic Fracture Mechanics Analyses of Notches," Elastic-Plastic Fracture. ASTM STP 668, J. D. Landes, J. A. Begley, and G. A. Clarke, Eds., American Society for Testing and Materials, Philadelphia, PA, 1979, pp. 703-719.
  70. J. C. Chesnutt, A. W. Thompson, and J. C. Williams, "Influence of Metallurgical Factors of the Fatigue Crack Growth Rate in Alpha-Beta Titanium Alloys," Air Force Materials Laboratory Report AFML-TR-78-68, Wright-Patterson AFB, OH, 1978.
  71. E. A. Starke, Jr. and G. Lütjering, "Cyclic Plastic Deformation and Microstructure," Fatigue and Microstructure, American Society for Metals, Metals Park, OH, 1979, pp. 205-243.
  72. R. O. Ritchie, "Near-Threshold Fatigue-Crack Propagation in Steels," Int. Metall. Rev., 1979, Vol. 5 and 6, pp. 205-230.

73. M. E. Fine and R. O. Ritchie, "Fatigue-Crack Initiation and Near-Threshold Crack Growth," Fatigue and Microstructure, American Society for Metals, Metals Park, OH, 1979, pp. 245-278.
74. J. C. Williams and G. Lütjering, "The Effect of Slip Length and Slip Character on the Properties of Titanium Alloys," Titanium '80 - Science and Technology, H. Kimura and O. Izumi, Eds., TMS-AIME, Warrendale, PA, 1980, pp. 671-681.
75. H. Margolin, J. C. Williams, J. C. Chesnutt, and G. Lütjering, "A Review of the Fracture and Fatigue Behavior of Ti Alloys," Titanium '80 - Science and Technology, H. Kimura and O. Izumi, Eds., TMS-AIME, Warrendale, PA, 1980, pp. 169-216.
76. J.-P. Baille and S. D. Antolovich, "Effect of Microstructure on Fatigue Crack Propagation: A Review of Existing Models and Suggestions for Further Research," Fatigue Mechanisms: Advances in Quantitative Measurement of Physical Damage, ASTM STP 811, J. Lankford, D. L. Davidson, W. L. Morris, and R. P. Wei, Eds., American Society for Testing and Materials, Philadelphia, PA, 1983, pp. 313-349.
77. G. T. Gray, III, A. W. Thompson, J. C. Williams, and D. H. Stone, "Influence of Microstructure on Fatigue Crack Growth Behavior in Fully Pearlitic Steels," Fatigue Thresholds - Fundamentals and Engineering Applications, J. Backlund, A. F. Bloom, and C. J. Beevers, Eds., Engineering Materials Advisory Services, Ltd., 1982, pp. 345-361.
78. G. T. Gray, III, J. C. Williams, and A. W. Thompson, "Roughness-Induced Crack Closure: An Explanation for Microstructurally Sensitive Fatigue Crack Growth," Metall. Trans., 1983, Vol. 14A, pp. 421-433.
79. J. C. Williams and E. A. Starke, Jr., "The Role of Thermomechanical Processing in Tailoring the Properties of Aluminum and Titanium Alloys," Deformation, Processing, and Structure, American Society for Metals, Metals Park, OH, 1984, pp. 279-354.
80. J. C. Chesnutt, J. C. Williams, and A. W. Thompson, "Fatigue Crack Propagation in Titanium Alloys," Fatigue 84, C. J. Beevers, Ed., Engineering Materials Advisory Services, Ltd., West Midlands, UK, 1984, pp. 341-350.
81. G. T. Gray, III, A. W. Thompson, J. C. Williams, "The Effect of Microstructure on Fatigue Crack Path and Crack Propagation Rate," Fatigue Crack Growth Threshold Concepts, D. Davidson and S. Suresh, Eds., TMS-AIME, Warrendale, PA, 1984, pp. 131-143.
82. G. Lütjering and A. Gysler, "Fatigue," Titanium, Science and Technology, Vol. 4, G. Lütjering, U. Zwicker, and W. Bunk, Eds., DGM, Oberursel, West Germany, 1985, pp. 2065-2083.

83. J. E. Allison, J. C. Chesnutt, J. C. Williams, and A. W. Thompson, "Room Temperature Fatigue Crack Propagation in  $\alpha/\beta$  Titanium Alloys," in press: Effect of Microstructure on Fracture Toughness and Fatigue Crack Growth, A. K. Chakrabarti and J. C. Chesnutt, Eds., TMS-AIME, Warrendale, PA.
84. R. A. Smith, "On the Short Crack Limitations of Fracture Mechanics," Int. J. Frac., 1977, Vol. 13, pp. 717-720.
85. J. Lankford, "On the Small Crack Fracture Mechanics Problem," Int. J. Frac., 1980, Vol. 16, pp. R7-R9.
86. D. Taylor and J. F. Knott, "Fatigue Crack Propagation Behavior of Short Cracks; The Effect of Microstructure," Fat. Eng. Mats. Struc., 1981, Vol. 4, pp. 147-155.
87. D. Taylor, "Euromech Colloquium on Short Fatigue Cracks," Fat. Eng. Mats. Struc., 1982, Vol. 5, pp. 305-309.
88. D. Taylor, "The Effect of Crack Length on Fatigue Threshold," Fat. Eng. Mats. Struc., 1984, Vol. 7, pp. 267-277.
89. A. W. Thompson, The Effect of Grain Size on Fatigue, Ph.D. dissertation, Massachusetts Institute of Technology, 1970.
90. A. W. Thompson and W. A. Backofen, "The Effect of Grain Size on Fatigue," Acta Met., 1971, Vol. 19, pp. 597-606.
91. A. W. Thompson, "The Influence of Grain and Twin Boundaries in Fatigue Cracking," Acta Met., 1972, Vol. 20, pp. 1085-1094.
92. W. L. Morris, "A Comparison of Microcrack Closure Load Development for Stage I and II Cracking Events for Al 7075-T651," Metall. Trans., 1977, Vol. 8A, pp. 1087-1093.
93. W. L. Morris, "Microcrack Closure Phenomena for Al 2219-T851," Metall. Trans., 1979, Vol. 10A, pp. 5-11.
94. W. L. Morris, "The Noncontinuum Crack Tip Deformation Behavior of Surface Microcracks," Metall. Trans., 1980, Vol. 11A, pp. 1117-1123.
95. T. S. Cook, J. Lankford, and G. P. Sheldon, "Research on Growth of Microcracks in Nickel Base Superalloys," Air Force Materials Laboratory Report AFML-TR-78-133, Wright-Patterson AFB, OH, 1978.
96. J. Lankford, T. S. Cook, and G. P. Sheldon, "Growth of Small Fatigue Cracks at High Temperatures," Advances in Fracture Research, ICF-5, D. Francois, et al., Ed., Pergamon Press, New York, NY, 1980, pp. 2449-2456.
97. G. P. Sheldon, T. S. Cook, J. W. Jones, and J. Lankford, "Some Observations on

- Small Fatigue Cracks in a Superalloy," Fat. Eng. Mats. Struc., 1981, Vol. 6, pp. 219-228.
98. J. Lankford, T. S. Cook, and G. P. Sheldon, "Fatigue Microcrack Growth in a Nickel-Base Superalloy," Int. J. Frac., 1981, Vol. 17, pp. 143-155.
  99. P. D. Hobson, "The Formulation of a Crack Growth Equation for Short Cracks," Fat. Eng. Mats. Struc., 1982, Vol. 5, pp. 323-327.
  100. E. R. De Los Rios, Z. Tang, and K. J. Miller, "Short Crack Fatigue Behavior in a Medium Carbon Steel," Fat. Eng. Mats. Struc., 1984, Vol. 7, pp. 97-108.
  101. K. J. Miller, H. J. Mohamed, M. W. Brown, and E. R. De Los Rios, "Barriers to Short Fatigue Crack Propagation at Low Stress Amplitudes in a Banded Ferrite-Pearlite Structure," Small Fatigue Cracks, R. O. Ritchie and J. Lankford, Eds., The Metallurgical Society, Inc., Warrendale, PA, 1986, pp. 639-656.
  102. K. Tanaka, M. Hojo, and Y. Nakai, "Fatigue Crack Initiation and Early Propagation in 3% Silicon Iron," Fatigue Mechanisms: Advances in Quantitative Measurement of Physical Damage, ASTM STP 811, J. Lankford, D. L. Davidson, W. L. Morris, and R. P. Wei, Eds., American Society for Testing and Materials, Philadelphia, PA, 1983, pp. 207-232.
  103. K. Tanaka and Y. Akiniwa, "The Propagation of Short Fatigue Cracks at Notches," Presented at the ASTM Symposium on Fundamental Questions and Critical Experiments on Fatigue, Dallas, TX, Oct., 1984. In press: ASTM STP.
  104. K. Tanaka, "Modeling of Propagation and Non-Propagation of Small Fatigue Cracks," Small Fatigue Cracks, R. O. Ritchie and J. Lankford, Eds., The Metallurgical Society, Inc., Warrendale, PA, 1986, pp. 343-361.
  105. M. R. James and W. L. Morris, "Fatigue Induced Changes in Surface Residual Stress," Scripta Met., 1983, Vol. 17, pp. 1101-1104.
  106. M. R. James and W. L. Morris, "The Role of Microplastic Deformation in Fatigue Crack Initiation," Fatigue Mechanisms: Advances in Quantitative Measurement of Physical Damage, ASTM STP 811, J. Lankford, D. L. Davidson, W. L. Morris, and R. P. Wei, Eds., American Society for Testing and Materials, Philadelphia, PA, 1983, pp. 46-70.
  107. P. J. E. Forsyth, "Fatigue Damage and Crack Growth in Aluminum Alloys," Acta Met., 1963, Vol. 11, pp. 703-715.
  108. S. J. Hudak, Jr., J. Lankford, A. C. Howland, and M. A. Hicks, "Growth of Small Cracks in Turbine Disk Materials -- First Interim Report", Air Force Wright Aeronautical Laboratories Contract F33615-85-C-5051, Wright-Patterson AFB, OH, February, 1986.
  109. S. J. Hudak, Jr., D. L. Davidson, A. C. Howland and M. A. Hicks, "Growth of Small

Cracks in Turbine Disk Materials -- Second Interim Report", Air Force Wright Aeronautical Laboratories Contract F33615-85-C-5051, Wright-Patterson AFB, OH, August, 1986.

110. S. J. Hudak, Jr., D. L. Davidson, A. C. Howland, M. J. Walsh, and M. A. Hicks, "Growth of Small Cracks in Turbine Disk Materials -- Third Interim Report", Air Force Wright Aeronautical Laboratories Contract F33615-85-C-5051, Wright-Patterson AFB, OH, February, 1987.
111. A. K. Zurek, M. R. James, and W. L. Morris, "The Effect of Grain Size on Fatigue Growth of Short Cracks," Metall. Trans., 1983, Vol. 14A, pp. 1697-1705.
112. C. Gerdes, A. Gysler, and G. Lütjering, "Propagation of Small Surface Cracks in Ti-Alloys," Fatigue Crack Growth Threshold Concepts, D. Davidson and S. Suresh, Eds., TMS-AIME, Warrendale, PA, 1984, pp. 465-478.
113. L. Wagner, J. K. Gregory, A. Gysler, and G. Lütjering, "Propagation Behavior of Short Cracks in a Ti-8.6Al Alloy," Small Fatigue Cracks, R. O. Ritchie and J. Lankford, Eds., The Metallurgical Society, Inc., Warrendale, PA, 1986, pp. 117-128.
114. C. W. Brown, J. E. King, and M. A. Hicks, "Effects of Microstructure on Long and Short Crack Growth in Nickel Base Superalloys," Met. Sci., 1984, Vol. 18, pp. 374-380.
115. M. A. Hicks and C. W. Brown, "Short Fatigue Crack Growth in Planar Slip Materials," International Journal of Fatigue, 1982, Vol. 6, pp. 167-169.
116. C. W. Brown and M. A. Hicks, "A Study of Short Fatigue Crack Growth Behavior in Titanium Alloy IMI 685," Fat. Eng. Mats. Struc., 1983, Vol. 6, pp. 67-76.
117. R. K. Bolingbroke and J. E. King, "The Growth of Short Fatigue Cracks in Titanium Alloys IMI550 and IMI318," Small Fatigue Cracks, R. O. Ritchie and J. Lankford, Eds., The Metallurgical Society, Inc., Warrendale, PA, 1986, pp. 129-144.
118. M. A. Daeubler and A. W. Thompson, "Microstructural Effects on Short Fatigue Cracks in Eutectoid Steels," Small Fatigue Cracks, R. O. Ritchie and J. Lankford, Eds., The Metallurgical Society, Inc., Warrendale, PA, 1986, pp. 157-164.
119. H. M. Kim, The Effect of Slip Character on Low Cycle Fatigue Behavior of Ti-Al Alloys, Ph.D. dissertation, Carnegie Mellon University, Pittsburgh, PA, 1980.
120. H. M. Kim, H. G. Paris, and J. C. Williams, "Monotonic and Cyclic Deformation Behavior of Alpha-Phase Ti-Al Alloys," Titanium '80 - Science and Technology, H. Kimura and O. Izumi, Eds., TMS-AIME, Warrendale, PA, 1980, pp. 1825-1835.
121. E. Hornbogen and K. Zum Gahr, "Microstructure and Fatigue Crack Growth in a  $\gamma$ -Fe-Ni-Al Alloy," Acta Met., 1976, Vol. 24, pp. 581-592.



122. J. E. Allison, The Effect of Slip Character and Microstructure on Fatigue Crack Growth in Alpha and Alpha + Beta Titanium Alloys, Ph.D. dissertation, Carnegie Mellon University, Pittsburgh, PA, 1982.
123. J. E. Allison and J. C. Williams, "The Role of Crack Closure in Rationalizing the Variations in Fatigue Crack Growth Behavior in Titanium Alloys," Titanium, Science and Technology, G. Lütjering, U. Zwicker, and W. Bunk, Eds., DGM, Oberursel, West Germany, 1985, pp. 2243-2250.
124. J. E. Allison and J. C. Williams, "The Role of Deformation Character on Fatigue Crack Growth in Titanium Alloys," Strength of Metals and Alloys ICSMA 6, R. C. Gifkins, Ed., 1983, pp. 1219-1224.
125. J. K. Gregory, A. Gysler, and G. Lütjering, "The Influence of Texture on Fatigue Microcrack Propagation in an Al-Zn-Mg-Cu Alloy," Fatigue 84, Vol. II, C. J. Beevers, Ed., Engineering Materials Advisory Services, Ltd., West Midlands, UK, 1984, pp. 847-856.
126. C. W. Brown and D. Taylor, "The Effects of Texture and Grain Size on the Short Fatigue Crack Growth Rates in Ti-6Al-4V," Fatigue Crack Growth Threshold Concepts, D. Davidson and S. Suresh, Eds., TMS-AIME, Warrendale, PA, 1984, pp. 433-446.
127. J. C. Newman, Jr. and I. S. Raju, "Analyses of Surface Cracks in Finite Plates Under Tension or Bending Loads," NASA Technical Paper 1578, National Aeronautics and Space Administration, 1979.
128. J. C. Newman, Jr. and I. S. Raju, "Stress-Intensity Factor Equations for Cracks in Three-Dimensional Finite Bodies," Fracture Mechanics: Fourteenth Symposium - Volume I: Theory and Analysis, ASTM STP 791, J. C. Lewis and G. Sines, Eds., American Society for Testing and Materials, Philadelphia, PA, 1983, pp. I-238-I-265.
129. G. R. Leverant, B. S. Langer, A. Yuen, and S. W. Hopkins, "Surface Residual Stresses, Surface Topography and the Fatigue Behavior of Ti-6Al-4V," Metall. Trans., 1979, Vol. 10A, pp. 251-257.
130. J. E. Hack and G. R. Leverant, "Influence of Compressive Residual Stress on the Crack-Opening Behavior of Part-Through Fatigue Cracks," Residual Stress Effects in Fatigue, ASTM STP 776, American Society for Testing and Materials, Philadelphia, PA, 1982, pp. 204-223.
131. P. Clement, J. P. Angeli, and A. Pineau, "Short Crack Behavior in Nodular Cast Iron," Fat. Eng. Mats. Struc., 1984, Vol. 7, pp. 251-265.
132. A. Pineau, "Short Fatigue Crack Behavior in Relation to Three-Dimensional Aspects and Crack Closure Effect," Small Fatigue Cracks, R. O. Ritchie and J. Lankford, Eds., The Metallurgical Society, Inc., Warrendale, PA, 1986, pp.

191-211.

133. A. F. Grandt, Jr., R. Perez, and D. E. Trisch "Cyclic Growth and Coalescence of Multiple Fatigue Cracks," Advances in Fracture Research, ICF6, Vol. 3, S. R. Valluri, D. M. R. Taplin, P. Rama Rao, J. F. Knott, and R. Dubey, Eds., Pergamon Press, New York, 1984, pp.1571-1578.
134. H. Tada, P. Paris, and G. Irwin, The Stress Analysis of Cracks Handbook, Del Research Corp., Hellertown, PA, 1973, pp 21.1-21.6.
135. W. Elber, "Fatigue Crack Closure Under Cyclic Tension," Eng. Fract. Mech., 1970, Vol. 2, pp. 37-45.
136. W. Elber, "The Significance of Fatigue Crack Closure," Damage Tolerance in Aircraft Structures, ASTM STP 486, American Society for Testing and Materials, Philadelphia, PA, 1971, pp. 230-242.
137. S. Suresh and R. O. Ritchie, "Near-Threshold Fatigue Crack Propagation: A perspective on the Role of Crack Closure," Small Fatigue Cracks, R. O. Ritchie and J. Lankford, Eds., The Metallurgical Society, Inc., Warrendale, PA, 1986, pp. 227-261.
138. S. Banerjee, "A Review of Crack Closure," Air Force Wright Aeronautical Laboratories Report AFWAL-TR-84-4031, Wright-Patterson Air Force Base, OH, 1984.
139. J. E. Allison, "On the Measurement of Crack Closure During Fatigue Crack Growth," In press: Fracture Mechanics: Eighteenth Symposium, ASTM STP 945, D. T. Read and R. P. Reed, Eds., American Society for Testing and Materials, Philadelphia, 1987.
140. Fatigue Crack Closure, ASTM STP 982, J. C. Newman and W. Elber, Eds., American Society for Testing and Materials, Philadelphia, PA. in press.
141. P. C. Paris, R. J. Bucci, E. T. Wessel, W. G. Clark, and T. R. Mager, "Extensive Study of Low Fatigue Crack Growth Rates in A533 and A508 Steels," Stress Analysis and Growth of Cracks, Part I, ASTM STP 513, American Society for Testing and Materials, Philadelphia, PA, 1972, pp. 141-176.
142. A. T. Stewart, "The Influence of Environment and Stress Ratio on Fatigue Crack Growth at near Threshold Stress Intensities in Low-Alloy Steels," Eng. Fract. Mech., 1980, Vol. 13, pp. 463-478.
143. R. O. Ritchie, S. Suresh, and C. M. Moss, "Near-Threshold Fatigue Crack Growth in 2 1/4Cr-1Mo Pressure Vessel Steel in Air and Hydrogen," J. Eng. Mater. Technol., Trans. ASME, 1980, Vol. 102, pp. 293-299.
144. R. J. Cooke and C. J. Beevers, "Slow FCP in Pearlitic Steels," Mater. Sci. Eng., 1974, Vol. 13, pp. 201-210.

145. N. Walker and C. J. Beevers, "A Fatigue Crack Closure Mechanism in Titanium," Fat. Eng. Mats. Struc., 1979, Vol. 1, pp. 135-148.
146. S. Purushothaman and J. K. Tien, "A Model for Fatigue Crack Closure in Ductile Materials," Strength of Metals and Alloys, ICSMA 5, Vol. 2., P. Haasen et al, Eds., 1979, Pergamon Press, New York, p. 1267-1271.
147. J.-L. Tzou, S. Suresh, and R. O. Ritchie, "Fatigue Crack Propagation in Oil Environments - I. Crack Growth Behavior in Silicone and Paraffin Oils," Acta Met., 1985, Vol. 33, pp. 105-116.
148. J.-L. Tzou, C. H. Hsueh, A. G. Evans, and R. O. Ritchie, "Fatigue Crack Propagation in Oil Environments - II. A Model for Crack Closure Induced by Viscous Fluids," Acta Met., 1985, Vol. 33, pp. 117-127.
149. R. M. McMeeking and A. G. Evans, "Mechanics of Transformation-Toughening in Brittle Materials," J. Amer. Cer. Soc., Vol. 65, 1982, P. 242-246.
150. B. Budiansky, J. W. Hutchinson, and J. C. Lambropoulos, "Continuum Theory of Dilatant Transformation Toughening in Ceramics," Int. J. Solids Struct., Vol. 19, 1983, pp. 337-355.
151. R. O. Ritchie and W. Yu, "Short Crack Effects in Fatigue: A Consequence of Crack Tip Shielding," Small Fatigue Cracks, R. O. Ritchie and J. Lankford, Eds., The Metallurgical Society, Inc., Warrendale, PA, 1986, pp. 167-189.
152. Broek, D., Elementary Engineering Fracture Mechanics, First Edition, Noordhoff International Publishing, Leyden, The Netherlands, 1974, p. 320.
153. N. A. Fleck and R. A. Smith, "Crack Closure - Is It Just a Surface Phenomenon?," Int. J. Fatigue, 1982, pp. 157-160.
154. N. A. Fleck, "Finite Element Analysis of Plasticity-Induced Crack Closure Under Plane Strain Conditions," Eng. Fract. Mech., 1986, Vol. 25, pp. 441-449.
155. B. Budiansky and J. W. Hutchinson, "Analysis of Closure in Fatigue Crack Growth," J. Appl. Mech., Trans. ASME, 1978, Vol. 45, pp. 267-275.
156. J. C. Newman, Jr., "A Nonlinear Fracture Mechanics Approach to the Growth of Small Cracks," Behavior of Short Cracks in Airframe Components, AGARD conference Proceedings No. 328, NATO Advisory Group for Aerospace Research and Development, 1982, pp. 6.1-6.26.
157. J. C. Newman, Jr., "A Crack Opening Stress Equation for Fatigue Crack Growth," Int. J. Frac., 1984, Vol. 24, pp. R131-R135.
158. J. C. Newman, Jr., M. H. Swain, and E. P. Phillips, "An Assessment of the Small-Crack Effect for 2024-T3 Aluminum Alloy," Small Fatigue Cracks, R. O.

Ritchie and J. Lankford, Eds., The Metallurgical Society, Inc., Warrendale, PA, 1986, pp. 427-451.

159. J. C. Newman, Jr., M. H. Swain, and E. P. Phillips, In press: Fatigue Crack Closure. ASTM STP 982, J. C. Newman and W. Elber, Eds., American Society for Testing and Materials, Philadelphia, PA.
160. J. J. Lee and W. N. Sharpe, Jr., "Short Fatigue Cracks in Notched Aluminum Specimens," Small Fatigue Cracks, R. O. Ritchie and J. Lankford, Eds., The Metallurgical Society, Inc., Warrendale, PA, 1986, pp. 323-339.
161. J. J. Lee and W. N. Sharpe, Jr., "Closure Measurements on Short Fatigue Cracks," In press: Fatigue Crack Closure. ASTM STP 982, J. C. Newman and W. Elber, Eds., American Society for Testing and Materials, Philadelphia, PA.
162. X. Su and W. N. Sharpe, "An Experimental Study of Closure Behavior of Naturally Initiated Small Cracks," Fatigue 87, Vol. I, E. A. Starke and R. O. Ritchie, Eds., Engineering Materials Advisory Services, Ltd., West Midlands, U. K., 1987, pp. 343-350.
163. S. Suresh, G. F. Zamiski, and R. O. Ritchie, "Oxide-Induced Crack Closure: An Explanation for Near-Threshold Corrosion Fatigue Crack Growth Behavior," Metall. Trans., 1981, Vol. 12A, pp. 1435-1443.
164. J. Lankford and D. L. Davidson, "Wear Debris Due to Mode II Opening of Mode I Fatigue Cracks in an Aluminum Alloy," Metall. Trans., 1983, Vol. 14A, pp. 1227-1230.
165. G. T. Gray, III and G. Lütjering, "The Influence of Crack Closure on the Fatigue Crack Propagation of Ti-6Al-4V and Ti-8.6Al," Fatigue 84, Vol. II, C. J. Beevers, Ed., Engineering Materials Advisory Services, Ltd., West Midlands, UK, 1984, pp. 707-716.
166. K. T. Venkateswara Rao, W. Yu, and R. O. Ritchie, "On the Growth of Small Fatigue Cracks Aluminum-Lithium Alloy 2090," Scripta Met., 1986, Vol. 20, pp. 1459-1464.
167. W. Yu and R. O. Ritchie, "Fatigue Crack Propagation in 2090 Aluminum-Lithium Alloy: Effect of Compression Overload Cycles," J. Eng. Mater. Technol. Trans. ASME, 1987, Vol. 109, pp. 81-85.
168. K. T. Venkateswara Rao, W. Yu, and R. O. Ritchie, "Fatigue Crack Propagation in Aluminum-Lithium Alloy 2090: Part I. Long Crack Behavior," Submitted for publication in Metall. Trans. A.
169. K. T. Venkateswara Rao, W. Yu, and R. O. Ritchie, "Fatigue Crack Propagation in Aluminum-Lithium Alloy 2090: Part II. Small Crack Behavior," Submitted for publication in Metall. Trans. A.

170. S. Suresh and R. O. Ritchie, "A Geometric Model for Fatigue Crack Closure Induced by Fracture Surface Roughness," Metall. Trans., 1982, Vol. 13A, pp. 1627-1631.
171. R. L. Carlson and C. J. Beevers, "A Multiple Asperity Fatigue Crack Closure Model," Eng. Fract. Mech., 1984, Vol. 20, pp. 687-690.
172. R. L. Carlson and C. J. Beevers, "Fatigue Crack Closure Models," Fatigue 84, C. J. Beevers, Ed., Engineering Materials Advisory Services, Ltd., West Midlands, UK, 1984, pp. 655-665.
173. K. Minakawa, J. C. Newman, Jr., and A. J. McEvily, "A Critical Study of the Crack Closure Effect on Near Threshold Fatigue Crack Growth," Fat. Eng. Mats. Struc., 1983, Vol. 4, pp. 359-365.
174. E. Zaiken and R. O. Ritchie, "On the Location of Crack Closure and the Threshold for Fatigue Crack Growth," Scripta Met., 1984, Vol. 18, pp. 847-850.
175. E. Zaiken and R. O. Ritchie, "On the Development of Crack Closure and the Threshold Condition for Short and Long Fatigue Cracks in 7150 Aluminum Alloy," Metall. Trans., 1985, Vol. 16A, pp. 1467-1477.
176. M. N. James and J. F. Knott, "Near-Threshold Fatigue Crack Closure and Growth in Air and Vacuum," Scripta Met., 1985, Vol. 19, pp. 189-194.
177. M. N. James, "The Effect of Grain Size on the Location of Crack Wake Closure During Load Shedding," Scripta Met., 1985, Vol. 19, pp. 1301-1306.
178. J. E. Allison, R. C. Ku, and M. L. Pompetzki, "A Comparison of Measurement Methods and Numerical Criteria for the Experimental Characterization of Fatigue Crack Closure," In press: Fatigue Crack Closure. ASTM STP 982, J. C. Newman and W. Elber, Eds., American Society for Testing and Materials, Philadelphia, PA.
179. Round robin testing and analysis program, ASTM Task Group E24.04.04 on Crack Closure Measurement and Analysis, American Society for Testing and Materials.
180. J. W. Jones, D. E. Macha, and D. M. Corbly, "Observations on Fatigue Crack Opening Load Determinations," Int. J. Frac., 1978, Vol. 14, pp. R25-R30.
181. D. E. Macha, D. M. Corbly, and J. W. Jones, "On the Variation of Fatigue-Crack-Opening Load with Measurement Location," Experimental Mechanics, 1979, pp. 207-213.
182. W. J. D. Shaw and I. Le May, "Crack Closure During Fatigue Crack Propagation," Fracture Mechanics. ASTM STP 677, C. W. Smith, Ed., American Society for Testing and Materials, Philadelphia, PA, 1979, pp. 233-246.
183. H. Nisitani and K. Takao, Bul. of the JSME, Vol. 20, 1977, pp. 264-270.

184. A. Ohta, M. Kosuge, and E. Sasaki, "Change of Fatigue Crack Closure Level with Gage Location Along Crack Line," Int. J. Frac., Vol. 15, 1979, pp. R53-R57.
185. D. L. Davidson, personal communication, Southwest Research Institute, San Antonio, TX, 1985.
186. N. E. Ashbaugh, "Effects of Load History and Specimen Geometry on Fatigue Crack Closure Measurements," In press: Fatigue Crack Closure, ASTM STP 982, J. C. Newman and W. Elber, Eds., American Society for Testing and Materials, Philadelphia, PA.
187. S. Ray, A. F. Grandt, Jr., and S. Andrew, "Three-Dimensional Measurements of Fatigue Crack Opening and Closure," Presented at the ASTM Symposium on Fundamental Questions and Critical Experiments on Fatigue, Dallas, TX, 1984. In press: ASTM STP.
188. M. N. James and G. C. Smith, "Surface Microcrack Closure in Fatigue: A Comparison of Compliance and Crack Sectioning Data," Int. J. Frac., 1983, Vol. 22, pp. R69-R75.
189. N. A. Fleck, I. F. C. Smith, and R. A. Smith, "Closure Behaviour of Surface Cracks," Fat. Eng. Mats. Struc., 1983, Vol. 6, pp. 225-239.
190. W. A. Troha, T. Nicholas, and A. F. Grandt, Jr., "Three-Dimensional Aspects of Fatigue Crack Closure in Surface Flaws in a Transparent Material," In press: Fatigue Crack Closure, ASTM STP 982, J. C. Newman and W. Elber, Eds., American Society for Testing and Materials, Philadelphia, PA.
191. A. J. McEvily and K. Minakawa, "Crack Closure and the Conditions for Fatigue Crack Propagation," Fatigue Crack Growth Threshold Concepts, D. Davidson and S. Suresh, Eds., TMS-AIME, Warrendale, PA, 1984, pp. 517-530.
192. J. Telesman and D. M. Fisher, "Evaluation of the Effect of Crack Closure on Fatigue Crack Growth of Simulated Short Cracks," NASA Technical Memorandum 83778, National Aeronautical and Space Administration, Washington, D. C., 1984.
193. K. Minakawa, H. Nakamura, and A. J. McEvily, "On the Development of Crack Closure with Crack Advance in a Ferritic Steel," Scripta Met., 1984, Vol. 18, pp. 1371-1374.
194. B. N. Leis, D. P. Goetz, J. Ahmad, M. F. Kanninen, and A. T. Hopper, "Mechanics Aspects of Microcrack Growth in Inconel 718 - Implications for Engine Component Retirement for Cause Analysis," Air Force Wright Aeronautical Laboratories Report AFWAL-TR-84-4041, Wright-Patterson AFB, OH, 1984.
195. W. L. Morris and O. Buck, "Crack Closure Load Measurements for Microcracks Developed During the Fatigue of Al 2219-T851," Metall. Trans., 1977, Vol. 8A, pp. 597-601.

196. W. L. Morris, "The Early Stage of Fatigue Crack Propagation in Al 2048," Metall. Trans., 1977, Vol. 8A, pp. 589-595.
197. W. L. Morris, "Crack Closure Load Development for Surface Microcracks in Al 2219-T851," Metall. Trans., 1977, Vol. 8A, pp. 1079-1085.
198. W. J. Pardee, W. F. Morris, and R. C. Addison, "Quantitative Nondestructive Evaluation (NDE) for Retirement-for-Cause," Annual Technical Report No. 1 on Defense Advanced Research Projects Agency Contract No. MDA903-80-C-0641, Rockwell International Science Center, Thousand Oaks, CA, 1981.
199. M. R. James and W. L. Morris, "Effect of Fracture Surface Roughness on Growth of Short Fatigue Cracks," Metall. Trans., 1983, Vol. 14A, pp. 153-155.
200. W. L. Morris, M. R. James, and O. Buck, "A Simple Model of Stress Intensity Range Threshold and Crack Closure Stress," Eng. Fract. Mech., 1983, Vol. 4, pp. 871-877.
201. K. Tanaka and Y. Nakai, "Propagation and Non-Propagation of Short Fatigue Cracks at a Sharp Notch," Fat. Eng. Mats. Struc., 1983, Vol. 6, pp. 315-327.
202. K. Tanaka and Y. Akiyawa, "The Propagation of Short Fatigue Cracks at Notches," Presented at the ASTM Symposium on Fundamental Questions and Critical Experiments on Fatigue, Dallas, TX, Oct., 1984. In press: ASTM STP.
203. N. S. Iyyer and N. E. Dowling, "Opening and Closing of Cracks at High Cyclic Strains," Small Fatigue Cracks, R. O. Ritchie and J. Lankford, Eds., The Metallurgical Society, Inc., Warrendale, PA, 1986, pp. 213-223.
204. R. P. Gangloff, "The Criticality of Crack Size in Aqueous Corrosion Fatigue," Res Mechanica Letters, 1981, Vol. 1, pp. 299-306.
205. R. P. Gangloff, "Electrical Potential Monitoring of Crack Formation and Growth from Small Defects," Report No. 79CRD267, General Electric Company, 1980.
206. R. P. Gangloff, "Electrical Potential Monitoring of Crack Formation and Subcritical Growth from Small Defects," Fat. Eng. Mats. Struc., 1981, Vol. 4, pp. 15-33.
207. R. P. Gangloff, "Quantitative Measurements of the Growth Kinetics of Small Fatigue Cracks in 10Ni Steel," Fatigue Crack Growth Measurement and Data Analysis, ASTM STP 738, S. J. Hudak, Jr., and R. J. Bucci, Eds., American Society for Testing and Materials, Philadelphia, PA, 1981, pp. 120-138.
208. A. Saxena, W. K. Wilson, L. D. Roth, and P. K. Liaw, "The Behavior of Small Fatigue Cracks at Notches in Corrosive Environments," Int. J. Frac., 1985, Vol. 28, pp. 69-82.
209. J. Lankford, "The Effect of Environment on the Growth of Small Fatigue Cracks,"

Fat. Eng. Mats. Struc., 1983, Vol. 6, pp. 15-31.

210. Metals Handbook Ninth Edition. Vol. 2. Properties and Selection: Nonferrous Alloys and Pure Metals, American Society for Metals, Metals Park, OH, 1979, pp. 814-816.
211. J. E. Allison and J. C. Williams, "Near-Threshold Fatigue Crack Growth Phenomena at Elevated Temperature in Titanium Alloys," Scripta Met., Vol. 19, 1985, pp. 773-778.
212. M. J. Blackburn, "The Ordering Transformation in Titanium:Aluminum Alloys Containing up to 25 at. pct Aluminum," Transactions of the Metallurgical Society of AIME, 1967, Vol. 239, pp. 1200-1208.
213. M. J. Blackburn and J. C. Williams, "Strength, Deformation Modes, and Fracture in Titanium-Aluminum Alloys," Transactions of the American Society for Metals, 1969, Vol. 62, pp. 398-409.
214. J. D. Boyd and R. G. Hoagland, "Slip in Titanium-Aluminum Alloys Containing Small  $Ti_3Al$  Precipitates," Titanium Science and Technology, R. I. Jaffee and H. M. Burte, Eds., TMS-AIME, Warrendale, PA, 1973, pp. 1071-1083.
215. J. C. Chesnutt and N. E. Paton, "Hold Time Effects on Fatigue Crack Propagation in Ti-6Al and Ti-6Al-4V," Titanium '80 - Science and Technology, H. Kimura and O. Izumi, Eds., TMS-AIME, Warrendale, PA, 1980, pp. 1855-1863.
216. J. C. Chesnutt and J. C. Williams, "Comments on the Electron Fractography of  $\alpha$ -Titanium," Metall. Trans., 1977, Vol. 8A, pp. 514-515.
217. F. A. Crossley and W. F. Carew, "Embrittlement of Ti-Al Alloys in the 6 to 10 Pct Al Range," J. of Metals, 1957, pp. 43-46.
218. K. R. Evans, "The Embrittlement and Fracture of Ti-8 pct Al Alloys," Transactions of the Metallurgical Society of AIME, 1969, Vol. 245, pp. 1297-1303.
219. G. T. Gray, III and G. Lütjering, "The Effect of Oxygen Content on the Fatigue Crack Propagation of Ti-8.6Al," Titanium. Science and Technology, G. Lütjering, U. Zwicker, and W. Bunk, Eds., DGM, Oberursel, West Germany, 1985, pp. 2115-2122.
220. A. Gysler, J. Lindigkeit, and G. Lütjering, "Correlation Between Microstructure and Fatigue Fracture," Strength of Metals and Alloys, Vol. 2, P. Haasen, Ed., Pergamon Press, New York, NY, 1979, pp. 1113-1118.
221. A. Gysler and G. Lütjering, "Influence of Test Temperature and Microstructure on the Tensile Properties of Titanium Alloys," Metall. Trans., 1982, Vol. 13A, pp. 1435-1443.
222. A. Gysler, G. Terlinde, and G. Lütjering, "Influence of Grain Size on the Ductility



- of Age-Hardened Titanium Alloys," Titanium and Titanium Alloys, Vol. 3, J. C. Williams and A. F. Belov, Eds., Plenum Press, New York, 1982, pp. 1919-1931.
223. A. Gysler and S. Weissmann, "Deformation Behavior of Age-Hardened Titanium-Aluminum Alloys at Elevated Temperatures," Proceedings of the Second International Conference on Mechanical Behavior of Materials, 1976, pp. 339-343.
  224. A. Gysler and S. Weissmann, "Effect of Order in  $Ti_3Al$  Particles and of Temperature on the Deformation Behavior of Age-hardened Ti-Al Alloys," Mater. Sci. Eng., 1977, Vol. 27, pp. 181-193.
  225. J. M. Larsen, T. Nicholas, A. W. Thompson, and J. C. Williams, "Small-Crack Growth in Titanium-Aluminum Alloys," Small Fatigue Cracks, R. O. Ritchie and J. Lankford, Eds., The Metallurgical Society, Inc., Warrendale, PA, 1986, pp. 499-512.
  226. J. M. Larsen, J. C. Williams, and A. W. Thompson, "Crack Closure Effects on the Growth of Small Surface Cracks in Titanium-Aluminum Alloys," In press: Fatigue Crack Closure, ASTM STP 982, J. C. Newman and W. Elber, Eds., American Society for Testing and Materials, Philadelphia, PA.
  227. G. Lütjering and S. Weissmann, "Mechanical Properties of Age-Hardened Titanium-Aluminum Alloys," Acta Met., 1970, Vol. 18, pp. 785-795.
  228. J. Lindigkeit, G. Terlinde, A. Gysler, and G. Lütjering, "The Effect of Grain Size on the Fatigue Crack Propagation Behavior of Age-Hardened Alloys in Inert and Corrosive Environment," Acta Met., 1979, Vol. 27, pp. 1717-1726.
  229. T. K. G. Nambloodhiri, C. J. McMahon, Jr., and H. Herman, "Decomposition of the  $\alpha$ -Phase in Titanium-Rich Ti-Al Alloys," Metall. Trans., 1973, Vol. 4, pp. 1323-1331.
  230. N. E. Paton, R. G. Baggerly, and J. C. Williams, "Deformation and Solid Solution Strengthening of Titanium-Aluminum Single Crystals," Rockwell International Science Center final report on Contract No. F44620-72-C-0043, Air Force Office of Scientific Research Report AFOSR-TR-76-0147, 1976.
  231. N. E. Paton and J. C. Williams, "Effect of Hydrogen on Titanium and Its Alloys," Hydrogen in Metals, American Society for Metals, Metals Park, OH, 1974, pp. 409-432.
  232. N. E. Paton, J. C. Williams, and G. P. Rauscher, "The Deformation of Alpha-Phase Titanium," Titanium Science and Technology, R. I. Jaffee and H. M. Burte, Eds., TMS-AIME, Warrendale, PA, 1973, pp. 1049-1069.
  233. J. L. Robinson and C. J. Beevers, "Some Observations on Fatigue Crack Growth in Alpha-Titanium," Titanium Science and Technology, R. I. Jaffee and H. M. Burte, Eds., TMS-AIME, Warrendale, PA, 1973, pp. 1245-1256.

234. G. Terlinde and G. Lütjering, "Influence of Grain Size and Age-Hardening on Dislocation Pileups and Tensile Fracture for a Ti-Al Alloy," Metall. Trans., 1982, Vol. 13A, pp. 1283-1292.
235. D. R. Thornberg and H. R. Piehler, "Cold-Rolling Texture Development in Titanium and Titanium-Aluminum Alloys," Titanium Science and Technology, R. I. Jaffee and H. M. Burte, Eds., TMS-AIME, Warrendale, PA, 1973, pp. 1187-1197.
236. D. J. Truax and C. J. McMahon, Jr., "Plastic Behavior of Titanium-Aluminum Alloys," Mater. Sci. Eng., 1974, Vol. 13, pp. 125-139.
237. C. M. Ward-Close and C. J. Beevers, "The Influence of Grain Orientation on the Mode and Rate of Fatigue Crack Growth in  $\alpha$ -Titanium," Metall. Trans., 1980, Vol. 11A, pp. 1007-1017.
238. J. C. Williams and M. J. Blackburn, "The Structure, Mechanical Properties, and Deformation Behavior of Ti-Al and Ti-Al-X Alloys," in Ordered Alloys: Structural Applications and Physical Metallurgy, Claitor's Publishing Division, Baton Rouge, LA, 1970, pp. 425-445.
239. J. C. Williams, A. W. Sommer, and P. P. Tung, "The Influence of Oxygen Concentration on the Internal Stress and Dislocation Arrangements in  $\alpha$  Titanium," Metall. Trans., 1972, Vol. 3, pp. 2979-2984.
240. J. C. Williams, A. W. Thompson, C. G. Rhodes, and J. C. Chesnutt, "Strengthening and Fracture Mechanisms in Titanium Alloys," Titanium and Titanium Alloys, J. C. Williams and A. F. Belov, Eds., Plenum Press, New York, 1982, pp. 467-496.
241. J. E. Allison, Personal communication, Ford Research Laboratory, Detroit, MI, 1983.
242. ASTM E112 - 84, "Standard Methods for Determining Average Grain Size", 1985 Annual Book of ASTM Standards, Vol. 03.03, American Society for Testing and Materials, Philadelphia, PA, 1985, pp. 117-149.
243. A. W. Thompson, Metallography, Vol. 5, 1972, pp. 366-369.
244. G. E. Dieter, Mechanical Metallurgy, Second Edition, McGraw-Hill, New York, 1976, pp. 435-438.
245. ASTM E8 - 85b, "Standard Methods of Tension Testing of Metallic Materials", 1986 Annual Book of ASTM Standards, Vol. 03.01, American Society for Testing and Materials, Philadelphia, PA, 1986, pp. 124-145.
246. ASTM E466 - 82, "Standard Practice for Conducting Constant Amplitude Axial Fatigue Tests of Metallic Materials", 1986 Annual Book of ASTM Standards, Vol. 03.01, American Society for Testing and Materials, Philadelphia, PA, 1986, pp.

571-576.

247. J. Cammett, Personal communication, Metcut Research, Cincinnati, OH, 1983.
248. ASTM E399 - 83, "Standard Methods for Plane-Strain Fracture Toughness of Metallic Materials", 1986 Annual Book of ASTM Standards, Vol. 03.01, American Society for Testing and Materials, Philadelphia, PA, 1986, pp. 522-557.
249. ASTM E647 - 86, "Standard Test Method Measurement of Fatigue Crack Growth Rates", 1987 Annual Book of ASTM Standards, Vol. 03.01, American Society for Testing and Materials, Philadelphia, PA, 1987, pp. 899-926.
250. Hudak, S. J., Jr., Saxena, A., Bucci, R. J., and Malcolm, R. C., "Development of Standard Methods of Testing and Analyzing Fatigue Crack Growth Rate Data," Air Force Materials Laboratory Report AFML-TR-78-40, Wright-Patterson Air Force Base, OH, 1978.
251. ASTM Committee E24 Round Robin Test Program for Determination of Crack Growth Rates Below  $10^{-8}$  m/cycle, American Society for Testing and Materials, Philadelphia, PA, 1984.
252. J. M. Larsen, "An Automated Photomicroscopic System for Monitoring the Growth of Small Fatigue Cracks," Fracture Mechanics: Seventeenth Volume, ASTM STP 905, J. H. Underwood, R. Chait, C. W. Smith, D. P. Wilhem, W. A. Andrews, and J. C. Newman, Eds., American Society for Testing and Materials, Philadelphia, PA, 1986, pp. 226-238.
253. R. E. Peterson, Stress Concentration Factors, Wiley Co., 1974, p. 37.
254. A. M. Rajendran, Personal communication, University of Dayton Research Institute, Dayton, OH, 1983.
255. J. M. Larsen, J. R. Jira, and T. Weerasooriya, "Crack Opening Displacement Measurements on Small Cracks in Fatigue," In press: Fracture Mechanics: Eighteenth Symposium, ASTM STP 945, D. T. Read and R. P. Reed, Eds., American Society for Testing and Materials, Philadelphia, 1987.
256. Eastman Kodak Co., Kodak Professional Black-and-White Films, Second Addition, Eastman Kodak Co., 1976.
257. W. N. Sharpe, Jr., "A New Optical Technique for Rapid Determination of Creep and Fatigue Thresholds at High Temperature," Air Force Wright Aeronautical Laboratories Report AFWAL-TR-84-4028, Wright-Patterson AFB, OH, 1984.
258. W. N. Sharpe, Jr., "Interferometric Surface Strain Measurement," International Journal of Nondestructive Testing, 1971, pp. 59-76.
259. W. N. Sharpe, Jr. and D. R. Martin, "An Optical Gage for Strain/Displacement Measurement at High Temperature Near Fatigue Crack Tips," Air Force Materials

Laboratory Report AFML-TR-77-153, Wright-Patterson AFB, OH, 1977.

260. W. N. Sharpe, Jr. and M. Ward, "Benchmark Cyclic Plastic Notch Strain Measurements," J. Eng. Mater. Technol. Trans. ASME, 1983, Vol. 105, pp. 235-241.
261. J. M. Larsen, "Advanced Experimental Methods for Monitoring the Growth of Small Fatigue Cracks," Damage Tolerance Concepts for Critical Engine Components, AGARD Conference Proceedings No. 393, NATO Advisory Group for Aerospace Research and Development, 1985, pp. 14.1-14.15.
262. C. Mattheck, P. Morawietz, and D. Munz, "Stress Intensity Factor at the Surface and at the Deepest Point of a Semi-Elliptical Surface Crack in Plates Under Stress Gradients," Int. J. Frac., 1983, Vol. 23, pp. 201-212.
263. E. E. Underwood, "Quantitative Fractography," Handbook of Applied Metallography, G. f. Vander Voort, Ed., Reinhold Co., Inc., New York, 1986, pp. 101-122.
264. L. M. Keer and T. Mura, "Stationary Crack and Continuous Distributions of Dislocations," Proceeding of the First International Conference on Fracture, T. Yokobori, Ed., Japanese Society for Strength and Fracture of Materials, 1965, pp. 99-115.
265. J. R. Rice and D. M. Tracey, "Computational Fracture Mechanics," Numerical and Computer Methods in Structural Mechanics, S. J. Fenves et al, Eds., Academic Press, New York, 1973, pp. 585-623.
266. T. Nicholas, A. Palazotto, and E. Bednarz, "An Analytical Investigation of Plasticity Induced Closure Involving Short Cracks," In press: Fatigue Crack Closure, ASTM STP 982, J. C. Newman and W. Elber, Eds., American Society for Testing and Materials, Philadelphia, PA.